# GUSSOW 2024

## Montney Subsurface Evaluation: Drive Towards Excellence

Banff, AB | October 2-4

# EXTENDED ABSTRACT BOOK

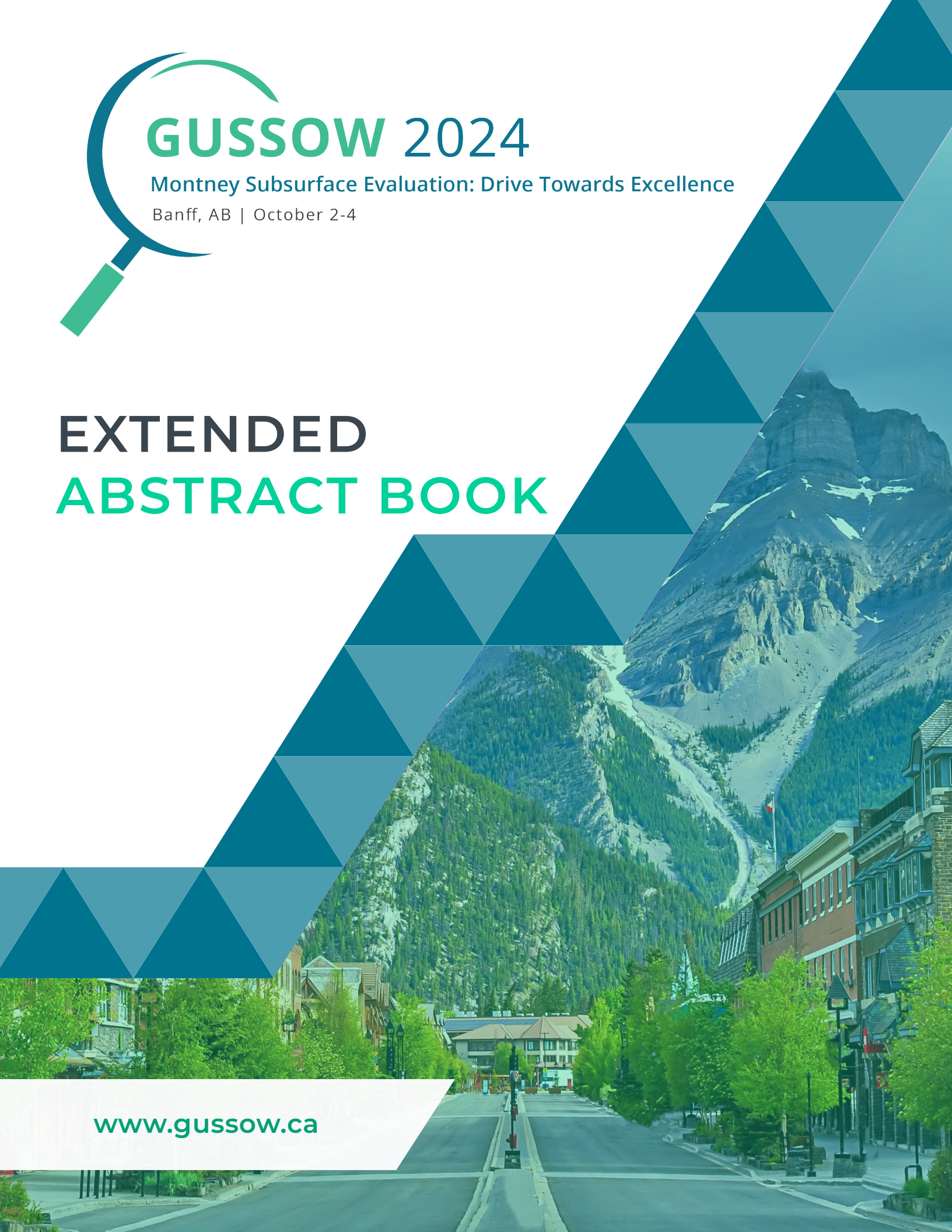

www.gussow.ca

# TABLE OF CONTENTS

GUSSOW 2024
Montney Subsurface Evaluation: Drive Towards Excellence
Banff, AB | October 2-4

# Basin-scale high-resolution stratigraphic architecture of the Montney Formation: structural and depositional controls

Tristan Euzen[1], Thomas F. Moslow[2], Charles M. Henderson[3] and Steve Power[4].

1. IFP Technologies (Canada) Inc.; 2. Moslow Geoscience Consulting Ltd.; 3. University of Calgary; 4. Gear Energy Ltd.

## Abstract

Inconsistencies in the nomenclature and stratigraphic correlations of internal subdivisions of the Montney Formation have hindered for decades efficient communication among stakeholders in industry, governmental agencies and academia. To address this challenge, we propose a comprehensive approach to building a unified basin-wide high-resolution and self-consistent stratigraphic architecture model of the Montney Formation. In this paper, we illustrate how a 550-km long regional seismic-like, along-strike, cross-section with a high density of well, as well as core and biostratigraphic control across British Columbia and Alberta helps define a more reliable basin-wide, high-resolution stratigraphic framework of the Montney Formation.

Our interpretation reveals lateral onlap of Smithian stratigraphic units in the Peace River Arch area, influenced by the structural framework and top-Dienerian Stoddart paleo-high to the north. Depositional compensation is also suggested by lateral shifts of depocentres between successive stratigraphic units within the Smithian and Spathian Lower Triassic substage sequences. This analysis suggests that some of the turbidite facies in the La Glace and Valhalla areas were deposited during the Smithian late lowstand and early highstand systems tracts, postdating early lowstand deposits confined within the Fort St John Graben structural low. Along-strike depositional architecture also highlights the influence of major structural elements on Montney deposition. These include the Fort St John Graben, the Hay River Fault Zone, the northern boundary fault of the Laurier Embayment and the southern margin of the Peace River Arch.

A better understanding of along-strike depositional architecture laid the foundation for the stratigraphic log correlation of over 5,400 wells using a careful data-driven approach, calibrated with available core descriptions and conodont biostratigraphy. The Montney Formation is subdivided into 18 internal units, using a nomenclature based on Triassic informal substages (Griesbachian, Dienerian, Smithian and Spathian) calibrated to conodont biostratigraphy.

Owing to a precise stratigraphic assignment of Montney horizontal wells across the basin, this updated stratigraphic model can help better predict spatial variations of facies and reservoir properties both at local and regional scales and provides a robust framework to compare production performances within and between operators' assets.

## Statement of the background

The Montney Formation provides an exceptional case study to help improve our understanding of shallow water mixed siliciclastic/carbonate depositional systems. The quality and the quantity of data from thousands of wells drilled by the industry over the past three decades, made publicly available by the British Columbia and Alberta Energy Regulators, is staggering and probably unique in the world. But beyond the academic endeavour, understanding the stratigraphic architecture of the Montney depositional system and its underpinning geological controls has many practical benefits to help optimize the exploration and development of this massive unconventional play. However, building a high-resolution and consistent stratigraphic framework of the Montney Formation at the basin-scale is a daunting task. It requires a dedicated team of experienced geologists that can spend hundreds of hours focusing on core logging and calibration, well-log correlation, and geological mapping. This process cannot be automated using AI techniques (at least to our knowledge, at this time), nor should it be fragmented between separate asset teams for self-consistency. Furthermore, highly skilled geoscientists working in oil and gas companies usually don't have the luxury of time to achieve such a massive undertaking due to business and operational constraints. In this paper, we present a high-resolution, basin-wide stratigraphic architecture

of the Montney Formation, that was built thanks to a collaboration between dedicated consultants, academia and industry in addition to accessing public data through energy regulator portals.

## Aims and Objectives

The Montney Formation has been extensively studied over the past three decades. It is now well established that this sedimentary wedge is composed of three 3rd-order stratigraphic sequences. Numerous published dip-oriented cross-sections and sedimentological evidence from core descriptions clearly illustrate sub-aqueous clinoform geometries and the overall ENE-WSW prograding trend of this mixed siliciclastic/carbonate shelf depositional system (Davies et al., 1997, 2018; Wood, 2012; Crombez et al., 2016; Prenoslo et al., 2018; Proverbs et al., 2018, Euzen et al., 2018; 2021). However, the basin-wide along-strike stratigraphic architecture of the Montney Formation is comparatively poorly understood, and a simple layer cake geometry is often implicitly assumed when correlating different parts of the basin.

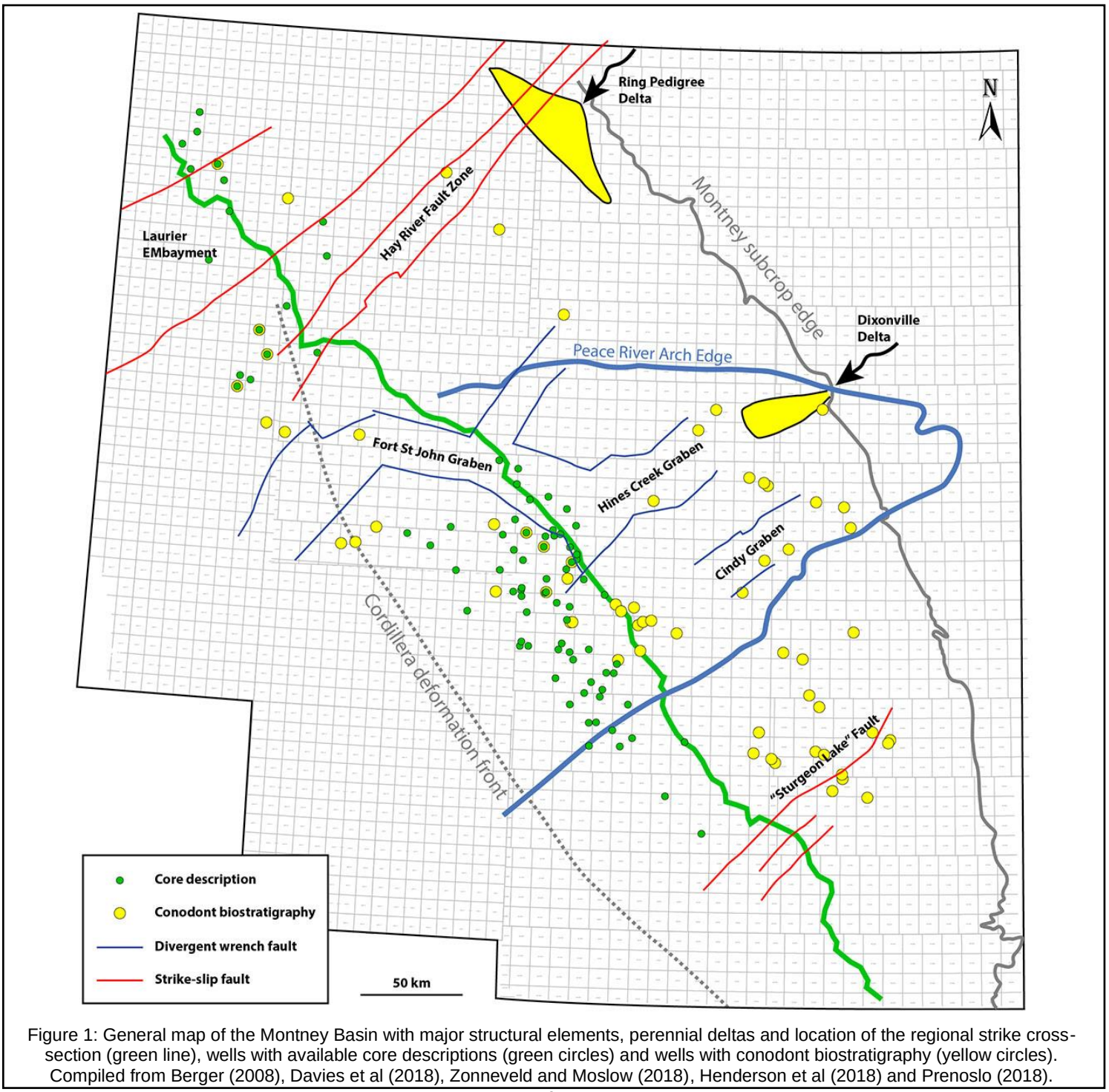


Figure 1: General map of the Montney Basin with major structural elements, perennial deltas and location of the regional strike cross-section (green line), wells with available core descriptions (green circles) and wells with conodont biostratigraphy (yellow circles). Compiled from Berger (2008), Davies et al (2018), Zonneveld and Moslow (2018), Henderson et al (2018) and Prenoslo (2018).

However, a careful analysis illustrates complex along-strike stratal relationships that result in common regional inconsistencies of the current high-resolution stratigraphic nomenclature of Montney tops between operators, government ministries and published studies. To overcome this challenge and build a more reliable high-resolution stratigraphic framework of the Montney Formation at the basin scale, we constructed a 550-km long regional along-strike cross-section with a high density of well control (287 wells) across British Columbia and Alberta (green line on Figure 1).
Our observations demonstrate that along-strike geometries are controlled by spatial and temporal variations in accommodation space and sediment supply source-location and intensity, influenced by the structural framework and auto-cyclic depositional processes, such as lateral compensation. This documentation of basin-scale along-strike architecture of the Montney has provided the foundation for high-resolution, time-correlative, stratigraphic log correlation of over 5,400 wells with Belloy penetration across Montney sub-basins. The Montney Formation is subdivided into 18 internal units, using a nomenclature based on Triassic informal substages (Griesbachian, Dienerian, Smithian and Spathian) calibrated with conodont biostratigraphy (Henderson et al., 2018). This work aims at providing a robust framework to better understand the influence of regional depositional geometries on facies distribution and reservoir properties, and ultimately enhance the predictability of horizontal well performance based on an accurate determination of stratigraphic landing zones.

## Materials and methods

Stratigraphic correlation techniques rely on various data sources (well logs, cores/cuttings, seismic, outcrops…) and types (electrical, acoustic properties, radioactivity, geochemistry, paleobiology, visual description…) and is guided by preconceived models derived from sedimentology and sequence stratigraphy. The degree to which each of these elements influences the interpretation depends on the available dataset, the scale of investigation and the practical objective motivating the stratigraphic correlations. For instance, on a local reservoir scale with high-resolution 3-D seismic and good well control, a data-driven approach is preferred and understanding how the reservoir model fits into a more regional stratigraphic framework is not always key for practical purposes. In an underexplored basin with limited data on the other hand, a model-driven approach strongly relying on sequence stratigraphy principles and depositional system analogues prevails. Sequence stratigraphy provides an invaluable tool to better understand depositional systems, but it is essential to recognize that our ability to identify stratigraphic surfaces and systems tracts and their hierarchical order is strongly dependant on the scale of observation and the density and type of data available (Catuneanu et al., 2009). Furthermore, the expression of these stratigraphic elements varies widely between depositional systems, and even within a single system, due to local changes in accommodation and sediment supply as well as auto-cyclic processes (Catuneanu et al, 2011).
The Montney Formation provides a world-class case study to understand the stratigraphic architecture of a shallow water depositional system, thanks to over 30 years of oil and gas development and a high density of well control at regional scale, especially along the unconventional fairway covering an area of approximately 80,000 $km^2$. This exceptional dataset allows for using a data-driven approach to reveal large-scale depositional geometries and stratal relationships, thus minimizing the risk of forcing the interpretation into a preconceived idealized model. To this end, we constructed a basin-wide, along-strike, 550 km-long cross-section following a path that minimizes the distance between successive wells (average distance between wells is 2 km). A seismic-like display using properly scaled gamma ray logs was constructed to visualize along-strike lateral geometries prior to any interpretation. Note that this seismic-like display was only used as a general guide and for illustrative purposes. The stratigraphic well-log correlations were performed at a finer scale using the gamma ray and resistivity logs in combination. This proved to be much more powerful than using either log independently. This basin-wide cross-section provided the foundation to propagate the correlations throughout the basin to over 5,400 wells with Belloy penetrations. Correlated surfaces were selected and calibrated based on sedimentological core descriptions from 80 wells and using publicly available conodont biostratigraphic data from 69 wells (see locations on Figure 1). Figure 2 provides an illustration of this calibration for the 315 m-long full Montney core from well 06-03-079-13W6 (Pouce Coupe area). The conodont samples collected from this core provide the most detailed and complete biostratigraphic record in a single Montney well to date (Brar, 2021).
For practical purposes, another important criterion for selecting a surface is that its log character must be strong enough to be correlated regionally. Most significant stratigraphic surfaces are generally demarcated by a flooding event that is expressed downhole as an abrupt increase in API value on the GR log and an increase or a drop in conductivity on the resistivity log. However, the log expression of a surface can sometimes become very subtle in instances where lithologic and/or mineralogic contrast is muted. Minimizing distances between successive wells as much as possible is very helpful in overcoming this challenge.

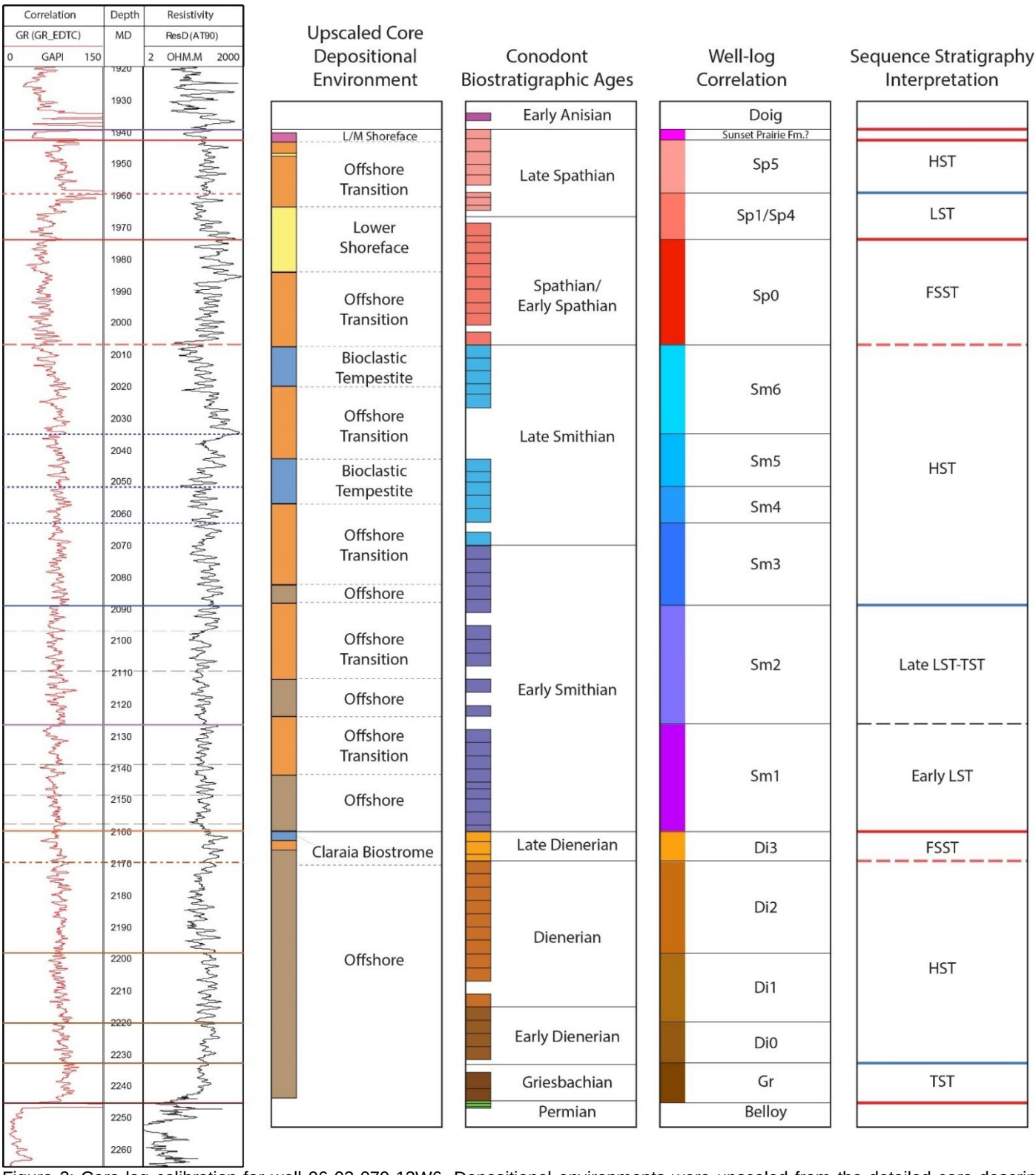


Figure 2: Core-log calibration for well 06-03-079-13W6. Depositional environments were upscaled from the detailed core description. Conodont biostratigraphic ages from Brar (2021). Colour codes used for depositional environment and stratigraphic units are the same in Figure 4, 5 and 6.

As illustrated in Figure 3, close well spacing allows for tracking individual cycles/bed-sets from one well to the next, almost like interpreting an outcrop section. This approach is particularly useful in distal fine-grained deposits (offshore/offshore transition depositional environments) where lateral facies changes are generally gradual. Another key practice to minimize uncertainty in correlations is to ensure self-consistency by “circling around” and checking intersections of multiple cross-

sections with different orientations. This is a very time-consuming process that often involves multiple passes, with each modification requiring the update of tens or even hundreds of wells. However, this approach significantly improves the robustness of the stratigraphic interpretation. From a sequence stratigraphic standpoint, correlated surfaces correspond to 3rd-order stratigraphic surfaces (sequence boundary, maximum flooding surface, basal surface of forced regression) and 4th-order stratigraphic surfaces (marine flooding surface topping parasequence sets).

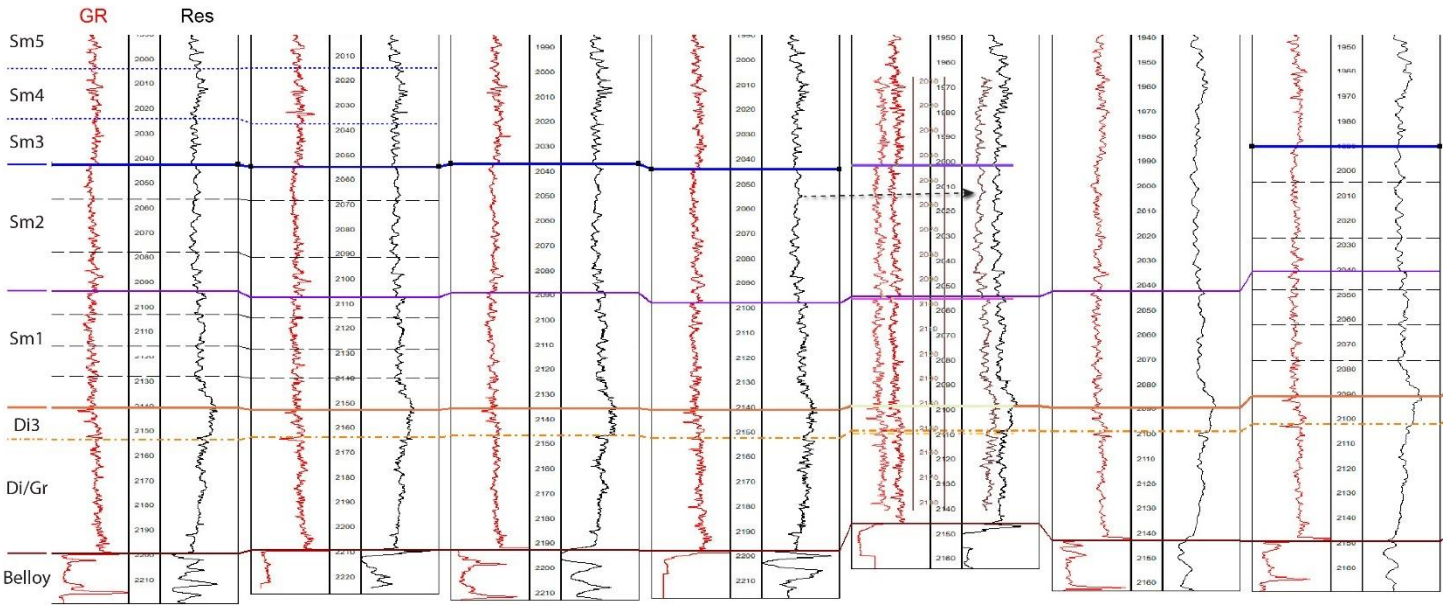


Figure 3: Correlation technique using tight well spacing in offshore transition to offshore sedimentary facies. Logs from the middle well are duplicated and superimposed to the next well on the right (dashed arrow) to illustrate how individual cycles/bedsets can be tracked laterally.

## Results and discussion

### Regional stratigraphic architecture

The map of Figure 1 shows the location of the regional strike cross-section (green line) along with major structural elements of the Montney basin (Barclay et al., 1990; Berger et al., 2008; Zonneveld and Moslow, 2018; Davies et al., 2018; Prenoslo et al., 2018). This cross-section extends over the entire Montney basin from township 55-22W5 in the southeast to township I/94-G6 in the northwest. Figure 4 shows the seismic-like display of the cross-section (Fig. 4a), the stratigraphic interpretation derived from detailed correlations (Fig. 4b) and the structural profile (elevation) along the path of the cross-section (Fig. 4c). Thanks to the high density of wells along the seismic-like cross-section, it is possible to visualize large scale along-strike depositional geometries and stratal relationships without any interpretive overlay. Note that the distance between successive wells can depart from the average of 2 km in areas with fewer or higher density of wells, resulting in mild lateral distortion of observed geometries. Changes of character in the gamma ray log signature can also be observed, such as high amplitude variations highlighting turbidite facies in the Valhalla area (Moslow, 2000). Besides depositional geometries, structural features are also recognized by abrupt thickness and/or slope changes across inferred faults along the stratigraphic cross-sections (Datum: base Doig Phosphate). The structural profile along the path of the cross-section highlights that present-day structural offset is associated with some of these faults (marked by double arrows on Fig. 4c). A transcurrent component to the structural offset is likely along strike slip faults nearly perpendicular to the Cordillera and parallel to the maximum horizontal stress orientation (red faults on Figure 1).

Based on this structural framework and on depositional geometries, five areas with different tectono-stratigraphic makeup can be defined:

(1) Along the southern part of the cross-section between Placid and Wembley fields (see field locations on Fig. 4b), the apparent dip to the northwest suggests that there is a southeast to northwest component to sediment transport and progradation during Dienerian and Smithian times. Some of the turbidite facies of the Valhalla area that are visible on the seismic-like cross-section (darker high GR amplitude intervals over Valhalla area highlighted with arrows on Fig. 4a) appear to be associated with this progradation. Valhalla-La Glace turbidites are also located downdip from the Cindy graben that was proposed as a sediment fairway (Davies et al., 1997; Moslow and Davies, 1997; Moslow, 2000; location of Cindy Graben on Fig. 1 and 4b). The southern margin of the Peace River Arch is associated with a structural offset with thin remnant Spathian deposits north of the Elmworth field (Fig. 4b).

(2) North of this inferred fault in the Peace River embayment (collapsed Peace River Arch), a major Montney depocentre is associated with the Fort St. John Graben (Pouce Coupe and Mica fields). Early lowstand deposits of Smithian unit Sm1 (purple unit on Fig. 4b) are mostly confined within the graben area and onlap laterally to the northwest and southeast. This depocentre is aligned with the Dixonville delta (Zonneveld and Moslow, 2017) and the Hines Creek Graben (Barclay et al., 1990) that may have sourced and funneled Smithian lowstand deposits in the Peace River Arch (yellow arrow on Fig. 4b). Based on our correlations most of Valhalla turbidite facies postdates Smithian early lowstand deposits (Sm1) of the Fort St John Graben and were likely deposited during the late Lowstand (Sm2) and early highstand (Sm3/Sm4) of the Smithian sequence. Older relatively thin turbiditic deposits of the Di3 unit are likely associated with the late Dienerian forced regression.

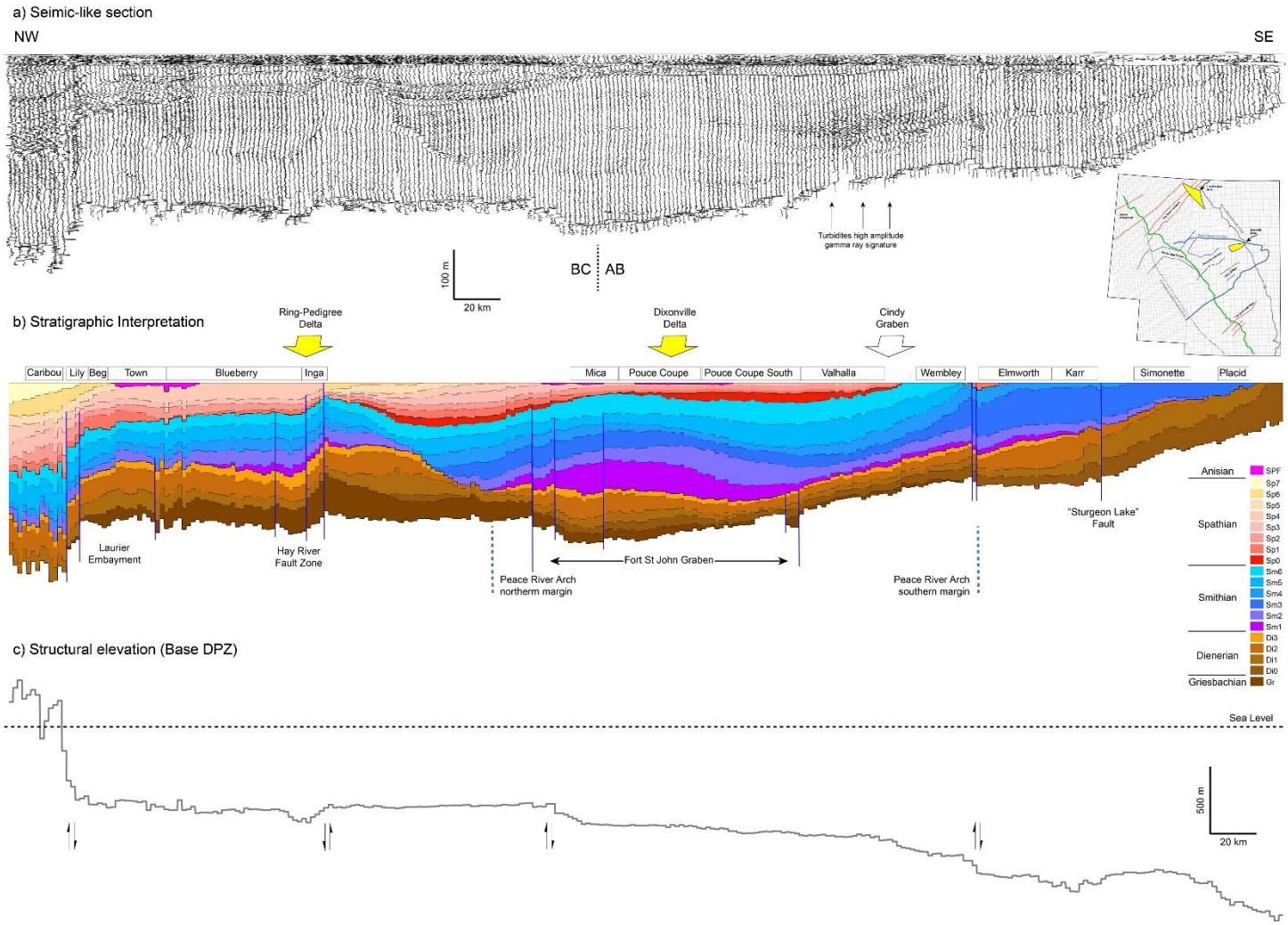


Figure 4: Basin-wide along-strike cross-section of the Montney Formation. a) Seismic-like display using closely spaced gamma ray logs. Note that there is no superimposed interpretation. b) Stratigraphic architecture based on detailed correlation using gamma ray and resistivity logs. c) Structural elevation profile along the path of the cross-section (DPZ: Doig Phosphate Zone; SPF: Sunset Prairie Formation). Datum is base of the Doig Phosphate Zone.

(3) Just north of the Peace River embayment, lowstand and early highstand Smithian deposits onlap an apparent paleohigh inherited from Griesbachian-Dienerian depositional topography. This feature, herein referred to as the Stoddart paleohigh, was discussed in Davies et al. (2018) as an alternative correlation option (see their figures 14 and 30). Thanks to the very high density of well control over the Stoddart field (targeting the Belloy Formation), we confirm that this alternative interpretation is the most likely (top Dienerian sequence boundary dipping south in Stoddart area). The location of this Stoddart depositional paleohigh suggests that it may have been sourced by the Ring Pedigree Delta that was active during Griesbachian and Dienerian times (Zonneveld et al., 2010). The Stoddart paleohigh is fringed to the north by the Hay River Fault zone, a possible fairway for the transport of sediment basinward from the Ring Pedigree Delta. Along the cross-section, Spathian deposits thin over the Hay River Fault zone suggesting that this structure may have been active at this time. A vertical offset is visible along the Hay River Fault Zone on the structural profile (Fig. 4c). However, this may also be partly caused by a change in the orientation of the cross-section in this area. Lastly, changes of slope and/or thickness observed across the Hay River Fault zone can also partly result from lateral movements along strike-slip faults.

(4) North of the Hay River Fault Zone, internal Montney stratigraphic units appear relatively isopachous (ie. Blueberry field). Further to the northwest, Spathian deposits start thickening again in the Laurier Embayment area (ie. Town field). The Laurier Embayment is also associated with the occurrence of the early Anisian Sunset Prairie Formation along the cross-section (Furlong et al., 2020).
(5) Finally, the Montney Formation thickens abruptly to the north across the northern bounding fault of the Laurier Embayment, with the preservation of thick uppermost Spathian units (Sp6 and Sp7) under the basal Doig erosional unconformity (ie. Caribou and Lily fields). This indicates that this fault was active during Montney deposition, at least during Spathian times. Geochemical evidence also suggests that rejuvenation of the Yukon-Tanana arc and associated tectonic activity influenced ocean circulation during the Spathian (Schoepfer et al, 2024). The northern bounding fault of the Laurier Embayment is associated with a major positive vertical offset to the north of over 400 m (Fig. 4c) suggesting that thrust sheets to the north might end laterally against this strike slip fault.

### Facies distribution in Peace River Arch area

In this section we focus on the Peace River Arch area to discuss in more detail the lateral facies relationships within the Montney stratigraphic architecture. Figures 5 and 6 present respectively a strike-oriented and a dip-oriented cross-section in the Peace River embayment with stratigraphic subdivisions (Fig. 5a and 6a) and the distribution of facies and depositional environments calibrated to available core descriptions (Fig. 5b and 6b).

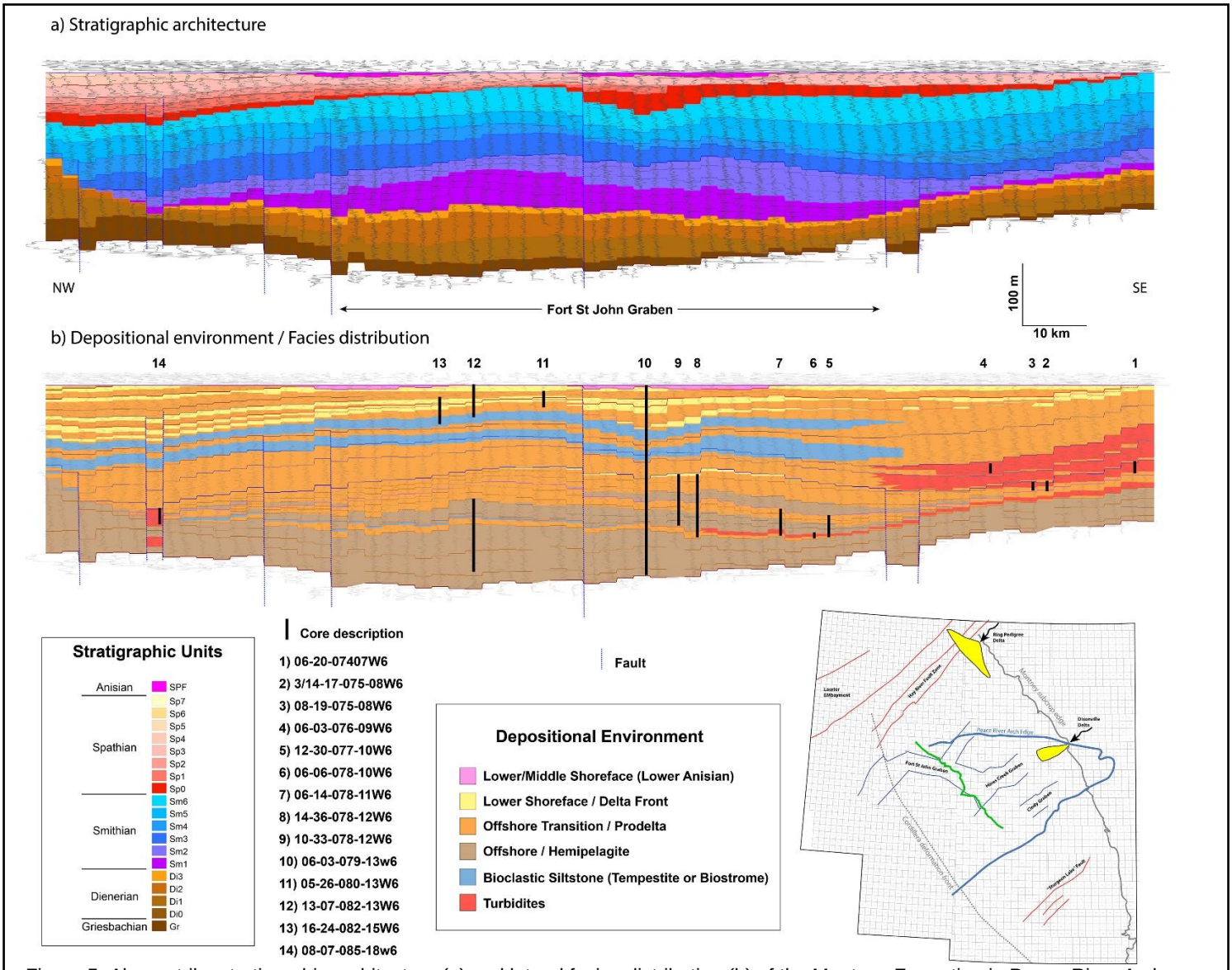


Figure 5: Along-strike stratigraphic architecture (a) and lateral facies distribution (b) of the Montney Formation in Peace River Arch area. The cross-section is the green line in the map insert.

These two cross-sections intersect each other at the well 06-03-079-13W6 with a full Montney core illustrated in Fig.2. Facies and depositional environments were upscaled from detailed core descriptions and extrapolated laterally away from cored wells based on the stratigraphic architecture and gamma ray log signature. Along the strike cross-section (Fig. 5), Dienerian and Griesbachian deposits mostly consist of bituminous fine to medium-grained siltstone interbedded with dolomitic hemipelagites of the offshore depositional environment (stratigraphic units Gr, Di1 and Di2).
In the late Dienerian (unit Di3), facies transition upward to fine to coarse-grained laminated siltstone topped by thin *Claraia* biostrome bioclastic deposits, just below the Dienerian-Smithian boundary (Pocketknife Member of Zonneveld and Moslow, 2018). The stratigraphic position of *Claraia* biostrome deposits seem to be consistent regionally, making it a good time marker for correlations. *Claraia* valves can however be found transported in tempestite beds higher within the Smithian sequence. Laterally toward the southeast of the strike cross-section (Fig. 5), the *Claraia* biostrome facies is absent and the uppermost Dienerian deposits consist of thin-bedded fine-grained turbidites. These turbidites are interpreted to be associated with the late Dienerian forced regression (falling stage systems tract). Turbidites are also present in the Dienerian and lower Smithian further north as observed along the strike cross-section (well 2/08-07-085-18W6) and seem to be localized at the toe of the Stoddart paleohigh slope (Eagle Flatrock turbidites of Davies et al, 2018).

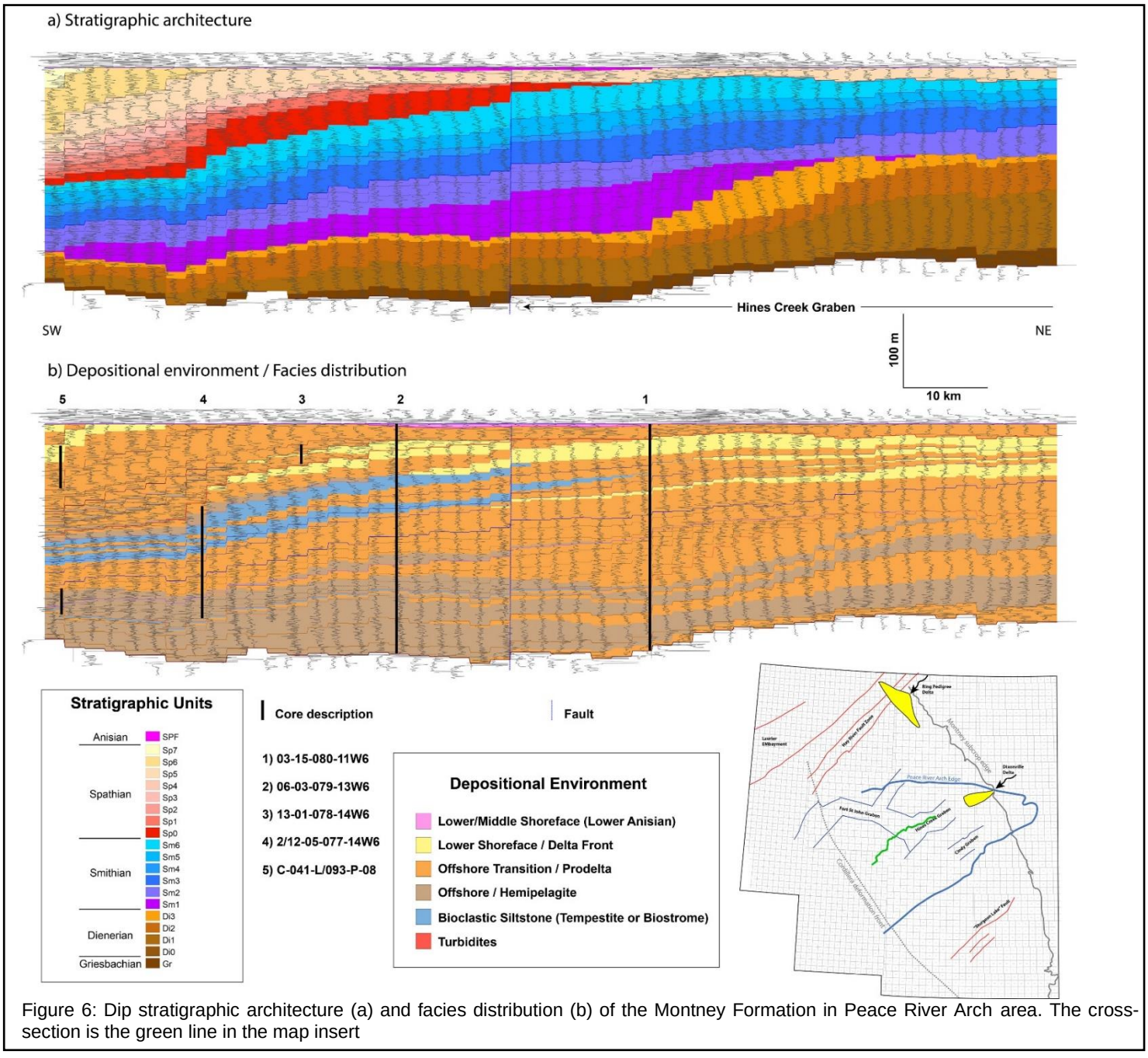


Figure 6: Dip stratigraphic architecture (a) and facies distribution (b) of the Montney Formation in Peace River Arch area. The cross-section is the green line in the map insert

Along the dip-cross-section of Figure 6, up-dip from well 06-03-079-13W6, the unit Gr and the upper part of units Di1 and Di2 consist of fine to coarse-grained laminated siltstone of the offshore transition depositional environment. The unit Di3 thickens up-dip and consists of offshore transition deposits with frequent seismite beds deformed by liquification attributable to cyclic shock (core from well 03-15-080-11W6). This suggests potential tectonic activity contemporaneous to the late Dienerian forced regression.

Early Smithian lowstand deposits (unit Sm1) are confined in a paleolow centred on the Fort St John Graben. It onlaps laterally to the north against the Stoddart paleohigh and thins down to a few metres above late Dienerian turbidite facies to the south (Fig. 5). Along the dip cross-section (Fig. 6), unit Sm1 onlaps to the northeast and downlaps to the southwest on the Dienerian-Smithian sequence boundary. This depocentre was formerly interpreted as a turbiditic fan complex based on gamma ray response (Sereda and Fur, 2017), but core descriptions show no evidence of turbidite facies and suggests that it consists predominantly of distal tempestites of the offshore transition environment of deposition (core descriptions from wells 03-15-080-11W6, 06-03-079-13W6, 13-07-082-13W6, 10-33-078-12W6 and 14-36-078-12W6).

Unit Sm2 interpreted as Smithian late lowstand is more aggradational and seems to shift to the southeast along depositional strike (see cross-section;Fig. 5), possibly due to lateral compensation over the unit Sm1. In the Fort St John Graben, Sm2 consist mostly of distal tempestites of the offshore transition environment of deposition. Further southeast along the strike cross-section (Fig. 5) it passes laterally to turbiditic deposits (core description from wells 3/08-19-075-08W6, 3/14-17-075-08W6 and 06-20-074-07W6). Above Sm2 in the Valhalla area, early highstand deposits from units Sm3 and Sm4 are also interpreted as turbidites (red shading on figure 5b) based on log response and supported by core description from well 06-03-076-09W6.

Late Smithian units Sm4 to Sm6 are interpreted as prograding highstand deposits and show the first appearance of lower shoreface/delta front depositional environment along the proximal part of the dip cross-section of Figure 6 (yellow shading). Downdip to the southwest in the offshore transition depositional environment, interbedded bioclastic tempestites are present in these units (Altares Member; Zonneveld and Moslow, 2018). This facies extends along-strike to the north up to the Laurier Embayment, but does not seem to be present south of the Fort St John Graben, although the facies transition should be better documented with additional core control (Fig. 5b). In Alberta, south of the Peace River embayment, the northwest dipping slope of clinoforms in Smithian highstand units along the basin-wide cross-section (Fig. 4a/b) suggests the existence of an active sediment source at the southeast margin of the Montney basin during middle/late Smithian times.

The Smithian-Spathian transition is marked by the disappearance of bioclastic beds and the common occurrence of skeletal debris (fish and marine reptiles; Zonneveld and Moslow; 2018), phosphatic clasts, soft sediment deformation, bioturbation, and an increase of the organic matter content in early Spathian deposits. The basal Spathian unit defined here as Sp0 was previously misinterpreted as late Smithian (Middle Montney) based on well log correlations (Euzen et al., 2018; Davies et al., 2018; Proverbs et al., 2018, Prenoslo et al, 2018). This early Spathian interval has since been well documented from core descriptions in wells 06-03-079-13W6 and 2/12-05-077-14W6 (Figure 6a; dark red shading). The reason why this basal Spathian unit was missed is probably because its upper boundary (surface between Sp0 and Sp1) is associated with a major flooding event (marking the end of the forced regression) and has a much stronger expression on the gamma ray log than its lower boundary. This unit also marks a basinward shift of facies with a rapid progradation of shoreface deposits along the dip cross-section of Figure 6b. It forms a localized depocentre south of the Fort St John Graben and is tentatively interpreted here as a falling stage systems tract restricted to a topographic low (forced regression). Above this basal Spathian unit Sp0, unit Sp1 corresponds to highly bioturbated lower shoreface siltstone to very fine-grained sandstone (well 06-03-079-13W6; “Dawson bioturbated siltstone-sandstone zone” of Davies et al, 2018). Along the dip cross-section of Figure 6, units Sp2 to Sp4 seem to onlap on unit Sp1, but this is because this section is located along the southern margin of these units that develop further north. The geometry and spatial distribution (isopach maps) of these Spathian stratigraphic units were discussed in detail by Euzen et al. (2018). Spathian units Sp5 to Sp7 prograde further into the basin and lower shoreface deposits in unit Sp6 are described in the most distal well of the dip cross-section of Figure 6 (core of well C-41-L/093-P08). These late Spathian units are not preserved up dip where they are eroded under the top Montney unconformity below the Doig Phosphates or the Sunset Prairie Formation (Furlong et al., 2018; SPF, purple shading on Figure 4-6).

## Conclusion

After decades of academic research and oil and gas development, the geoscience community is still missing a unified high-resolution stratigraphic framework for the Montney Formation at basin scale. In this paper, we provide the foundation for such a unified stratigraphic model, taking advantage of the exceptionally large well dataset publicly available in this formation. A key element to the robustness of this model is a better understanding of large-scale along-strike depositional geometries and structural controls, that was achieved thanks to the construction of a basin wide cross-section with a high density of well control. The model was then propagated throughout the basin over more than 5,400 wells using a data-driven approach with careful core-log calibration of facies and biostratigraphy, and a correlation technique minimizing distance between successive wells insuring self-consistency both on local and regional scales. The Montney Formation was subdivided into 18 internal units using a nomenclature based on Triassic informal substages (Griesbachian, Dienerian, Smithian and Spathian) calibrated with conodont biostratigraphy.

This high-resolution stratigraphic architecture provides a framework in which spatial facies variations can be better predicted and their influence on reservoir properties analyzed. A basin-wide consistent stratigraphic framework is also key to compare and rank production performances within and between operator's assets based on an accurate determination of stratigraphic landing zones. Our database to date comprises the landing zone stratigraphic assignment of over 10,500 Montney horizontal wells.

**Acknowledgements**

The authors thank Vermilion Energy Inc. management for their strong support to this work. Birchcliff Energy Ltd. provided permission for use of sedimentologic interpretations from a core description of the 6-3-79-13W6.

**References**

Barclay, J.E., Krause, F.F., Campbell, R.I. and Utting, J. 1990. Dynamic casting and growth faulting of the Dawson Creek Graben Complex: Carboniferous-Permian Peace River Embayment, Western Canada. In: Geology of the Peace River Arch. S.C. O'Connell and J.S. Bell (eds.). Bulletin of Canadian Petroleum Geology, v. 38A, p. 115–145

Berger, Z., Boast, M. and Mushayandebvu, M. 2008. The contribution of integreated HRAM studies to exploration and exploitation of unconventional plays in North America. Reservoir, v. 35, no. 10, p. 42–47.

Brar, R. S. 2021. Sequence Biostratigraphy and Chronostratigraphy of the Lower Triassic Montney Formation, northeast British Columbia and west-central Alberta (Unpublished master's thesis). University of Calgary, Calgary, AB.

Catuneanu, O., Abreu, V., Bhattacharya, J. P., Blum, M. D., Dalrymple, R. W., Eriksson, P. G., Fielding, C. R., Fisher, W. L., Galloway, W. E., Gibling, M. R., Giles, K. A., Holbrook, J. M., Jordan, R., Kendall, C. G. S. C., Macurda, B., Martinsen, O. J., Miall, A. D., Neal, J. E., Nummedal, D., Winker, C. (2009). Towards the standardization of sequence stratigraphy. Earth-Science Reviews, 92(1–2), 1–33.

Catuneanu, O., Galloway, W. E., Kendall, C. G. S. C., Miall, A. D., Posamentier, H. W., Strasser, A., and Tucker, M. E, 2011. Sequence Stratigraphy: Methodology and nomenclature. Newsletters on Stratigraphy, 44(3), 173–245. https://doi.org/10.1127/0078-0421/2011/0011

Crombez, V., Rohais, S., Baudin, F. and Euzen, T. 2016. Facies, well-log patterns, geometries and sequence stratigraphy of a wave-dominated margin: insight from the Montney Formation (Alberta, British Columbia, Canada). Bulletin of Canadian Petroleum Geology, v. 45, p. 474–505.

Davies, G. R., Moslow, T.F. and Sherwin, M.D. 1997. The Lower Triassic Montney Formation, West-Central Alberta. Bulletin of Canadian Petroleum Geology, v. 45, p. 474–505.
Davies et al (2018)

Euzen, T., Moslow, T. F., Crombez, V., and Rohais, S. 2018. Regional stratigraphic architecture of the Spathian Deposits in Western Canada — Implications for the Montney Resource Play. Bulletin of Canadian Petroleum Geology, 66(1), 175–192.

Euzen, T., Watson, N., Fowler, M., Mort, A., and Moslow, T. F. 2021. Petroleum distribution in the Montney hybrid play: Source, carrier bed, and structural controls. AAPG Bulletin, 105(9), 1867–1892.

Furlong, C. M., Gingras, M. K., Moslow, T. F., and Zonneveld, J.-P. 2018. The Sunset Prairie Formation: designation of a new Middle Triassic formation between the Lower Triassic Montney Formation and Middle Triassic Doig Formation in the Western Canada Sedimentary Basin, northeast British Columbias. Bulletin of Canadian Petroleum Geology, 66(1), 193–214.

Furlong, C. M., Gingras, M. K., and Zonneveld, J. P. 2020. High-resolution sequence stratigraphy of the Middle Triassic Sunset Prairie Formation, Western Canada Sedimentary Basin, north-eastern British Columbia. Depositional Record, 6(2), 383–408.

Henderson, C. M., Golding, M. L, and Orchard, M. J. 2018. Conodont sequence biostratigraphy of the Lower Triassic Montney Formation, Canada. Bulletin of Canadian Petroleum Geology, v. 66, no. 1, p. 7–22

Moslow, T. F., and Davies, G. R. 1997. Turbidite reservoir facies in the Lower Triassic Montney formation, west-central Alberta. Bulletin of Canadian Petroleum Geology, 45(4), 507–536.

Moslow, T. F. 2000. Reservoir architecture of a fine-grained turbidite system. Lower Triassic Montney Formation, Western Canada Sedimentary Basin. GCSSEPM Foundation 20th Annual Research Conference 686. Deep-Water Reservoirs of the World, December 3–6, 2000.

Prenoslo, D., Furlong, C. M., Gingras, M. K., Playter, T., and Zonneveld, J. P. 2018. The sedimentology, stratigraphy and reservoir characteristics of the Montney D1 and D2 horizons in the greater Pouce Coupe area. Bulletin of Canadian Petroleum Geology, 66(1), 338–358.

Proverbs, I. P., Bann, K. L., Fratton, C. M., Frostad, C. J., and Juska, A. 2018. Facies architecture and sequence stratigraphy of the lower Triassic Montney formation, NE British Columbia: Fundamental controls on the distribution of 'sweet spots' in a world-class unconventional reservoir. Bulletin of Canadian Petroleum Geology, 66(1), 237–258.

Schoepfer, S. D., Henderson, C. M., Moslow, T. F., and Shen, C., 2024. Extremely high resolution XRF core scanning reveals the Early Triassic depositional history of the Montney Formation in northeastern British Columbia, Canada. Palaeogeography, Palaeoclimatology, Palaeoecology, 637(August 2023), 112019.

Sereda, R. (2017). The Montney Turbidite Complex of Northwest Alberta and Northeast British Columbia: Evolution of an Oil and Gas Play From Conventional to Unconventional. Proceedings of the 5th Unconventional Resources Technology Conference. https://doi.org/10.15530/urtec-2017-2674327

Wood, J. M. 2013. Water Distribution in the Montney Tight Gas Play of the Western Canadian Sedimentary Basin: Significance for Resource Evaluation. SPE Reservoir Evaluation and Engineering, 16(03), 290–302.

Zonneveld, J. P., Macnaughton, R. B., Utting, J., Beatty, T. W., Pemberton, S. G., and Henderson, C. M. 2010. Sedimentology and ichnology of the lower Triassic Montney formation in the pedigree-ring/border-Kahntah river area, northwestern Alberta and northeastern British Columbia. Bulletin of Canadian Petroleum Geology, 58(2), 115–140.

Zonneveld, J. P., and Moslow, T. F. 2017. Palaeogeographic evolution of the Montney in the Western Canada Sedimentary Basin. GeoConvention, Calgary, Canada, May 15-19, 2017.

Zonneveld, J. P., and Moslow, T. F. 2018. Palaeogeographic setting, lithostratigraphy, and sedimentary framework of the lower Triassic Montney formation of western Alberta and northeastern British Columbia. Bulletin of Canadian Petroleum Geology, 66(1), 93–127.

GUSSOW 2024
Montney Subsurface Evaluation: Drive Towards Excellence
Banff, AB | October 2-4

# Determinant geological parameters of reservoir quality and deliverability in the Montney Formation, Northeastern British Columbia.

John-Paul Zonneveld[1], Thomas F. Moslow[2]

1.University of Alberta. 2. Moslow Geoscience Consulting

## Synopsis

The Montney Formation comprises an unusual unconventional hydrocarbon reservoir play that it is dominated by bituminous dolomitic siltstone and very fine-grained sandstone. Claystone is sparsely distributed, occurring in very specific stratigraphic, geographic and depositional settings, most typically perennial deltaic, prodeltaic and delta-fed turbidite successions (Zonneveld and Moslow, 2014; 2018). Some successful wells are completed in horizons wherein an end-member lithology dominates, such as horizons that are strongly siltstone dominated with minor coarser laminae or amalgamated very fine-grained sandstone beds with only minor siltstone interbeds. Important criteria that influence reservoir characteristics include the proportion and distribution of calcite, the distribution of bioturbation, particularly cryptobioturbation and the occurrence and distribution of thin clay beds.

## Discussion

In contrast to many 'basin-centred unconventional plays, the Montney produces hydrocarbons from a myriad of depositional settings, including shallow marine (shoreface, deltaic, etc…), proximal clastic ramp, turbidite and distal offshore (e.g. Zonneveld and Moslow, 2018; Baniak et al., 2023). Although the primary depositional environment of Montney successions can be difficult to interpret due to the limited grain-size variability, consistent mineralogy, hybrid lithology and subtle fabric heterogeneity between settings, there are several fundamental parameters, such as grain size, matrix / cement composition and bioturbation (Figure 1) that have proven essential to successful reservoir deliverability.

*Carbonate cement.*— Primary among these parameters is the proportion of carbonate. Where analyses indicate higher volumes of calcite, either as a matrix or framework component, the Montney tends to exhibit greater cementation and higher anisotropy and is thus more challenging to exploit. Problematic intervals include the Altares Member, particularly in the western part of the Montney play (eg. Sanders et al., 2018). The Altares Member comprises an extreme end member, wherein bituminous siltstone and subordinate very

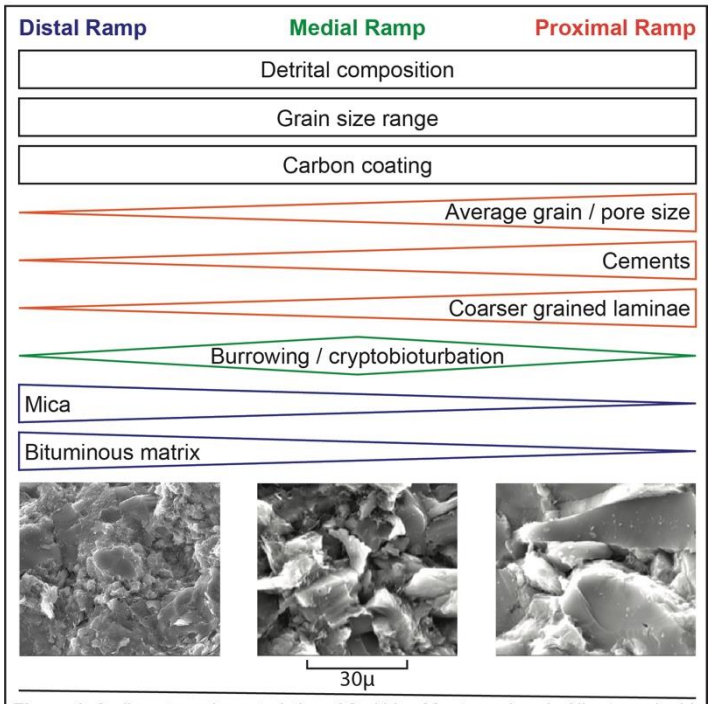


**Figure 1.** Sedimentary characteristics of Smithian Montney plays in Alberta and mid- to late Spathian Montney plays in northeastern British Columbia. In these intervals and areas, distal ramp successions are characterized by the smallest average grain size, smallest pore throats and the highest proportion of clay-sized grains and proximal ramp successions have the largest average grain size, largest pore throats, more abundant bituminous laminae and the highest proportion of cement. Medial ramp successions tend to exhibit smaller overall grain size than more proximal setings but also exhibit significant cryptobioturbation, well-mixed grain and pore throat size distribution and higher overall porosity.

fine-grained sandstone layers occur interbedded with bivalve-dominated bioclastic rudstone layers (Sanders et al., 2018; Zonneveld and Moslow, 2018; Baniak et al., 2023).

More commonly, coarse siltstone and very fine-grained sandstone beds exhibit early calcite cementation. These layers are typically interbedded with bituminous dolomitic siltstone and range from isolated interbeds roughly equivalent in thickness and abundance, to bituminous siltstone intervals.

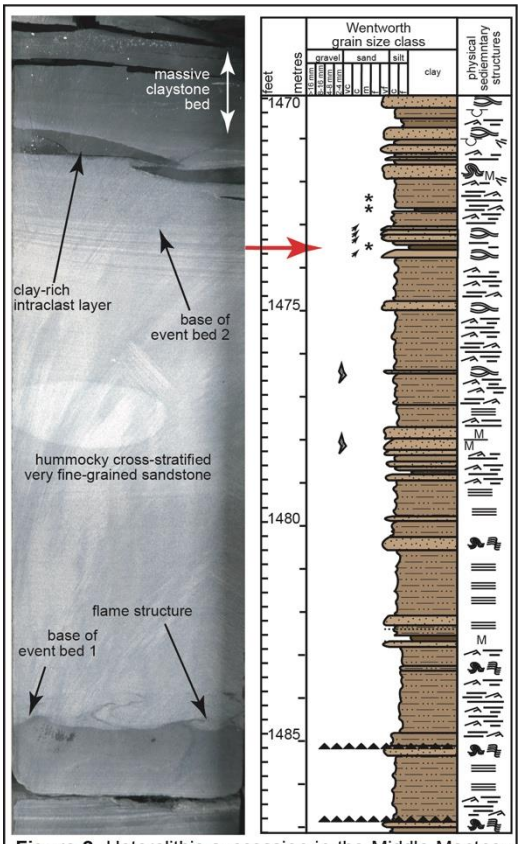


**Figure 2.** Heterolithic succession in the Middle Montney Formation in northeastern British Columbia, well b-066-D/94-H-12. Core photograph at left, shows the interval from 1473.95 to 1473.60 metres. This interval consists of two event beds. The basal event bed comprises a sharp-based hummocky cross-stratified sandstone bed that is abruptly overlain by a thin sandstone-claystone couplet. The basal bed is interpreted to record a coastal storm, while the upper bed is interpreted to record land fall of the storm and a resultant freshet transporting rainfall from the coastal interior, flushing sand and mud through a perennial delta channel into a medial ramp setting. This core occurs adjacent to the Hay River Fault zone, which also hosts the Ring-Pedigree delta complex, a major perennial delta succession on the Alberta BC Border. The three asterisks between 1472 and 1474 metres identify three thin (2-4 cm) claystone beds. XRD analyses indicate that the claystone bed illustrated includes 38.2% illite/mica and 13.1 % chlorite. Claystone beds like these are limited to delta front and prodeltaic settings associated with perennial Montney deltas.

A unit which has proven to be a consistent quality producer occurs just above a prominent stratigraphic break at the base of the Smithian (the Middle Montney Member of Zonneveld and Moslow, 2018). XRD analyses illustrate that this interval is subtly silica enriched and exhibits lower clay and carbonate than adjacent horizons. Although its porosity and permeability do not exceed those of adjacent units, this horizon is the most prolific Montney hydrocarbon producing interval in much of the basin, including northeastern British Columbia. The facies homogeneity and consistently laminated and thin bedded nature of the lowermost Middle Montney member yields an isotropic fabric, lower poisons ratio and higher young's modulus with a subsequently greater propensity to hydraulic fracture stimulation.

Early carbonate cement occurs most commonly in the coarsest siliclastic sediment in the Montney Formation (coarse siltstone and very fine grained sandstone). These lithologies dominate in proximal ramp settings, and consequently, cement-induced porosity reduction is more prevalent in these settings (Figure 1).

*Clay beds.*— Also significant is the occurrence of thin clay beds in some areas (Figure 2). Although the sediment along much of the Montney coastline was sourced from ephemeral fluvial systems that operated intermittently and deposited little clay, several perennial river systems have been identified (Zonneveld and Moslow, 2014; 2018). These include the Ring-Pedigree delta complex on the Alberta-British Columbia Border and the Dixonville Delta complex in the centre part of the basin (Zonneveld and Moslow, 2014; 2018). Prodelta and delta front successions associated with perennial systems are characterized by proportionately higher clay (typically detrital illite) in the depositional matrix. Conventional reservoir successions in the Ring-Pedigree region preserve numerous clay-rich intervals hosting thick, massive to convolute-bedded sandstone successions

Pro-deltaic successions, and clastic ramp successions adjacent to the main delta, commonly preserve sharp-based event beds, interpreted as hyper- and hypo- pycnal flow deposits that are normally-graded, planar to cross-ripple laminated, coarse to fine-grained siltstone beds capped by thin (0.5 to 10 cm) clay-rich beds (Figure 2). These latter units may occur significantly basinward, or lateral to, perennial deltaic depocentres. Overall, proximity to perennial deltas, particularly on the down-drift margin of the delta mouth, degrades Montney reservoir quality through fines occlusion of pore throats and concomitant permeability reduction. It is worth noting that clay-rich interlaminae are associated primarily with sparsely distributed perennial deltaic successions and have not been noted in association with deltaic successions associated with ephemeral feeder systems.

*Bioturbation.*— The third primary criterion that impacts Montney reservoir quality is bioturbation. The Montney was deposited during an interval of prolonged regional dysoxia. As a consequence, bioturbation in the Montney differs profoundly from most other formations. Macroscopic bioturbation in the Lower Montney is, limited primarily to discrete areas where turbulent water aerated the upper part of the water column, such as some deltas and estuaries (Beatty et al., 2008; MacNaughton and Zonneveld, 2010; Zonneveld et al., 2010a, 2010b). In the upper Montney, macroscopic bioturbation can be pervasive and is a common factor in porosity retention and water saturation (Wood, 2012; Zonneveld and Moslow, 2018; Baniak et al., 2023).

Although macroscopic bioturbation is common in the upper Montney, particularly in the eastern part of the British Columbia, most areas lack large trace fossils. More common are zones of microscopic bioturbation where meiofauna, not much larger than sand or silt grains, re-arranged the sediment, destroying discrete bedding planes and reducing overall fabric anisotropy

In addition, bioturbation inhibits the precipitation of calcite cement and enhances vertical permeability. Supportive evidence is derived from thin section petrography, permeability measurements and MICP pore throat aperture frequency distribution histograms.

## Summary

In summary, primary depositional controls play an integral role in Montney reservoir quality. Although parameters such as grain size, and detrital grain composition are important, criteria such as depositional environment, carbonate cement, the nature and distribution of bioturbation and the proximity and nature of fluvial point sources of sediment, have a particularly significant influence on Montney reservoir performance. The interface of sedimentologic, ichnologic, diagentic and fabric anisotropy parameters within Montney facies greatly impact (and commonly are the determining factors of) ultimate reservoir quality and deliverability.

## References


Baniak, G.M., Moslow, T.F., Michailides, S and Adams, M.G. 2023. Sequence stratigraphic architecture of the Lower Triassic Montney Formation, northeastern British Columbia, Canada. AAPG Bulletin, v. 107, p. 283-310.

Beatty, T.W., Zonneveld, J-P. and Henderson, C.M. 2008. Anomalously diverse Early Triassic ichnofossil assemblages in northwest Pangea: A case for a shallow marine habitable zone. Geology, v. 36, p. 771-774

Sanders, S., Etienne, C., Gegolick, A., Kelly, D. and Zonneveld, J-P. 2018. The Middle Montney Altares Member: lithology, depositional setting and significance for horizontal drilling and completion in the Altares Field, British Columbia. Bulletin of Canadian Petroleum Geology, v. 66, p. 318-337.

MacNaughton, R.B. and Zonneveld, J-P. 2010. Trace-fossil assemblages in the Lower Triassic Toad Formation, La Biche map area, southeastern Yukon. Bulletin of Canadian Petroleum Geology, v. 58, p. 100-114.

Wood, J.M. 2012. Water distribution in the Montney tight gas play of the Western Canada Sedimentary Basin: Significance for resource evaluation SPE 151824, 20 p.

Zonneveld, J-P. and Moslow, T.F. 2014. Perennial River Deltas of the Montney Formation: Alberta and British Columbia Subcrop Edge. Geoconvention 2014, May 12–16 2014, Calgary, AB.

Zonneveld, J-P. and Moslow, T.F. 2018. Palaeogeographic setting, lithostratigraphy and sedimentary framework of the Lower Triassic Montney Formation of western Alberta and northeastern British Columbia. Bulletin of Canadian Petroleum Geology, v. 66, p. 93-127.

Zonneveld, J-P., MacNaughton, R.B., Utting, J., Beatty, T.W., Pemberton, S.G. and Henderson, C.M. 2010a. Sedimentology and ichnology of the Lower Triassic Montney Formation in the Pedigree-Ring/Border-Kahntah River area, northwestern British Columbia. Bulletin of Canadian Petroleum Geology, v. 58, p. 115-140.

Zonneveld, J-P., Gingras, M.K. and Beatty, T.W. 2010. Diverse ichnofossil assemblages following the P-T mass extinction, Lower Triassic, Alberta and British Columbia, Canada: evidence for shallow marine refugia on the northwestern coast of Pangaea. Palaios, v. 25, p. 368-392.

GUSSOW 2024
Montney Subsurface Evaluation: Drive Towards Excellence
Banff, AB | October 2-4

# Geological controls on unconventional well productivity in the north Montney sub-basin: Lower Triassic, northeast British Columbia

Peter Proverbs[1], Kerrie Bann[2], James Nasen[1], Brad Taylor[1].
1. Tourmaline Oil Corp., 2. Ichnofacies Analysis Inc.

## Abstract

The Montney Formation in northeast BC was deposited in a tectonically active basin that can be subdivided into three sub-basins, the north, central and south, each of which underwent separate histories of tectonic subsidence and uplift, along with differences in the volume and direction of sediment input. Detailed correlations of regional dip and strike-oriented cross-sections suggest that the Montney Formation comprises at least four depositional sequences, Sequence 1, 2, 3 and 4, in ascending order. In the north sub-basin, following deposition of Sequence 1, accommodation was not available for the deposition of Sequence 2, which, instead was confined to the central (and south) sub-basin, compartmentalized by the reactivation of the deeper-seated structural feature known as the North Monias Hinge. In the north sub-basin, the hiatus following deposition of Sequence 1 lasted until late Sequence 3 time, after which accommodation was available in the sub-basins for the deposition of late Sequence 3 and overlying Sequence 4 strata.

Sedimentological and Ichnological analysis of cores from 45 wells across the northern and central sub-basin, suggests that the Montney Formation was deposited in a subaqueous deltaic setting that was influenced by rivers, storms and waves. The sequence stratigraphic and facies architecture in the north sub-basin reveals that each successive sequence was deposited in shallower water than the previous and confirms that each systems tract within the respective sequences is associated with a landward increase in the abundance and thickness of relatively more proximal facies. Horizontal well performance within the liquids-rich fairway of the north Montney sub-basin generally reflects these stratigraphic and depositional relationships. Wells producing from the lowstand and highstand systems tracts of Sequence 4, significantly outperform those in the highstand and falling stage of Sequence 1, and the highstand systems tract of Sequence 3. Also, the evaluation of horizontal well performance in the falling stage systems tract of Sequence 1, suggests that wells producing from more proximal facies outperform those producing from the distal equivalents. These relationships demonstrate the fundamental control of primary deposition on unconventional well productivity. Ongoing, increasingly sophisticated efforts to optimize the performance of wells in this prolific liquids-rich play, must continue to include careful consideration of these fundamental geologic controls.

## Statement of the background

Canada is the world's 5 largest natural gas producer, ranking ahead of Qatar and Australia, 2 of the 3 largest global suppliers of LNG. The Montney Formation supplies almost two-thirds of Canada's natural gas production, making it a world class resource. The innovative horizontal drilling and completions technology responsible for the rapid growth of Montney production has been informed by a growing geological understanding of the nature, distribution and character of unconventional reservoirs in the succession (Zonneveld et al, 2010b, 2016; Zonneveld and Moslow, 2018; Proverbs et al, 2010, 2018, 2021, 2024 in press; Wood, 2012, Wood et al, 2015, 2020, 2021; Crombez et al, 2016; Vaisblat & Harris, 2016; Vaisblat et al, 2017; Furlong et al, 2018, 2020; Nieto et al, 2018; Moslow et al, 2018; Prenoslo et al, 2018; Sanders et al, 2018; Davies et al, 2018; Euzen et al, 2018, 2021; Gonzales et al, 2022; Mackie et al, 2022; Watt et al, 2022; Bann and Proverbs, 2023; Baniak et al, 2023; Bann et al, 2024). As the play has continued to expand across northeastern BC and the Peace River Arch and Deep Basin regions of western Alberta, it has become apparent that refinements to the prevailing

understanding of the depositional, stratigraphic and structural controls are required. These refinements will be essential to improving predictability as efforts to optimize this globally significant resource continues.

This study attempts to place the expansive Montney play fairway into regional context incorporating the role of deeper-seated structures and syndepositional tectonism, on the evolution of depositional sequences in the Montney Formation. Integrating sedimentological and ichnological analysis into this context provides the basis for reconstructing the geological history of the succession, enhancing predictive capabilities that contribute to more effective development and exploration efforts.

## Aims and Objectives

The objective of this study is to review the regional geologic setting of the Montney Formation in northeast British Columbia and northwest Alberta, summarizing the main structural features that influence the Montney, both regionally and locally. The large scale regional stratigraphic architecture will be reviewed, along with an overview of the high frequency sequence stratigraphy of the interval. The stratigraphic architecture that has emerged reveals complexity along depositional strike that is summarized in a stratigraphic chart that depicts the sequence stratigraphic relationships that have previously proven difficult to resolve. The spatial and temporal evolution of the Montney succession across the region will be reviewed using a series of interval isopach maps, which clearly demonstrate the direct influence of syndepositional tectonism on the Montney Formation.

Another key objective of this study is the continued refinement of the Montney depositional model that has emerged from the integrated sedimentological and ichnological analysis of slabbed, full diameter cores across the region. Analysis of additional cores in this study have confirmed previous findings that deltaic processes dominate the Montney succession and are variously influenced by waves, storms and river floods. The stratigraphic and facies architecture in the north Montney sub-basin is utilized as the framework for evaluating horizontal well performance in the liquids-rich gas portion of the play fairway and demonstrates the fundamental importance of primary deposition on well productivity.

## Materials and methods

The main study area spans the Alberta / British Columbia border and includes the city of Fort St John, British Columbia near the centre of the map sheet and Grand Prairie, Alberta in the extreme southeast (Fig. 1A and B). There are approximately 11,670 wells that penetrate the Montney Formation of which 8000 are productive including 6000 horizontal wells. The regional Montney unconventional play fairway can be subdivided into northern, central and southern sub-basins, each of which displays separate subsidence histories, as well as separate physiographies (Fig. 1A). Superimposed on the regional Montney Isopach Map are some of the major structural features that influenced deposition during the Montney. These include the Hay River Fault Zone, which is a major suture zone between Precambrian basement terranes, the Paleozoic Peace River Arch outlined by the Devonian Leduc fringing Reef Complex., the Fort St. John Graben, which marks the Late Paleozoic collapse of the Peace River Arch and the Rocky Mountain Fold and Thrust belt, which formed during the Jura-Cretaceous Columbian and Laramide Orogenies and defines the western margin of the study area. Another important feature is the Monias High, which is a present-day, fault-bounded, structural high that originated as the southwestern extension of the Fort St. John Graben but was later inverted during the Cretaceous Laramide Orogeny.

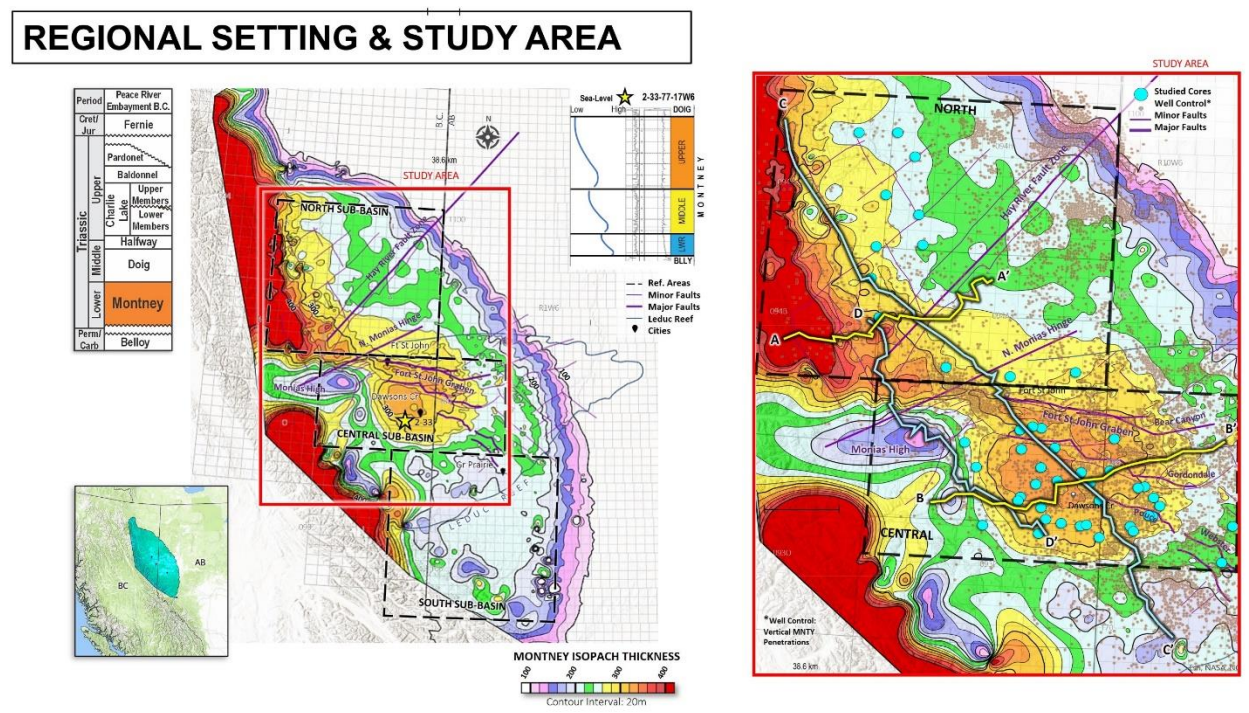


Figure 1: A) Montney location, regional geological setting and isopach map. B) Study Area Map showing the location of cross-sections and the cored wells included in this study (Modified after Proverbs et al, 2024).

This study is based on a regional subsurface dataset that includes modern log suites from over 2000 vertical and directional wells, each of which is tied to a dense, core calibrated grid of regional, depositional-dip and strike oriented cross-sections, constructed using closely spaced wellbores. This close well-spacing served to minimize the potential for miscorrelations between adjacent wells. Regionally significant, chronostratigraphic surfaces were identified and rigorously correlated across the study area, and sequence stratigraphic surfaces were interpreted (sensu Plint & Nummedal 2000; Posamentier & Allen, 1999). Representative cores from 45 wells were logged and interpreted using an integrated sedimentological and ichnological approach, with the aim of establishing the depositional processes and resultant facies present within the succession. Facies were calibrated to wireline logs in efforts to extrapolate between cores, resulting in a stratigraphic and depositional framework within which to conduct the subsequent analysis of producing horizontal wells. Horizontal well performance was assessed using various production plots including rate vs time, rate vs cumulative production, and cumulative production vs time, for gas, liquids and combined gas and liquids on a barrel of oil equivalent basis. This part of the study was focused on the north Montney sub-basin and the corresponding production data and analysis was conducted and visualized using IHS/S&P Accumap software and McDaniel Research and EVA by Turing Analytics software.

## Results and discussion

The large-scale stratigraphic architecture of the Montney Formation is illustrated by depositional dip-oriented cross-sections A-A' and B-B' and strike-oriented cross-section C-C' (Fig 2). The Montney is typically subdivided into 3 sequences, the lower, middle and upper, based largely on stratigraphic relationships evident in regional dip-oriented cross sections such as A-A', representative of the north sub-basin and B-B', representative of the central. However, regional strike-oriented cross-sections such as C-C', reveal that stratigraphic relationships between the sub-basins are more complex than inferred from the dip-sections. The strike section demonstrates that the basal sequence in the northern sub-basin is nearly three times thicker than that of the central, suggesting greater accommodation and tectonic subsidence, coupled with greater sediment supply. Also, internal markers in the overlying middle succession in the central sub-basin, progressively onlap the thick basal lobe occupying the northern sub-basin, indicating it was a paleotopographic high. The onlapping middle sequence progressively infilled the pre-existing paleotopography, so that the uppermost Montney sequence was more continuously deposited along-strike across the northern and central sub-basins.

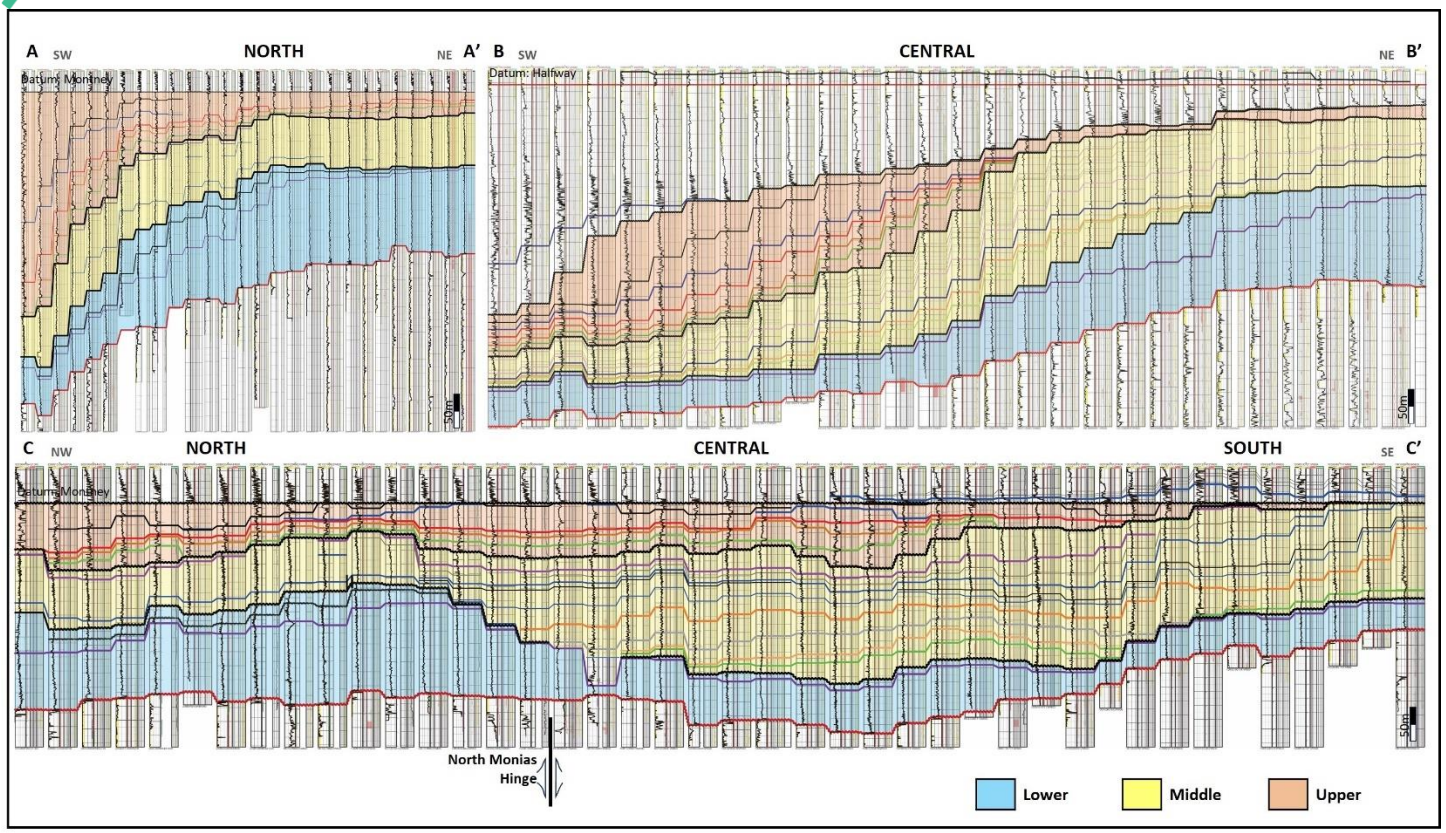


Figure 2: A) and B) Regional dip-oriented cross-sections A-A' and B-B' demonstrate the stratigraphic architecture of sequences characterizing the north and central sub-basins, respectively. C) Regional strike-oriented cross-section C-C' showing the stratal relationships along-strike between the sub-basins (Modified after Proverbs et al, 2024)..

The abrupt lateral change in stratigraphic architecture along-strike, is interpreted to result from the reactivation of deeper-seated fault systems associated with the Monias High, which is a present-day fault-bounded structural high that originated as the southwest extension of the Fort St John Graben. The graben collapsed following the Mississippian, was infilled during the Pennsylvanian and capped by the Permian (Fig 3). It then underwent a major tectonic inversion during the Late Cretaceous Laramide Orogeny

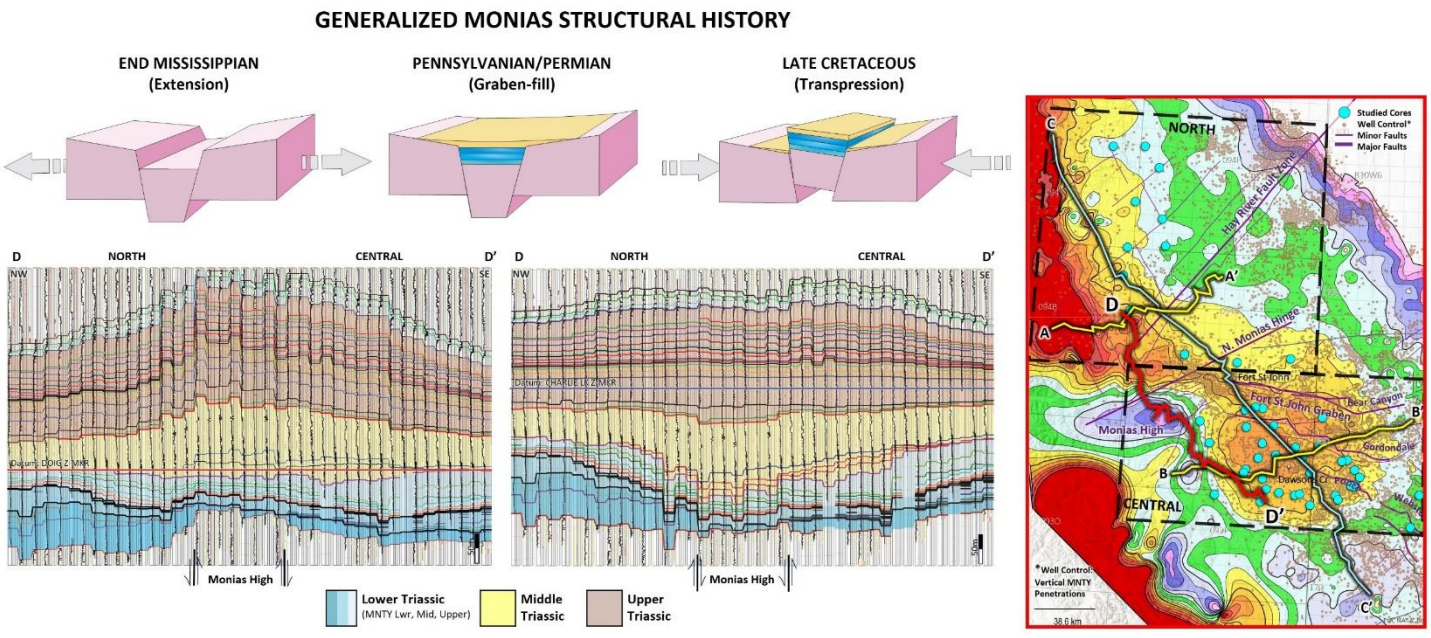


Figure 3: Schematic depiction of the origin of the Monias High, and strike-oriented cross-section D-D' revealing the history of reactivation and inversion of the Monias High during the Triassic.

Cross-section D-D', is a strike-oriented cross-section through the apex of the Monias High and demonstrates that this feature was also active throughout the intervening Triassic period (Fig. 3). Two versions of the cross-section are presented, hung on different datums to highlight the sequential changes in accommodation that occurred through time. The version on the left is hung on the informally named Doig Z Mkr, a chronostratigraphic marker between the Montney Formation, highlighted in shades of blue, and the overlying Doig Phosphate. The section shows pronounced thinning of the Montney above the crest of the Monias high, and progressive thickening along the flanks. Especially notable is the anomalous thinning of the basal Montney interval over the crest of the high, indicating that very little accommodation was locally available at this time. However, the increase in accommodation north of the high is abrupt and pronounced, while to the south and across the central sub-basin, the increase in accommodation is more subdued.

The second version of Cross-section D-D' is hung on a chronostratigraphic marker near the base of the Upper Triassic, known informally as the Charlie Lake Z Mkr. It demonstrates that the Monias High collapsed following deposition of the Montney Formation, and a thicker middle Triassic succession infilled the local depression.

The history of recurrent movement and inversion along the Monias High and related structures is interpreted to have had a profound influence on deposition during the Montney and will be demonstrated following a brief overview of the Montney high resolution sequence stratigraphic architecture, which was defined by correlating regionally significant chronostratigraphic surfaces across a grid of strike and dip-oriented cross-sections such as those depicted in Figure 4.
The dip cross-sections A-A' and B-B' reveal a relatively simple offlapping internal geometry, however the strike cross-section C-C' reveals more complexity, reflecting abrupt lateral changes in accommodation. These changes in accommodation are interpreted as the result of both differential subsidence associated with syndepositional tectonism, as well as the result of local paleotopography and paleobathymetry associated with the deposition of preceding units.

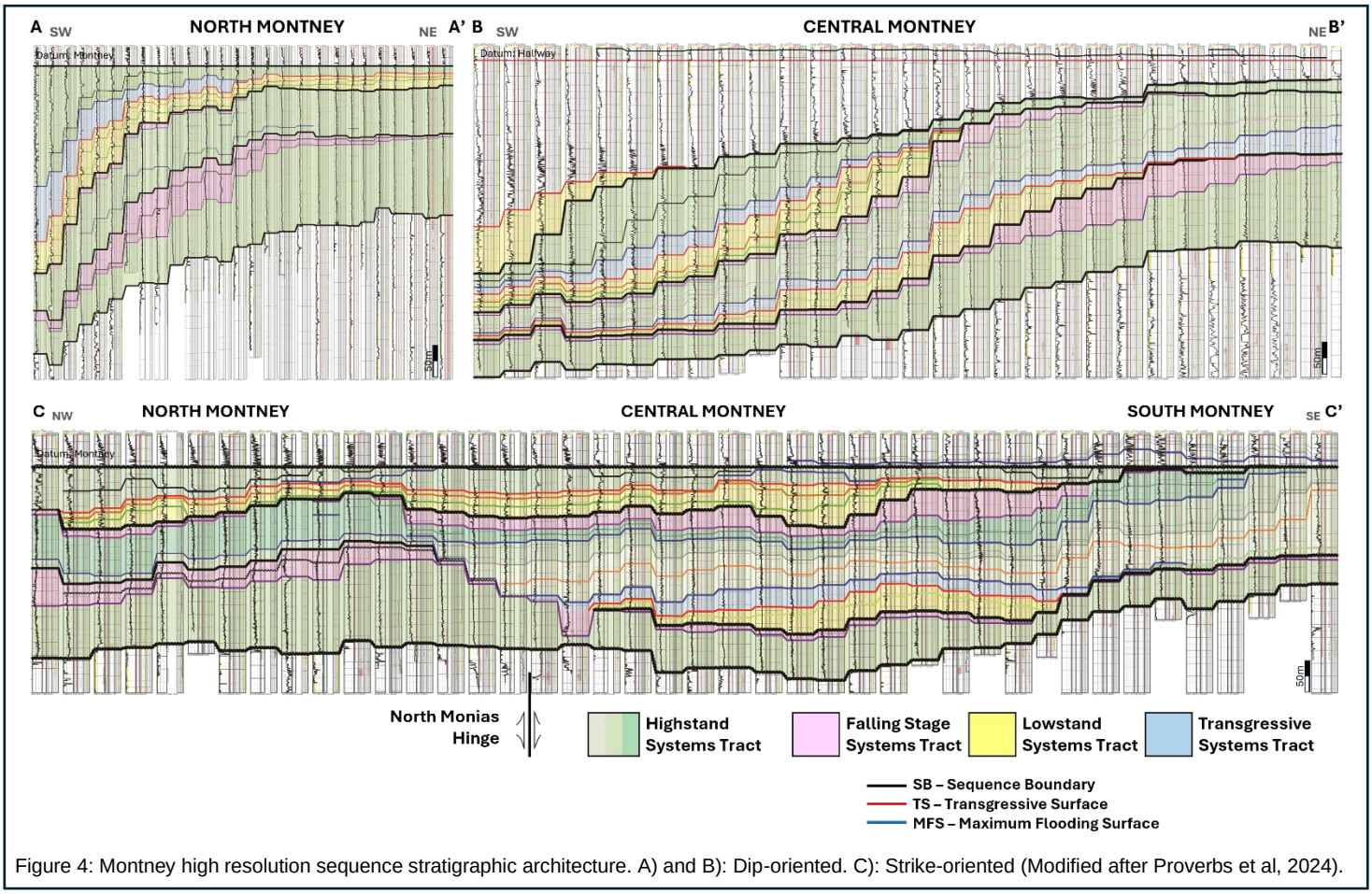


Figure 4: Montney high resolution sequence stratigraphic architecture. A) and B): Dip-oriented. C): Strike-oriented (Modified after Proverbs et al, 2024).

The stratigraphic chart (Fig. 5) summarizes the relationships that best resolve the architecture observed along-strike between the north and central sub-basins and takes into consideration the dynamic history of tectonic rejuvenation and inversion that characterizes the intervening Monias High. Superimposed for reference, is the stratigraphic nomenclature from Davies et al, 2018. The Montney is subdivided into four depositional sequences and the basal sequence in the respective north and central sub-basins are not coeval. Sequence 1 is older and confined to the northern sub-basin, where

reactivation of the North Monias Hinge focused subsidence, initially, in the region north of the fault. Conversely, Sequence 2 is younger and confined to the central sub-basin where subsequent fault movement reduced accommodation in the north sub-basin and accelerated subsidence in the central. The sequence boundary capping Sequence 1 in the north is interpreted as a subaerial exposure surface and represents a significant hiatus that is not coeval with the sequence boundary at the top of Sequence 2 in the central sub–basin. The sequence boundary capping Sequence 2 is younger and is interpreted as a correlative conformity that, together with the overlying lowstand and transgressive systems tracts of Sequence 3, are observed to onlap the thick lobe occupying the northern sub-basin. This relationship confirms that accommodation was not available for these onlapping intervals, including the highstand and falling stage systems tracts of Sequence 2. The hiatus associated with the sequence boundary capping Sequence 1, lasted until at least middle Sequence 3 time, when accommodation finally became available. Late Sequence 3 and the overlying Sequence 4 successions were then deposited more continuously along-strike between the two sub-basins.

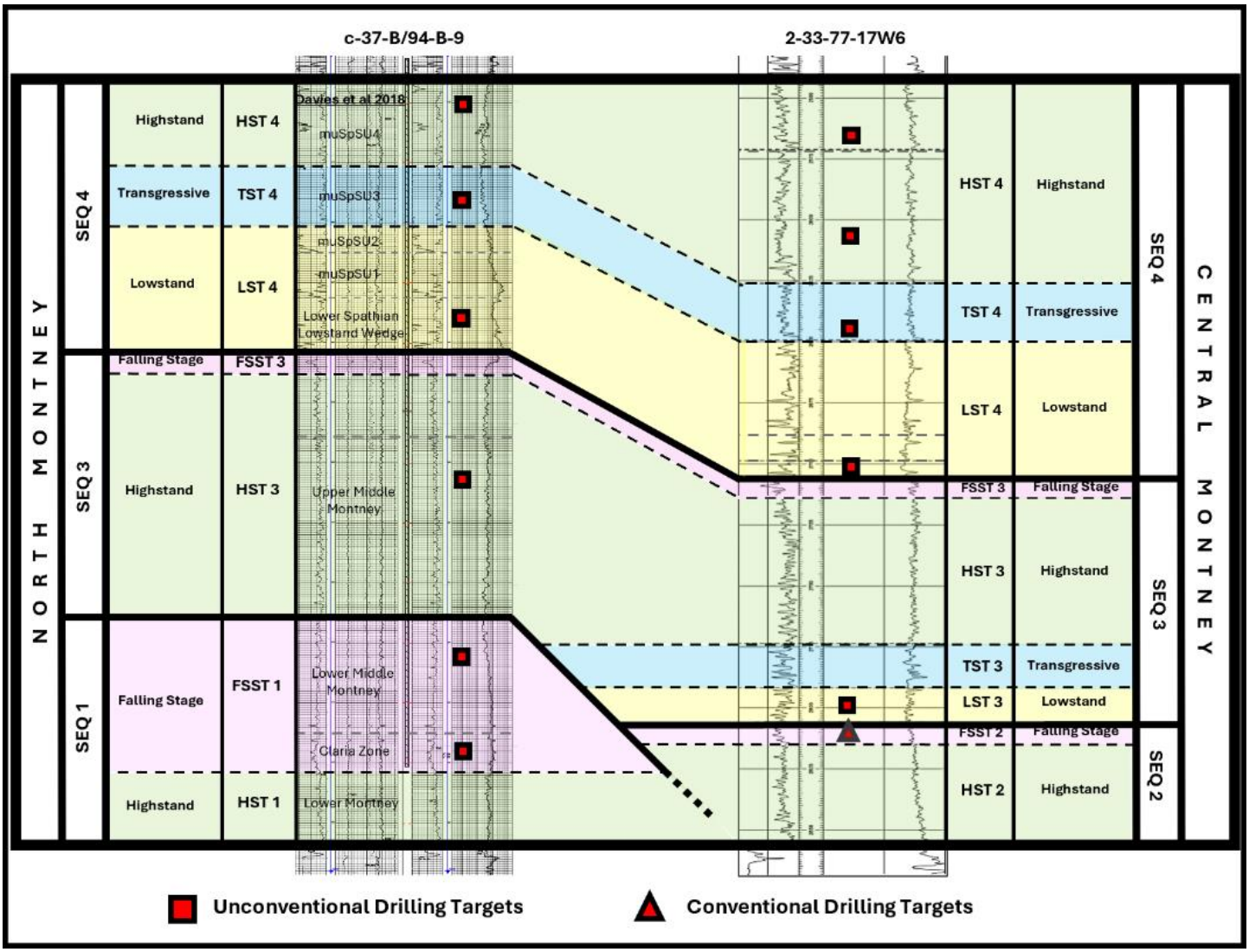


Figure 5: Montney Stratigraphic correlation chart summarizing the sequence stratigraphic relationships between the north and central sub-basin (Modified after Proverbs et al, 2024). For reference, the stratigraphic nomenclature from Davies et al, 2018 is superimposed.

The Isopach maps (Fig 6) demonstrate the sequential evolution of the Montney Formation across the northern and central sub-basins and represent the spatial and temporal changes in accommodation that occurred during deposition. The Sequence 1 Isopach Map (Fig 6A) reveals a generally northwest trending depocenter that's confined to the north sub-basin. The depocenter thins progressively basinward to the southwest, reflecting a sediment source that fed the basin from the northeast. However, the depocentre also thins abruptly to the southeast along a linear SW to NE trend that parallels the NE bounding fault of the Monias High, which is informally named the North Monias Hinge. We interpret that reactivation of the fault system associated with the North Monias Hinge provided the accommodation for Sequence 1 in the northern sub-basin, while concurrently reducing accommodation in the central sub-basin.

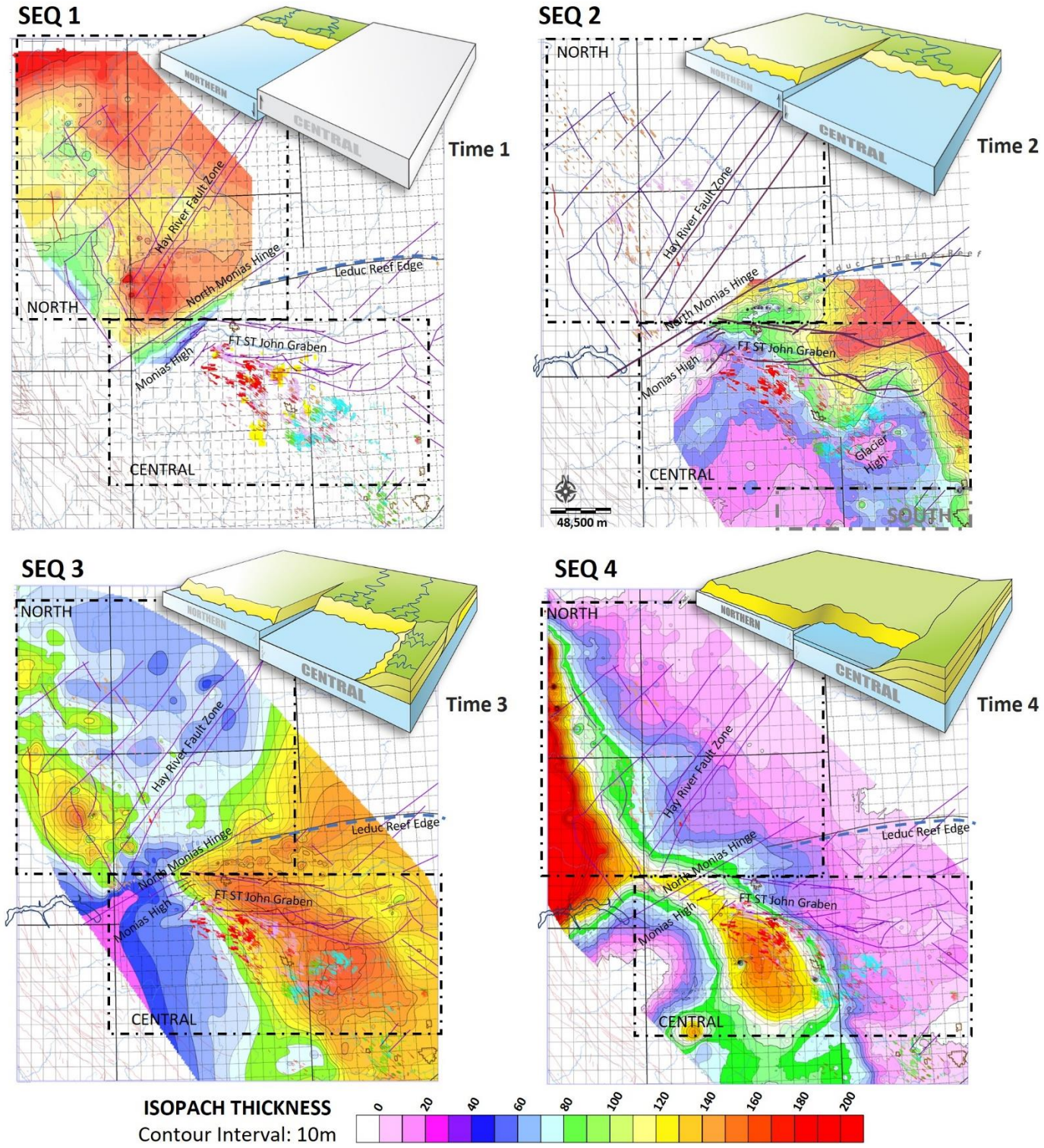


Figure 6: Interval isopach maps and corresponding block diagrams demonstrating the evolution of Montney sequences across the north and central sub-basins

The Sequence 2 Isopach Map (Fig 6B) reveals a northwest trending depocenter that's restricted to the central sub-basin and is compartmentalized by the North Monias Hinge. This pattern suggests that reactivation of the North Monias Hinge during Sequence 2 time resulted in tectonic inversion whereby accommodation accelerated in the central sub-basin while in the northern sub-basin, accommodation was greatly reduced. The Sequence 2 depocenter thins basinward to the southwest, suggesting a northeast supply and is offset landward relative to the Sequence 1 depocenter, suggesting that sediment influx in the central sub-basin was significantly less than that which occurred in the north. Localized Isopach thin areas near the northwestern and southeastern corners of the central sub-basin are interpreted as paleobathymetric highs

that received little sedimentation relative to their flanks. These highs, named the Monias and Glacier Highs, respectively, suggest that syndepositional tectonism greatly influenced sedimentation during Sequence 2 time.

The Sequence 3 Isopach Map (Fig 6C) shows an overall reciprocal relationship with the underlying sequences, whereby the interval is generally thin over the north sub-basin and thicker in the central. This pattern reflects compensational stacking and suggests that the North Monias Hinge may have been tectonically quiescent such that the resulting stratal architecture is controlled by the inherited paleotopography. In the central sub-basin, the Sequence 3 depocenter offsets basinward the underlying Sequence 2 depocenter reflecting the overall progradation of the Montney succession from the northeast, however the stratigraphic architecture near the boundary with the south sub-basin, suggests that a source from the southeast may have been locally present. This is illustrated by the corresponding block diagram (Fig. 6C).

The Sequence 4 Isopach Map (Fig 6D) shows that accommodation was more continuous across the North Monias Hinge, which was no longer active in compartmentalizing sediment accumulation. In the north sub-basin, the Sequence 4 depocenter occurs along the western margin of the sub-basin and is very thick, in comparison to the depocenter in the central sub-basin, indicating that sediment supply in the north was significantly greater than in the south. In the central sub-basin, the depocenter is pendant-shaped and offsets basinward the depocenter of the preceding Sequence 3, again reflecting overall progradation from the northeast. Thinning along the seaward margin of the depocenter in the central sub-basin results from a combination of seaward downlap in response to reduced sedimentation, as well the result of onlap onto a paleobathymetric high related to the Monias High. The observed tapering of the isopach values along-trend to the northwest of the depocenter, is the expression of the depositional onlap onto this paleobathymetric high. Isopach patterns in the region updip of the depocentres in both sub-basins are controlled by differential uplift and erosion prior to deposition of the overlying Doig/Halfway sequence. Recurrent movement along the bounding faults of the Fort St John Graben and the region bounded by the Hay River Fault Zone and the North Monias Hinge, may have been responsible for the inferred differential uplift.

Integrated sedimentological and ichnological studies of cores from over 45 wells suggest that the Montney Formation was deposited in a deltaic setting. This contradicts most recent studies, which suggest an offshore to shoreface origin (Crombez et al, 2016; Moslow et al, 2018; Zonneveld and Moslow, 2018; Prenoslo et al, 2018; Euzen et al 2018, 2021; Gonzales et al, 2022; Baniak et al, 2023). These studies generally cite the characteristic lack of bioturbation in the Montney as the result of a lag in recovery after the end-Permian mass extinction event or the result of persistent bottom-water anoxia (Proverbs et al, 2018; Gonzales et al, 2022). However, the processes recorded by the physical and biogenic structures in the Montney are consistent with deposition in a deltaic setting.

The split core diagrams in Figure 7, illustrate the diagnostic features that distinguish marine shoreface successions from deltaic successions (MacEachern and Bann, 2020, 2022). The shelf at the base of both successions is muddy and thoroughly bioturbated by ichnofauna of the characteristic Zoophycus Ichnofacies, which is generally created by organisms that mine systematically through the sediment, forming elaborate traces in the process. The overlying prodelta, which is deposited above storm wave base, is heterolithic and features common dark structureless carbonaceous mudstone interbeds and drapes, interpreted as fluid muds, which are the deposits of flocculated muds that settled rapidly from buoyant (hypopycnal) plumes discharged by rivers during floods. Bioturbation in the prodelta is characteristically sporadic and relatively sparse due to paleoenvironmental stress caused by fluctuating salinities, rapid sedimentation and water turbidity, which is reflected in the Phycosiphon Ichnofacies assemblage, defined by MacEachern & Bann, 2020, 2022. This assemblage includes traces indicative of rapid deposition, such as escape traces (Fugichnia) and sediment swimming traces (Navichnia).

In contrast, the offshore deposits, which are the normal marine equivalent of the prodelta, and also deposited above storm wave base, are so thoroughly bioturbated that virtually no primary sedimentary structures are preserved. The Cruziana Ichnofacies characterizes the offshore and is dominated by the traces of organisms that feature a wide range of behaviours.

In the delta front setting, situated above fairweather wave base, the deposits are characterized by sandy event beds that commonly display soft sediment deformation structures, attesting to rapid sedimentation. These event beds are commonly draped by dark structureless carbonaceous fluid muds representing the rapid settling of muds from buoyant hypopycnal plumes associated with river floods. Also common are sandstone event beds that display normal and inverse grading, interpreted as hyperpycnal deposits, which are pulsating bottom hugging undercurrents that record the waxing and waning stages of rivers floods. Carbonaceous detritus and synaeresis cracks are also diagnostic features of delta fronts. Bioturbation is sparse and sporadic and contains the newly defined Rosselia Ichnofacies (MacEachern & Bann, 2020, 2022), which includes the common occurrence of escape traces.

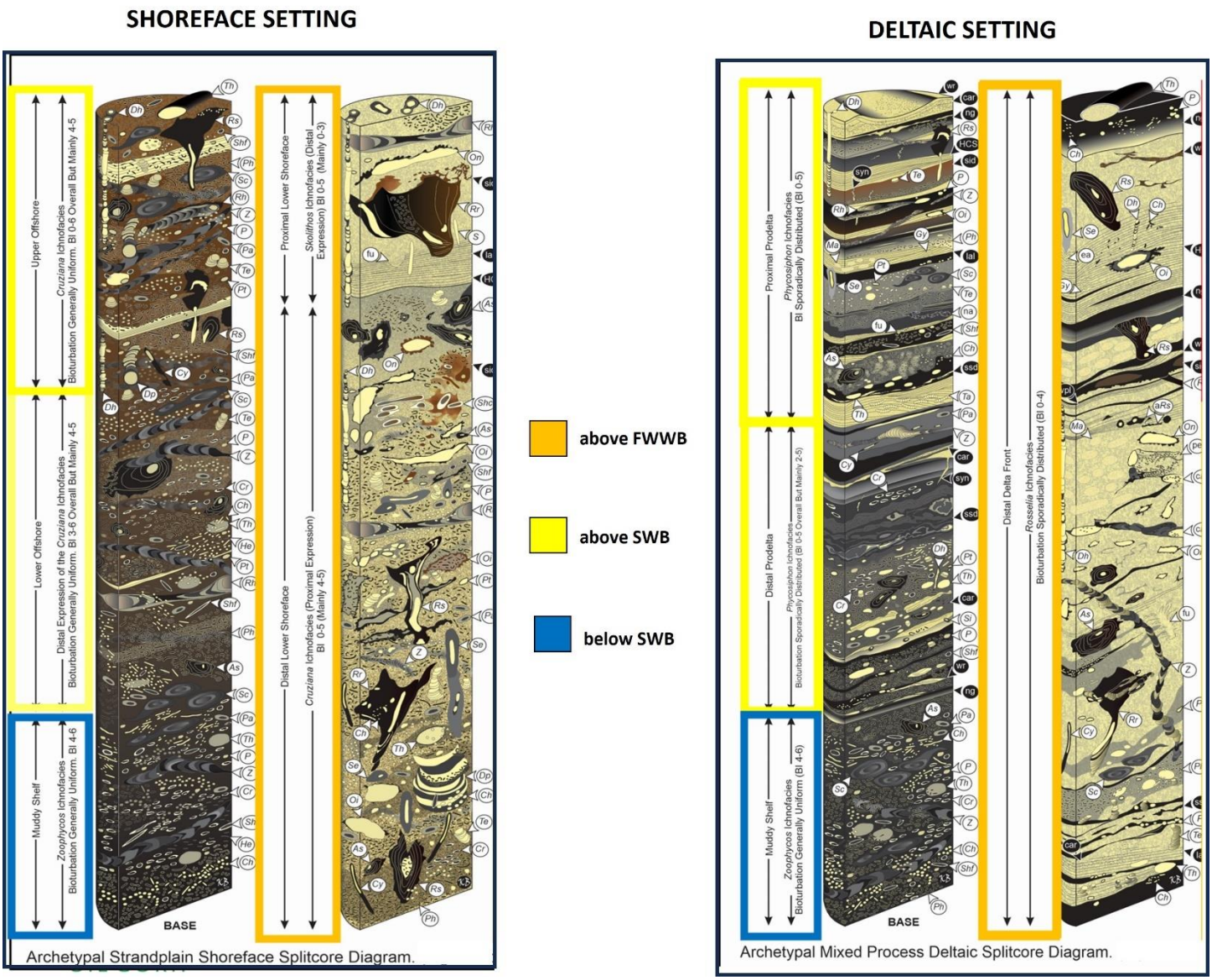


Figure 7: Split core diagrams contrasting physical and biogenic structures characteristic of shoreface and deltaic successions (after MacEachern and Bann, 2020).

In contrast, sandstone event beds in the shoreface, which is the normal marine equivalent of the delta front, and also deposited above fairweather wave base, are generally emplaced by storms and lack fluid mud drapes. Bioturbation is more abundant and may thoroughly homogenize the sandstones during extended fairweather periods between storms. The Skolithos Ichnofacies characterizes the shoreface and features common vertical traces of filter feeders that are adapted to the shifting sandy substrates that occur above fairweather wave base. In contrast, these vertical traces are rare in the delta front because elevated water turbidity inhibits the filter feeding process.

The Montney depositional framework is summarized in Figure 8, and is established by 5 facies interpreted as shelf, distal prodelta, proximal prodelta, distal delta front and, locally by sediment gravity flow deposits including hyperpycnites. The hyperpycnites indicate a direct linkage to riverine processes. Not preserved in the study area are the deposits of the proximal delta front, distributary channels nor the delta plain, which are interpreted to have been removed by some combination of wave ravinement and subaerial erosion.

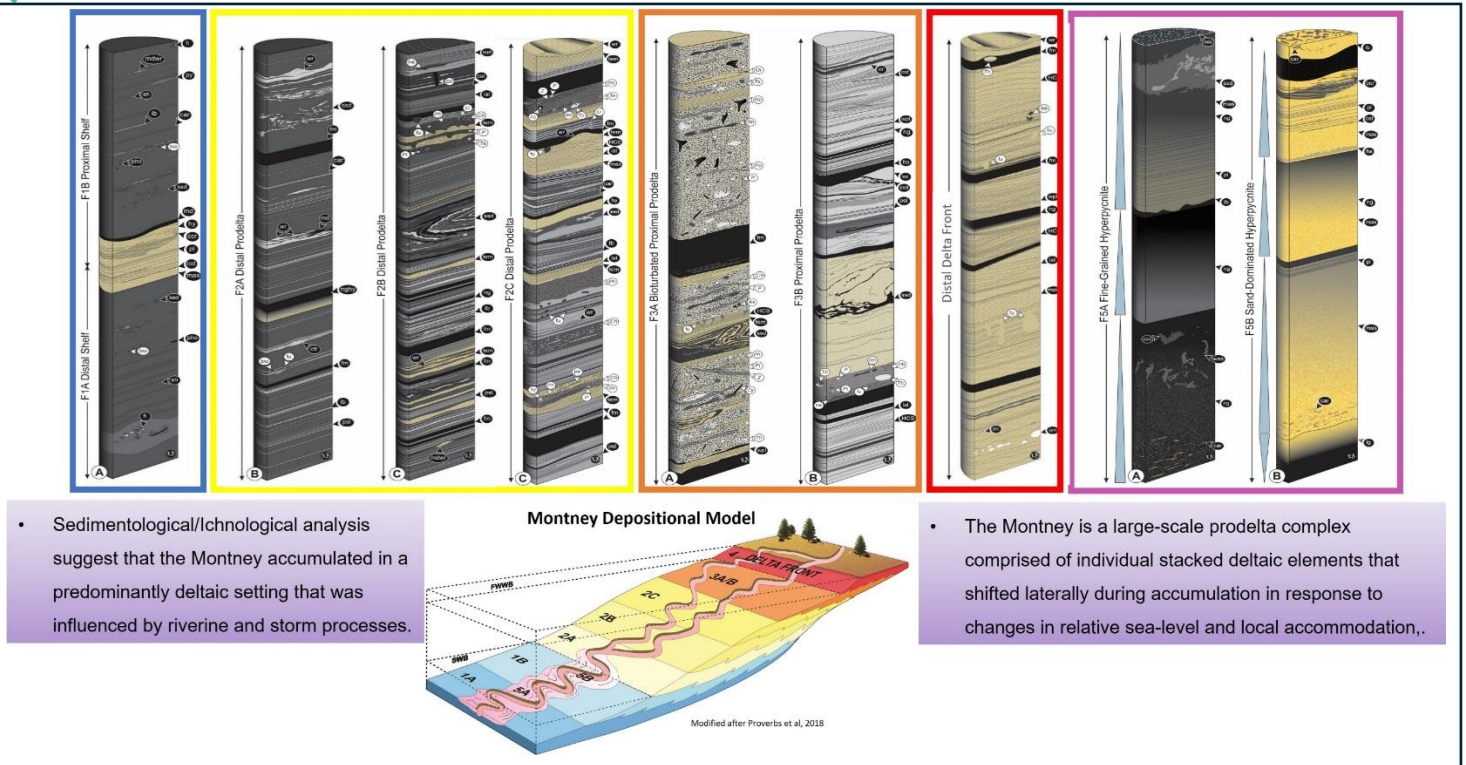


Figure 8: Split core diagrams representing the facies and depositional framework of the Montney Formation.

There are two notable facies variants that are important within specific intervals of the Montney Formation. These facies include the Fugichnia/Navichnia facies (Fig. 9), which is common in portions of the upper Montney and is generally associated with excellent unconventional reservoir quality. This facies shares many of the features of the prodelta setting but is characterized by abundant to pervasive fugichnia, which are escape traces, navichnia, which are sediment swimming traces and less common equilibrichnia, which are equilibrium adjustment structures. Each of these traces are bivalve-generated and reflect heightened sedimentation. Marine traces are uncommon and diminutive, and together the assemblage comprises the Archetypal Phycosiphon Ichnofacies diagnostic of prodeltaic settings. The abundance of biogenic structures that reflect very soft substrates are indicative of rapid deposition in a storm-influenced prodeltaic setting.

The second variant is the carbonate cemented subfacies of the prodelta setting, which is most common in the uppermost portions of Sequence 3 (Fig. 9). This facies is heterolithic and shares similar features as the typical prodelta setting. However, it's characterized by light grey, calcareous cemented, coarse siltstone lenses, that may locally deform the surrounding bedding, indicating that the cement is an early diagenetic phenomenon. Locally the lenses may contain bioclastic fragments within sharp-based normally-graded centimeter to decimeter thick beds, which may suggest winnowing of the substrate by storm processes. The record of early diagenesis and concentration of bioclasts reflects accumulation during periods of reduced siliciclastic input, when substrate exposure to minerals in the seawater and winnowing of fines may have been relatively prolonged.

The sedimentological and ichnological analysis and interpretations have been integrated into the sequence stratigraphic framework and is summarized on the N-S cross-section representing the north sub-basin, which is oriented oblique to depositional dip (Fig. 10). The colours reflect three main facies, shelf, distal prodelta and proximal prodelta. The cross-section demonstrates that each of the three sequences preserved in the north sub-basin, comprises overall shallowing upwards successions and that there is a progressive increase in the proportion of shelf facies in the more distal portions of each sequence. Also, the three sequences are progradationally stacked, such that the overall Montney succession comprises a large-scale shallowing upwards sequence, in which each successive sequence was deposited in progressively shallower water. The most common targets for horizontal wells in the north sub-basin include the Falling Stage Systems Tract of Sequence 1 (FSST 1), the Highstand Systems Tract of Sequence 3 (HSST 3), the Lowstand Systems Tract of Sequence 4 (LST $) and the Highstand Systems Tract of Sequence 4 (HST 4).

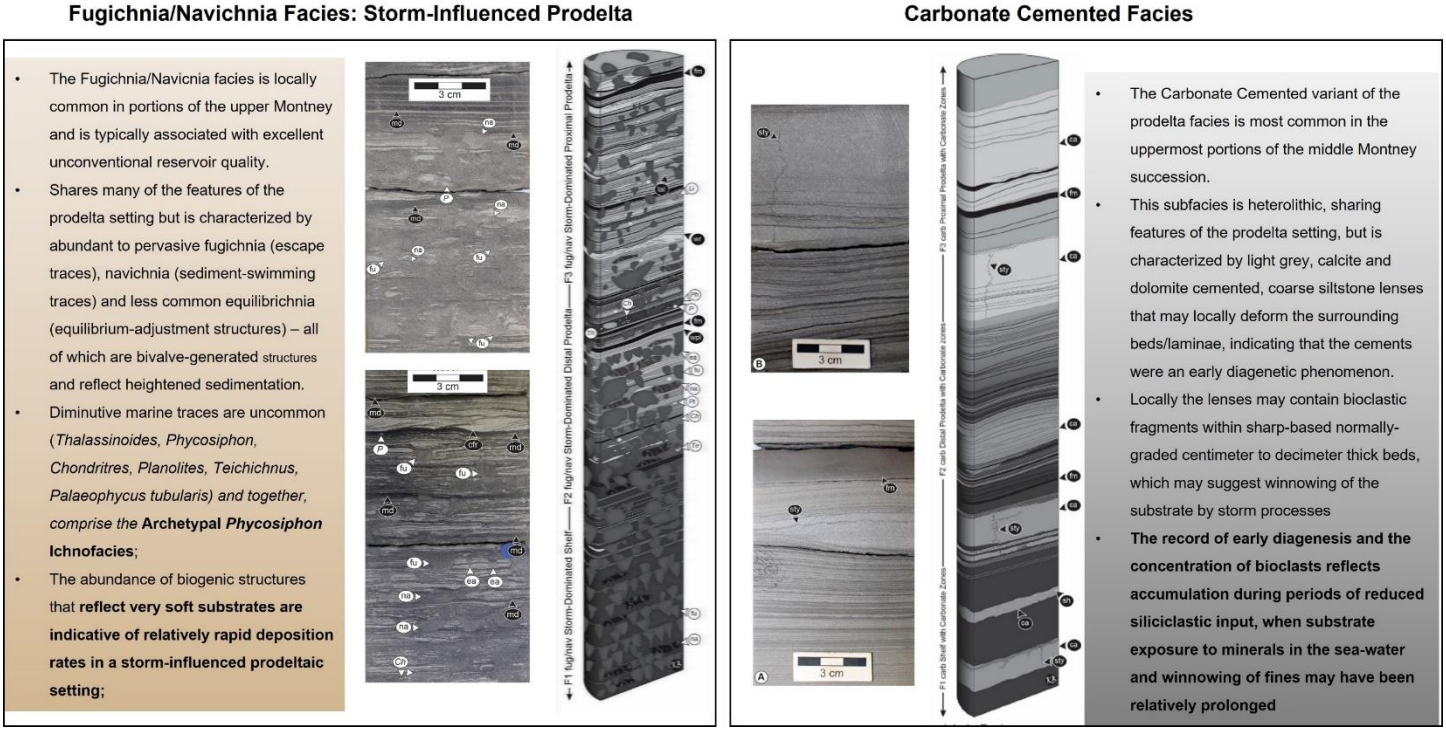


Figure 9: Core photos and split core diagrams of the storm-influenced prodelta facies and carbonate cemented prodelta facies that occur commonly in HST 4 and uppermost HST 3 intervals, respectively.

The location of producing Montney horizontal wells in the liquids-rich gas fairway in the north Montney sub-basin is depicted on the map in Figure 11. The fairway is defined by contours that represent the proportion of methane in the gas stream and is highlighted between the 79% and 85% contour values. The wells are colour-coded by systems tract and the pie chart shows the relative proportions of producing wells in each systems tract. The inset pie chart shows that the HST 4 and FSST 1 intervals are the most common targets, and that the LST 4 and HST 3 are targeted in lesser but roughly equal proportions. By comparison, wells targeting HST 1 are rare.

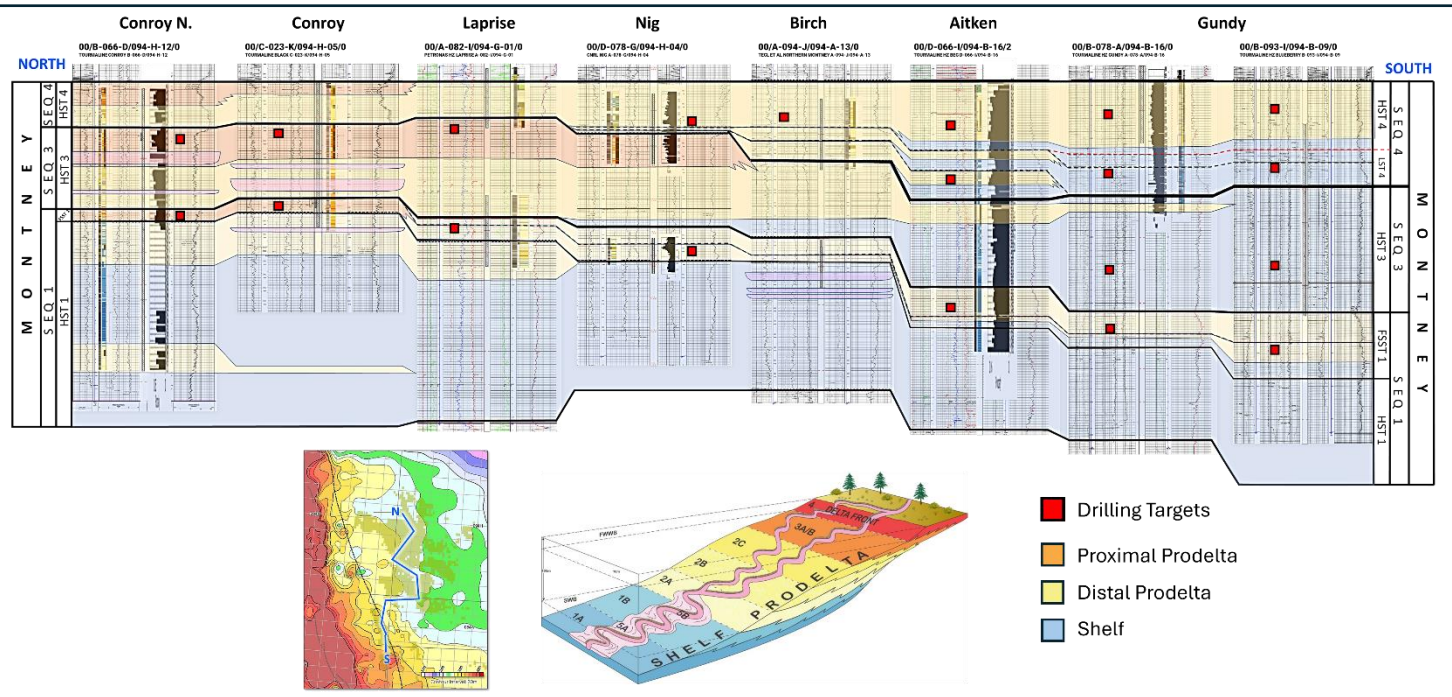


Figure 10: Stratigraphic and facies architecture of the Montney Formation in north Montney sub-basin, showing common targets for horizontal wells.

The chart in Figure 12, demonstrates the growth of gas production from the north Montney liquids-rich fairway since 2010 and the relative contribution from each of the five main horizontal targets. Total production is currently 1.2 billion cubic feet per day (Bcf/d), roughly half of which is contributed by wells in the HST of Sequence 4.

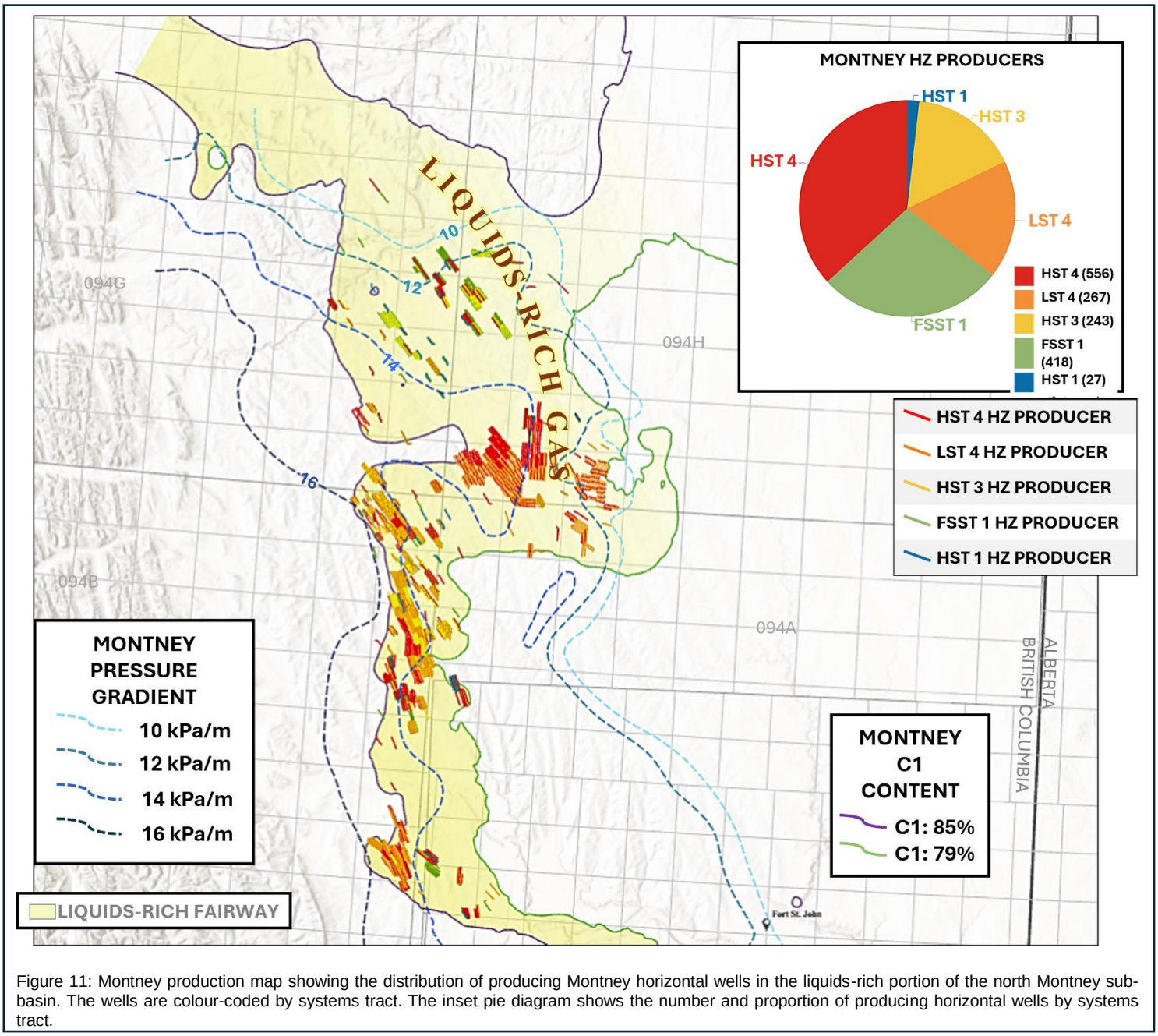


Figure 11: Montney production map showing the distribution of producing Montney horizontal wells in the liquids-rich portion of the north Montney sub-basin. The wells are colour-coded by systems tract. The inset pie diagram shows the number and proportion of producing horizontal wells by systems tract.

The chart in (Fig. 13) compares the average performance of wells from each of the horizontal target intervals in the north sub-basin and demonstrates that wells in the HST and LST of Sequence 4 outperform, while wells in the HST of Sequence 1 and Sequence 3 generally underperform. Wells in the FSST of Sequence 1 are intermediate in performance.

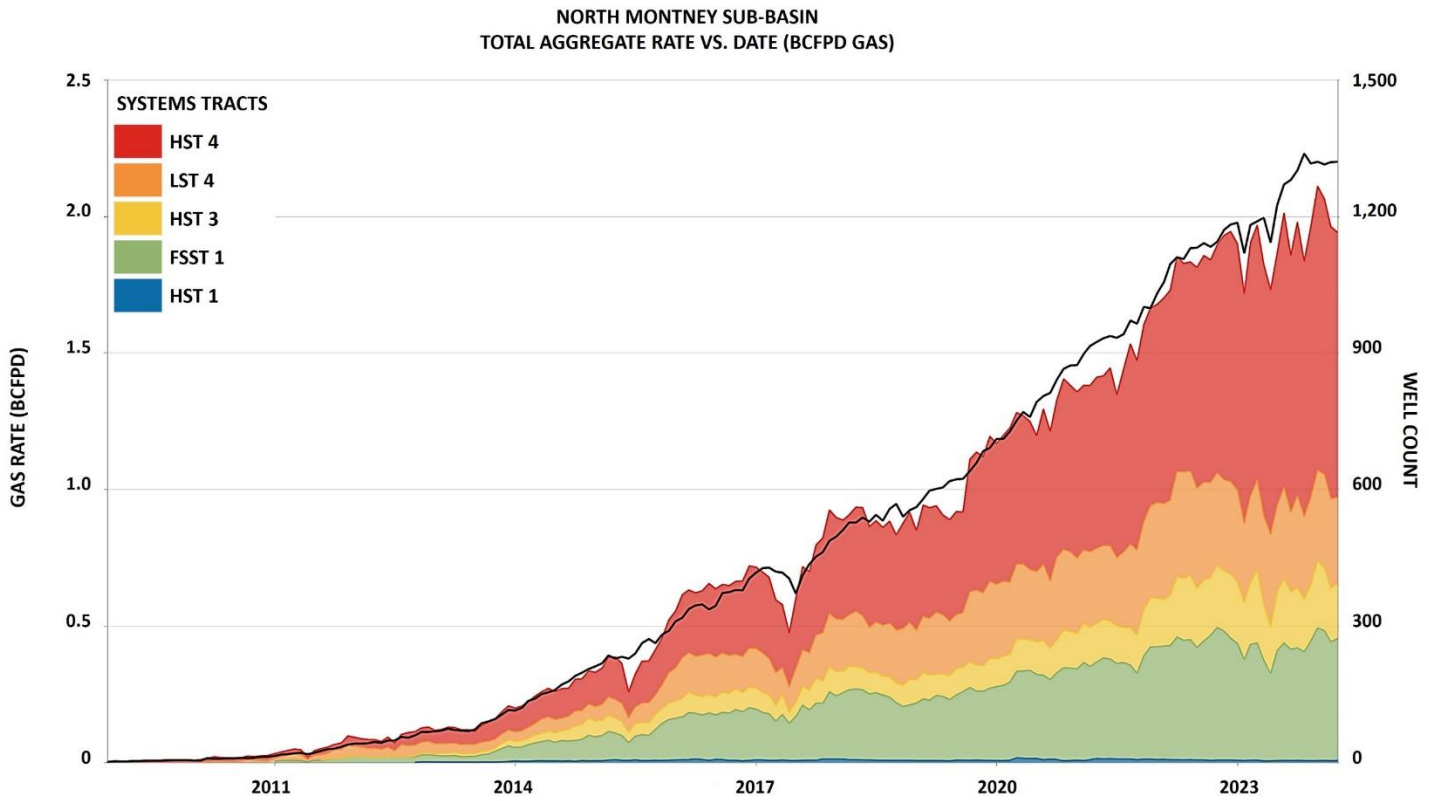


Figure 12: This chart shows the growth in the number of wells and associated total gas production from the liquids-rich fairway of the north Montney sub-basin, demonstrating the relative contributions from each systems tract.

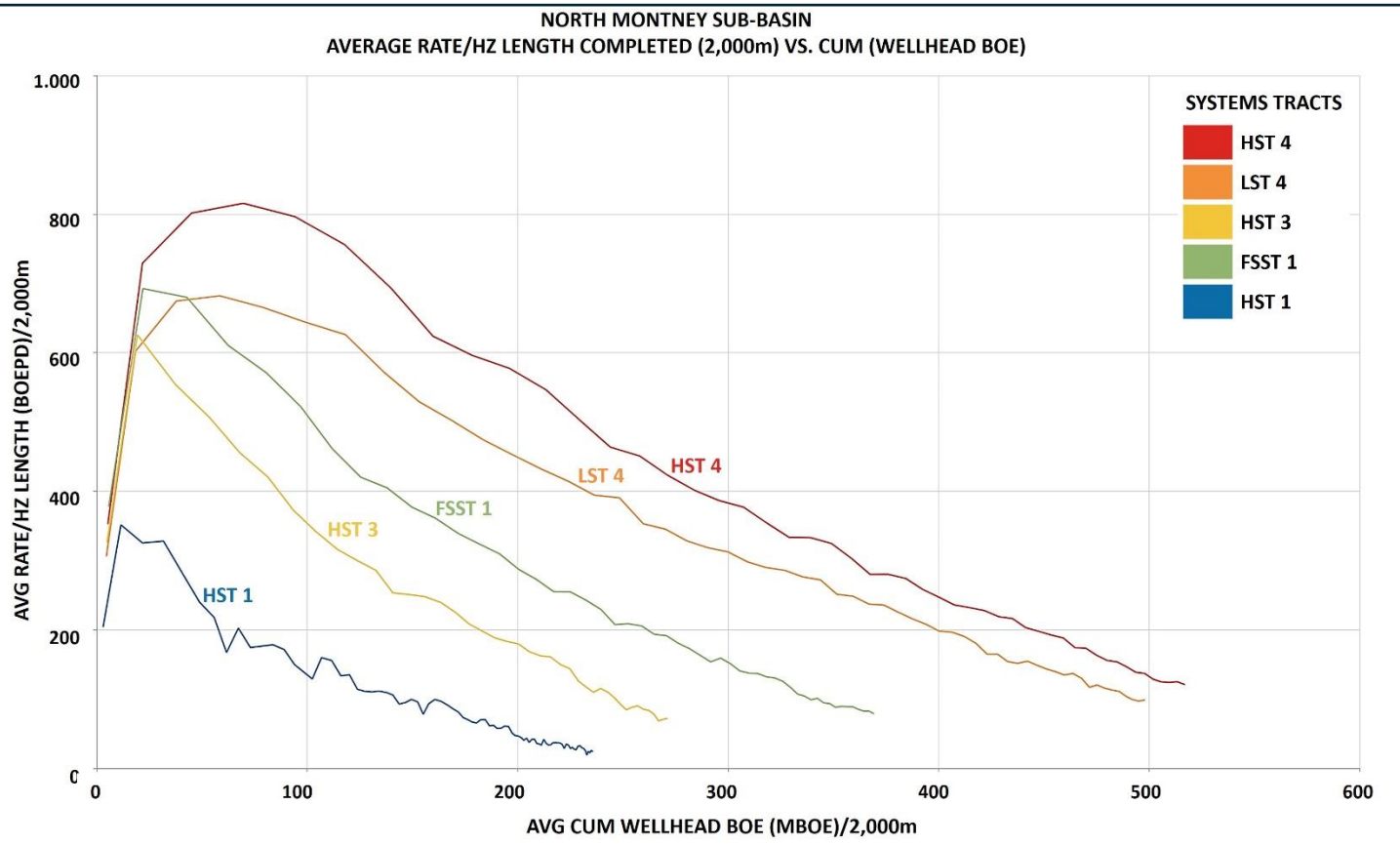


Figure 13: Chart comparing normalized average well performance by systems tract for wells in the liquids rich fairway of the north Montney sub-basin.

The analysis of production from wells in the FSST of Sequence 1, demonstrates that there is also a facies control to horizontal well performance, in addition to the stratigraphic control. The map in Figure 14 shows the distribution of horizontal wells producing from the FSST 1 interval within the liquids-rich fairway. The contours superimposed on the map represent the proportion of the total (gross) FSST 1 interval that exceeds core calibrated and log normalized values of 5% porosity. Values greater than 0.20 are consistent with the distribution of proximal prodelta facies in the FSST 1 interval, while those less than this value represent the distal prodelta facies. The wells are colour-coded to reflect these two populations. The pie chart in Figure 15 shows the proportion of producing wells from the proximal prodelta and distal prodelta facies, and these proportions reflect the limited areal distribution of the proximal prodelta facies in the FSST 1 interval relative to the distal prodelta facies. The histogram compares the average initial well performance during the first three months of production normalized for well length and demonstrates that the proximal prodelta wells outperform those producing from the distal prodelta, despite the lower reservoir pressure typically associated with the area in which the proximal prodelta reservoir occurs (Fig. 14).

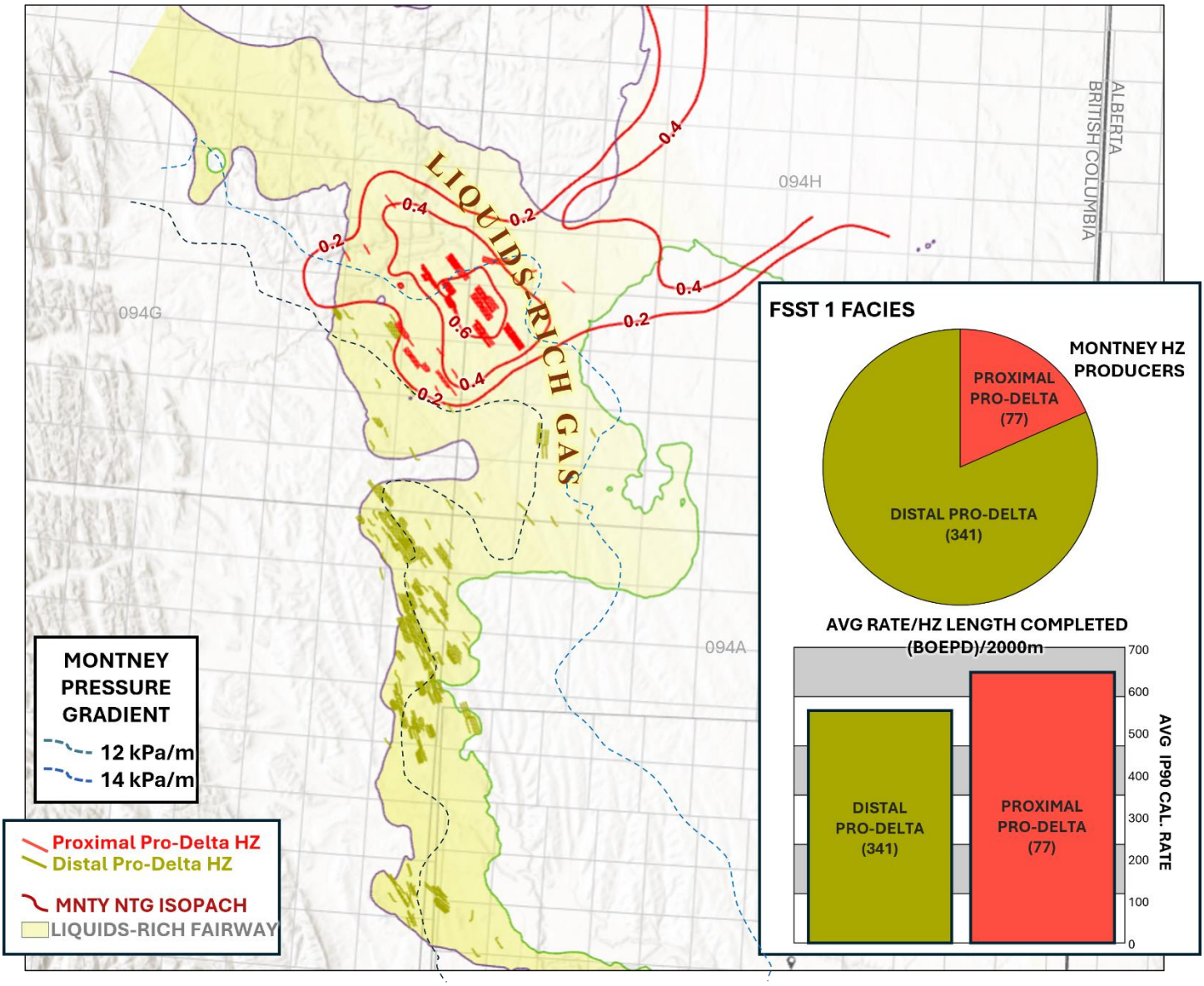


Figure 14: Contour map of the net to gross ratio (cut-off = 5% porosity) in FSST 1. Horizontal wells associated with values exceeding 0.20, are generally consistent with the occurrence of proximal prodelta facies. The pie diagram depicts the proportion of wells producing from the proximal prodelta facies relative to distal prodelta, while the histogram demonstrates that average performance of proximal prodelta wells that exceed that of the distal prodelta

## Conclusions

In conclusion, the Montney Formation in northeast BC and northwest Alberta accumulated in 3 sub-basins, the north, central and south, each of which experienced separate histories of tectonic subsidence and sediment influx. High-resolution sequence stratigraphic analysis reveals that the Montney comprises four depositional sequences in the study area, in contrast to the typical tripartite subdivision. Sequence 1 is confined to the north sub-basin where reactivation of the North Monias Hinge, resulted initially in subsidence in the region north of the fault. Sequence 2 accumulated in the central sub-basin, when subsequent fault movement reduced accommodation in the north and accelerated subsidence in the region south of the North Monias Hinge. Sequence 3 successions progressively infilled the paleotopography inherited from deposition of the preceding sequences and Sequence 4 was deposited relatively more continuously along-strike between the north and central sub-basins. These observations suggest that local tectonism may have played a more significant role in driving the evolution of Montney sequences than global eustasy.

Sedimentological and ichnological analysis suggests that the Montney Formation represents the deposits of stacked prodelta successions that were commonly influenced by river-flood and storm processes. The analysis of horizontal well production within the liquids-rich gas fairway of the north Montney sub-basin demonstrates that well performance is stratigraphically controlled, as well as controlled by facies within the individual target intervals. Primary deposition is, therefore, of fundamental importance to understanding the character and distribution of prolific unconventional reservoirs in the Montney Formation. As such, ongoing, increasingly sophisticated efforts to optimize this globally significant resource, must continue to include careful consideration of the fundamental geological controls.

## References


Baniak, G.M, Moslow, T.F., Michailides, S. and Adams, M.G. 2023. Sequence stratigraphic architecture of the Lower Triassic Montney Formation, northeastern British Columbia, Canada. AAPG Bulletin, v. 107, p. 283-310.

Bann, K.L. and Proverbs, I.P. 2023. The record of river flood and storm events in unconventional reservoirs of the Montney Formation, northeastern British Columbia. In: 2023 CEGA Core Conference Abstracts. https://www.cspg.org/common/Uploaded%20files/pdfs/documents/conference_website/core/2023CCAbstractBook.pdf

Bann, K.L., Proverbs, I.P. and Landi, M. Mixed influence (river-, wave-storm- and tide-influenced) deltaic deposits and hybrid event beds in unconventional reservoirs of the Montney Formation, northwestern Alberta. In: 2024 CEGA Core Conference Abstracts. https://coreconference.ca/wp-content/uploads/2024-core-conference-abstract-book.pdf/(coreconference.ca)

Crombez, V., Rohais, S., Baudin, F. and Euzen, T. 2016. Facies, well-log patterns, geometries and sequence stratigraphy of a wave-dominated margin: insight from the Montney Formation (Alberta, British Columbia, Canada). Bulletin of Canadian Petroleum Geology, v. 64, p. 516-537.

Davies, G.R., Watson, N., Moslow, T.F. and MacEachern, J.A. 2018. Regional subdivisions, sequences, correlations and facies relationships of the Lower Triassic Montney Formation, west-central Alberta to northeastern British Columbia, Canada—with emphasis on role of paleostructure. Bulletin of Canadian Petroleum Geology, v. 66, p. 23-92.

Euzen, T., Moslow, T.F., Crombez, V. and Rohais, S. 2018. Regional stratigraphic architecture of the Spathian deposits in western Canada—Implications for the Montney resource play. Bulletin of Canadian Petroleum Geology, v. 66, p. 175-192.

Euzen, T., Watson, N., Fowler, M., Mort, A. and Moslow, T.F. 2021. Petroleum distribution in the Montney hybrid play: Source, carrier bed, and structural controls. AAPG Bulletin, v. 105, p. 1867-1892.

Furlong, C.M., Gingras, M.K., Moslow, T.F. and Zonneveld, J.P. 2018. The Sunset Prairie Formation: designation of a new middle Triassic formation between the lower Triassic Montney formation and middle Triassic Doig formation in the Western Canada Sedimentary Basin, northeast British Columbias. Bulletin of Canadian Petroleum Geology, v. 66, p. 193-214.

Furlong, C.M., Gingras M.K. and Zonneveld J.P. 2020. High-resolution sequence stratigraphy of the Middle Triassic Sunset Prairie Formation, Western Canada Sedimentary Basin, north-eastern British Columbia. The Depositional Record. v. 6, p. 383-408.

González, P.D., Furlong, C.M., Gingras, M.K., Playter, T. and Zonneveld J.P. 2022. Depositional framework and trace fossil assemblages of the lower Triassic Montney formation, northeastern British Columbia, Western Canada Sedimentary Basin. Marine and Petroleum Geology. v. 143, Article 105822

Mackie, S.J., Furlong, C.M., Pedersen, P.K. and Ardakani, O.H. 2022. Relation of Stratigraphy and Facies Heterogeneities to Hydrogen Sulphide Distribution in the Montney Formation of Northeastern British Columbia (Parts of NTS 093, 094); in Geoscience BC Summary of Activities 2022: Energy and Water, Geoscience BC, Report 2022-02, p. 13-22

MacEachern, J.A. and Bann, K.L. 2020. The Phycosiphon Ichnofacies and the Rosselia Ichnofacies: Two new ichnofacies for marine deltaic environments. Journal of Sedimentary Research. v. 90, p. 855-886.

MacEachern, J.A. and Bann, K.L. 2022. Departures from the archetypal deltaic ichnofacies, in Console-Gonella, C., de Valais, S., Diaz-Martinez, I., Citton, P., and McIlroy, D. eds, Ichnology in Shallow-marine and Transitional Environments. Geological Society, London, Special Publications. v. 522, https//doi.org/10.1144/SP522-2022-56.

Moslow, T.F., Haverslew, B., Henderson, C.M. 2018. Sedimentary facies, petrology, reservoir characteristics, conodont biostratigraphy and sequence stratigraphic framework of a continuous (395m) full diameter core of the Lower Triassic Montney Fm, northeastern British Columbia. Bulletin of Canadian Petroleum Geology, v. 66, p. 259-287.

Nieto, J., Janega, G., Baltai, B. and Martinez, H. 2018. An integrated approach to optimizing completions and protecting parent wells in the Montney Formation N.E.B.C. *In* Unconventional Resources Technology Conference, Houston, TX, USA, 23-25 July 2018. Society of Exploration Geophysicists, American Association of Petroleum Geologists, Society of Petroleum Engineers, p 2346-2360.

Norgard, G. 1997. Structural inversion of the Middle Triassic Halfway Formation, northeast British Columbia. Bulletin of Canadian Petroleum Geology, v. 45, p. 614-623.

Plint, A.G. and Nummedal, D. 2000. The falling stage systems tract: recognition and importance in sequence stratigraphic analysis. In: Sedimentary Responses to Forced Regressions. D. Hunt and R.L. Gawthorpe (eds.), p. 1-17.

Posamentier, H. W., and Allen, G. P. 1999. Siliciclastic Sequence Stratigraphy - Concepts and Applications. Society of Economic Petrologists and Paleontologists, 216 pages.

Prenoslo, D., Furlong, C.M., Gingras, M.K., Playter, T. and Zonneveld, J.P. 2018. The sedimentology, stratigraphy and reservoir characteristics of the Montney D1 and D2 horizons in the Greater Pouce Coupe area. Bulletin of Canadian Petroleum Geology, v. 66, p. 338-358.

Proverbs, I.P., Bann, K.L. and Fratton, C. 2010. Integrated Sedimentology, Ichnology and Petrography of Unconventional Gas Reservoirs of the Montney Formation; Dawson Creek Region, Northeastern BC. In Canadian Society of Petroleum Geologists, abstract of Joint Convention.

Proverbs, I.P., Bann, K.L., Fratton, C.M., Frostad, C.J., and Juska, A. 2018. Facies architecture and sequence stratigraphy of the Lower Triassic Montney Formation, NE British Columbia: Fundamental controls on the distribution of 'sweet spots' in a world-class unconventional reservoir. Bulletin of Canadian Petroleum Geology, v. 66, p. 237-258.

Proverbs, I.P., Taylor, B., and Bann, K.L. 2021. Deltaic depositional processes, fluctuating relative sea-level and syndepositional tectonism: controls on the geometry and distribution of fine-grained reservoirs, Montney Formation, northeast British Columbia, northwest Alberta. CSPG CSEG CWLS Joint Annual Convention, September 13-15, 2021 Calgary, AB. Available from: https://geoconvention.com/wp-content/uploads/abstracts/2021/67387-deltaic-depositional-processes-fluctuating-relati.pdf

Proverbs, I.P., Bann, K.L., Taylor, B., Nasen, J.A., Frostad, C.J. 2024 in press. Depositional, stratigraphic and structural controls on the geometry of Montney Formation reservoirs: Lower Triassic, northeast British Columbia, northwest Alberta. Bulletin of Canadian Energy Geoscience, v. 71, p. 63-100

Sanders, S., Etienne, C., Gegolick, A., Kelly; D., Zonneveld; J.P. 2018. The Middle Montney Altares Member: lithology, depositional setting and significance for horizontal drilling and completion in the Altares Field, British Columbia. Bulletin of Canadian Petroleum Geology, v. 66, p. 318-337.

Vaisblat, N., Harris, N.B., DeBhur, C., Euzen, T., Gasparrini, M., Crombez, V., Rohais, S., Krause, F. and Ayranci, K. 2017. Diagenetic model for the deep Montney Formation, northeastern British Columbia; in Geoscience BC Summary of Activities 2016, Geoscience BC, Report 2017-1, p. 37-48.

Vaisblat, N. and Harris, N.B. 2016. A burial history model for the Montney Formation - an insight to porosity distribution and hydrocarbon migration; in Geoconvention 2016: Optimizing Resources, Canadian Society of Petroleum Geologists, Canadian Society of Exploration Geophysicists, Canadian Well Logging Society, Joint Annual Meeting, Calgary, Alberta, March 7–11, 2016, abstract, 1 p., URL [December 2016]

Watt, E.A., Laycock, D.P., Michael, E., Tobin, R.C., Kelly, S. and Johnston, M.N. 2022. Hydrocarbon charge and petroleum system evolution of the Montney Formation: A multidisciplinary case study of the Blueberry sub-play in Northeast British Columbia, Canada. Bulletin of Canadian Energy Geoscience, v. 69, p. 21-50.

Wood, J.M. 2012. Water distribution in the Montney tight gas play of the Western Canada Sedimentary Basin: Significance for resource evaluation. SPE 161824.

Wood, J.M., Sanei, H., Curtis, M.E. and Clarkson, C.R. 2015. Solid bitumen as a determinant of reservoir quality in an unconventional tight siltstone play. International Journal of Coal Geology, http://dx.doi.org/10.1016/j.coal.2015.03.015

Wood, J.M., Haeri-Ardakani, O., Sanei, H., Curtis, M.E., and Royer, D. 2020. Application of paleoporosity and bitumen saturation concepts to tight-gas accumulations containing solid bitumen. International Journal of Coal Geology. v. 1, p. 228:103547.

Wood, J.M., Euzen, T., Sharp, L. and Leroux, S. 2021. Phase separation and secondary migration of methane-rich gas accompanying uplift of an unconventional tight hydrocarbon system, Montney Formation, western Canada. Marine and Petroleum Geology, 124, 104808.

Zonneveld, J.P., MacNaughton, R.B., Utting, J., Beatty, T.W., Pemberton, S.G. and Henderson, C.M. 2010b. Sedimentology and ichnology of the Lower Triassic Montney Formation in the Pedigree-Ring/Border-Kahntah River area, northwestern Alberta, and northeastern British Columbia; Bulletin of Canadian Petroleum Geology, v. 58, p. 115-140.

Zonneveld, J.P., Furlong, C.M., Gegolick, A., Gingras, M.K., Golding, M., Moslow, T.F., Orchard, M., Playter, T., Prenoslo, D. and Sanders, S.C. 2016. The Montney-Doig boundary and the “Anisian wedge”. International Core Conference Abstracts. Canadian Society of Petroleum Geologists. p. 63-66.

Zonneveld, J.P. and Moslow, T.F. 2018. Palaeogeographic setting, lithostratigraphy, and sedimentary framework of the Lower Triassic Montney Formation of western Alberta and northeastern British Columbia. Bulletin of Canadian Petroleum Geology, v. 66, p. 93-127.

GUSSOW 2024
Montney Subsurface Evaluation: Drive Towards Excellence
Banff, AB | October 2-4

# Towards Understanding the In-Situ Stress Regime in the Montney Formation – Lessons from the 2027 CEGA Atlas of the WCSB

Pat McLellan[1]

1. McLellan Energy Advisors Inc., Lead Author of the 2027 CEGA Atlas In-Situ Stress Chapter.

## Abstract

This presentation outlines the progress made to date on the compilation, analysis and interpretation of data for the in-situ stress chapter of the 2027 CEGA Atlas of the WCSB. Examples of horizontal stress orientations and minimum horizontal stress magnitudes from the Montney Play area are shown, as well as the methodologies being used to measure and analyze this data. Important applications of in-situ stress data for well design, hydraulic fracturing, and the assessment of induced seismicity hazards in the Montney are mentioned.

## Background

Building on the compilation of in-situ stress orientations and magnitudes in the 1994 CSPG AGS GSC Atlas of the Western Canadian Sedimentary Basin (Mossop et al, 1994), our sub-committee has been busy for a few years compiling stress data for four provinces and a portion of two territories. The new enlarged 2027 Atlas area stretches from the BC interior to eastern Manitoba and from the US border to the Arctic coast as shown in Figure1.

Figure 1: Western Canada showing the outline of the area covered by the 2027 CEGA Geological Atlas of the WCSB in four provinces and two territories. (https://atlas2027.ca)

## Methodology

Methods typically used for measuring in-situ stress magnitudes and orientations in the WCSB are summarized in Table 1 Most of the data that we have ready access to is derived from a limited number of sources, e.g., for stress orientations the historical data on borehole breakouts analyzed on oriented caliper logs and image logs are expected to comprise more than 90% of the data in our compilation. Maximum horizontal stress orientations derived from earthquake focal mechanism inversion is an important type of information, which may either be compiled in this chapter or perhaps in the Seismicity chapter of the Atlas. Regardless of where the data is presented there will be a comparison of the wellbore scale determinations of SHmax versus those analyzed from natural and induced earthquakes in the basin.

Vertical stress magnitude determinations are typically undertaken by integrating bulk density log data. As they are often the most accurate and the most easily determined stress component in the basin, we have not, to date, spent a lot of effort compiling this information from public domain sources. Minimum horizontal stress magnitude determinations from mini-fracs or DFITs (Diagnostic Fracture Injection Tests) are of considerable interest for applications like hydraulic fracturing, induced seismicity, wellbore stability and other issues. Only limited amounts of this information makes its way into the public domain, so we have spent a considerable effort compiling such information from industry sources and publications. Step-rate tests, pressuremeter testing, and mining measurements are similarly rarely performed and only a few such datasets are published. Drilling leakoff tests (LOTs), while popular in the offshore, are less commonly conducted in the WCSB with a desire to obtain a quality SHmin stress measurement, and as such are not included in our database.

Table 1: Main sources of in-situ stress orientation and magnitude data measured in the WCSB that are compiled for the 2027 CEGA Atlas

| **In-situ Stress Orientations** | **In-Situ Stress Magnitudes** |
|---|---|
| • Oriented caliper logs | • Bulk density logs for vertical stress |
| • Borehole image logs | • DFITs, mini- and micro-fracs for SHmin |
| • Sonic log shear wave anisotropy | • Pressuremeter stress data |
| • Hydraulic fracturing microseismic and DAS | • Step rate tests (waterflooding, disposal operations) |
| • Earthquake focal mechanism inversion | • Underground mining stress measurements |
| • Core-based methods (ASR, DSCA, overcoring) | |

## Early Results and Discussion

Figure 2 shows an example of horizontal in-situ stress orientations (SHmax) determined largely from borehole breakouts in the Montney play area of NEBC and Alberta, as initially reported by Bell et al (1994) and compiled with additional data by Haug and Bell (2016), and later by McLellan (2021). Note the relatively consistent NE-SW orientation of SHmax for the area shown. More detailed investigations for selected parts of the Montney, like the Kiskatinaw Seismic Monitoring and Mitigation Area (KSMMA), will also be summarized in the chapter.

Figure 3 is an example of the type of detailed DFIT data that has been collected by some operators in well-developed parts of the Montney play. McLellan et al (2016) reported on the statistical variation of both SHmin magnitude and reservoir pressure gradients across Talisman Energy's Farrell Creek field in NEBC. Using consistent interpretation methods with the same software, 32 DFIT tests were analyzed. Note the considerable variation in both gradient values, probably due to the influence of the local faulted structure and perhaps some degree of reservoir depletion.

An important development in the interpretation of DFIT fracture closure pressures (FCP), in the last decade, has been the recognition of an alternative selection for this value, often referred to as the "compliance closure". While still controversial in some parts of the well testing community, our Atlas chapter will present examples of the latter development and its comparison to the classic or "holistic" FCP pick. Differences in the order of 10-15% between the two FCP values, our best proxy for the SHmin magnitude, have been reported by several workers. (Virues et al, 2023).

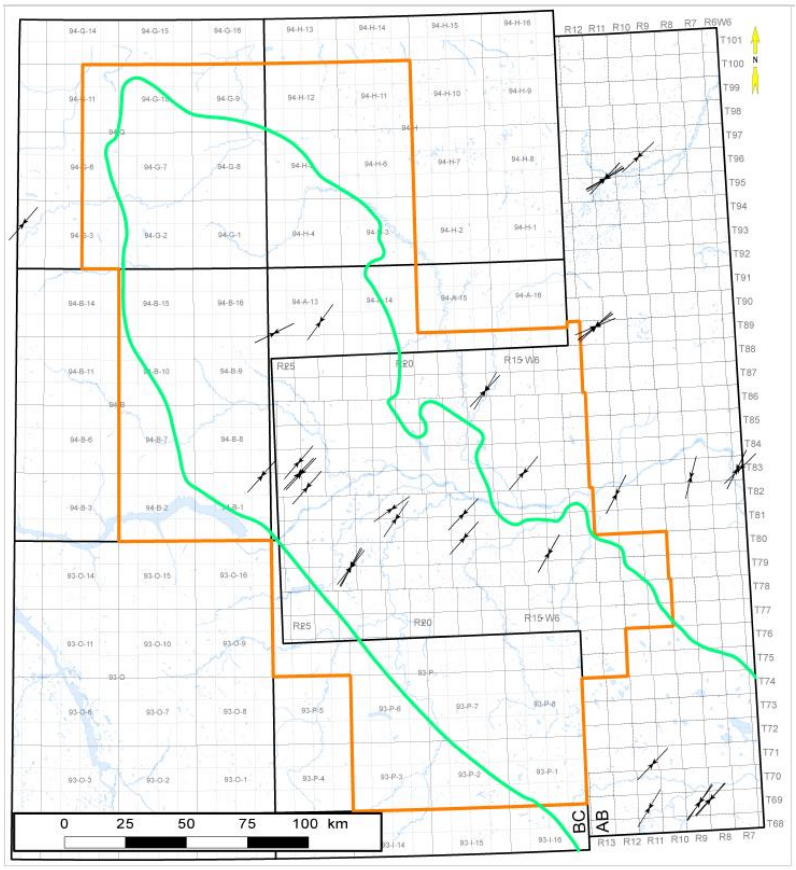


Figure 2: Map of NEBC and part of Alberta showing the Montney play outlined in green and the orientation of SHmax derived from selected borehole breakouts and drilling induced fractures. (McLellan, 2021).

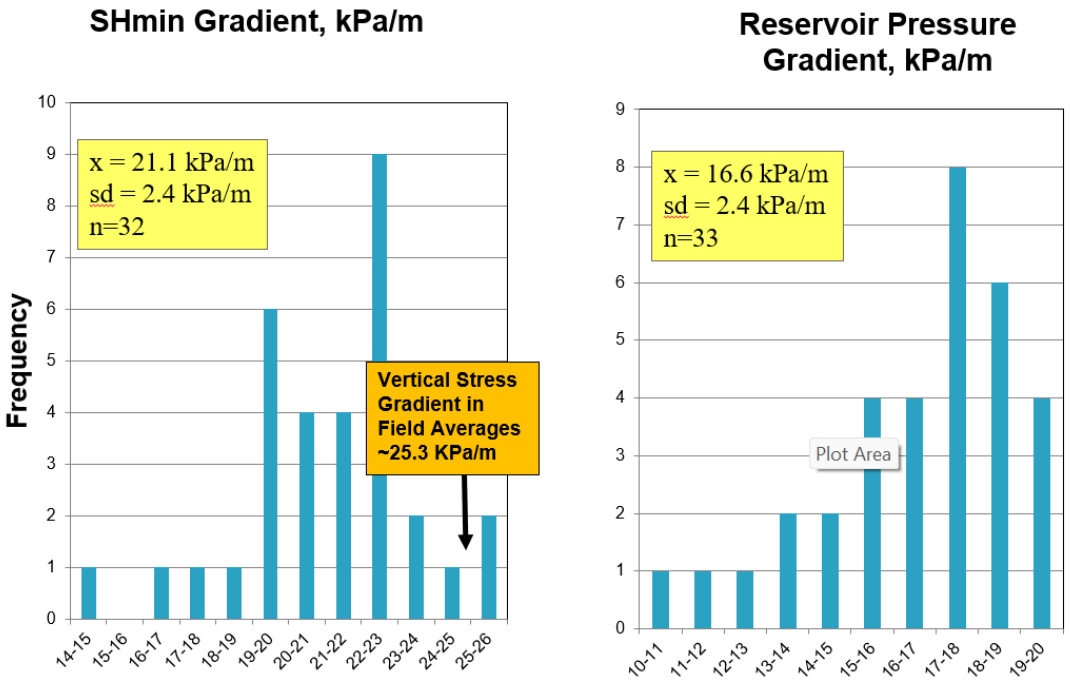


Figure 3: Example of DFIT derived SHmin and reservoir pressure gradients measured by Talisman Energy in the Montney Formation in the Farrell Ck field, NEBC. McLellan et al (2016). Fracture closure pressures were selected using the FCP pick on a Gdp/dG vs time plot after Barree et al. (2009). x = mean value, sd = standard deviation.

## Key Takeaways

- The In-situ Stress chapter of the 2027 CEGA Atlas project is progressing well and we expect to have our draft maps, figures and text completed in the fall of 2025. The complete Atlas publication is scheduled for release in digital and printed versions in 2027.
- There is relatively good coverage of the orientation of the maximum horizontal principal stress SHmax in the Montney Formation of Alberta and British Columbia, obtained mainly from borehole breakouts and drilling induced fractures identified in caliper and image logs.
- There is a rich dataset of DFIT-derived SHmin magnitudes for many formations in the Atlas, especially as measured in fracture stimulated horizontal wells in unconventional reservoirs such as the Montney and Duvernay.
- SHmax magnitude measurements in the Montney formation are scarce, as it is rarely tested in vertical openhole wellbores. It can, however, be calculated based on hole enlargement and with a knowledge of rock mechanical properties.
- Vertical stress is easily and accurately calculated from bulk density logs, ideally from wells with good log coverage below surface casing

## Acknowledgements

The sub-committee of professionals currently working on the In-Situ Stress chapter of the Atlas also includes: Chris Hawkes (University of Saskatchewan), Doug Schmitt (Purdue University), Claudio Virues (AER), Baohong Yang (AGS/AER), Michelle Gaucher (BCER), Juan Arias (Suncor), and Ken Glover (RESPEC). The content and commentary provided in this talk were prepared by the presenter, and do not necessarily represent the views of the other sub-committee members nor their respective organizations.

## References

Barree, R.D., Barree, V.L., and Craig, D. (2009). Holistic Fracture Diagnostics: Consistent Interpretation of Pre-frac Injection Tests Using Multiple Analysis Methods. *SPE Prod & Oper* 24, 396–406.

Bell, J.S., Price, P.R. and McLellan, P.J. (1994) In-situ stress in the Western Canada Sedimentary Basin; *In* Geological Atlas of the Western Canada Sedimentary Basin, G.D. Mossop and I. Shetsen (comp.), Canadian Society of Petroleum Geologists and Alberta Research Council.

CEGA 2027 Atlas website. https://atlas2027.ca

Haug, K. and Bell, J.S. (2016) Compilation of in-situ stress data from Alberta and northeastern British Columbia; Alberta Energy Regulator, AER/AGS Digital Data 2016-0040.

McLellan, P.J. (2016) Geomechanical characterization of the Farrell Creek Montney reservoir, northeast British Colombia; Society of Petroleum Engineers Workshop: The Montney Play, October 18, 2016, Calgary, Alberta.

McLellan, P.J., (2021) Geomechanical Analysis Chapter, *In* Wastewater Disposal in the Maturing Montney Play Fairway of Northeastern British Columbia, Prepared by Petrel Robertson Consulting Ltd. for Geoscience BC, Report GCBR 2021-14.

Mossop, G.D. and Shetsen, I., comp. (1994) Geological Atlas of the Western Canada Sedimentary Basin; Canadian Society of Petroleum Geologists and Alberta Research Council.

Virues, C., Robertson, A., and Sendecki, B. (2023) Best Practices in DFIT Interpretation - Comparative Analysis of 80 DFITs in the Canadian Montney Shale Play, SPE-215017-MS, Presented at the SPE Annual Technical Conference and Exhibition, San Antonio, Texas, October 2023.

GUSSOW 2024
Montney Subsurface Evaluation: Drive Towards Excellence
Banff, AB | October 2-4

# Fracture distribution in Montney outcrops in Kananaskis, its all in the fabric

Per K. Pedersen[1], Patricia E. Fraino[1], Simon Poirier[1], Carolyn M. Furlong[2], Nicole Virginillo[1] and Zach Toews[1]

[1] University of Calgary, Department of Earth, Energy and Environment, Calgary, Alberta, [2] MacEwan University, Department of Physical Science, Edmonton, Alberta

## Abstract

Fracture geometries are a primary control on productivity in low-permeability reservoirs such as the Lower Triassic Montney Formation. However, assessing the dimensions of natural and hydraulically induced fractures in subsurface reservoirs relies mainly on indirect methods, including cores, well logs, seismic, microseismic, DAS, DFIT, completion and production data.

This study focuses on characterizing natural fractures in numerous outcrops of the Sulphur Mountain Formation, which is equivalent to the subsurface Montney Formation, in the Kananaskis area. Studied outcrops are located on different thrust sheets in different structural positions within the thrust sheets, allowing for assessing fractures related to thrusting. Fractures were observed on centimetre to 10-meter scales on vertical rock walls, bedding planes, and cores drilled behind the outcrops to characterize the fractures at various scales and their 3D fracture geometry.
Our research showed consistently that the different sedimentological facies of the Montney have unique fracture characteristics. While minor differences in compositions of the various facies contribute to these variations, the first order of control on the observed differences in fracture geometries is the rock mechanical fabric of the facies, specifically the mechanical bed thickness.

Although the outcrops have experienced a different tectonic history than the subsurface Montney, significant horizontal stress, bending and uplift, the observations from this study provide a visualization of the differences in fracture complexity of the reservoir facies of the Montney. These observations can serve to optimize the choice of the landing zone, stage spacing and completion design to estimate fracture height to optimize production, lateral and vertical spacing of horizontal wells, and reduce the risk of fracture hits and induced seismicity.

## Statement of the background

The siltstone-dominated, Lower Triassic Montney Formation is a premier tight gas and oil play in western Alberta and northeastern British Columbia. Despite over two decades of exploitation and extensive data collection, many aspects of this unconventional reservoir remain poorly understood. While the Montney is a relatively monotonous thick succession of siltstones with only minor change in grain size and composition, hydraulic fracture completion data show a significant variability both in and between landing zones, revealing differences in rock mechanics of the reservoir rock mass. This variability in the distribution and variability of natural and hydraulically induced fractures is reflected in well productivity, even between closely spaced wells (e.g. Maxwell et al., 2011, Rodgers et al., 2014, MacFarlane and Davis, 2015). Similar variations in production have been observed across other shale and tight gas plays, often attributable to the presence of natural fractures, which can either enhance or hinder production (Gale et al., 2014 and references therein).

To address this, this study examines the distribution of natural fractures in outcrops of the Montney equivalent Sulphur Mountain Formation to provide an analogue for the natural and induced fractures in the subsurface. Several outcrops located in various structural positions within different thrust sheets were examined at different scales using a broad suite of techniques characterizing facies and fractures to evaluate their relationship.

In this study, we focus on outcrops studies to answer the following questions:

1. What is the vertical and lateral variability in fracture intensity and height in the Montney Formation?
2. How large are the differences between landing zones in the Montney in terms of fracture height and intensity?
3. Are large, low-offset fractures within the reservoir interval geologically realistic? If so, how may they be predicted or recognised in the subsurface to optimise well completion?

Recent technological advances and increased availability of unmanned areal vehicles (UAVs) and photogrammetric software have made the generation of detailed digital outcrop models relatively easy and inexpensive (Westoby et al., 2012, Bemis et al., 2014). Digital outcrop models have proved a useful tool for collecting large amounts of structural data, including fractures, particularly where outcrop is inaccessible (Gillespie et al., 2011; Lato and Malte, 2012; Bisdom et al., 2015; Pless et al., 2015; Casini et al., 2016, Cawood et al., 2017; Theiele et al., 2017; Zhang et al., 2018). In this study, we utilize UAV based digital outcrop modeling, coupled with edge-detection based automatic fracture picking, to collect a large amount of fracture data from Montney equivalent outcrops. Integrated with detailed field-based observations, these data provide insights into the questions mentioned above.

## Aims and Objectives

In unconventional hydrocarbon resource plays, such as the Montney Formation, effective, reliable, and repeatable hydraulic fracturing stimulation is essential for economical production. However, in most resource plays, a significant number of hydraulic fracture stages within and between landing zones have unexpected treatment programs.
In this study, we use characteristics of natural fractures in outcrops of the Sulphur Mountain Formation in the thrust belt of the Rocky Mountains as a proxy for natural and hydraulic induced the subsurface equivalent Montney Formation. In the outcrops, for each sedimentary facies the fracture characteristics were quantified, depending on the outcrop including fracture intensities, fracture area, fracture height, etc.

## Materials and methods

Numerous outcrops of the Lower Triassic Phroso Siltstone and Vega Siltstone members of the Sulphur Mountain Formation were examined in the Kananaskis and Canmore area (Figures. 1 and 2). To assess for the influence of structural deformation, outcrops were studied in various structural positions within different thrust sheets. Fractures were observed on vertical rock walls, bedding planes, and cores drilled behind the outcrops to characterize the fractures from centimetre to 10-meter scales and their 3D fracture geometry. Transitional structural workflows on vertical outcrops and bedding planes were integrated with drone generated model and image analyses.
Mineralogy and petrology were determined by XRF, XRD integrated with thin sections and SEM to determine the grain and cement distribution. Mechanical properties of select samples were determined using a Proceq EQUOTIP Piccolo 2.

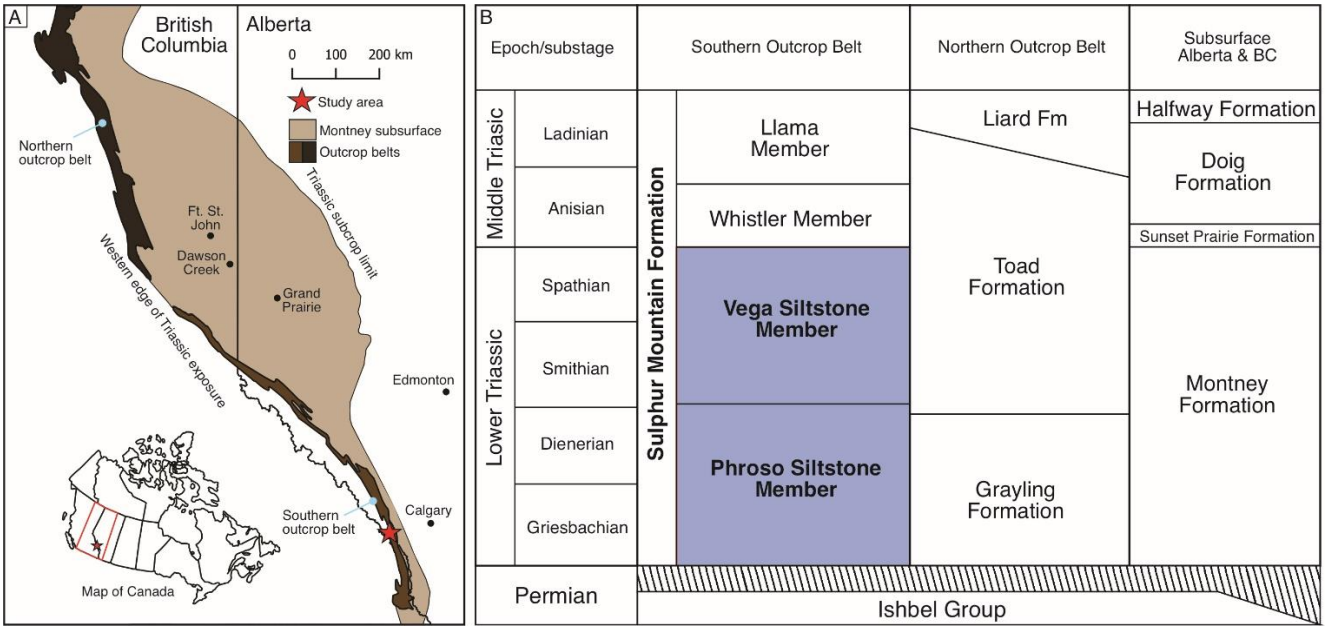


Figure 1. Map showing the location of the study area in the red box relative to the Montney play, modified from Zonneveld et al. (2011). Stratigraphic chart of the outcrop and subsurface, studied members of the Sulphur Mountain Formation highlighted. Figure modified from Fraino et al (in prep).

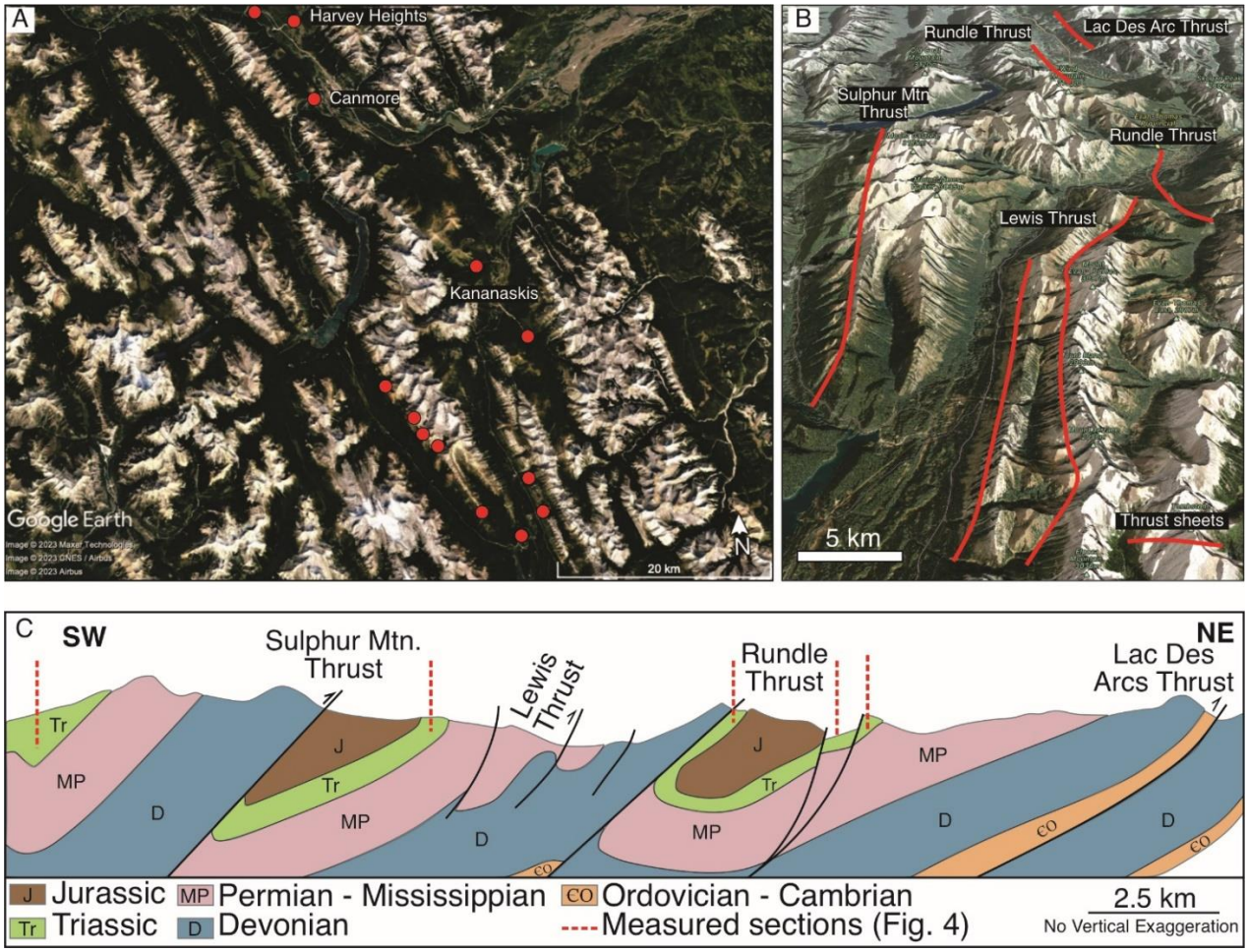


Figure 2. A) Google image showing the outcrop locations in the Kananaskis and Canmore area. B) Satellite image showing the main thrust faults in red. C) Structural cross section showing some of the studied outcrop locations in relation to position within thrust sheets. Figure modified from Fraino et al (in prep).

## Results and discussion

At Evan Thomas Creek a rock wall provides a 170m thick and over 1500m long exposure of the of the Montney Eq. (Vega and Phroso Siltstone members). At this section the Montney Eq overlies unconformably a transgressive conglomerate on the Permian Rocky Ishbel Group and is unconformably overlain by the Jurassic Nordegg Formation. Measured sedimentological section was complemented by handheld gamma and XRF data to characterize the vertical changes in sedimentary facies and composition and define sedimentary units (Figure 3). Integration with fracture characterization revealed a weak relationship between the fracture intensity and fracture height. Average fracture height appears to be controlled mainly be sedimentary fabric and bed thickness, with the shortest average fracture height occurring where thinly bedded siltstones are interbedded with 10-30cm sandstone beds. Surprisingly a significant change in composition at ~49m to a more carbonate-rich succession above is not reflected in a significant change in the fracture intensity or their height as can also been seen on the orthomosaic image (Figure 3). This highlight that while composition and rock mechanics often correlate with natural fractures, this relationship is not always the case, as also shown in previous Montney subsurface studies (Vaisblat, N., 2020; Becerra Rondon, D., 2022).

The lateral variation in the abundance of fractures was characterized by manual fracture picking and edge detection algorithms on drone images of the rock wall at Evan Thomas Creek. Firstly, the lateral variation in fracture intensity (fracture/m) along the rock wall was characterized along scan lines, each scan line located within a single bed (Figure 4). To highlight the variation in fracture intensity, the fractures were averaged over 10 and 100m. Each scan line shows a significant variation in fractures along their length, with areas of high fracture intensity corresponding to shear zones with no significant vertical offset. The scan lines provide a proxy for the lateral variation in natural fractures along a horizontal well in the subsurface, although likely not with the fracture intensities observed in the outcrop. Also note the similarities and

differences in fracture intensities along the two scan lines located immediately above each other, reflecting the difference in rock mechanical properties and bed thickness.

To further characterize both the vertical and lateral variations in fracture abundance, a heat map of areal fracture density (m/m2) was generated using edge detection algorithms (Figure 4). While the heat map shows similar vertical variation in fracture abundance, as shown in Figure 1, the heat map highlights more significant lateral variation in areal fracture density. Note along the rock wall the presence of vertical oriented areas of high fracture abundance. These are interpreted as shear zones as they don't have any vertical offsets. Such shear zones facilitate vertical fluid migration, in the subsurface likely of both hydrocarbons and frac fluids, with the latter potentially resulting in frac hits between vertically stacked horizontal wells. Note the difference in widths of the shear zones, reflecting their different appearance in subsurface datasets such as 3D seismic, microseismic, well logs, completion and production data.

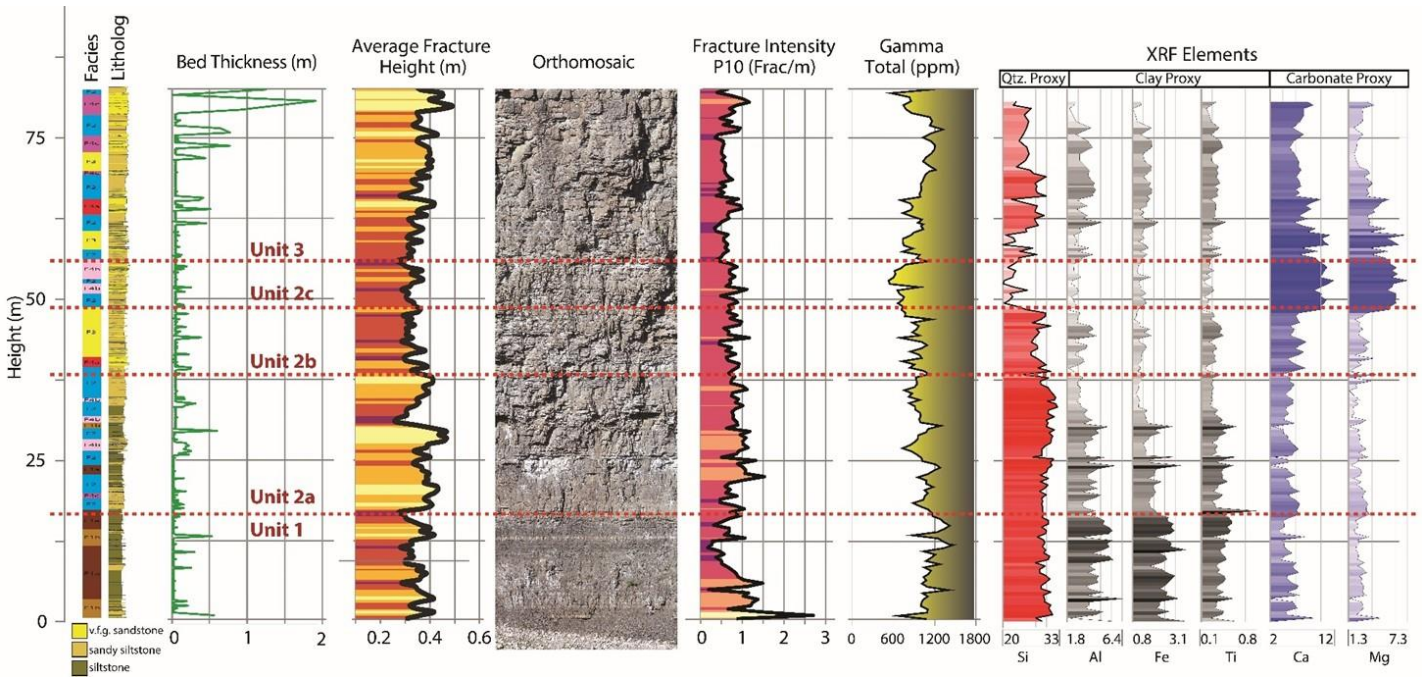


Figure 3. Measured section of the basal Montney Eq. section at Evan Thomas Creek complemented by handheld gamma and XRF data defining several sedimentary units. Modified from Poirier (2020).

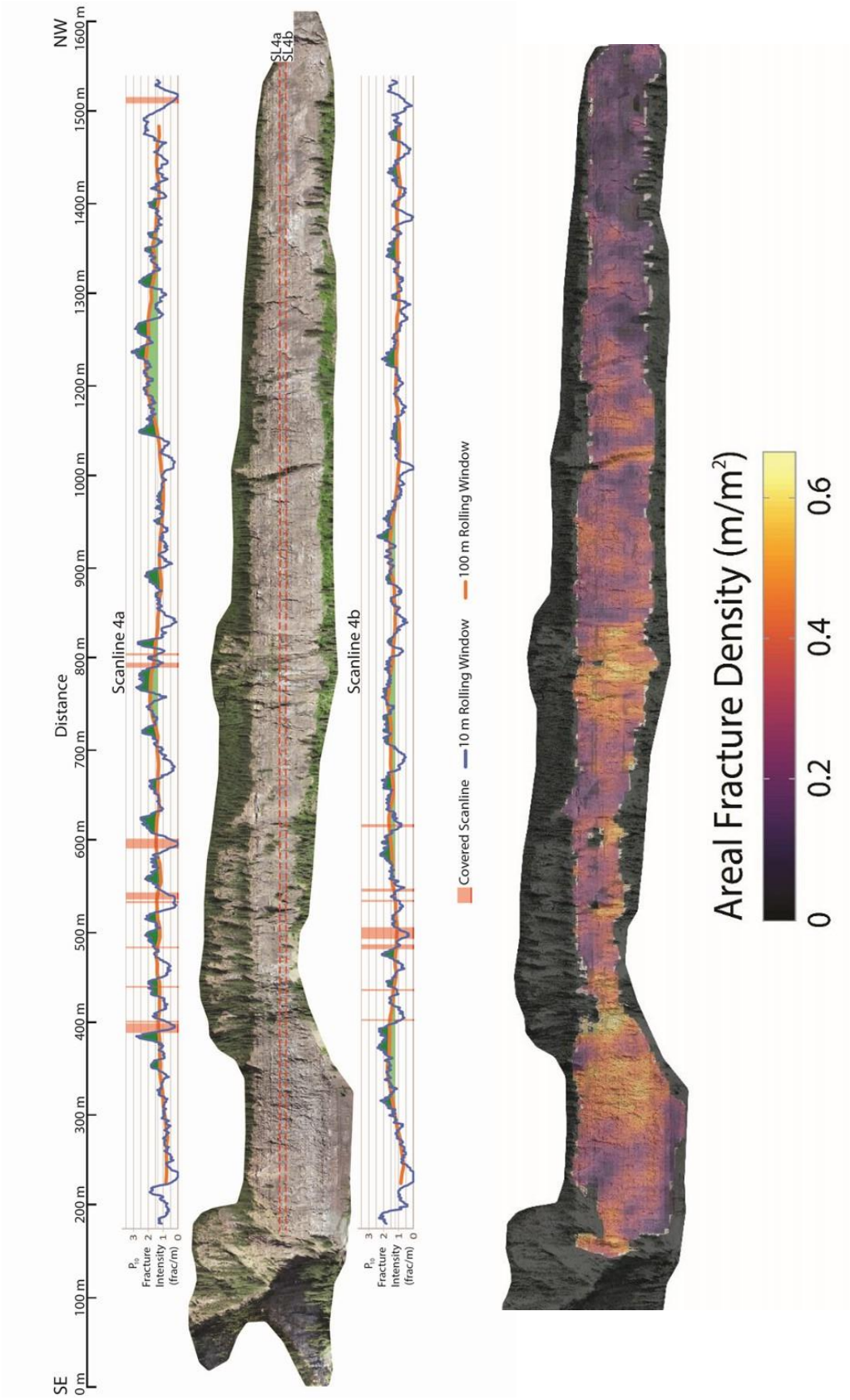


Figure 4. Drone image of the rock wall at Evan Thomas Creek. A) Drone image overlain my two scan lines each located in the same bed showing the lateral variation in fracture intensity (fracture/m) average over 10 and 100m. B) Heat map of areal fracture density ($m/m^2$). Figures shows the lateral variation in fracture intensity and density, with areas of high abundance of fractures corresponding to shear zones. Note, the shear zones have no offset and are thus not faults. Modified from Poirier (2020).

To further understand the vertical variation in fracture intensities observed at Evan Thomas Creek (Figures 3 and 4), three bedding planes exposed by Hood Creek in Kananaskis were analyzed, which occur in a different thrust sheet to that of Evan Thomas Creek (Figure 2B; Figure 5). These strata occur in the upper portion of the Montney Eq. in offshore deposits that consists of thinly-bedded, planar-laminated siltstone interbedded with medium-bedded siltstone beds, with the three bedding planes occurring within 2 m of stratigraphic section. Thin sections and XRD show the composition of the three beds is very similarly, consisting of dolomite-cemented siltstones, with the beds having similar thicknesses of ~20cm. However, the mineralized fractures exposed on the three bedding planes have very different fracture characteristics, not only in fracture abundance but also in dominant fracture orientation (Figure 5). To quantify these differences in the observed fractures, the fractures were mapped and analyzed using FracPaQ. Analyses showed that while all three bedding planes have a common east-west (EW) fracture set, each bedding plane features a secondary fracture set with orientation varying up to 90 degrees. This is surprising, considering that all the bedding planes have undergone the same tectonic stress history and appear to have similar rock mechanical properties. Additionally, fracture lengths also show unique distribution for each bedding plane. These findings imply that although the beds are relatively intensively fractured, the vertical fluid conductivity through the fractures would be very limited due to the different orientations and lengths of the fractures. Further, while not directly observable in the outcrop, the fractures are likely bed-bound and may be linked by bedding plane-parallel fractures.

The nature of bedding plane-parallel fractures is well illustrated in a 50 m long core from the Kamenka Quarry in Harvie Heights. The core was similar to the strata examined at Hood Creek within offshore siltstones within the upper part of the Montney Eq. A full suite of analyses was performed on the core, including core description, CT scan, white light RGB, hyperspectral core scan complemented by thin section petrography, XRD, XRF and Microhardness, see Toews (2023) master thesis for details. The core shows relatively few vertical mineralized fractures but frequent bedding plane parallel mineralized fractures (Figure 6). While the location of the bedding plane fractures might appear random, clusters based on short wavelength and long wavelength hyperspectral imaging show that the bedding plane fractures preferentially occur at boundaries between different hyperspectral classes (Figure 6). The hyperspectral classes reflect variations in mineralogy, as confirmed by thin section, XRD, and XRF, each corresponding to units with different rock mechanical properties, as revealed by microhardness data. Therefore, the fabric and heterogeneity strongly control the location of these bedding plane fractures.

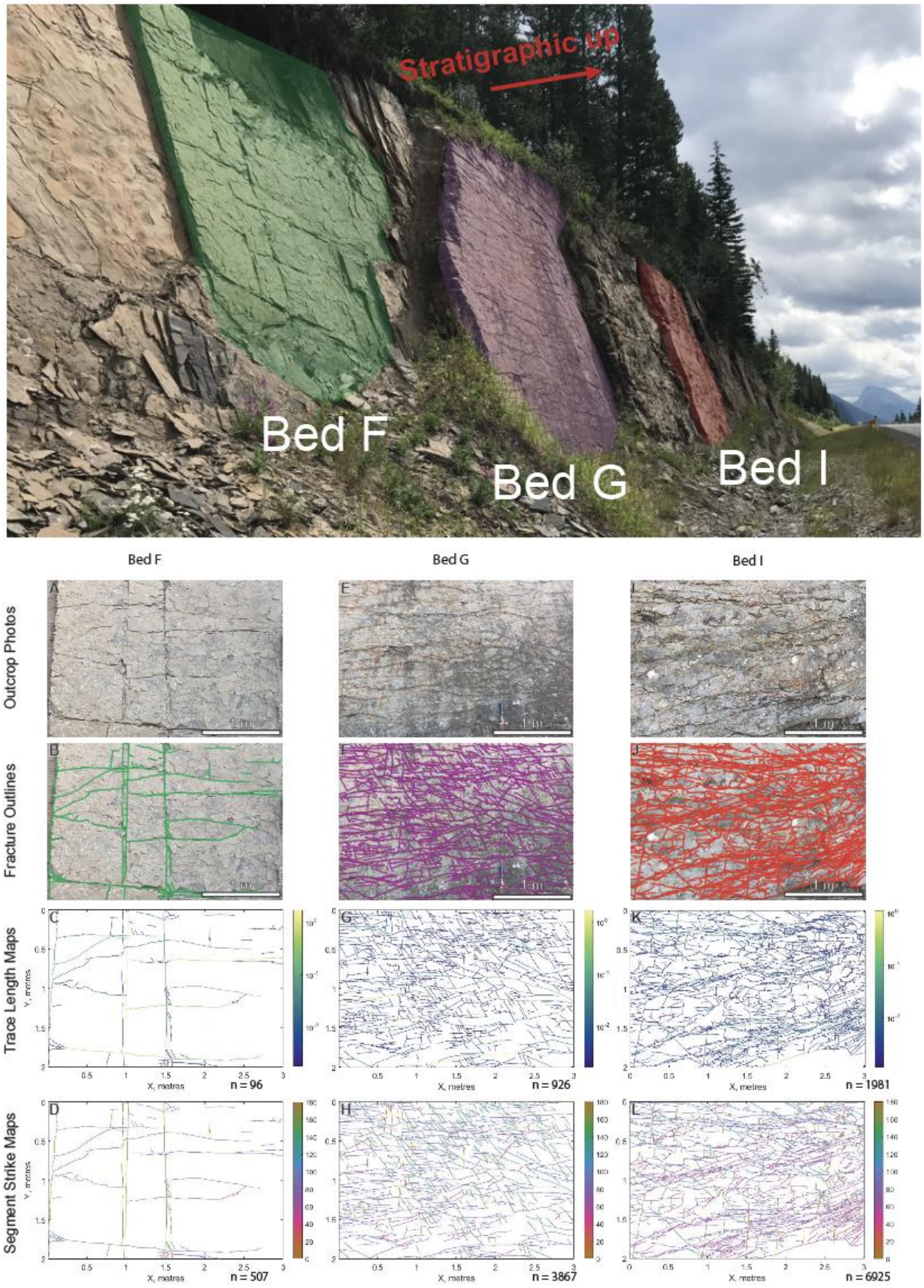


Figure 5. Bedding plane located along Highway 40 by Hood Creek in Kananaskis displaying unique fracture orientations and fracture lengths. Modified from Furlong et al in prep).

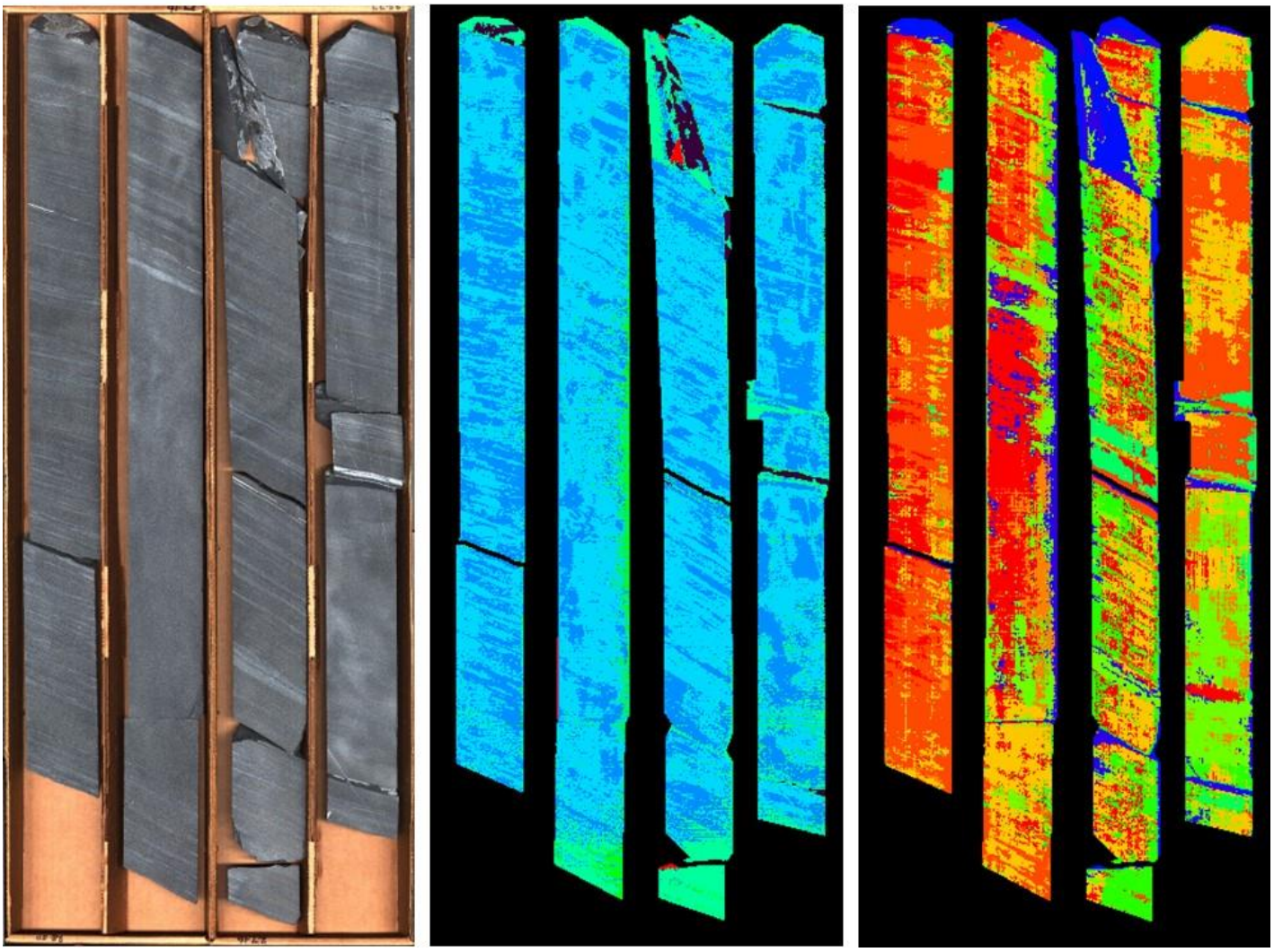


Figure 6. Core from the Kamenka Quarry in Harvie Heights in white light and clusters based on short wavelength and long wavelength hyperspectral imaging. The core shows relative few vertical fractures but frequent bedding plane parallel fractures, all mineralized. Note how the bedding plane fractures preferentially occur at boundaries between different hyperspectral classes and thereby units with different mineralogy and rock mechanical properties. Modified from Toews (2023).

## Conclusions

This study focussed on a large number of outcrops of Montney Eq strata within the thrust belt in Kananaskis and Canmore. Across all the studied outcrops, a strong relationship was observed between the sedimentary fabric, particularly the rock mechanical fabric, and the natural fracture characteristics. Although the studied outcrops have undergone a different tectonic uplift history compared with the Montney in the subsurface, the outcrop findings likely relate to the subsurface. To highlight the implications from our outcrop-based findings, a recent study by Virginillo (2024) showed that stages completed in different Montney sedimentary facies have distinct hydraulic pressure completion curves (Figure 7). These findings challenge some of the existing subsurface models of fracture behavior in the Montney. Traditional models often assume more homogeneity in fracture distribution and intensity across the formation, but our outcrop-based observations, supported by subsurface pressure data, suggests that fracture networks are more complex and influenced by subtle variations in mechanical properties. These insights could lead to more optimized strategies for well placement, stage spacing, and hydraulic fracture stimulation in the Montney Formation. Recognizing the role of bedding plane-parallel fractures could help mitigate risks such as frac hits between vertically stacked wells, improving the overall efficiency of hydraulic fracturing operations

The outcrop-based study presented here not only provides a clearer visualization of fracture complexity in the Montney but also highlights the need to refine existing models to account for the significant lateral and vertical variability in fracture characteristics across different sedimentary facies. This approach emphasizes the importance of integrating field observations with subsurface data to improve the predictability and effectiveness of hydraulic fracturing in unconventional reservoirs like the Montney Formation.

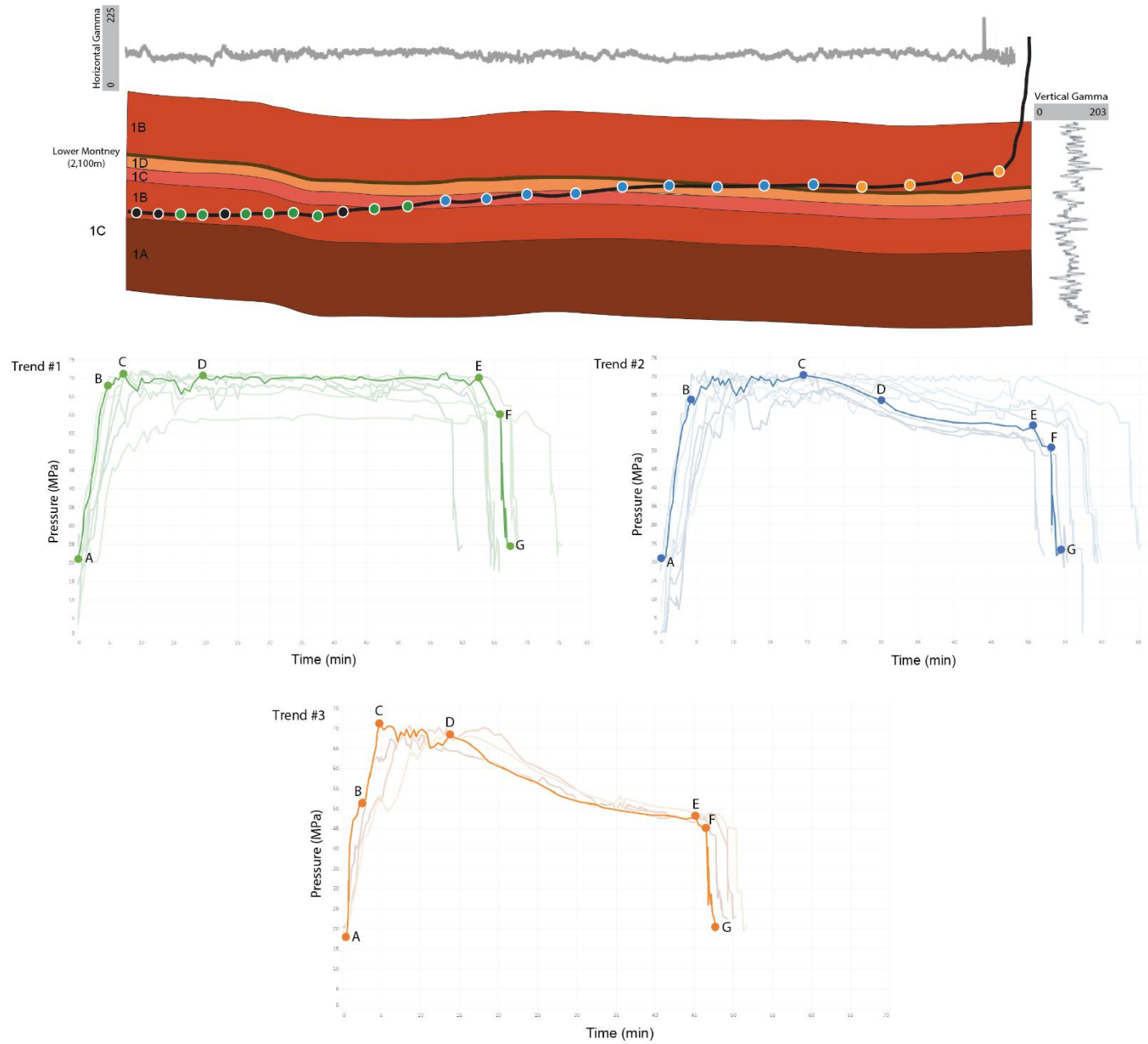


Figure 7. Cross-section generated in StarSteer showing the wellbore trajectory of a Montney horizontal well drilled and completed in several units with unique sedimentary facies. Hydraulic pressure completion curves group by units, show distinct different pressure curve trends likely reflecting the different geometry of the hydraulic induced fractures. Modified from Virginillo (2024).

## References


Becerra Rondon, D. M. (2022). Geological characterization and evaluation of reservoir quality in the Montney Formation in west-central Alberta (Doctoral thesis, University of Calgary, Calgary, Canada).

Bemis, S.P., Micklethwaite, S., Turner, D., James, M.R., Akciz, S., T. Thiele, S., & Bangash, H. A. (2014). Ground-based and UAV-Based photogrammetry: A multi-scale, high-resolution mapping tool for structural geology and paleoseismology. Journal of Structural Geology, 69, p. 163–178.

Bisdom, K., Gauthier, B.D.M., Bertotti, G., & Hardebol, N.J. (2015). Calibrating discrete fracture-network models with a carbonate three- dimensional outcrop fracture network: Implications for naturally fractured reservoir modeling. AAPG Bulletin, 98, p. 1351–1376.

Casini, G., Hunt, D.W., Monsen, E., & Bounaim, A. (2016). Fracture characterization and modeling from virtual outcrops. AAPG Bulletin, 100(1), p. 41–61.

Cawood, A.J., Bond, C.E., Howell, J.A., Butler, R.W.H., & Totake, Y. (2017). LiDAR, UAV or compass-clinometer? Accuracy, coverage and the effects on structural models. Journal of Structural Geology, 98, p. 67–82.

Gale, J.F., Laubach, S.E., Olson, J.E., Eichhubl, P., & Fall, A. (2014). Natural fractures in shale: A review and new observations. AAPG bulletin 98.11, p. 2165-2216.

Gillespie, P., Monsen, E., Maerten, L., Hunt, D., Thurmond, J., & Tuck, D. (2011). Fractures in Carbonates: From Digital Outcrops to Mechanical Models. In Outcrops Revitalized: Tools, Techniques and Applications, SEPM Concepts in Sedimentology and Paleontology No. 10.

Lato, M.J., & Malte, V. (2012). International Journal of Rock Mechanics & Mining Sciences Automated mapping of rock discontinuities in 3D lidar and photogrammetry models. International Journal of Rock Mechanics and Mining Sciences, 54, p. 150–158.

MacFarlane, T. & Davis, T. (2015). Fracture Characterization of the Montney Formation Using Amplitude Inversion of Converted Wave Seismic. Conference Paper, Unconventional Resources Technology Conference, San Antonio, Texas, USA.

Maxwell, S. C., Cho, D., Pope, T. L., Jones, M., Cipolla, C. L., Mack, M. G., Leonard, J. A. (2011). Enhanced Reservoir Characterisation Using Hydraulic Fracture Microseismicity. Conference Paper, SPE Hydraulic Fracturing Technology Conference and Exhibition, The Woodlands, Texas.

Pless, J.C., McCaffrey, K.J.W., Jones, R.R., & Holdsworth, R.E. (2015). 3D characterization of fracture systems using Terrestrial Laser Scanning: an example from the Lewisian basement of NW Scotland. Geological Society, London, Special Publications, (421), p. 125–141.

Poirier, S. S. P. (2020). Assessment of sedimentary fabric and natural fracture distribution of the Sulphur Mountain Formation using digital outcrop modeling: an analogue of the Montney Formation (Master thesis, University of Calgary, Calgary, Canada).

Rogers, S., McLellan, P. & Webb, G. (2014). Investigation of the Effects of Natural Fractures and Faults on Hydraulic Fracturing in the Montney Formation, Farrell Creek Gas Field, British Columbia. Conference Paper, International Discrete Fracture Network Engineering Conference 2014, Vancouver, British Columbia, Canada.

Thiele, S.T., Grose, L., Samsu, A., Micklethwaite, S., Vollgger, S.A. & Cruden, A.R. (2017). Rapid, semi-automatic fracture and contact mapping for point clouds, images and geophysical data. Solid Earth, 8, p. 1241–1253.

Toews, Z. D. (2024). Investigation of Fine-Scaled Reservoir Heterogeneity within the Sulphur Mountain Formation (Master thesis, University of Calgary, Calgary, Canada).

Vaisblat, N. (2020). Controls on reservoir quality in the Montney formation. PhD thesis, Department of 950 Earth and Atmospheric Sciences, University of Alberta, Edmonton, Alberta, Canada.

Virginillo, N. A. (2024). Analysis of the Relationship between Hydraulic Fracture Pressure Trends and Facies of the Montney Formation (Master thesis, University of Calgary, Calgary, Canada).

Westoby, M.J., Brasington, J., Glasser, N.F., Hambrey, M.J. & Reynolds, J.M. (2012). “Structure-from-Motion” photogrammetry: a low-cost, effective tool for geoscience applications. Geomorphology 179, p. 300 - 314.

Zhang, P., Du, K., Tannant, D. D., Zhu, H., & Zheng, W. (2018). Automated method for extracting and analysing the rock discontinuities from point clouds based on digital surface model of rock mass. Engineering Geology, 239, p. 109–118.

GUSSOW 2024
Montney Subsurface Evaluation: Drive Towards Excellence
Banff, AB | October 2-4

# Structural Fabric of the Montney Formation: A Study on Bedding Plane Microjoints and Fracture Distribution Observed in Core

Carolyn M. Furlong[1], Patricia E. Fraino[2], Per K. Pedersen[2]

1. MacEwan University, 2. University of Calgary

## Abstract

Structural fabrics, sedimentological fabrics and geomechanical properties are inherently intertwined and play an important role in understanding the behavior of hydraulic fracturing within unconventional reservoirs. Most studies use outcrops to understand the relationship between facies and fracture networks due to vertical and lateral trends being more easily characterized than within subsurface core datasets. However, core-based studies on natural (produced by geological forces) and induced features (formed by coring and handling processes) have been conducted but are underutilized. Within this study, features associated with structural fabric were identified and described from cores throughout the Montney Formation to identify vertical and lateral distribution of the components across the geographic area from the Pouce Coupe to Groundbirch fields. Structural fabric features described included bedding plane features like microjoints, polished surfaces and slicken lines, as well as horizontal, inclined, and vertical fractures (typically filled with calcite). Documentation of bedding plane features requires the examination of the ends of all core segments. Each core segment that exhibited bedding plane features were identified and the most abundant type of bedding plane feature was microjoints. At each core segment that exhibited microjointing, the following data was also collected: core depth, number of microjoint lineations on the bedding plane, maximum and minimum spacing of microjoint lineations, and morphology.

Results from this study conducted on five cores along the Groundbirch-Pouce Coupe production trend a total of 125 vertical to sub-vertical fractures and 14 horizontal fractures were observed. Fractures occurred in several different stratigraphic intervals within each of the cores, however, the highest occurrences of fractures typically occurred in bioclastic intervals of the upper Middle Montney (Altares Member). Generally, the more western located wells had a higher abundance of fractures. Bedding plane features included 1492 bedding planes with microjoints and 4 polished slip surfaces. The number of lineation, distance between lineations, lineation preservation, and morphology did not show any vertical trends within each cored well. All facies that exhibited microjoints on bedding planes had a range of minimum and maximum distance between lineations, number of lineations, lineation preservation, and morphology. However, increased frequency of microjoints occurred in facies with moderate to high heterogeneity index and included facies 2B, 3A, 2B, 3C, 4, 5A, which exhibited interbedding of different lithologies. Although the exact cause of the microjoints is unclear, this work suggests that specific facies are more prone to structural fabrics including fractures and microjoints on bedding planes.

## Statement of the background

Sedimentary and facies analyses are standard workflows when characterizing unconventional reservoirs; however, structural fabrics in core datasets have received limited attention even though structural fabrics and fracture networks likely play a significant role influencing the behavior of multi-stage hydraulic fracturing used to stimulate horizontal wells in these plays. Studies investigating structural fabrics commonly focus on the distribution of fractures using field-based methods (scanline and selection methods; (Manda and Mabee, 2010, Zeeb et al., 2013, Poirier, 2020) or image-based methods (drone orthomosaic; Poirier, 2020). However, core-based fractures studies stemming from seminal work conducted by Nelson (1985, 2001), Kulander et al. (1990), and Lorenz and Cooper (2017) characterized, described, and photographed examples of natural fractures (produced by geological forces) and induced fractures (formed by coring and handling processes). Mechanical stratigraphy (e.g. Ferrill et al., 2017) and fracture stratigraphy (e.g. Laubach et al., 2009) have also

been used in core and outcrop datasets to describe the distribution of fractures and mechanical properties to determine zones that are more prone to fracturing. Distinguishing natural fractures from induced fractures can be difficult in core, but it is important to make the differentiation for reservoir characterization because non-natural fractures do not contribute to reservoir permeability. However, induced fractures can be used to determine in-situ stress orientation (Lorenz et al., 1990; Li and Schmitt, 1998).

In addition to fracture distribution, bedding-parallel features can also provide insight on the structural fabric, zones of elevated pore pressure, and in-situ stress field orientation of unconventional reservoirs (e.g. Kulander et al., 1990; Aydin and Engelder, 2014; Lorenz and Cooper, 2017). Bedding-parallel features include slickenlines, slickensides, polish slip faces (PSF), pencil cleavage, and microjoints (Engelder and Geiser, 1979; Aydin and Engelder, 2014; Davies et al., 2014; Lorenz and Cooper, 2017; Gillen et al., 2019). Bedding-parallel features have been described from several siltstone-mudstone dominated formations within the Western Canada Sedimentary Basin, including the Second White Specks, Fish Scales, Montney, Duvernay, and Muskwa formations (Davies et al., 2014). Specifically, within the Montney Formation, studies on structural fabric have been conducted within the Farrell Creek Field (Rogers et al., 2014; McLellan, 2014), Middle Montney of the Karr-Kakwa area (Davies et al., 2014, 2016), and other non-disclosed locations (Roger, 2018; Gillen et al., 2019). Other studies have noted the distribution of vertical and horizontal fractures in Montney core (Gasparrini et al., 2021) and outcrop equivalent (Sulphur Mountain Formation) (Poirier, 2020), and have investigated the timing and control factors of fracture generation (Gasparrini et al., 2021).

Varying interpretations have been made for the generation of the different bedding plane features. Davies et al. (2013, 2014, 2018) suggested that striae of PSF were oriented parallel to maximum principal horizontal stress ($SH_{max}$) and cleavage being (orthogonal to striae) parallel to $SH_{min}$ and wellbore breakouts. It was also suggested that the striae on polished slip faces probably formed by shear in a relatively ENE-WSW direction, orthogonal to thrust-born displacement and shortening along the Laramide deformation belt (Davies et al., 2014, 2018). Cleavage was interpreted to record early-onset, low-grade metamorphic cleavage, which increased in frequency in occurrence in cores westward towards the ‘Laramide’ deformation belt (Davies et al., 2014, fig. 2). It was suggested by Davies et al. (2014) that the cleavage observed in Western Canadian samples were similar to pencil cleavage seen in the Appalachian Basin (Engelder and Geiser, 1979).

Gillen et al. (2019) observed similar bedding plane features as Davies et al. (2013, 2014, 2018) and described the vertical distribution of pencil cleavage (referred to as microjoints within the conference paper). An orthogonal relationship between cleavage/microjoints and slickenlines was also observed; however, Gillen et al. (2019) interpreted the microjoints to be induced artificially after the core was cut and formed in response to stress release while tripping the core to the surface. Bedding planes with microjoints that are artificially induced by drilling exhibit microjoint lineations that curve towards the perimeter of the core or are confined within an oval-shaped central zone in the core (Figure 1; Gillen et al., 2019, fig. 4). Rarely was it observed that the lineations extended all the way to the core edge (Gillen et al., 2019), which may have formed in-situ within the subsurface. Gillen et al. (2019) also observed that the microjoints were most common within intervals consisting of low porosity, silt-rich beds.

## Aims and Objectives

In this study, borehole-scale structural fabric was integrated with detailed geological attributes to better understand where and why bedding plane structural fabrics and fractures exist within the Middle Triassic Montney Formation of Western Canada. Structural fabric described in this study include characteristics and the distribution of vertical, sub-vertical, and horizontal fractures, as well as bedding plane features (polished slip surfaces, slickensides, and microjoints). Through this study, a better understanding of the relationship between facies and the vertical and lateral distribution of fracture networks and bedding-parallel features throughout the Montney Formation can be established.

## Materials and methods

Facies analysis was conducted on 11 cores within the study area and are briefly described within the results. Facies were described based on sedimentological (lithology, grain size, sedimentary structures), ichnological (trace fossils), and paleontological (body fossil) characteristics of the strata. A sedimentological heterogeneities index of low, moderate or high, was assigned to each meter of core based on the complexity of sedimentary fabric and lithological interbedding. Lithofacies were correlated to well log signatures, which were then used to extrapolate sedimentological trends between cored wells to make stratigraphic correlations.

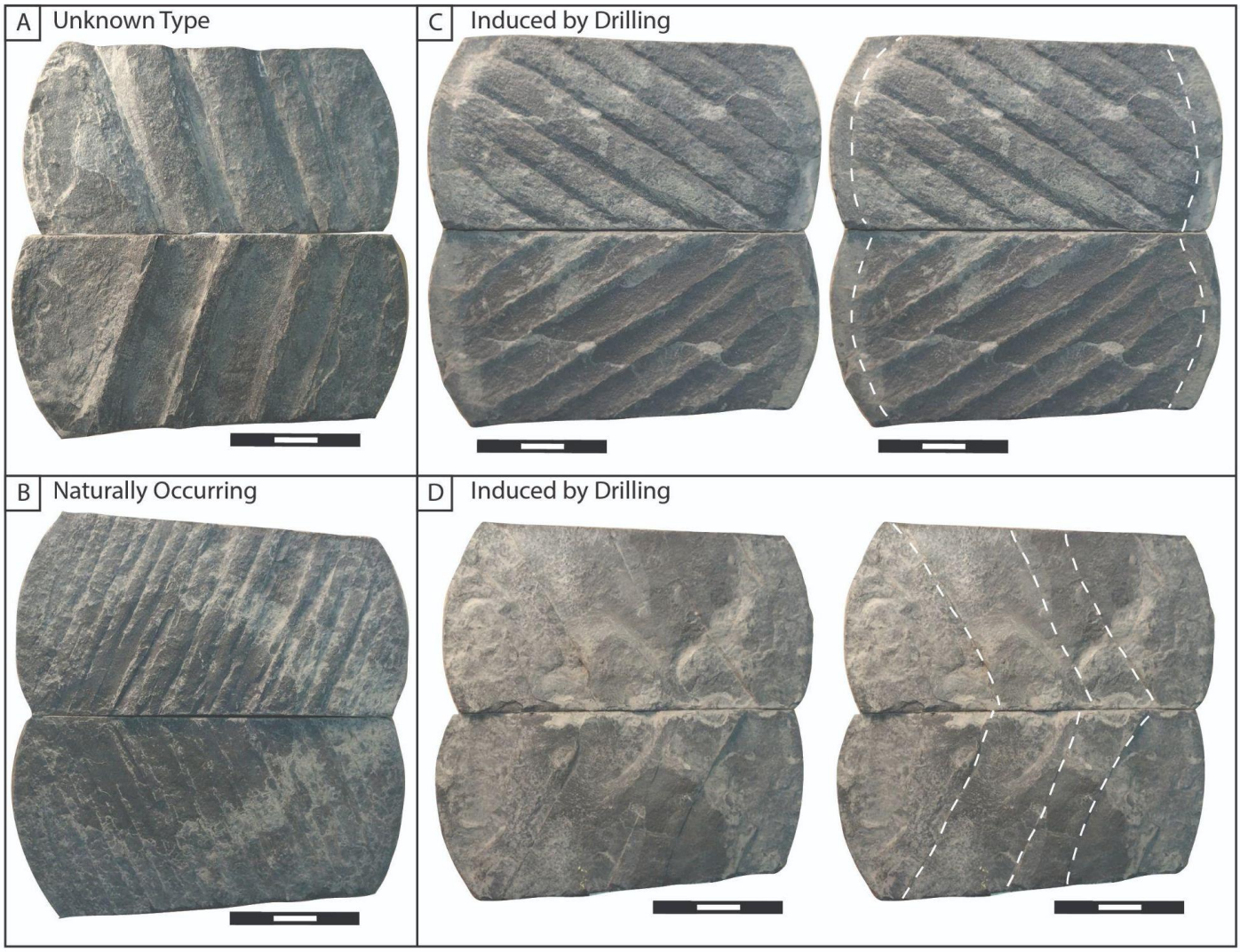


Figure 1: Microjoint lineation morphology examples from the Birchcliff PCoupe 06-03-079-13W6 core. In each photograph, the upper core photo represents the bedding plane at the base of the upper core piece, whereas the bottom core photo represents the bedding plane of the top of the lower piece of core. A) The termination of the lineations along the core edge is unknown due to the limited portion of core that was available for viewing. B) Lineations terminate along the edge of the core and remain parallel. This suggests that the microjoints might have been naturally occurring at depth within the subsurface. C) Lineations are confined to a central circle. Dashed line represents the outline of the area where lineations occur. This morphology is interpreted to have been induced by drilling. D) Curved lineations interpreted to have been induced by drilling. Dashed lines outline of the curved lineation. Similar observations of lineation morphology have been suggested by Gillen et al. (2019).

Five cores located along the Pouce Coupe-Groundbirch production trend were investigated for structural fabric and included documentation of vertical, sub-vertical, and horizontal fractures, as well as bedding plane features (polished slip surfaces, slickensides, and microjoints). Data collected by Gillen (2017) and Gillen et al. (2019) was integrated into the dataset. Fractures were classified based on their orientation (vertical, sub-vertical, and horizontal), length, width, and fill (mineralized with calcite or quartz, bitumen filled, or open). The documentation of bedding-parallel features required the examination of the top and base of all core segments. Each core segment that exhibited bedding-parallel features was identified by depth and the feature type was assigned (e.g. slicken line, polished surface, microjoinst). Additionally, for bedding planes exhibiting microjoints, the following data was collected: number of microjoint lineations on the bedding plane, maximum and minimum spacing of microjoint lineations, and preservation of the sample (e.g. poor, fair, or well). The morphology of the microjoint lineation was also described and interpreted as being formed in-situ or induced from core drilling (Figure 1; after Gillen et al., 2019). The number of bedding plane surfaces with cleavage and the number of core segments per meter length of drill core are also recorded to construct a structural fabric log.

***Pitfalls in Investigating Fractures and Bedding-parallel Features in Core Datasets***

Since this study is using a drill core dataset, a few assumptions and pitfalls need to be addressed when investigating fractures and bedding-parallel features. Large vertical and sub-vertical fractures may be more widely spaced than the

diameter of the borehole (~8 cm). Smaller fractures may be clustered, and the apparent local intensity observed may not reflect the fracture intensity away from the borehole (Gale et al., 2007). In either occurrence, underestimating or overestimating fracture frequency and spacing in the formation is not obtainable. To avoid this problem, workers have used seismic attributes to measure anisotropy with fractures (Simon, 2005), and microfracture distribution, orientation, and size-scaling relationships (Laubach, 1997, Marrett et al., 1999, Gale et al., 2007); however, this was outside of the scope of this preliminary study. Future studies on Montney fractures may consider using similar approaches to understand fracture distribution.

When investigating bedding-parallel features, it is best to use full-diameter cores that have not been slabbed. The 100/12-33-080-17W6/02 core from the Gillen et al (2019) study was the only non-slabbed core within the dataset. All remaining cores had been slabbed, with either 1/3 or 2/3 slabbed core available to be investigated. Due to the core being slabbed, bedding-parallel features, especially cleavage morphology, number of lineations, and lineation spacing, could not always be identified and quantified with high confidence. However, the area of the core investigated for bedding-parallel features remained constant within each individual core, making vertical trends more reliable than trends between cores.

## Results and Discussion

### *Lithofacies and Sedimentological Heterogeneities*

Eleven facies within the study area have been interpreted to be deposited within the offshore, offshore transition and lower shoreface (Figure 2). Heterogeneity within the Montney Formation is mainly controlled by composition (e.g. lithology and mineralogy) and fabric (e.g. sedimentary bedforms and bioturbation). Each facies was qualitatively assigned a heterogeneity index of low, moderate, or high based on the complexity of the composition and fabric. Seven facies have identified as having low sedimentary heterogeneity (Facies 1A, 1B, 1C, 2A, 5B, 6A, and 6B), three facies had moderate sedimentary heterogeneity (Facies 1D, 3A, and 5A), and five facies had high sedimentological heterogeneity (Facies 2B, 3B, 3C, 3D, and 4). Lithofacies, dominant lithology, and sedimentological heterogeneity for the 100/06-03-079-13W6/00 in the Pouce Coupe Field is shown in Figure 3.

### *Structural Fabric*

*Fracture Distribution*

A total of 125 vertical to sub-vertical fractures were observed in all five cores investigated in this study Figure 4). Fracture frequency is highest in western region, with 100/14-29-080-20W6/00 having 40 vertical fractures (0.67 fractures per meter) and 100/16-08-080-18W6/00 having 28 vertical fractures (0.17 fractures per meter) that cross cut the cored intervals (Figure 4). Each well exhibited vertical fractures in different stratigraphic intervals, but the majority of the fractures are observed in the upper Middle Montney in bioclastic interval of Facies 3B and the lower portion of the Upper Montney in facies that exhibited the faintly planar laminated fine-grained siltstone (Facies 1A), planar laminated fine-grained siltstone (Facies 1B) and interbedded siltstone unit (Facies 4) (Figure 5). In particular, the bioclastic interval within the upper Middle Montney has a high carbonate content (up to 50% calcite and dolomite content according to XRD) and increases the brittleness of the interval. Vertical fractures within the Lower and lower Middle Montney are concentrated in the western region of the study area (100/14-29-080-20W6/00 and 100/16-08-080-18W6/00) and occur in faintly planar laminated fine-grained siltstone (Facies 1A) and laminated fine-grained siltstone (Facies 1B) intervals. The fracture distribution in the Upper Montney is poorly understood within this study due to the lack of cores penetrating that interval and additional cores from the Upper Montney need to be investigated.

The length of the vertical fractures varied between wells and ranged from 1-41 cm in length, with the mean length being 9.59 cm (Figure 4). Widths of vertical fractures ranged from < 1 to 3.91 mm. Most fractures were filled with calcite cement, with a few being filled with calcite and pyrite or being open, non-mineralized fractures. A total of 6 open vertical fractures were observed. Horizontal fractures were less common, with only 14 being observed in the 100/14-29-080-20W6/00 core (Figure 4). Horizontal fractures were filled with calcite.

| Facies | 1A | 1B | 1C | 1D | 2A |
|---|---|---|---|---|---|
| Core Expression |  | 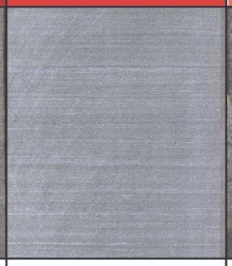 |  |  |  |
| Lithological Description | Dark grey, laminated, bituminous siltstone with very faint planar laminae. | Dark grey siltstone with occasional (<30%) light grey, planar laminae. | Dark grey planar laminated siltstone with medium grey event bed deposits, HCS and distal turbidite deposits. | Dark grey siltstone with shell debris interbeds with planar and wavy laminae. | Dark grey siltstone with increased (<50%) light grey, planar laminae |
| Depo. Enviro. | Offshore | Offshore | Offshore | Offshore / Offshore Transition | Offshore |

| Facies | 2B | 3A | 3B | 3C | 3D |
|---|---|---|---|---|---|
| Core Expression |  |  |  |  |  |
| Lithological Description | Medium grey siltstone with light grey, planar laminae, wavy laminae, unidirectional ripples, starved ripples, HCS, very dark grey mud laminae | Dark to medium grey siltstone with light grey, planar and wavy laminae, occasional shell-rich laminae and very dark grey mud laminae. | Dark to medium grey siltstone with light grey, planar and wavy laminae, shell-rich laminae and beds, concretions, and very dark grey mud laminae. | Interbedded light and dark grey siltstone with Bouma sequences. Concretions present throughout; potential evidence of algal mats. | Interbedded light and dark grey siltstone, with thin light silt/shells beds. Planar laminae, wavy lamiane, unidirectional ripples, dark grey mud lamiane. |
| Depo. Enviro. | Offshore Transition | Offshore / Offshore Transition | Offshore / Offshore Transition | Offshore / Offshore Transition | Offshore Transition |

| Facies | 4 | 5A | 5B | 6A | 6B |
|---|---|---|---|---|---|
| Core Expression |  |  |  |  |  |
| Lithological Description | Interbedded light and very dark grey siltstone with fining upward beds. Bouma sequences present. Light grained siltstone content increases up (bed thickness also increases up). | Medium to light grey siltstone with interbedded bioturbated and non-bioturbated intervals. Planar laminae, wavy laminae, dewatering strucutes, few mud laminae, rare HCS, rare current ripples. | Medium grey siltstone to very fine-grained sandstone with high bioturbation intensity (BI = 5-6). Interclasts and phosphate nodules present. | Medium grey siltstone. Planar and wavy laminae are cross-cut by trace fossils. Moderate to low bioturbation intensity (BI = 2-3). Dominant trace fossil is *Bergaueria*. | Medium grey siltstone. Planar and wavy laminae are cross-cut by trace fossils. High bioturbation intensity (BI = 4-6) renders massive appearance. Dominant trace fossil is *Bergaueria*. |
| Depo. Enviro. | Offshore | Offshore Transition | Offshore Transition / Lower Shoreface | Offshore / Offshore Transition | Offshore Transition |

Figure 2: Lithofacies within the 100/06-03-079-13W6/00 core in the Pouce Coupe Field.

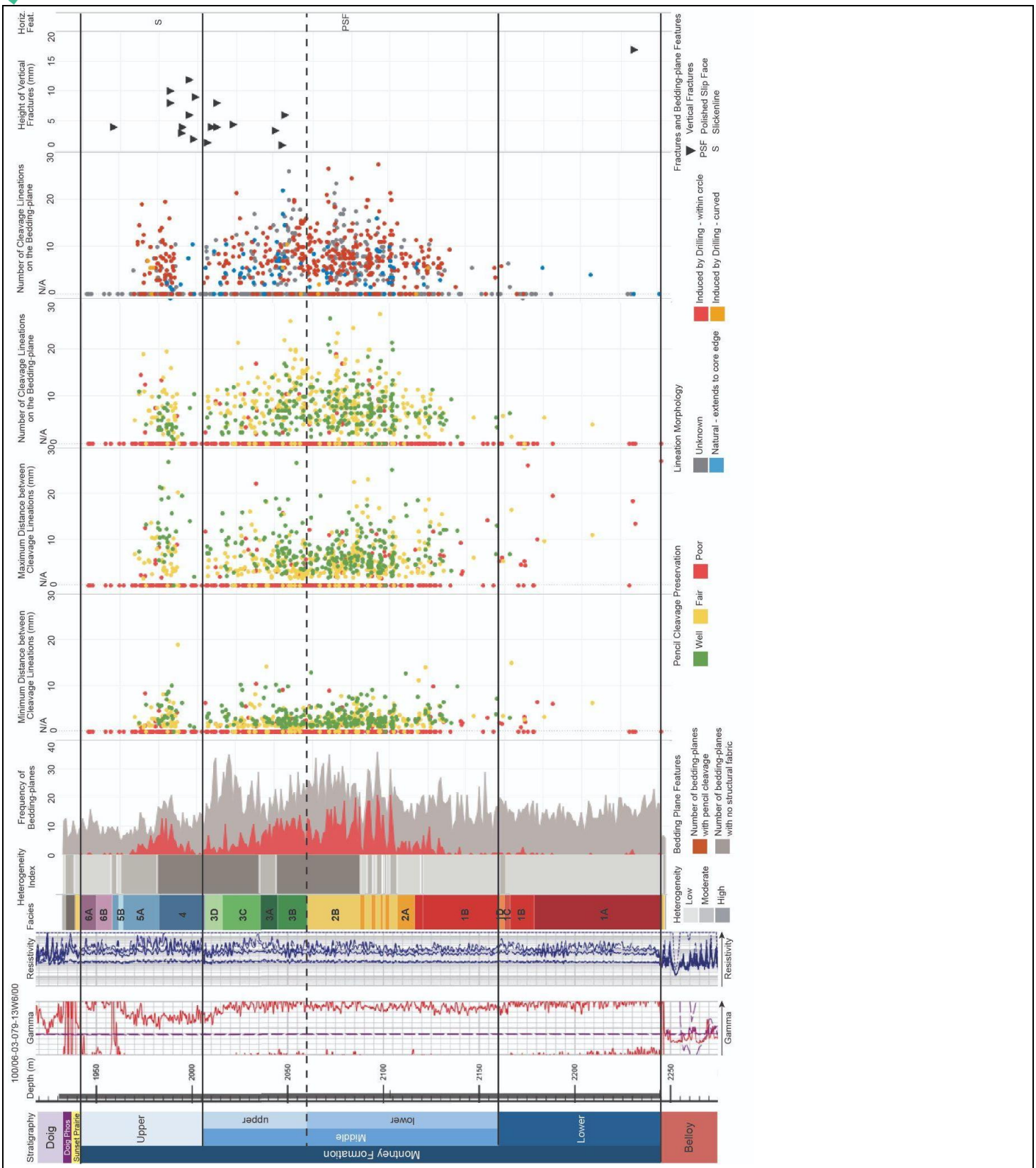


Figure 3: Detailed log depicting structural fabric of the Birchcliff PCoupe 06-03-079-13W6 core. Stratigraphy, well logs (gamma ray and resistivity), facies, and heterogeneity index are denoted. Frequency of bedding planes with no structural fabric (grey) and with structural fabric (red) were recorded for each meter of the core. Minimum and maximum diameter between microjoint lineations are colored by the preservation of the microjoints on the bedding plane. Note that many poorly preserved samples plot along the y-axis due to the distance between lineations not being measurable. The number of lineations are colored by preservation, as well as morphology of lineation. Vertical fractures are denoted by black triangles, PSF = polished slip face, and S = slickenline. Gamma and resistivity logs from GeoSCOUT, which was provided by geoLOGIC systems ltd. © 2024.

| A Core UWI | 100/14-29-080-20W6/00 | 100/16-08-080-18W6/00 | 100/12-33-080-17W6/02 | 100/06-03-079-13W6/00 | 100/14-36-078-12W6/00 |
|---|---|---|---|---|---|
| Total Core Length (m) | 109 | 218 | 222 | 314 | 115 |
| Total Number of Core Segments | 2434 | 3898 | 1255 | 5208 | 4215 |
| Fractures per Meter | Horizontal: 0.67<br>Vertical: 0.13 | Horizontal: 0.17<br>Vertical: 0 | Horizontal: 0.12<br>Vertical: N/A | Horizontal: 0.06<br>Vertical: 0 | Horizontal: 0.03<br>Vertical: 0 |
| Total Number of Fractures | Horizontal: 40<br>Vertical: 14 | Horizontal: 38<br>Vertical: 0 | Horizontal: 26<br>Vertical: N/A | Horizontal: 18<br>Vertical: 0 | Horizontal: 3<br>Vertical: 0 |
| Bedding Planes with Microjoints per Meter | 0.09 | 0.27 | 1.14 | 3.42 | 0.77 |
| Bedding Planes with Microjoints | 17 | 58 | 254 | 1075 | 88 |
| Bedding Planes with Slickensides or Polished Slip Surfaces | 1 | 0 | N/A | 2 | 1 |

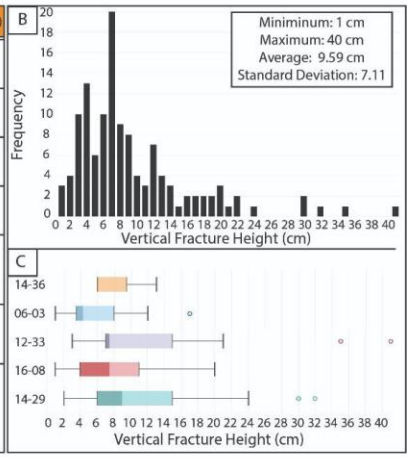


Figure 4: A) Summary of core lengths, number of core segments, bedding-plane features, and fractures. Data from 100/12-33-080-17W6/02 was taken from Gillen (2017) and Gillen et al. (2019). B) Frequency of vertical fracture length (cm) from all cores. Minimum, maximum, average, and standard deviation provided. C) Box and whisker plot of the vertical fracture heights for each core (cm). Graphs are colored by core location.

*Microjoint Distribution*

A total of 1492 bedding planes with microjoints were identified within the five cores investigated in this study (Figure 4). Within the 100/06-03-079-13W6/00 core, 1075 bedding planes with microjoints were identified and on average, there were 3.42 bedding planes per meter with microjoints (Figure 4). Within this core, microjoints was mainly present within the upper portion of the lower Middle Montney where the content of coarse-grained siltstone increases (Facies 2A and 2B), the upper Middle Montney where carbonate material occurs (Facies 3A, 3B, 3C), and the lower portion of the Upper Montney in interbedded fine- and coarse-grained siltstone (Facies 4 and 5A) (Figure 3). Facies that have an increased frequency of microjoints commonly exhibit thin interbedding of differing lithologies, which have a moderate to high sedimentological heterogeneity index. Similar trends are observed in the other wells, with bioclastic-rich intervals seen in Facies 3 having the most bedding-parallel microjoints features compared to the other facies (Figure 5). The occurrence of microjoints is generally higher within the Middle Montney, in particular along the boundary between the lower and upper Middle Montney. The Lower Montney and Upper Montney have lower frequencies of microjoints, except for the base of the Upper Montney within the 100/06-03-079-13W6/00 core within Facies 4 (Figure 5). Few cores penetrate intervals where Facies 4 (interbedded fine- and coarse-grained siltstone) are present, thereby making it difficult to determine the lateral trends in microjoints frequency in this facies. However, a thin interval of Facies 4 was preserved within the core in 100/12-33-080-17W6/02, but it did not exhibit microjoints on bedding planes. It is possible that more proximal expressions of Facies 4 within eastern localities may possess an elevated frequency of microjoints.

The number of lineations on each bedding plane with microjoints ranged from 2-55 in the 100/06-03-079-13W6/00 (Figure 3, Figure 6). The distance between lineations varied per sample, with the minimum distance between lineations being 0.02 mm and the maximum distance being 30.07 mm (Figure 3, Figure 6). It is important to note that many of the lineations on the bedding planes were poorly preserved (35%), and the number of lineations and distance between lineations could not be recorded, making them plot along the Y-axis in the depth plots (Figure 3). Preservation and morphology of the lineations also varied vertically within the core, and there was not a distinct stratigraphic unit or facies that only exhibited well-preserved samples of microjoints (Figure 3). Most of the lineations had morphological characteristics that suggested they were induced from drilling core; however, due to only 1/3 and 2/3 slabbed core samples being available for the investigation, determination of how the lineations terminated at the edge of the core was uncertain for a large number of bedding planes (39%) and were classified as having an unknown morphology (Figure 1).

*Relationship Between Fractures and Microjoints*

Vertical fractures generally occur in stratigraphic intervals where little to no bedding-plane features exist. This is exemplified in the high occurrence of fractures in the 100/14-29-080-20W6/00 and 100/16-08-080-18W6/00 cores within western KSMMA, where there is a low frequency of bedding-plane features (< 5 bedding planes with microjoints per meter) (Figure 5). However, in the 100/06-03-079-13W6/00 core, the base of the upper Middle Montney exhibits vertical fractures where bedding-planes with microjoints occur at a higher frequency of 10-15 per meter (Figure 5). More work is needed to understand the relationship between vertical fractures and the occurrence of microjoints on bedding planes.

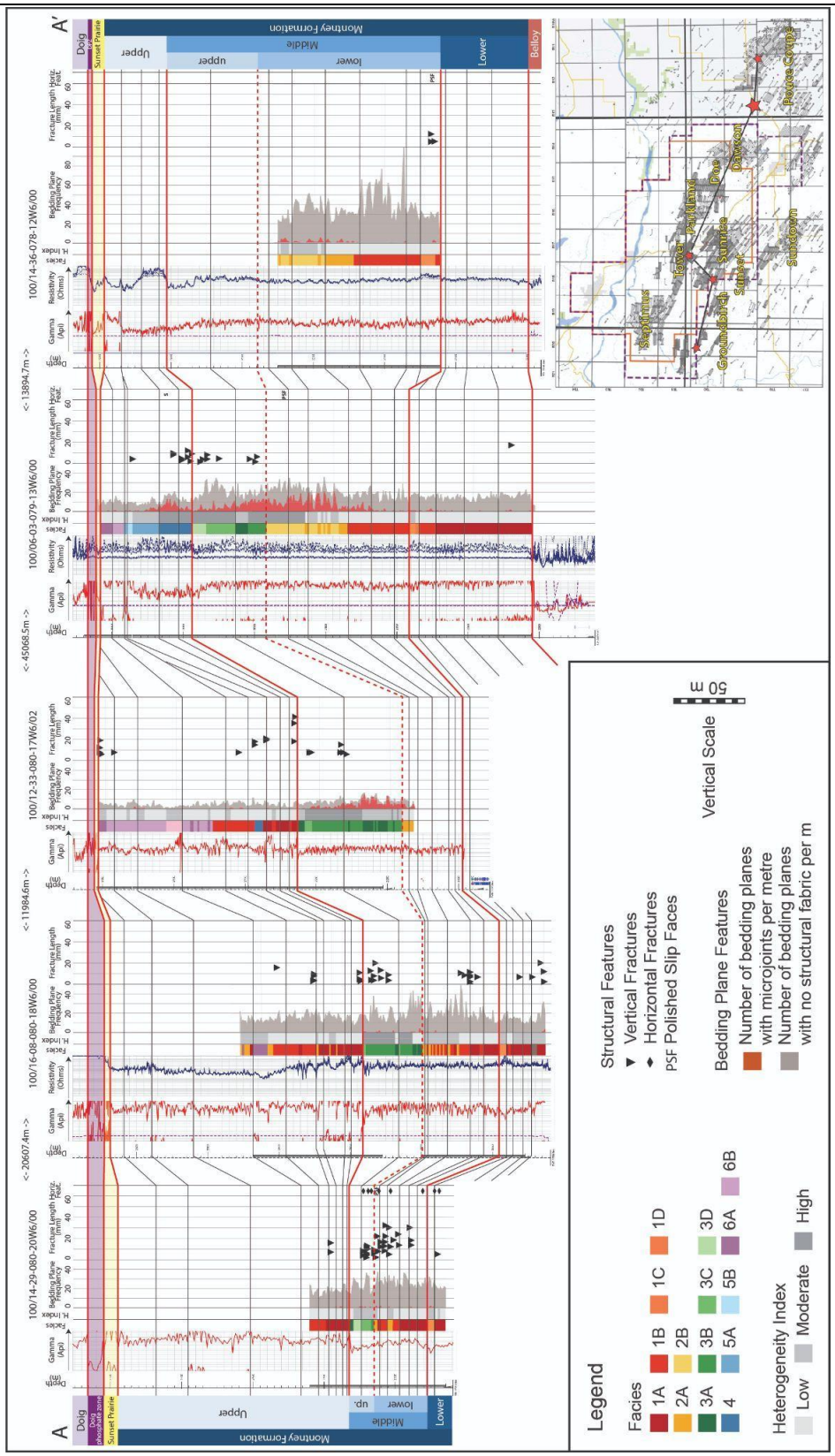


Figure 5: Cross section with cored wells where structural fabric data were collected. Well logs include gamma ray (red) and resistivity (blue). Colored bars represent facies and heterogeneity index (H. Index). Frequency of bedding planes with no structural fabric (gray) and with structural fabric (red) were recorded for each meter of the core. Vertical fractures are denoted by black triangles, horizontal fractures are denoted by black diamonds, PSF = polished slip face, and S = slickenline. Correlations were made to show boundaries between Montney members (Lower, Middle and Upper) in red, and parasequences are correlated by the thin black lines. Cross-section modified from GeoSCOUT provided by geoLOGIC systems ltd. © 2024.

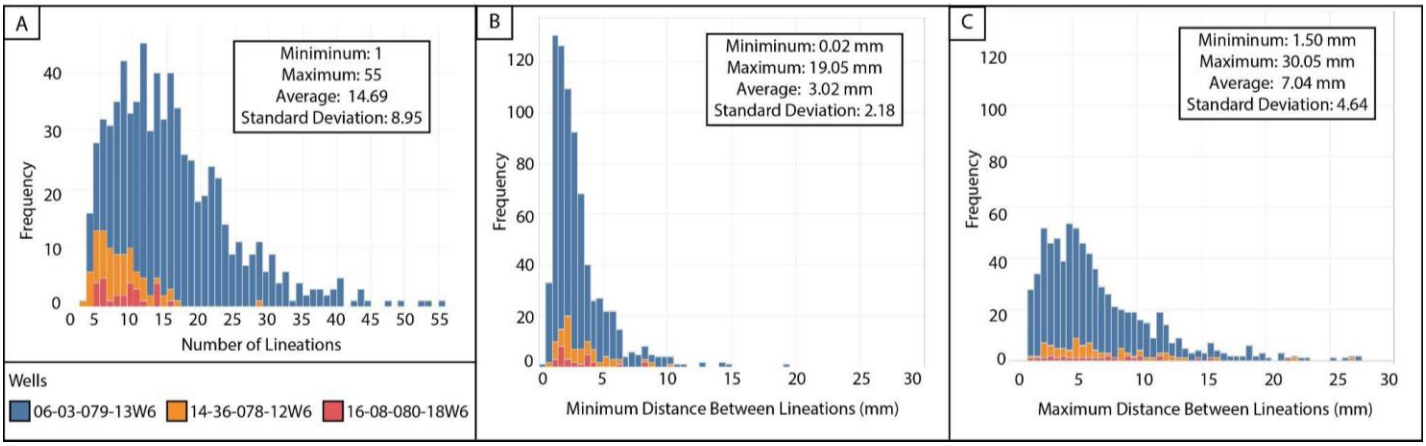


Figure 6: Frequency of lineation characteristics on bedding planes with microjoints. A) Number of lineations per bedding plane with microjoints. B) Frequency of the minimum distance between lineations (mm). C) Frequency of the maximum distance between lineations (mm). Minimum, maximum, average and standard deviation are provided for each graph. Bars are colored by well location.

## Conclusions

This study provides an investigation on the relationship between sedimentological fabrics and structural fabrics within the Montney Formation from subsurface drill cores across the Pouce Coupe to Groundbirch production trend. The study quantifies the size and distribution of vertical, inclined and horizontal fractures, as well as bedding planes that exhibit microjoints. These structural features were described from each core to showcase the vertical and lateral variability. Findings from this study include:

1. Fifteen facies were identified within the Montney Formation within the study area. Facies are dominated by fine-grained siltstone, coarse-grained siltstone, very fine-grained sandstone, and bioclastic-rich intervals that have a high carbonate content. Sedimentological heterogeneities within the Montney Formation are mainly controlled by composition (e.g. lithology and mineralogy) and fabric (e.g. sedimentary bedforms and bioturbation). Each facies were qualitatively assigned a heterogeneity index of low, moderate, or high based on the complexity of the composition and fabric. Seven facies have identified as having low sedimentary heterogeneity (Facies 1A, 1B, 1C, 2A, 5B, 6A, and 6B), three facies had moderate sedimentary heterogeneity (Facies 1D, 3A, and 5A), and five facies had high sedimentological heterogeneity (Facies 2B, 3B, 3C, 3D, and 4).
2. Vertical fractures are most commonly observed in the upper Middle Montney in the bioclastic interval of Facies 3B and the lower portion of the Upper Montney associated with Facies 1A, 1B, and 4. Vertical fractures are also most abundant in the cores within the Groundbirch and Sunrise Fields. Horizontal fractures were only observed in the 100/14-29-080-20W6/00 core in the Groundbirch Field.
3. Increased frequency of microjoints occurs in facies with moderate to high heterogeneity index. These facies (2B, 3A, 2B, 3C, 4, 5A) exhibit interbedding of different lithologies. The number of lineation, distance between lineations, lineation preservation, and morphology did not show any vertical trends within each cored well. All facies that exhibited microjoints on bedding planes had a range of minimum and maximum distance between lineations, number of lineations, lineation preservation, and morphology.
4. Vertical fractures can occur in intervals that lack microjoints or have a low to moderate frequency of microjoints. An increased occurrence of fractures (vertical and/or horizontal) was observed within cores that are located in Groundbirch (0.67 fractures per meter) and Sunrise Field (0.17 fractures per meter) and very few bedding parallel features are observed (0.09-0.27 bedding planes per meter with microjoints, respectably). In the Tower Field, the examined core exhibits both fractures (0.12 fractures per meter) and bedding parallel features (1.14 bedding planes with microjoints per meter) and is located within a structural corridor. In the Pouce Coupe Field, an increased occurrence of bedding parallel features (0.77-3.42 bedding planes with microjoints per meter) is observed, and few fractures are present (0.3-0.6 fractures per meter).

## Acknowledgements

This work was funded by NSERC Alliance Grant ALLRP 548576-2019 entitled" Dynamics of fault activation by hydraulic fracturing: Insights from new technologies", with partners ARC Resources, Ltd., Canadian Natural Resources Limited, ConocoPhillips Canada, Ovintiv, Tourmaline Oil Corp. Geoscience BC, Nanometrices and OptaSense. The authors would like to thank geoLOGIC systems ltd. for their contribution of data and software used in this study. All geoLOGIC systems ltd. Data and software is ©2024. Thanks to the AER Core Research Center and the BCOGC for the usage of core facilities, shipping, and handling core. All sponsors of the Consortium for Distributed and Passive Sensing (C-DaPs) are sincerely thanked for their financial support.

## References

Aydin, M. G., & Engelder, T. (2014). Revisiting the Hubbert‐Rubey pore pressure model for overthrust faulting: Inferences from bedding-parallel detachment surfaces within middle Devonian gas shale, the Appalachian basin, USA. Journal of Structural Geology, 69, 519‐537.

Davies, G., Haysom, S., Nevokshonoff, G., & Soltanzaded, M. (2016). Slip faces and cleavage in the Montney and other unconventional reservoirs in the WCSB: structural, geomechanical and drilling/fracking implications. CSPG International Core Conference

Davies, G. R., Watson, N., Moslow, T. F., & MacEachern, J. A. (2018). Regional subdivisions, sequences, correlations and facies relationships of the Lower Triassic Montney Formation, west-central Alberta to northeastern British Columbia, Canada - with emphasis on role of paleostructure. Bulletin of Canadian Petroleum Geology, 66(1), 23‐92.

Engelder, T., & Geiser, P. (1979). The relationship between pencil cleavage and lateral shortening within the Devonian section of the Appalachian plateau, New York. Geology, 7(9), 460‐464.

Ferrill, D. A., Morris, A. P., McGinnis, R. N., Smart, K. J., Wigginton, S. S., & Hill, N. J. (2017). Mechanical stratigraphy and normal faulting. Journal of Structural Geology, 94, 275‐302.

Gale, J. F., Reed, R. M., & Holder, J. (2007). Natural fractures in the Barnett shale and their importance for hydraulic fracture treatments. AAPG bulletin, 91(4), 603‐622.

Gasparrini, M., Lacombe, O., Rohais, S., Belkacemi, M., & Euzen, T. (2021). Natural mineralized fractures from the Montney-Doig unconventional reservoirs (Western Canada sedimentary basin): Timing and controlling factors. Marine and Petroleum Geology, 124, 104826.

Gillen, K., Wood, J., Sharp, L., Grimison, T., & Guerard, B. (2019). Natural and Induced Structural Fabrics in Drill Cores from the Montney Formation, Western Canada. Gussow 2019.

Gillen, K. (2017). Fracture Study of the Montney Formation from ECA HZ C16-6-81-17, N.E. British Columbia, Canada. Report prepared for Encana Corporation by Vox Terrae. Golding, M., Mortensen, J., Ferri, F., Zonneveld, J.-P., & Orchard

Kulander, B., Dean, S., & Ward, B. (1990). Fractured core analysis: Interpretation, logging, and use of natural and induced fractures in core: Aapg methods in exploration series, no. 8. Oklahoma, AAPG.

Laubach, S. E. (1997). A method to detect natural fracture strike in sandstones. AAPG bulletin, 81(4), 604‐623. Laubach, S. E., Olson, J. E., & Gross, M. R. (2009). Mechanical and fracture stratigraphy. AAPG Bulletin, 93(11), 1413‐1426.

Li, Y., & Schmitt, D. R. (1998). Drilling-induced core fractures and in situ stress. Journal of Geophysical Research: Solid Earth, 103(B3), 5225‐5239.

Lorenz, J. C., & Cooper, S. P. (2017). Atlas of natural and induced fractures in core. John Wiley; Sons.

Lorenz, J. C., Finley, S. J., & Warpinski, N. R. (1990). Significance of coring-induced fractures in Mesaverde core, Northwestern Colorado. AAPG Bulletin, 74(7), 1017‐ 1029.

Manda, A. K., & Mabee, S. B. (2010). Comparison of three fracture sampling methods for layered rocks. International Journal of Rock Mechanics and Mining Sciences, 47(2), 218‐226.

Marrett, R. (1996). Aggregate properties of fracture populations. Journal of Structural Geology, 18(2-3), 169‐178.

McLellan, P., Anderson, I., Wong, J., & Mostafavi, V. (2014). Geomechanical Characterization of the Farrell Creek Montney Reservoir, Northeast British Columbia. Geoconvention 2014

Nelson, R. A. (1985). The geologic analysis of naturally fractured reservoirs. Houston: Gulf Professional Publishing.

Nelson, R. A. (2001). The geologic analysis of naturally fractured reservoirs. Houston: Gulf Professional Publishing.

Poirier, S. S. P. (2020). Assessment of sedimentary fabric and natural fracture distribution of the sulphur mountain formation using digital outcrop modeling: An analogue of the Montney Formation [Master's thesis, Science].

Rogers, S. (2018). What Can Discrete Fracture Network Analysis Tell Us About Induced Seismicity In The Montney Formation? Geoconvention 2014.

Rogers, S., McLellan, P., & Webb, G. (2014). Investigation of the effects of natural fractures and faults on hydraulic fracturing in the Montney Formation, Farrell Creek Gas Field, British Columbia. International Discreet Fracture Engineering Conference, Vancouver.

Simon, Y. S. (2005). Stress and fracture characterization in a shale reservoir, north Texas, using correlation between new seismic attributes and well data [Doctoral dissertation, University of Houston, Texas].

Zeeb, C., Gomez-Rivas, E., Bons, P. D., & Blum, P. (2013). Evaluation of sampling methods for fracture network characterization using outcrops. AAPG Bulletin, 97(9), 1545‐1566.

GUSSOW 2024
Montney Subsurface Evaluation: Drive Towards Excellence
Banff, AB | October 2-4

# Understanding the Slow Slip Precursors of Induced Seismicity and Casing Deformation to De-risk Hydraulic Fracturing

Thomas de Boer[1,2], Matthew Adams[2], Giovanni Grasselli[1]
1. University of Toronto, 2. ShearFRAC Ltd

## Abstract

This study presents an approach for identifying slow slip precursors, allowing for risk assessment of hydraulic fracturing-induced seismic events using real-time pressure data analysis and machine learning models. The technique decomposes non-linear and non-stationary properties of time-series pressure measurements to identify periodic slow slip signals and forecast potential adverse events such as induced seismicity and casing deformation. We highlight the implementation of machine learning models for feature extraction and risk prediction to minimize environmental and structural risks. Further validation of this method of surface pressure analysis to detect stick-slip trends have been compared against full waveform Microseismic data and show coincident frequency amplitudes.

## Statement of the background

Hydraulic fracturing, a well-stimulation technique, is widely used in oil and gas production. However, it can induce various undesirable events, such as seismic activity, casing deformation and overall well integrity, due to the high-pressure fluid injections. These events pose risks to both surface and subsurface infrastructure, creating potential large cost overruns due to pausing/stopping operation (regulatory), or casing ID restrictions which may limit the ability to run plugs/ require additional milling operations. The need for accurate prediction of such events before their occurrence has become critical in modern hydraulic fracturing operations to avoid costs in pausing/stopping operations due to IS (regulatory) cost overruns associated with the reduction of casing ID due to deformation, which may limit the ability to run subsequent plugs, or require further milling. This work addresses the gap by developing a technique for decomposing time-series pressure measurements and extracting features capable of forecasting fracturing-induced events hours to days in advance and allowing intervention and mitigation.

## Aims and Objectives

The primary aim of this study is to develop a predictive framework for detecting seismic events induced by hydraulic fracturing. Specific objectives include:

- Data collection and segmentation of pressure measurements from hydraulic fracturing sites.
- Application of signal decomposition and machine learning techniques for feature extraction and event forecasting.
- Real-time assessment of seismicity risk to adjust fracturing parameters and mitigate potential damage.
- Validation of surface pressure analysis against full waveform Microseismic (See Fig 1)

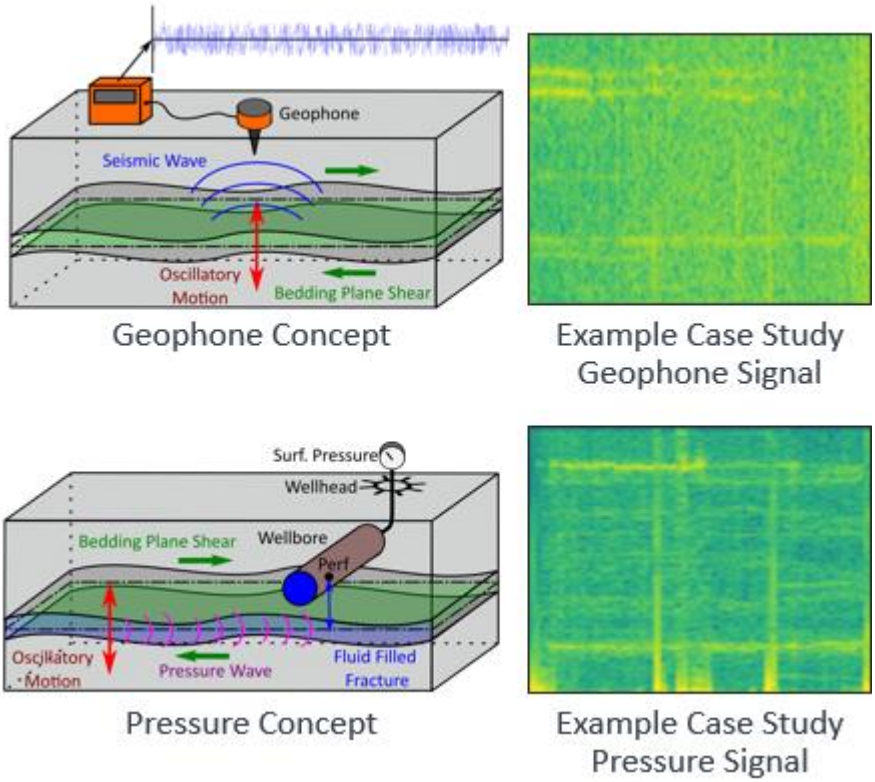


FIG 1: Comparative analysis of (Top) frequency amplitude derived from full waveform Microseismic with a generalized schematic diagram of Microseismic collection technique and the (Bottom) frequency amplitude derived from analysis of surface pressure gauge data with a generalized schematic diagram of surface pressure monitoring and the mode of bedding plane activation and slip.

## Materials and methods

This research is based on the integration of advanced signal processing techniques and machine learning for real-time event prediction during hydraulic fracturing. The system collects pressure measurements using sensors placed at the wellhead during fracturing operations (as shown in FIG. 1). These measurements form time-series data, which is segmented based on operational phases of the fracturing process (e.g., fluid injection, shut-in, and flowback).

Once segmented, the pressure data is decomposed using non-stationary and non-linear signal decomposition techniques to isolate components which capture the surface pressure behaviors inherent in the fracturing process. Each specific component of the signal decomposition is analyzed to extract relevant statistical properties describing their patterns and stability through time. Key features of the outputted analysis are extracted to provide insights into the subsurface stress state, fracture behavior, and occurrence of large-scale slip events.

Machine learning models capable of processing sequential data are trained on historic datasets with documented adverse events from previous hydraulic fracturing operations. This training allows the models to learn patterns that precede specific adverse events, such as induced seismicity and casing deformation. The model is then able to process live pressure data from actively fracked wells to identify precursory patterns and provide a risk assessment based on a combination of the learned data and site-specific knowledge.

For multi-well operations, the system correlates pressure data from adjacent wells, identifying cross-well behaviors that may indicate regional subsurface movements rather than localized fracturing effects. These correlations enhance the accuracy of predictions by providing a broader context for the subsurface changes.

## Results and discussion

The predictive modeling framework has shown promising results in forecasting seismic events and other adverse phenomena such as casing deformation. In a series of field tests, the model was able to identify patterns in the pressure data that corresponded to early indicators of induced seismicity, such as the “stick-slip” behavior associated with shear movement along subsurface faults or bedding planes. These precursory stick-slip events were identified several hours to days before the seismic events occurred, providing ample time for operational adjustments and potential mitigation in real time (As shown in Fig 2).

In particular, the analysis revealed distinct oscillatory modes in the pressure signal data, which were linked to subsurface tremor activity. For example, as seen in **Fig 1 and 2**, the analysis of pressure measurements over time highlighted the onset of Microseismic activity before larger seismic events. The system also demonstrated the ability to differentiate between typical fracturing behavior and anomalous activity that could lead to casing deformation or fracture-driven interactions.

The use of machine learning models further improved forecasting accuracy. By training on historical data, the models learned to associate certain pressure signal patterns with specific adverse events. The real-time nature of the system enabled immediate adjustments to the fracturing process, such as modifying fluid injection rates or changing the proppant concentration, to reduce the risk of triggering seismic events. This capability is critical in high-risk areas, where even small seismic events can cause significant damage.

## Conclusions

The development of this real-time predictive modeling framework represents a significant advancement in the safe and efficient operation of hydraulic fracturing. By combining advanced signal processing with machine learning, the system provides early warnings of the possibility of seismicity and other adverse events, enabling operators to take preventative action before damage occurs. The ability to adjust fracturing parameters in real-time based on the predicted risk has the potential to dramatically reduce the environmental and operational risks associated with hydraulic fracturing.

Future work will focus on refining the machine learning models to improve prediction accuracy, particularly in complex geological formations. Additionally, the system will continue to integrate data from other sensor types, such as Microseismic monitoring equipment, to provide a more comprehensive view of subsurface activity. Ultimately, this approach could be extended to other well-stimulation techniques, such as enhanced geothermal, ensuring cap rock containment in carbon and hydrogen storage projects, all providing broader applications for the oil and gas industry.

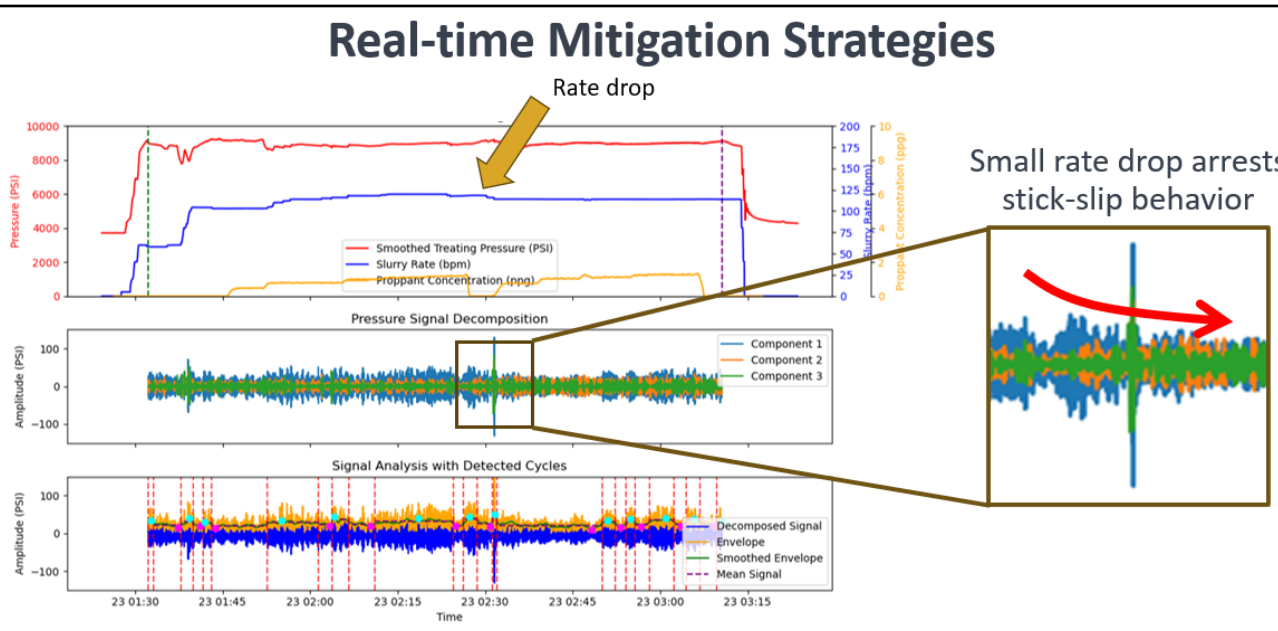


FIG 2: Typical output of surface pressure analysis showing pressure a rate (top), multicomponent amplitude analysis (middle) and multicomponent signal analysis with further decomposition, enveloping surface, smoothed envelope, and different detected signal cycles broken down to measure frequency of cyclic response.

## References


Abdelaziz, A., Aboayanah, K.R., Adams M.G., & Grassell G. (2023). Mechanical Characterization, Anisotropy, and Failure Pattern of Unconventional Reservoirs for Wellbore Stability and Fracture Enhancement. SPE/AAPG/SEG Unconventional Resources Technology Conference.

Baniak, G.M, Moslow, T.F, Michailides, S., Matthew G Adams (2023) Sequence stratigraphic architecture of the Lower Triassic Montney Formation, northeastern British Columbia, Canada. American Association of Petroleum Geologists Vol 107, Issue 2, 283-310

Zoback, M.D., & Gorelick, S.M. (2012). Earthquake triggering and large-scale geologic storage of carbon dioxide. Proceedings of the National Academy of Sciences, 109(26), 10164–10168.

Maxwell, S.C., & Cipolla, C.L. (2011). What Does Microseismic Tell Us About Hydraulic Fracturing? Society of Petroleum Engineers.

Rutqvist, J., & Tsang, C.F. (2002). A study of caprock hydromechanical changes associated with CO2 injection into a brine formation. Environmental Geology, 42(3), 296–305.

Warpinski, N.R., & Teufel, L.W. (1989). Influence of Geologic Discontinuities on Hydraulic Fracture Propagation. Journal of Petroleum Technology, 41(9), 990–997.

Eaton, D.W., Davidsen, J., Pedersen, P.K., & Boroumand, N. (2014). Breakdown of scaling in seismicity induced by hydraulic fracturing: Observations from the Montney Formation, Alberta, Canada. Journal of Geophysical Research: Solid Earth, 119(6), 4279–4295.

King, G.E., & Valencia, R.L. (2014). Environmental risk arising from well-integrity failure: Data and understanding from recent studies. SPE Journal, 19(05), 1172–1179.

GUSSOW 2024
Montney Subsurface Evaluation: Drive Towards Excellence
Banff, AB | October 2-4

# Geomechanical Aspects of Microseismicity

Shawn Maxwell[1], Amanda Greig[1],
1. Ovintiv

## Abstract

Microseismic monitoring of completion activities continues to provide key information about hydraulic fracture geometry, complimenting growing application of cross-well strain and offset pressure observations. Microseismic represents shear activations of pre-existing discontinuities associated with the hydraulic fracture itself, as well as potential poroelastic changes. Geomechanical understanding of these shear activations is important for both hydraulic fracture mapping and management of induced seismicity. A common microseismic observation in many reservoirs is increased microseismicity associated with trailing wells in a multiwell completion program, consistent with expected elevated susceptibility of shear slip after an initial fracture interaction. Conversely, microseismicity associated with reservoir depletion associated with parent wells can have a variable response depending on the specific geomechanical conditions associated with reservoir depletion. In some scenarios, depletion geomechanically stabilizes fractures suppressing microseismicity, while in others pressure reduction destabilizes fractures geomechanically enhancing susceptibility to shear activation and microseismicity. Understanding the geomechanical response associated with microseismic is thereby critical for quantitative interpretations.

## Statement of the background

Hydraulic fracturing involves the creation of a tensile fracture by injecting fluids at pressure above the minimum principal stress, whereby fluid pressure dilates and grows the induced fracture. Fracture growth characteristics are controlled by stratigraphic layering causing differences in mechanical and stress layering and geological heterogeneity including presence of natural fractures. Understanding hydraulic fracture geometry is fundamental to optimizing unconventional development, including well spacing and stacking between different reservoir benches and completion design. Various technologies have evolved to track fracture growth, many associated with monitoring geomechanical deformations during the fracturing, including tiltmeters and fiber optic strain monitoring as well as microseismic monitoring. Microseismicity is generated by shear deformation during the hydraulic fracturing through either pressure induced slip of pre-existing fractures or potentially poroelastic stress changes associated with the fracture dilation. These differing mechanisms can be classified as ‘wet’ interactions associated with microseismicity proximal to the fracture or ‘dry’ due to poroelastic changes at a distance from the fracture.

Microseismicity is typically used to interpret the fracture geometry based on the location of microseismicity. However, the rate of microseismicity also tends to be investigated in terms of quantitative interpretations. Interpretation of microseismic based hydraulic fracture images often includes aspects of the density of microseismicity. Rates of events or seismic energy release is important component of monitoring for anomalous induced seismicity, where occasionally a hydraulic fracture induces shearing of a pre-existing fault and potentially larger magnitudes. Various aspects can control the microseismicity including well sequencing and depletion effects. Understanding the factors that control microseismic rates is obviously important for interpreting microseismic imaging. Furthermore, with increasing attention on parent-child well interactions characterizing the geomechanical state of the depleted zones is also important.

## Aims and Objectives

This presentation examines microseismic results from projects in multiple basins, highlighting examples of rates of microseismicity associated with fracturing order and depletion. By comparing and contrast microseismic results across several basins we demonstrate that fracture order has a significant impact on microseismicity rates and locations across all

basins, indicating a fundamental underlying geomechanical causation. In contrast, microseismic response in depleted zones is variable with some regions experiencing enhanced microseismicity rates and others showing muted responses. This suggests that depletion in different basins responds differently and changes the susceptibility to shear slip, in some cases making it more likely and others less likely.

## Methods

While several examples will be highlighted in the presentation, here we focus solely on a published example from the Permian basin. A consortium led a comprehensive hydraulic fracture monitoring project the “Hydraulic Fracture Test Site - 2” (HFTS-2) using several technologies and have published the corresponding results. This makes for a convenient example to discuss microseismic fracture order and depletion effects in that specific example. Discussion of the results will then be generalized to other possible observations.

## Results and discussion

### *Microseismic Observations*

In HFTS-2, the microseismic was monitored during the fracturing of three wells offsetting shorter parent wells that had already been under production. Geophone arrays were deployed in horizontal and vertical sections of three monitoring wells and processed with a velocity model calibrated using perforation shots and microseismic events. Further details of the processing is described in Grechka et al, 2021. Figure 1 shows the resulting microseismic results. Each of the new wells were fractured sequentially, one after the other. This completion plan allows the impact of well sequencing to be easily identified. The existing parent wells were located adjacent to the toe ward half of the new wells, providing an opportunity to contrast differences in the microseismic results adjacent depletion with those in virgin conditions. The HFTS-2 dataset thereby provides a convenient example of both sequencing and depletion impacts.

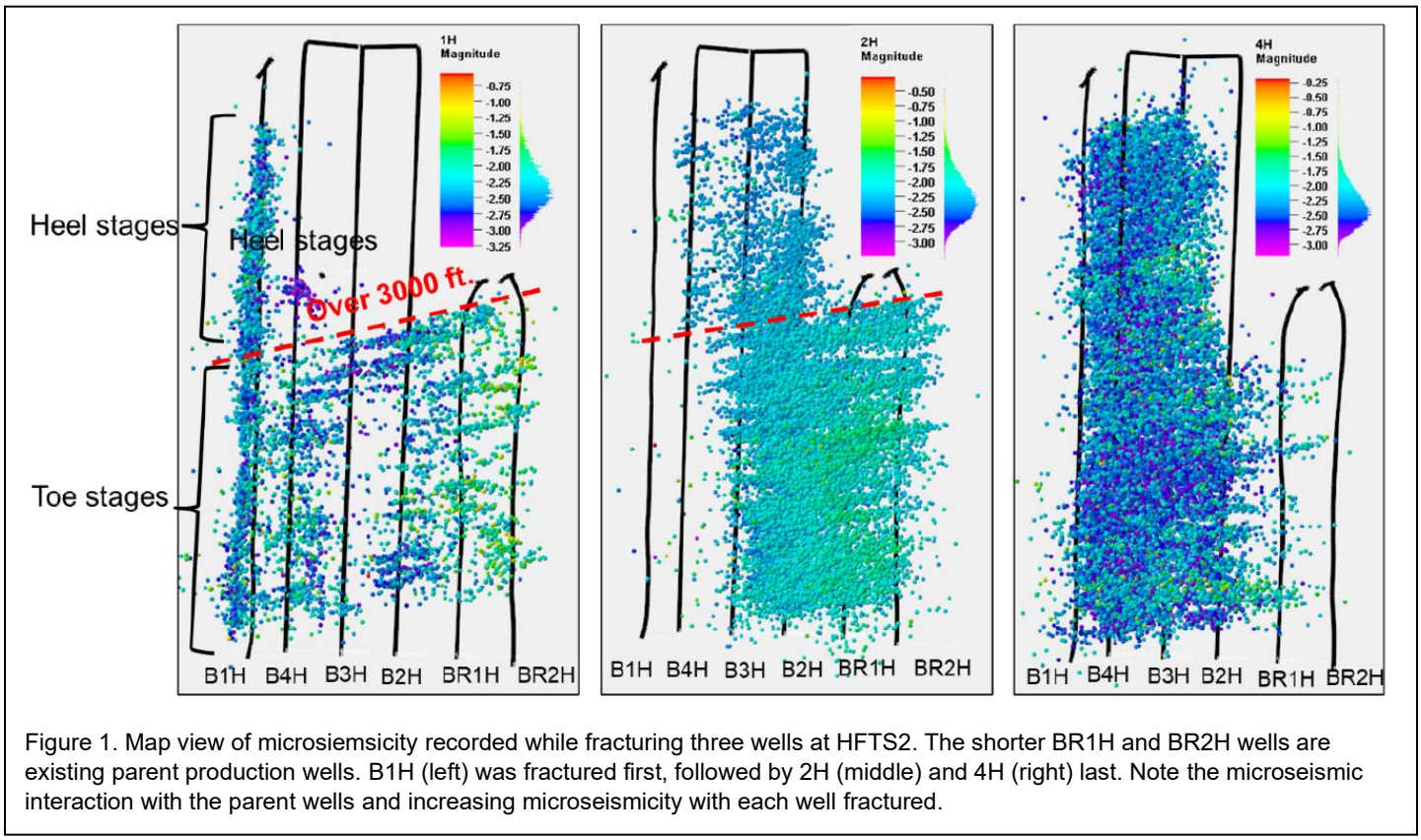


Figure 1. Map view of microsiemsicity recorded while fracturing three wells at HFTS2. The shorter BR1H and BR2H wells are existing parent production wells. B1H (left) was fractured first, followed by 2H (middle) and 4H (right) last. Note the microseismic interaction with the parent wells and increasing microseismicity with each well fractured.

The first HFTS-2 well fractured was the western most 1H well. The microseismic locations are clearly distinct between the toe and heel portions of the well. The figure is also annotated with the SHMax fracture orientation (ENE-WSW). Clearly the microseismicity associated with toe stages is located much further to the east interacting with the existing parent wells, in contrast with the heel stages which are concentrated much closer to the treatment well. The magnitude of the microseismicity is depicted by the event coloring. Microseismicity closest to the treatment well are predominantly in the

range between -3 and -2. The microseismic nearer the parent wells in the SE corner is largely between magnitude -2 and -1.5, with smaller magnitude events not being detected in this region with extended distance from the monitoring arrays.

The second well fractured was the 2H, which was also closest to the parent wells. Compared to the 1H well significantly more events were detected, although the magnitude range is largely similar suggesting it is not a detection difference. Toe stages were again clearly distinct from heel stages, with microseismicity extending further to the east over the parent wells. Higher magnitudes around -1.5 were again generated in the depleted zone. While heel stages showed some events overlapping the previously fractured 1H well to the west, the toe stages where predominantly asymmetric towards the parent wells.

Finally, the last well (4H) was fractured located between the previously completed 1H and 2H. Again, increased microseismicity rates were generated and were located predominantly between the 1H and 2H wells. There was some minor eastern extension over the depleted parents for the toe section, but within the depletion the number and eastern extent of microseismicity was significantly diminished compared to the two previous wells.

To summarize, an increasing number of microseismic events was detected with each completed well. Trailing wells that were interacting with already created fractures resulted in detection of more microseismic events, which is a common occurrence from many microseismic projects across multiple reservoirs. Regardless of distance from the parent wells, increased number of relatively higher magnitude events were also observed sitting over the presumed drainage region of these production wells. The microseismic response of the drainage zone is something that changes across reservoirs. The HFTS-2 Permian example represents a one scenario of increased microseismicity, whereas in areas such as the STACK in Oklahoma the microseismic response tends to be muted by production.

***Geomechanical Scenario***

The trailing well increase in microseismicity is easily explained by frictional stability theory. Figure 2 shows an example scenario of a  Mohr circle showing an original stress and Coulomb stability. During initial fracturing such as encountered by a first completed well, increased fracture pressure moves the effective stress state represented as the Mohr circle to the left, reducing the total normal stress. Conditions for induced slip (and hence microseismicity) could be encountered for preferentially oriented pre-existing fractures along the stability curve. Once perturbed, cohesion would tend to be reduced on these slipped fractures (change from orange dash stability curve to solid in Figure 2), for example overcoming the strength of mineralized fractures. Hence the fundamental stability conditions for the onset of slip are expected to be reduced within the previously microseismically active volume for trailing wells. Potentially even more impactful, the pore pressure will also slowly leak off and equilibrated after the initial stages. As shown in Figure 2 with the solid cyan Mohr circle stress representation, the initial effective stress is shifted to the left closer to the slip stability conditions. Together these two aspects of reduced stability with loss of cohesion along with lowered effective stress explain the common observation of increased microseismicity associated with trailing wells as observed during the HFTS-2 project amongst many others.

Next consider the geomechanical status and extension of this discussion to scenarios where microseismic interacts with depleted zones around existing parent wells. Production and associated reservoir depletion will of course tend to reduce the reservoir pressure, which could also result in some reduction in the minimum principal stress due to factors such as hydraulic fracture closure. These factors cause the offsetting hydraulic fracturing in new wells to want to preferentially grow towards the depleted region as shown in Figure 1. In many cases, this parent-child interaction can also be seen with pressure increases on the parent well during the timing of the child well fracs.

In terms of the Mohr circle and stability conditions, the original parent well frac may have at least partially reduced cohesion. However, the pressure depletion and associated increase in effective stress will tend to move the Mohr circle to the right and increase the initial state from the stability conditions (i.e. making the system more stable). Pore pressure could also tend to change the differential deviatoric stress, potentially increasing the shear/deviatoric stress in some instances (e.g. in the Bakken as described by Dohman et al., 2014) but perhaps also reducing the shear stress in others. Compared to the trailing well geomechanical stability scenario, there are more possible scenarios depending on the initial and final reservoir pressure and how associated stresses change. Nevertheless, the simple observation of susceptibility of depleted regions to generate microseismicity serves as an apparent indicator of the changes in stability with depletion.

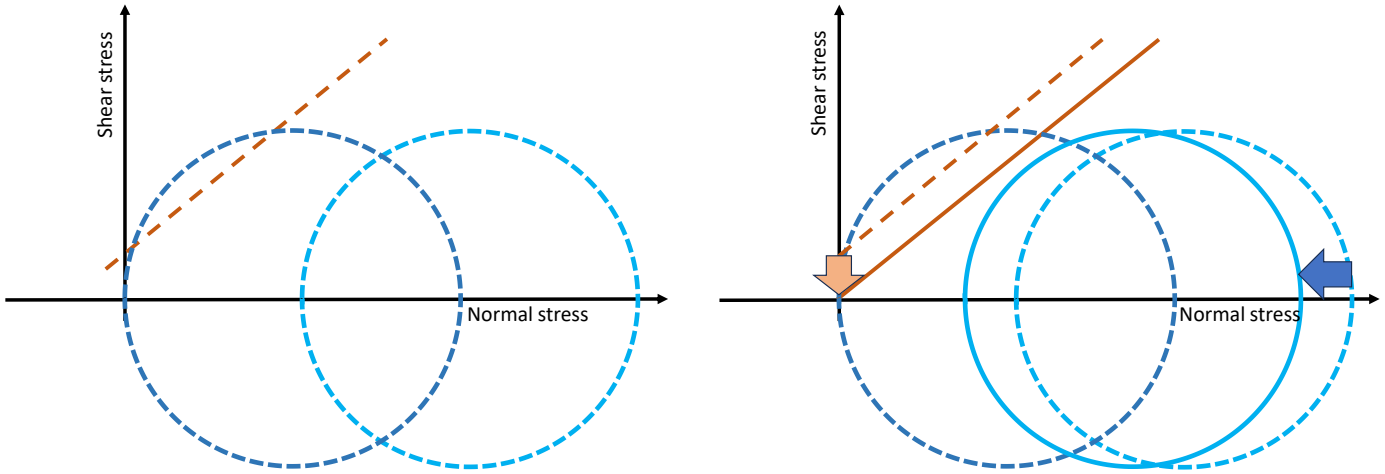


Figure 2. Mohr circle example for hydraulic fracture conditions. Left panel shows a hypothetical initial stress state (cyan circle) and stability condition (brown dashed line). During hydraulic fracture the effective normal stress is reduced moving the Mohr circle to the left (blue circle). Once stimulated, the conditions for a trailing well are shown in the right panel. Induced shear would overcome cohesion reducing the stability curve (solid brown). Increased pore pressure from the earlier frac could be expected to continue to have elevated pressure thereby reducing the effective normal stress (solid cyan circle). The system is thereby initially closer to conditions for slip.

In the HFTS-2 example, similar to Dohman et al., 2014, it appears that depletion increases the preponderance for microseismicity, with slightly larger magnitude events originating near the parent wells. However, in other reservoirs the depleted region appear to be aseismic, devoid of microseismicity next to parent wells that are clearly being hit as evidence of pressure changes, which may imply that the system is becoming more stable with depletion. The differences in behavior are potentially important both for microseismic interpretations but also a potential induced seismicity mitigation. If depletion results in increased stability and less seismic slip deformation, the seismicity generating potential of these regions may provide mitigation options for induced seismicity. The depletion state may also play a role in pre-drill hazard assessments, regardless if the system is becoming more or less stable during pressure reduction.

## Conclusions

Numerous microseismic projects have demonstrated increased microseismicity associated with trailing wells during multi-well hydraulic fracturing operations. This can be explained by expected changes in the Coulomb stress state, and increased probability for microseismicity. Microseismic changes during depletion near existing production wells, however, can respond differently with some reservoirs suppressing and some enhancing the probability of microseismicity. Understanding these differences is potentially impactful for microseismic interpretation as well as potential impacts on induced seismicity.

## References

Dohmen, T., Blangy, J-P. and Zhang, J. 2014. Microseismic depletion delineation. Interpretation 2, p. SG1-SG13.

Grechka , V., Howell, B., Li, Z., Furtado, D. and Straus C. 2021. Microseismic at HFTS2: A Story of Three Stimulated Wells. Presented at Unconventional Resources Technology Conference, paper 5517.

Tan, Y., Wang, J., Rijken, P., Zhang, Z., Fang, Z., Wu, R., Ning, I.L.C., and Liu, X. 2021. Mechanism of Microseismic Generation During Hydraulic Fracturing – With Evidence from HFTS2 Observations. Presented at Unconventional Resources Technology Conference, paper 5296.

GUSSOW 2024
Montney Subsurface Evaluation: Drive Towards Excellence
Banff, AB | October 2-4

# Integrating Lithology, Structural Fabric and Stress to Understand Ineffective Induced Fracture Growth and Casing Deformation in the Montney

Rick Schroeder[1], Alemayehu Aklilu[1]

1. ConocoPhillips

## Abstract

Geomechanical and structural controls on induced fracture growth have been key to horizontal well development of the Montney formation leading to stimulation designs changes as frac baffle properties and casing deformation mechanisms become better understood. This presentation focuses on ConocoPhillips Montney acreage in Northeast BC and highlights how different integrated diagnostic datasets have characterized lithology, natural fractures, as well as larger scale structure and stress states. A broad suite of integrated datasets that include distributive acoustic sensing (DAS) fibers, thin-sections, cuttings analysis, caliper logs, geomechanical testing, open-hole well logs, stimulation pressure data, and in-situ stress data provide strong support for casing deformation via bed-parallel slip. The stress state and rock fabric that facilitate bed-parallel slip are interpreted to cause ineffective T-shaped fracturing leading to production impairments. By understanding the mechanisms of ineffective fracturing, optimizations have been employed that improve well performance and/or reduce stimulation cost.

## Statement of the background

The impact of bed-parallel fractures on Montney oil and gas development have been recognized in different assets (Sanders et al., 2018). Key observations highlighting the slip on these geomechanically weak interfaces are evident from casing deformation that occurs while fracing wells both in the Montney, with similar natural bed-parallel fractures (beef) occurring in other basins globally (Cobbold et al., 2013). Slip on bed-parallel fractures, and associated observed casing deformation occurs due to result of a combination of factors that include the stress state, lithology and rock fabric, increased pore pressure caused by high frac treating pressures, and high injected water volume. Different completions can limit pore pressure increases and prevent or minimize the occurrence of slip on natural bed-parallel fractures.
Moreover, completions designs combined with pad designs like well spacing and stacking can change the cumulative impact of frac stimulations and influence the distance at which pore pressure increases occur from stages being stimulated (Figure 1).

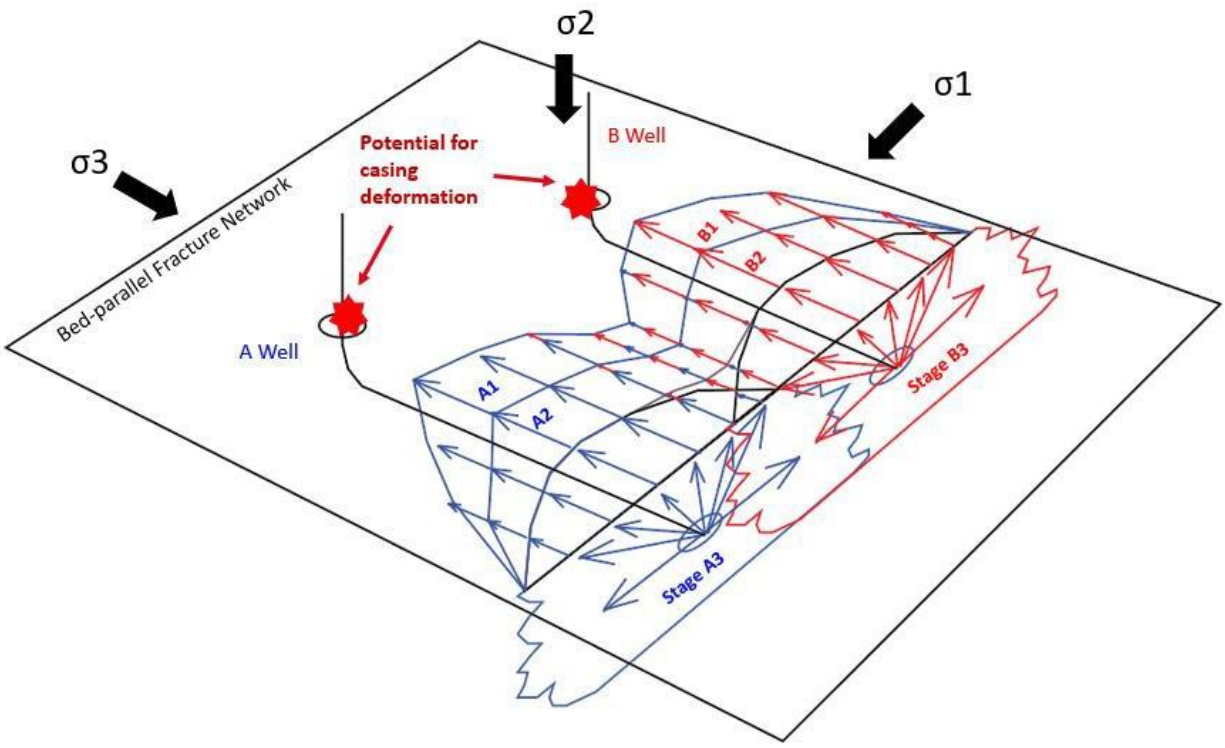


Figure 1: 3D Schematic view of 2 horizontal wells describing fracture fluid movement from three stages in each well where overburden (Sv=σ-2) stress is overcome. Increased pore pressure from stimulations can exceed Sv and allow fluid to move along bed-parallel fractures, preferentially in the same orientation as the horizontal well toward the build section, leading to casing deformation where the well intersects the same connected bed-parallel fracture set or expansion seam that is transmitting fluid and pressure. Successive stages in a lateral well cause minimum horizontal stress (σ-3) to escalate, coming closer to σ-2, thereby increasing the propensity to overcome Sv. Moreover, frac fluid from preceding stages that overcome Sv will add to subsequent stages (Stages A1, B1, A2, etc.) and stages in adjacent wells and increase the distance at which casing deformation can occur from active stages being stimulated.

## Aims and Objectives

The basis for this work is to understand the underlying mechanism driving the stimulation of off-azimuth fracturing, which have orientations that differ materially from the assumed minimum stress plane. Most notably, slip has occurred approximately parallel to bedding planes as identified from abundant casing deformation occurrences. Most off-azimuth fracturing requires increased pressure that comes at the expense of pressure used to grow the induced fracture in the preferred orientation, making them less effective and negatively impacting subsequent petroleum production. Through the understanding of the mechanisms driving off-azimuth fracturing, mitigations can be planned to reduce their occurrence or impact.

## Materials and methods

Data analyzed in this project are from the Blueberry sub play of the North Montney region in northeast British Columbia. The stress state of the Montney formation at this location is strike slip, with vertical stress (Sv) being the intermediate stress (σ-2) and only slightly more than the minimum principal stress (σ-3=Sh-min) depending on the area and depth of Montney development. The Montney formation is ~300m thick in this area and is largely composed of offshore facies with a mixture of siltstones and carbonates. ConocoPhillips has divided the formation into Upper, Middle, and Lower Montney (Moslow et al., 2018, Watt et al., 2022) with the highest occurrence of bed-parallel fracturing present in the Middle Montney and moderate to low frequencies in the Lower Montney and in the base of the overlying Doig Formation. Many of the observations that support results and discussions within this work are related to casing deformation, and DAS fiber observations within wells. Lab based studies also support observations through small stimulations in block tests (Grasselli et al, 2023, Laycock et al., 2024) where bed-parallel fracturing is activated under similar stress states as in the subsurface. InSAR data and microseismic has also been used to determine potential lateral extents of slip in the

subsurface (Eyre et al., 2022). Finally, correlations between key rock and stress parameters with well production were determined to understand the importance of impacts to oil and gas development.

## Results and discussion

Multiple pads with integrated diagnostic datasets, combined with an extensive database of casing deformation observations have formed the basis for understanding the mechanism driving slip on bed-parallel fracturing and resultant ineffective induced fracturing in the Montney Blueberry sub play. More specifically, high tensile strength rock adjacent to low cohesion bed-parallel fractures, combined with high induced frac pressures and escalated minimum horizontal stress from prior frac'd stages (Roussel, 2017), increase pore pressure within natural bed-parallel fractures permitting them to slip. The pressure increase that facilitates slip on bed-parallel fractures results in less pressure increase and fracture growth in the preferred frac orientation (perpendicular to σ-3). The impact is exacerbated in zones with higher frequencies of low cohesion bed-parallel fractures like the Middle Montney, and both fracture heights and lengths can be constrained resulting in reduced productivity in development wells (Figure 2).

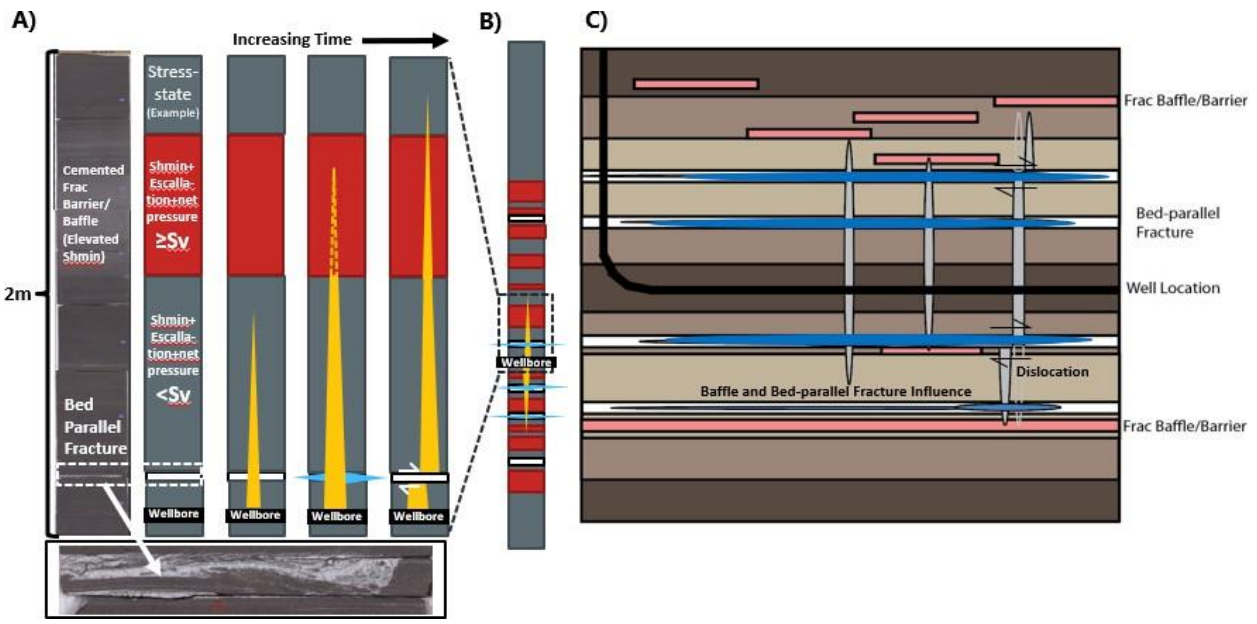


Figure 2: A) 2m interval of vertical core from Middle Montney that includes a high strength interval with a higher Sh-min (σ-3) than the more consistent Montney lithofacies above and below. A Bed parallel fracture is also present at the base of a core, with an inset image of the fracture at a higher resolution. The conceptual images to the right of the core photo show the interplay between the high strength rock, the more typical Montney lithology above and below, and the low cohesion bed-parallel fracture as a wellbore is stimulated beneath: Initially the induced fracture propagates from the wellbore but is temporarily arrested until pressure is increased at the frac tip such that it can overcome the strength of the frac baffle. At that point, there is enough pressure to overcome vertical stress (Sv) and push fluid into the bed-parallel fracture, which limits efficient fracture growth in the induced fracture orientation. Finally, as subsequent stages are stimulated in the wellbore, or adjacent wells, prior induced propped fractures can be displaced and reduce the induced fracture network connectivity. B) The conceptual model described in (A) is repeated as the induced fracture grows and intersects more pre-existing bed-parallel fractures and high strength units within the Montney stratigraphic section. C) Schematic cross-section view of the concepts described in Figures 2A and 2B, demonstrating how stages along a well can react differently depending on variability in Montney lithology and bed-parallel fracture network characteristics. Moreover, as fluid is pushed further toward the heels of wells via bed-parallel fracture networks as described in Figure 1, the re-activation of the same fracture network and ability for them to take fluid and pressure from subsequent stages is potentially easier if cohesion is further reduced or if natural asperities partially prop fractures open.

A key understanding from this work is the stratigraphic control of slip surfaces within the Montney formation, which allow for predictability laterally (Figure 3). Evidence for the stratigraphic control on slip surfaces was observed while stimulated a Lower Montney development layer, which caused deformation in the Middle Montney layer ~60m above the stages being stimulated and correlated with sheared bed-parallel fractures identified in offset core. Based on deformation in the heels of the stimulated wells and assumed stratigraphically controlled bed-parallel fractures, geomodels that integrated seismic and geosteering data, were used to predict the location of slip surfaces in the overlaying wells that were not yet stimulated. Caliper logs were run in the laterals of the 3 overlying wells and minor deformation was measured proximal to

prognosed depths confirming the stratigraphic relationship (Figure 3). While the lateral predictability is evident, centainty regarding which specific bed-parallel fractures will slip first is still highly enigmatic, as the geomechanical properties of adjacent rock and fracture fill can vary, which is further complicated by changes to the well and completions designs in different areas. Nevertheless, these observations have been helpful in making pad-level execution decisions, especially in the Blueberry sub play region where offshore marine depositional environments are more laterally continuous.

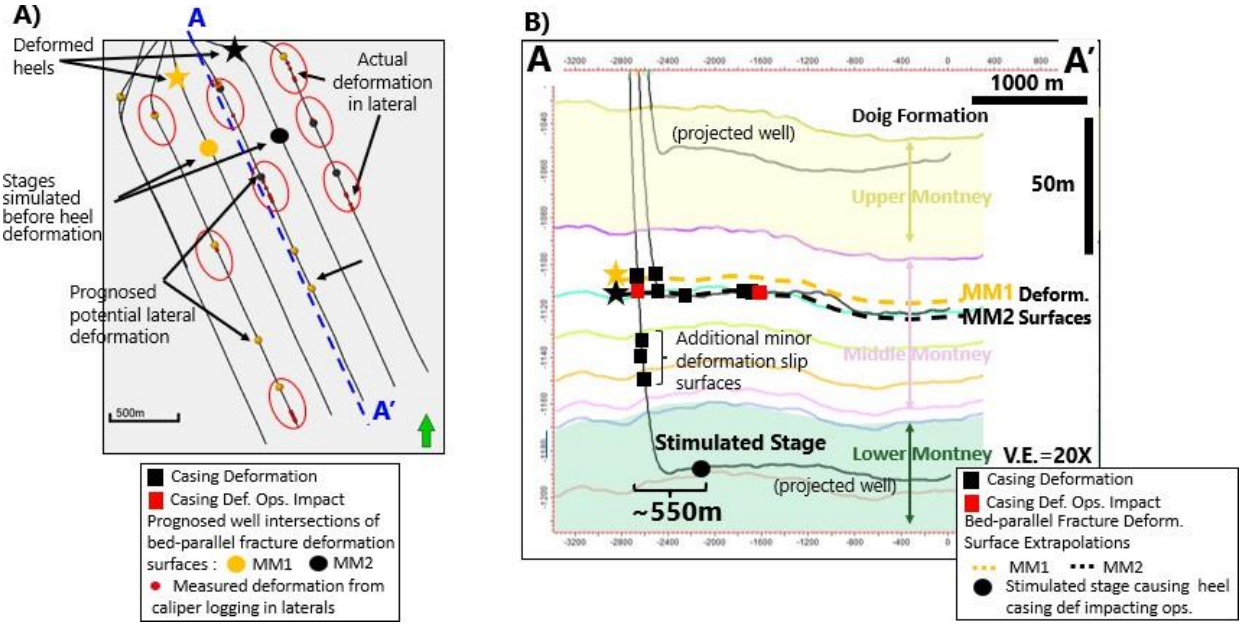


Figure 3: A) Map view of a pad where Lower Montney wells were stimulated prior to other wells and caused casing deformation in the build sections of the same wells where they intersect bed-parallel fractures in the Middle Montney. A geomodel was used to relatively accurately prognose where potential casing deformation depths within the overlying Middle Montney horizontal wells, which was confirmed on caliper logs. From this data the extent of bed-parallel fracture networks and their ability to create pad-scale cumulative rupture surfaces is interpreted. B) Cross-section view of center Middle Montney horizontal well from Figure 3A showing distance from the adjacent Lower Montney well stage that caused deformation. Deformation surfaces are also identified deeper in the Middle Montney section, indicating at that least 5 bed-parallel fracture networks have accommodated slip across areas of this pad.

Frac design changes were first made with the intent of mitigating the impacts on operations from casing deformation. Results from different completions design changes led to the realization that key parameters such as instantaneous shut-in pressures minus vertical stress (ISIP-Sv) can be used to monitored real-time to assess the risk of overcoming vertical stress (Figure 4A). A dashboard was then developed to assist real-time monitoring of frac stage ISIP-Sv at the frac stage location. From these completions design changes, reduced shut-in pressures are observed relative to the prior design.

While it can be difficult to prove effectiveness of mitigations to casing deformation and ineffective T-frac without clear baseline results, the example described in Figure 4A is taken to be more credible as minor deformation occurred in an adjacent well at the same stratigraphic interval as the well that simultaneously suffered major casing deformation. Based on many prior experiences, minor deformation instances always worsen and became impassable in the subsequent stages. After the design change on this pad however, all remaining stages were successfully executed without causing observable additional bed-parallel slip based on plug and perf operations and/or strain measured in offset well DAS fibers. Based on learnings from this pad a trial was executed to establish a relationship between stimulation proppant tonnage (used as a proxy for total slurry volumes), which determined that 5T proppant reduction can reduce ISIPs by ~1MPa. This pilot has determined a useful “rule of thumb” to make execution changes but is based on a high intensity (high proppant tonnage per meter) completions design and will differ depending on different completions strategies.

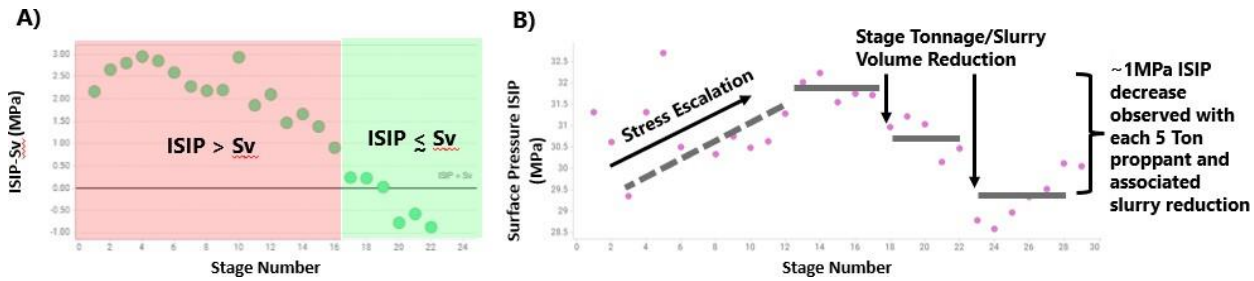


Figure 4: A) Instantaneous Shut-In Pressure (ISIP) – Vertical Stress (Sv) parameter plotted against stage count for a well that is adjacent to multiple wells that encountered casing deformation in their heels. A completions design change was made in all wells, which resulted in decreased ISIPs that were near or below Sv. Deformation did not occur in the example well and minor deformation in the adjacent well did not worsen, which is interpreted to be due to effective mitigation of the mechanism that causes ineffective fracturing and casing deformation. B) Surface ISIPs for a subsequent well where a trial was done after elevated ISIP-Sv values were observed. Proppant tonnage and associated slurry volumes were reduced to observe the impact on ISIPs and to reduce the ISIP-Sv imbalance.

Conditions that increase the likelihood of ineffective fracturing have been correlated to production and are integrated into multivariate analysis using competitor data. The impact on production is interpreted to be a combination of reduced fracture growth due to pressure loss when activating off azimuth bed-parallel fractures, and bed-parallel slip leading to offset of induced fractures from subsequent stages on the development pad (Figure 2). Proposed displacement of propped induced fractures are interpreted, but evidence for the frequency of occurrence in the subsurface is limited due to the difficulty to directly measure bed-parallel offsets of induced fractures.

## Conclusions

Integrated diagnostic datasets support the interpretation that bed-parallel slip is caused on natural fractures from frac operations, leading to less effective induced fracturing in the preferred frac orientation. By understanding Montney lithology, rock fabric, and stress conditions, the mechanism of ineffective fracturing is better understood. With the mechanism well characterized, key parameters like ISIP-Sv at stage locations are calculated and can be monitored during induced fracturing operations to determine the likelihood of ineffective induced fracture growth and casing deformation. Completions alterations described in this paper show effective mitigations to reduce stress conditions and have been demonstrated to mitigate ineffective fracture growth and associated casing deformation risk.

## References

Cobbold, P., Zanella, A., Rodrigues, N. and Løseth, H. 2013. Bedding-parallel fibrous veins (beef and cone-in-cone): Worldwide occurrence and possible significance in terms of fluid overpressure, hydrocarbon generation and mineralization. Marine and Petroleum Geology. v. 43. p. 1-20.

Eyre, Thomas S., Samsonov, S., Feng, W., Kao, H. and Eaton, D.W. 2022. InSAR data reveal that the largest hydraulic fracturing-induced earthquake in Canada, to date, is a slow-slip event. Scientific Reports 12, 2043.

Grasselli, G., Adams, M., & Abdelaziz, A. 2023. Rock Fabric Not Principal Stress Dictates SRV: The Story of How a ~70 Year Old Discounted Data Point Still Plagues Our Industry and How True Triaxial Testing Finally Confirms It. SPE/AAPG/SEG Unconventional Resources Technology Conference Abstract.

Laycock, D.P., Schroeder, R.D. and Safari, R. 2024. Breaking boulders: experimental examination of hydraulic fracturing in the Montney formation. Bulletin of Canadian Energy Geoscience, v. 71, n. 1, p.41-62.

Moslow, T.F., Haverslew, B. and Henderson, C.M. 2018. Sedimentary facies, petrology, reservoir characteristics, conodont biostratigraphy and sequence stratigraphic framework of a continuous (395m) full diameter core of the Lower Triassic Montney Fm, northeastern British Columbia. Canadian Society of Petroleum Geologists Reservoir, v. 66, p. 259– 287.

Roussel, N. P. 2017. Analyzing ISIP stage-by-stage escalation to determine fracture height and horizontal-stress anisotropy. SPE hydraulic fracturing technology conference and exhibition.

Sanders, S., Etienne, C., Gegolick, A., Kelly, D., Zonneveld, J.P. 2018. The Middle Montney Altares Member: lithology, depositional setting and significance for horizontal drilling and completion in the Altares Field, British Columbia. Bulletin of Canadian Petroleum Geology; 66 (1): 318–337.

Watt, E.A., Laycock, D.P., Michael, E., Tobin, R.C., Kelly, S. and Johnston, M.N. 2022. Hydrocarbon charge and petroleum system evolution of the Montney Formation: A multidisciplinary case study of the Blueberry sub-play in Northeast British Columbia, Canada. Bulletin of Canadian Energy Geoscience, v. 69, n. 1, p. 21–50.

GUSSOW 2024
Montney Subsurface Evaluation: Drive Towards Excellence
Banff, AB | October 2-4

# RTAPK: A New Approach for Estimating Permeability and Porosity using Montney Cores

Authors: Christopher R. Clarkson[1], Niloufar Rahimof[1], Mohammadebrahim Shabani[1], Chengyao Song[1], and Amin Ghanizadeh[1]. 1. University of Calgary

## Abstract

Laboratory-based measurements of permeability and porosity are routinely used to populate models for optimizing field development in unconventional reservoirs such as those hosted in the Montney Formation. However, most routine commercial laboratory tests do not reproduce the boundary conditions that wells are subjected to in the field, and the data is not analyzed in the same way. Therefore, the results of laboratory experiments are difficult to extrapolate to the field.

RTAPK (rate-transient analysis, porosity and permeability) is a new core analysis method that attempts to reproduce conditions under which wells produce in the field, with the data analyzed in the same way. After injection of gas into a sample cell and pressure stabilization, rates and pressures are measured during a production period. The RTAPK-derived rates and pressures are then analyzed using rate-transient analysis (RTA, a reservoir engineering technique commonly used for the analysis of field data to obtain fracture/reservoir properties and fluid-in-place estimates), to extract porosity and permeability from the core plug sample subjected to stress. Multiple estimates of permeability and porosity can be obtained in a fraction of the time of conventional laboratory techniques, such as pulse-decay or steady-state methods. Therefore, RTAPK not only better represents field conditions, but is more time-efficient than other methods.

One of the most important applications of RTAPK is to help solve problems related to field data RTA. For example, flow-regimes (e.g., characteristic patterns of flow occurring in the reservoir) interpreted from field data, and consequent model-derived reservoir and hydraulic fracture properties, can be significantly affected by reservoir heterogeneities. Because the in-situ reservoir cannot be directly observed at sufficient resolution to address these challenges, it is desirable to explore these effects at the laboratory scale where a reservoir sample can be thoroughly characterized. Another problem facing RTA of field data is inter-well communication. RTA has historically been developed for and applied to the analysis of single, isolated wells. However, the application of multi-fractured wells for field development has led to increased incidences of inter-well communication, which complicates RTA of field data.

In this study, RTAPK is used to evaluate the effects of reservoir heterogeneity on flow-regime sequences and permeability estimates using Montney samples. Previous studies using Montney samples have illustrated that a “typical” flow-regime sequence for relatively homogeneous core plug samples is transient linear flow (along the core plug), followed by boundary-dominated flow. In the current study, analysis of samples with visible heterogeneities (e.g., laminations or bedding) is performed and observed to cause deviations from this common sequence; in one example of a laminated Montney core, the flow-regime sequence resembled a field case where reservoir/fracture heterogeneity was inferred. The findings from RTAPK therefore suggest an alternative interpretation of the field case: layering effects.

Additionally, the RTAPK method is used herein to reproduce the effects of inter-well communication. A new RTAPK experimental setup and procedure was developed for this purpose: flow out of one side of the core sample is initiated to represent a “parent well”, after which flow out of the other side of the core sample is initiated to represent the “child well”. The resulting flow-regime sequence and contacted fluid-in-place plot for the parent well resembles that expected for communication through the reservoir matrix with a child well.

In summary, the RTAPK technique has proved to be tremendously useful for characterizing low-permeability Montney samples and can be applied to the study of outstanding problems facing RTA of field data.

## Background

Core analysis, or more generally, reservoir sample analysis, is commonly used to obtain critical reservoir properties such as porosity and permeability to aid in reservoir characterization. There are many uses of core data including calibration of well logs for use in the construction of a petrophysical model, population of models for performing pressure-transient analysis and rate-transient analysis, etc. However, for tight-rock analysis, there are many options for direct measurement of permeability (for example), related to the type of sample used (full-diameter core, slabbed core, sidewall core, core plug, crushed rock, cuttings, etc.), sample preparation (as-received, clean and dried, preserved, etc.), measurement conditions (confining pressure, pore pressure, temperature, etc.), measurement method (steady-state, unsteady-state), and physical measurement (pulse decay, pressure decay, rates and pressures). For low-permeability Montney samples, the pulse-decay permeability (PDP) method (Jones, 1997) is commonly applied to core plug samples under confining stress, along with various forms of pressure-decay analysis, including slabbed-core and crushed rock measurements (Ghanizadeh et al., 2018). As a result of different sample types used, and measurement conditions and methods that are applied, permeability estimates can vary widely for the same rock type/lithology, and even for analysis performed on the same sample. An additional problem is that scale-up of laboratory measurements to field scale is notoriously difficult to perform due to the fact that core samples cannot typically capture heterogeneities occurring at the field scale that affect flow to wells. This gap is even wider if one considers that typical commercial laboratory measurements, such as PDP, do not reproduce the operating conditions of wells producing in the field, and the data is not analyzed in the same way as pressure and rate data derived from these wells. The RTAPK (rate-transient analysis, porosity and permeability) core analysis method was developed to address the latter limitation of core analysis applied to tight rock, such as samples from low-/ultra-low ("unconventional") reservoirs within the Montney Formation.

After gas (or a fluid in general) is injected into the core holder of an RTAPK device, and the pressure is allowed to stabilize, the gas is produced out of the core holder at a controlled backpressure, and the flow rates are measured along with the flowing pressures. As with wells that are producing in the field, the RTAPK-derived rates and pressures are analyzed using rate-transient analysis (RTA) methods. Following the RTA workflow detailed in Clarkson (2021) for analysis of hydraulically-fractured vertical and multi-fractured horizontal wells (MFHWs) completed in unconventional reservoirs, flow-regimes (characteristic patterns of flow through the reservoir – a core plug in the case of RTAPK) are first identified using log-log diagnostic plots, and then each flow regime is analyzed through application of a model to obtain estimates of permeability and porosity.

RTA applied to MFHWs completed in unconventional reservoirs can encounter a variety of challenges related to heterogeneities in the reservoir, hydraulic fracture complexity, completion heterogeneity, multi-phase flow, stress-dependent reservoir properties, and inter-well communication, amongst others. RTAPK was developed in part to study some of these challenges in the laboratory; because the data are gathered and analyzed in the same way, a direct comparison of RTAPK results can be made with field data. Unlike subsurface reservoirs, core samples can be fully characterized in the laboratory using modern imaging/petrophysical/geochemical/geomechanical methods. This enables the controls on RTAPK-derived flow-regimes and permeability estimates to be ascertained, which can then (potentially) be extrapolated to field cases. This concept is explored herein for two of the aforementioned challenges for field-based RTA: reservoir heterogeneity and inter-well communication.

## Objectives

Rahimof (Rahimof et al., 2024; Rahimof, 2024) recently analyzed a suite of low-permeability core plug samples using the RTAPK method to evaluate the effect of permeability heterogeneity observed in the core plug samples on flow-regime signatures and permeability estimates. One of the objectives of the current study is to relate the findings of the lamination/bedding permeability heterogeneity study by Rahimof (2024), where flow in the core plug was parallel to bedding/laminations, to what is observed from field data. This will provide some insight into the effect of such heterogeneities on field-derived RTA flow-regime signatures, for example.

An additional objective of this study is to compare the results of experimentally simulated inter-well communication, using the RTAPK method by Rahimof (2024), to those obtained from field data.

## Materials and Methods

*Samples Studied.* Three low-permeability core plug samples extracted from the Montney Formation were used in this study. Samples 1 - 3 were selected to evaluate the effects permeability heterogeneity associated with laminations/bedding on

RTAPK-derived flow-regime signatures. Sample 4, a low-permeability core plug from a different formation (not Montney), was selected to perform the inter-well communication study. A brief description of these samples is provided below.

Sample 1 (**Fig. 1**), selected for studying the effects of permeability heterogeneity, is a 1.5” diameter, 1.34” long core plug that was extracted from a full-diameter core by drilling perpendicular to the axis of the core. The faintly visible (by color) beds (labeled “A” and “B”) in this siltstone sample are therefore aligned parallel to flow during RTAPK testing. Porosity, estimated from the combination of helium pycnometry (for grain volume) and calipering (for bulk volume), is around 3.7%. Pressure-decay profile permeability (PDPK, Jones, 1994) was performed on each of the beds by sealing the probe against the core plug end and injecting $N_2$ gas parallel to the axis of the core plug. Note that these permeability measurements are performed at ambient conditions (no confining stress applied to the core plug). The slip-corrected $N_2$ permeability for Bed A (darker bed) was determined to be 3 µD versus 6 µD for Bed B (lighter bed); the permeability contrast between beds was therefore determined to be about 2:1. This sample was selected to represent low permeability heterogeneity for RTAPK testing.

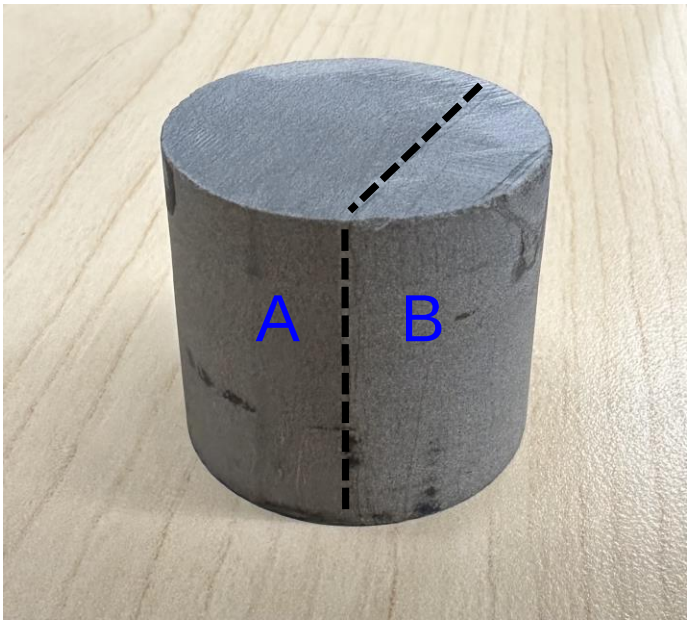


Figure 1: Image of core plug Sample 1. Two beds (labeled “A” and “B”) with slightly different coloring are observed and determined to have a permeability contrast of ~2:1. This sample was selected to represent low permeability heterogeneity for RTAPK testing. From Rahimof (2024).

Sample 2 (**Fig. 2**), selected for studying the effects of permeability heterogeneity, is a 1.5” diameter, 2.4” long core plug that was extracted from a full-diameter core by drilling perpendicular to the axis of the core. Unlike Sample 1, this sample is finely laminated where the laminations are sub-parallel to the core axis. For the purpose of this discussion, the laminations in this siltstone sample are grouped into two laminated regions (labeled “A” and “B”) which have different coloring. Porosity, estimated from the combination of helium pycnometry (for grain volume) and calipering (for bulk volume), is around 3%. PDPK was also performed on each of the regions; the slip-corrected $N_2$ permeability for Region A (darker region) was determined to be 0.5 µD versus 15 µD for Region B (lighter region). The permeability contrast between regions was therefore determined to be about 30:1 (noting that the permeability contrast between laminations could be considerably greater than this, but not measurable). This sample was selected to represent moderate permeability heterogeneity for RTAPK testing.

Sample 3 (**Fig. 3**), the last of the core plug samples selected for studying the effects of permeability heterogeneity, is a 1.5” diameter, 1.18” long core plug that was also extracted from a full-diameter core by drilling perpendicular to the axis of the core. This sample is very finely laminated, where the laminations are parallel to the core axis. CT images (not shown) reveal that laminations extend through the entire core plug, and that there are no fractures visible. Porosity, estimated from the combination of helium pycnometry (for grain volume) and calipering (for bulk volume), is around 3%. Distinct laminated regions could not be isolated for PDPK testing, and therefore the permeability contrast could not be quantified. However, due to the overall finer grain size of this sample, and darker overall color (suggesting possibly the presence of organic matter and/or clays), it was anticipated that the permeability contrast is even higher than for Sample 2; therefore, this sample was selected to represent high heterogeneity for RTAPK testing.

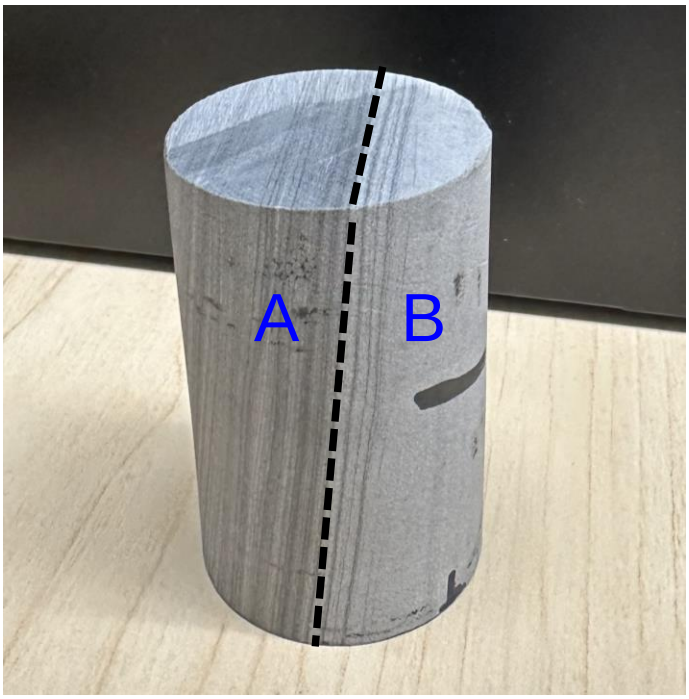


Figure 2: Image of core plug Sample 2. Two laminated regions labeled “A” and “B” with different coloring are observed and determined to have a permeability contrast of ~30:1. This sample was selected to represent moderate permeability heterogeneity for RTAPK testing. From Rahimof (2024).

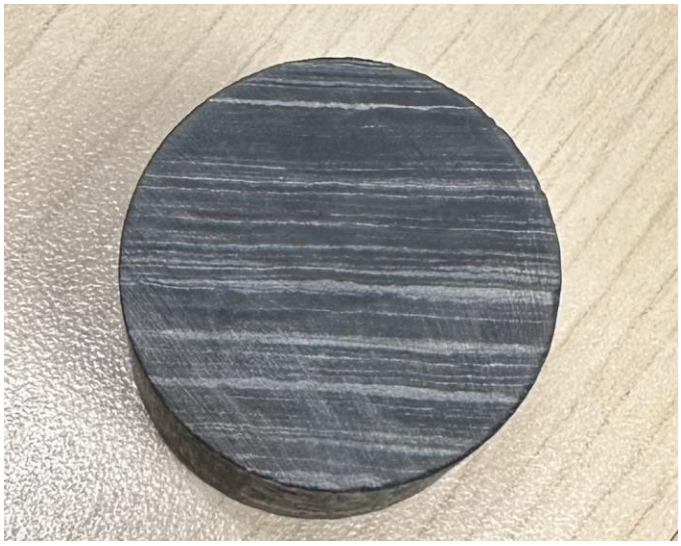

Figure 3: Image of core plug Sample 3. This sample is finely laminated. Distinct laminated regions could not be isolated for PDPK testing, and therefore the permeability contrast could not be quantified. This sample, however, was selected to represent high permeability heterogeneity for RTAPK testing. From Rahimof (2024).

Sample 4 (**Fig. 4**), selected for experimentally simulating inter-well communication, is a 2” diameter, 1.5” long, visibly coarser grained and homogeneous core plug (compared to Samples 1-3), that was also extracted from a full-diameter core by drilling perpendicular to the axis of the core. Porosity, estimated from the combination of helium pycnometry (for grain volume) and calipering (for bulk volume), is around 10%. The permeability of the sample, as determined using methane with RTAPK, is approximately 30 µd (at a pore pressure= 300 psia and confining pressure = 2000). PDPK results suggest a permeability of 58 µd permeability at an injection pressure= 20 psia and unconfined conditions.

Figure 4: Image of core plug Sample 4, selected for experimental simulation of inter-well communication. This sample is visibly coarser-grained, and more homogeneous, than the other samples studied. Unlike the other samples, it is not from the Montney Formation. From Rahimof (2024).

*Experimental Setup and Procedure.* Two versions of the RTAPK device were used for this study (**Fig. 5**). The single-side RTAPK device (Fig. 5, left) was used for evaluating the effects of permeability heterogeneity (Samples 1-3). Additional details of each experimental setup are provided by Rahimof (2024). With this device, the following experimental procedure is used:

- The core plug is first inserted into the core holder (Fig. 5, left) and confining pressure is applied
- Gas is injected into one side of the sample, and then injection is stopped
- Pressure in the sample cell is monitored using a pressure transducer (PT) until equilibration is achieved
- The gas is produced (from the same side as injection) through a backpressure regulator (BPR) to control flowing pressure
- Gas flow rates are measured using a flowmeter (FM) and flowing pressures measured with a PT.

The two-side RTAPK device (Fig. 5, right) was used for experimentally simulating inter-well communication (Sample 4). With this device, a similar experimental procedure to that of the single-side device is used with one important difference: gas is injected and produced out of two sides of the core holder (two ends of the core plug) containing the core plug sample and the flow rates and flowing pressures are measured for flow occurring from each side. To simulate parent-child effects, where the parent is placed on production first before a child well comes on production, one side of the RTAPK device is dedicated to the parent, and the other dedicated to the child (**Fig. 6**). The following experimental procedure is then used, after the sample is placed in the core holder:

- Gas is injected into both sides of the sample, and then injection is stopped
- Pressure in the sample cell is monitored until equilibration is achieved
- The valve (V2) on the parent well side is opened, while the valve (V4) on the child well side remains closed; this allows the parent to produce in isolation for a period of time while rates and pressures from that side of the device are measured
- After a short parent production period, the child well is put on production by opening V4, while the parent well is producing
- Flow rates and pressures on both sides of the device corresponding to the parent and child well are measured during this co-production period.

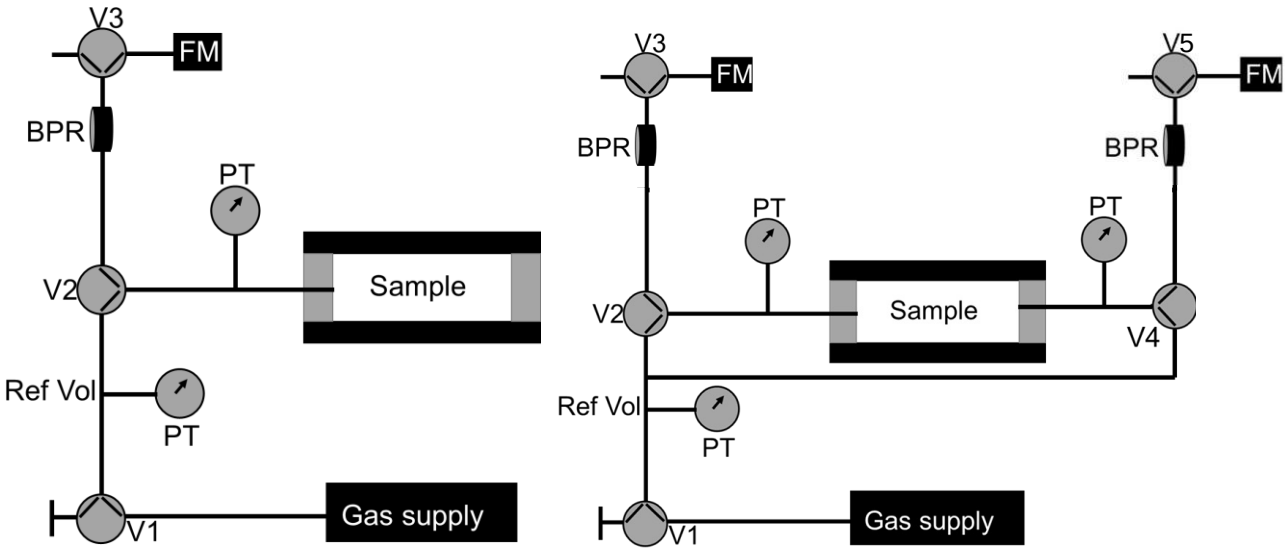


Figure 5: Schematics of the RTAPK experimental setups used for this study. (Left) The single-side RTAPK device used for studying the effects of permeability heterogeneity. Gas is injected into one side of the sample and produced out of the same side through a backpressure regulator and flowmeter. (Right) The two-side RTAPK device used for experimentally simulating inter-well communication. Gas can be injected into both sides of the sample and produced out of both sides with flow rates and flowing pressures being individually measured. From Rahimof (2024).

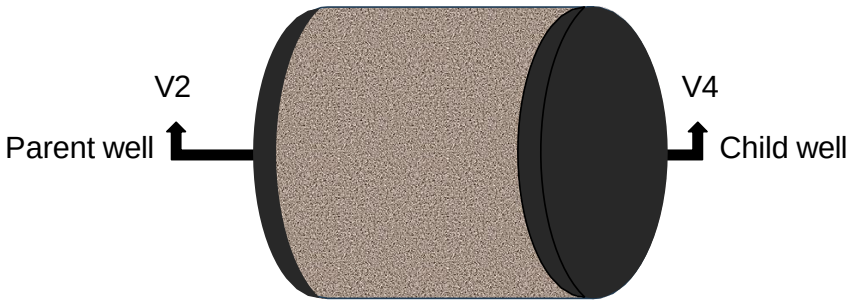


Figure 6: Illustration of the use of the two-side RTAPK device to experimentally simulate parent-child communication. Valve 2 (V2) is used to initiate parent well production, while valve 4 (V4) is used to initiate child well production. From Rahimof (2024).

*Rate-Transient Analysis.* A workflow for rate-transient analysis (RTA) applied to rates and flowing pressures measured for wells in the field producing from unconventional reservoirs, is described in detail by Clarkson (2021), along with RTA models used to analyze the data. This workflow, and associated RTA models, can also be applied to the analysis of RTAPK-derived rates and flowing pressures (as also described in detail by Clarkson, 2021), albeit with much higher quality data obtained for RTAPK (because of the careful measurements that can be made in the lab), and at a much smaller scale. While the reader is referred to Clarkson (2021) for the details, the RTA workflow, as applied to the analysis of both field and RTAPK data, can be summarized as follows:

- Flow-regime identification: a diagnostic plot is used to identify the sequence of flow regimes (e.g., characteristic patterns of flow occurring in the reservoir or hydraulic fractures)
- Straight-line analysis (SLA): production data is analyzed using specialized plots, applied to specific flow regimes identified in the previous step, to extract properties of interest
- Type-curve analysis (TCA): production data is matched to dimensionless type curves to extract properties of interest
- Model history-matching (MHM): production data is history matched using analytical/semi-analytical/numerical model in order to extract properties of interest

An example application of the first two steps of this workflow, applied to RTAPK data generated for a Montney core plug by Clarkson et al. (2019) and Clarkson (2021), is provided in **Fig. 7**. The flow-regime identification plot (Fig. 7, top) is a log-log plot of the rate-normalized gas pseudopressure derivative ($RNP'_{pg\_R}$) versus material balance pseudotime ($t_{MBag}$) – the reader is referred to Clarkson (2021) for definitions of these terms. This plot suggests the sequence of transient linear flow (propagation of pressure transient along the core plug) followed by boundary-dominated flow (pressure reaches the end of

the core plug and pressure depletion occurs). This sequence is what is expected for *homogeneous* samples (no heterogeneities in permeability, for example.) After the flow-regime sequence has been identified, the individual flow-regimes are individually analyzed for properties of interest. The square-root of time plot (Fig. 7, upper middle) can be used to provide two estimates of permeability: one estimate from the slope of a straight-line fit to the transient linear flow portion of the data ($k_{a\_SQRT}$ ), and one estimate using the time at the end of linear flow ($k_{a\_ELF}$ ). Note these are apparent gas permeabilities that are a function of pore pressure and effective stress, as well as the gas type used. Pore volume can also be estimated from the time at the end of linear flow ($V_{p\_ELF}$ ). $V_{p\_ELF}$ can then be used to estimate porosity (Clarkson, 2021). The flowing material balance plot (Fig. 7, lower middle) can be used to provide an estimate of permeability ($k_{a\_FMB}$ ) from the y-intercept of a straight-line fit to the boundary-dominated flow portion of the data and pore volume ($V_{p\_FMB}$ ) from the x-intercept of this line. Finally, the contacted gas-in-place plot (Fig. 7, bottom) can be used to estimate permeability from the y-intercept (at $t_{MBag}$ =1 day) of a straight-line fit to the transient linear flow data ($k_{a\_CGIP}$), and pore volume from a horizontal line fit to the boundary-dominated flow data ($V_{p\_CGIP}$). Clarkson (2021) compared the permeability and pore volume estimates for this sample using the various RTA methods and demonstrated them to be in good agreement.

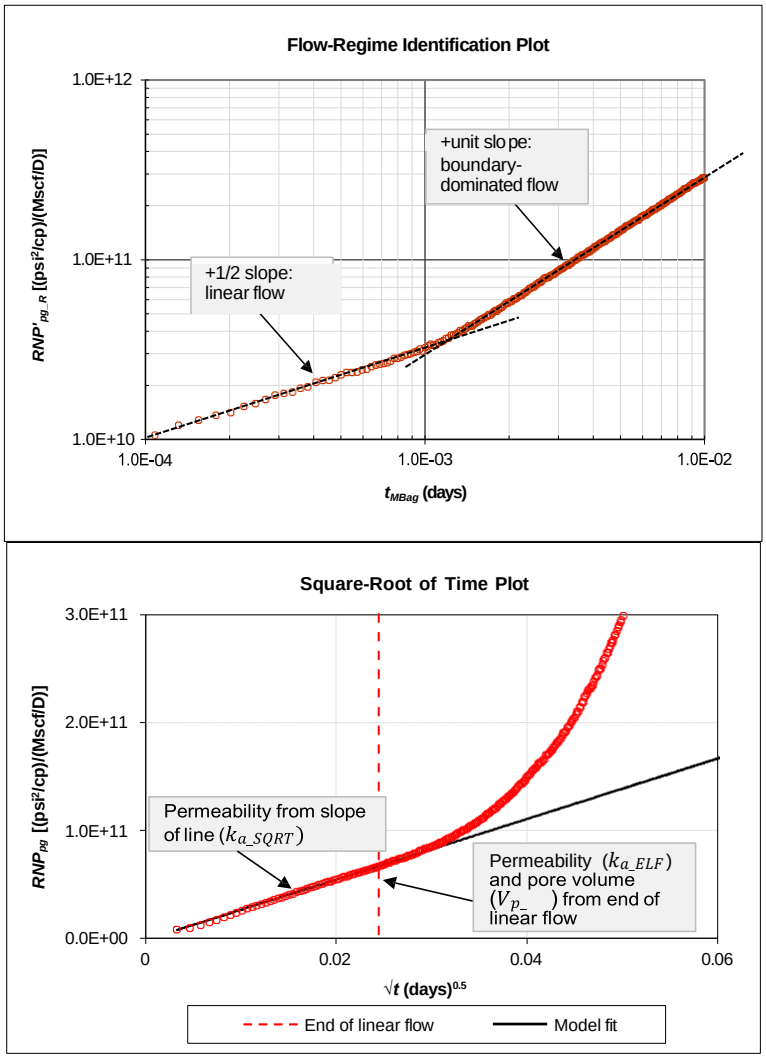

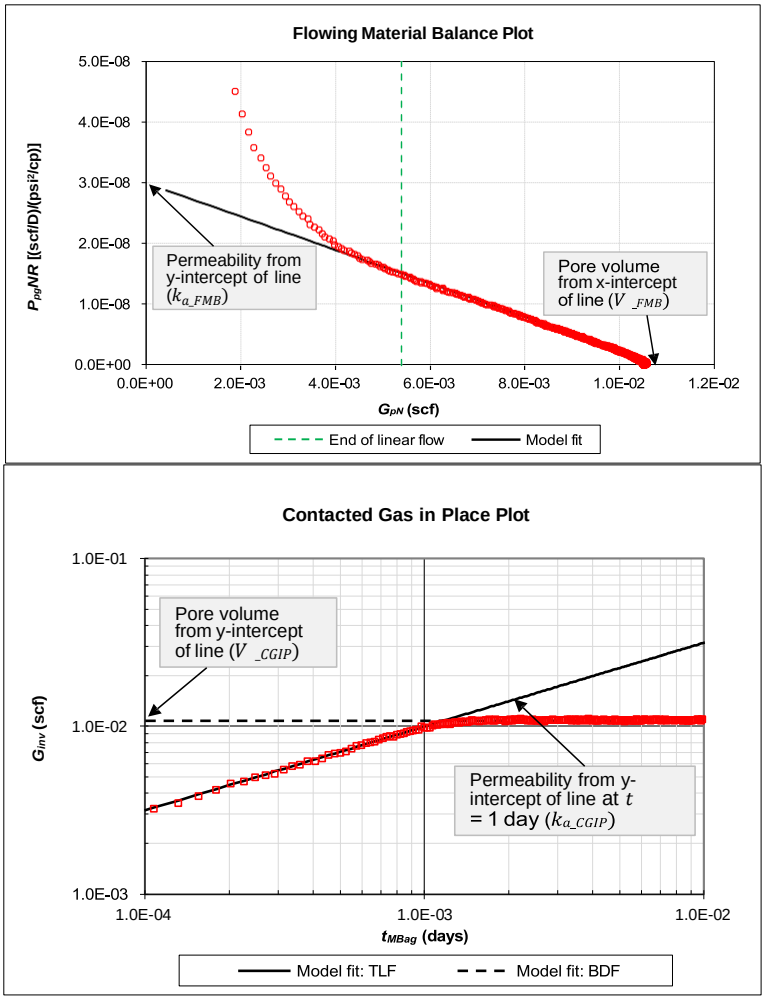


Figure 7: RTA workflow applied to RTAPK data collected for a low-permeability Montney core plug by Clarkson et al. (2019) and summarized by Clarkson (2021). (Top) Flow-regime identification plot. (Upper Middle) Square-root of time plot. (Lower Middle) Flowing material balance plot. (Bottom) Contacted gas-in-place plot. Plots modified from Clarkson (2021).

As noted above, the RTA analysis methods displayed in Fig. 7 are the same as those applied to field data. For example, **Fig. 8** provides a flow-regime identification plot generated for a MFHW completed in an oil-producing low-permeability interval of the Cardium Formation. As with the core plug analyzed above, the flow-regime sequence interpreted for this well is transient linear flow followed by boundary-dominated flow. Note that, for field examples, these plots tend to be quite noisy; the derivative of the integral of rate-normalized pressure (Fig. 8, right) can be used to denoise the data while preserving the flow-regime signature. Clarkson (2021) demonstrated application of the various straight-line analysis methods shown in Fig. 7 to this Cardium well.

For both the core plug and field examples provided in this section, the flow-regime signatures do not appear to be affected by reservoir heterogeneities. Consistency in the straight-line analysis results (e.g., permeability) also suggests that heterogeneities are not significant. Finally, there is no evidence of offset well interference for the field case (and the single-side RTAPK method was used for the core analysis in Fig. 7). In the following, the impact of reservoir heterogeneities on RTAPK results will be studied using Samples 1-3, and inter-well interference using Sample 4. The results will then be compared to field cases.

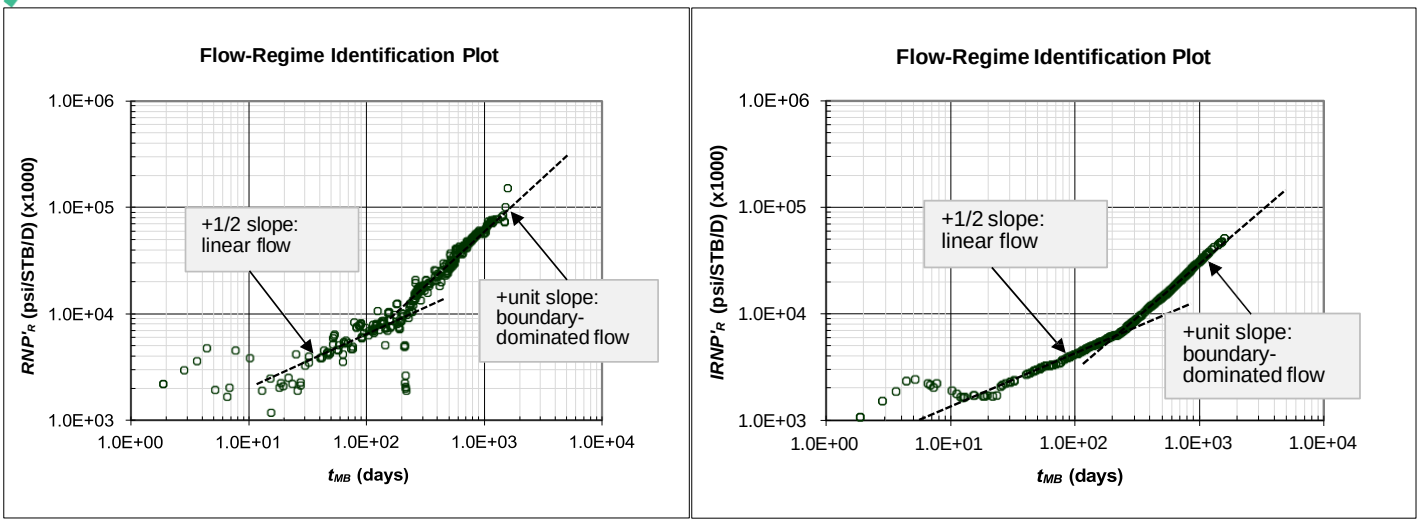


Figure 8: Flow-regime identification plot for multi-fractured horizontal well completed in a low-permeability intervals of the Cardium Formation. (Left) Plot generated using the derivative of rate-normalized pressure. (Right) Plot generated using the derivative of the integral of rate-normalized pressure. Early time data is affected by inaccurate flowing pressure estimates during pump off. Plots modified from Clarkson (2021).

## Results and Discussion

*RTAPK Experiments: Effect of Heterogeneity*. Flow-regime identification plots for Samples 1-3, generated from RTAPK rate/pressure data (**Fig. 9**), illustrate the varying effects of permeability heterogeneity associated with laminations/bedding aligned parallel to flow. The flow-regime sequence for Sample 1 (permeability contrast of 2:1 between beds) is interpreted to be transient linear flow followed by boundary-dominated flow, and the signature is comparable to that of the homogeneous sample in Fig. 7 (top). Therefore, the permeability contrast for this sample is insufficient to cause heterogeneous behavior. A similar signature is apparent for Sample 2 (permeability contrast of 30:1 between regions), although there is a subtle deviation from homogeneous behavior during the transition from transient linear flow to boundary-dominated flow (blue dashed circle in Fig. 7, top). In contrast, Sample 3 has a very different flow-regime signature than the other two samples; for this sample, a boundary-dominated flow signature is followed by a transition to transient linear flow. Rahimof (2024) simulated a laminated core plug with a permeability contrast of 100:1 between layers that exhibited a flow-regime sequence of boundary-dominated flow, followed by transient linear flow, followed by a second boundary-dominated flow period. The flow-regime signature for Sample 3 is similar to that simulation case, although the late boundary-dominated flow signature is missing for Sample 3. Rahimof (2024) noted that it was difficult to obtain an accurate flow rate measurement at the end of the test (approaching the resolution of the flowmeter), and therefore the late-time boundary-dominated flow signature (expected based on simulation) was not observed.

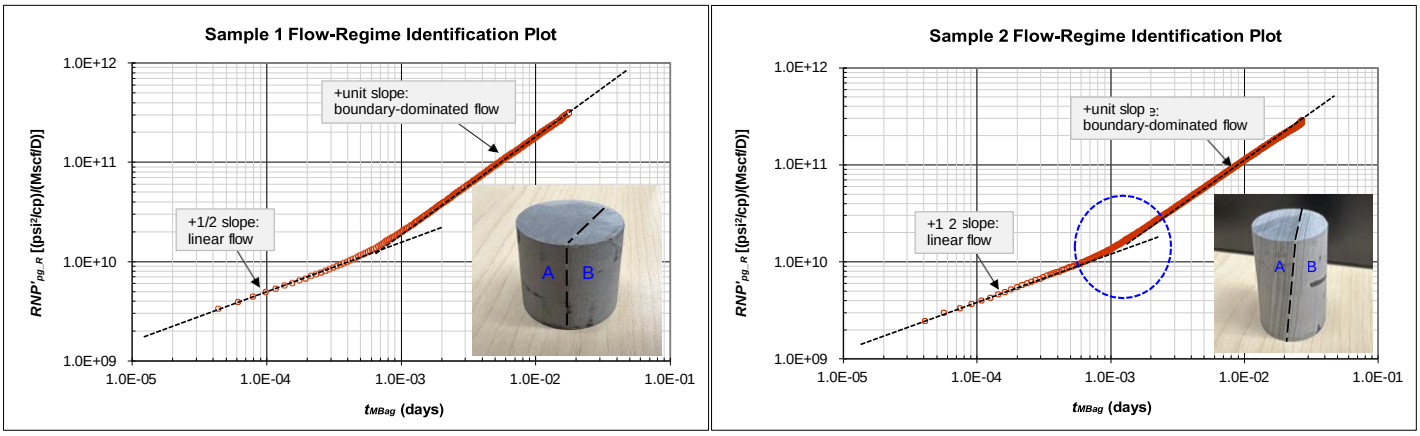

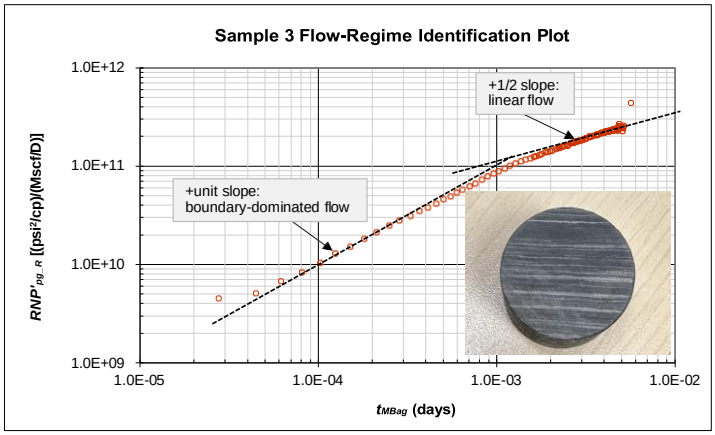


Figure 9: Flow-regime identification plots for Samples 1-3. (Top left) Sample 1 (Bed A permeability: 3 µD, Bed B permeability: 6 µD). (Top right) Sample 2 (Region A permeability: 0.5 µD; Region B permeability: 15 µD for Region B). A slight deviation from homogeneous behavior is indicated with the blue dashed circle. (Bottom) Sample 3. This sample exhibits an obvious departure from homogeneous behavior. Plots modified from Rahimof (2024).

Rahimof (2024) also provided the results of RTAPK-derived permeability for Samples 1 and 2 using the four different straight-line analysis methods described in the Materials and Methods section (and illustrated in Fig. 7 using a homogeneous Montney sample). As noted by Clarkson (2021), the four methods applied to the homogeneous Montney sample in Fig. 7 were in good agreement (within experimental and model fit error). As observed in **Table 1**, all permeability estimates for Sample 1 are also in good agreement, particularly for $k_{a\_SQRT}$ and $k_{a\_CGIP}$. $k_{a\_FMB}$ is slightly lower, possibly due to an increase in effective stress occurring during boundary-dominated flow due to pore depletion, and greater contribution to flow by lower-permeability regions. $k_{a\_ELF}$ is slightly higher than $k_{a\_SQRT}$ and $k_{a\_CGIP}$, but is more uncertain (Clarkson, 2021). This general agreement between permeability values is further evidence (along with the flow-regime signature in Fig. 9) that Sample 1 behaves like a homogeneous sample during the RTAPK experiment, despite its appearance and 2:1 permeability contrast between beds. $k_{a\_SQRT}$ and $k_{a\_CGIP}$ are again in good agreement for Sample 2 while $k_{a\_ELF}$ has an even greater contrast with $k_{a\_SQRT}$ and $k_{a\_CGIP}$ compared to Sample 1. This is due to the prolonged transition between linear and boundary-flow in this more heterogeneous sample, causing the time to reach the end of transient linear flow to be picked too early. A comparison with Sample 3 could not be made because of the difference in the flow-regime sequence.

Table 1. Apparent gas permeability values obtained from RTAPK experiments performed on Sample 1 and Sample 2.

| Sample # | Low-Permeability Bed/Region (µd)* | High-Permeability Bed/Region (µd)* | $k_{a\_SQRT}$ (µd)** | $k_{a\_CGIP}$ (µd)** | $k_{a\_ELF}$ (µd)** | $k_{a\_FMB}$ (µd)** |
|---|---|---|---|---|---|---|
| 1 | 3 | 6 | 1.32 | 1.34 | 1.56 | 0.91 |
| 2 | 0.5 | 15 | 2.74 | 2.72 | 3.33 | 1.78 |

*from PFPD measurements performed on bed/region under ambient conditions
**from RTAPK measurements performed on whole core plug under confined conditions (see Rahimof 2024 for experimental conditions and analysis plots)

*Comparison of RTAPK Results to Field Data*. The flow-regime signatures for Sample 1 and 2 (Fig. 9, top left and right, respectively), although determined using RTAPK data obtained from core plug samples using gas as the analysis fluid, are qualitatively similar to the flow-regime signature shown in Fig. 8 for a multi-fractured horizontal well producing oil from a low-permeability Cardium interval. Other examples of simulated and field cases exhibiting a similar signature were provided by Clarkson (2021). This sequence of flow regimes is expected for single-phase flow from a multi-fractured horizontal well completed in a homogeneous, isotropic reservoir. However, deviations from this ideal signature can occur, and have been the subject of much debate in the literature. For example, the flow-regime sequence for a shale-gas well provided in **Fig. 10** significantly deviates from this ideal signature; the well appears to be in boundary-dominated flow at early time, transitioning to transient linear flow, followed by a possible transition to boundary-dominated flow (noting that liquid-loading could be impacting this late-time signature). This flow-regime signature could be interpreted to be caused by reservoir and/or completion heterogeneity, amongst other factors. For example, Stalgorova and Mattar (2012) provided this example to support the development of their analytical enhanced fracture region (EFR) model. The EFR model assumes that secondary fractures form next to a primary hydraulic fracture during hydraulic fracture stimulation of shale wells due to reactivation of natural fractures. These secondary fractures create a region of enhanced reservoir properties (e.g., permeability), referred to as an enhanced fracture region (**Fig. 11**). In analytical modeling, the EFR can be assumed to have uniform properties

(Fig. 11, right) or a gradient in properties (Fig. 11, left) caused by the decay in fracture density and connectivity away from the primary fracture (Clarkson, 2021). For the former model, the sequence of flow-regimes would be linear flow in the EFR (missing from Fig. 10, possibly due high permeability in the EFR), followed by pseudo-boundary-dominated flow in the EFR, followed in turn by a second linear flow period in the non-stimulated reservoir (NSR). For the latter model, although linear flow occurs in the EFR, the flow-regime is distorted by the gradient in permeability (Yuan et al., 2019), appearing like pseudo-boundary-dominated flow. Once the pressure transient reaches the NSR, then normal transient linear flow will be seen. Comparing the flow-regime signature for Sample 3 with the shale-gas well, similarities can be observed; Sample 3 also exhibits a boundary-dominated flow signature before transitioning into transient linear flow. However, the signature of Sample 3 is assumed to be caused by permeability heterogeneity associated with laminations in the sample (aligned parallel to flow), not a permeability contrast associated with EFR/NSR, as for the EFR model. Therefore, one possible interpretation of the shale-gas signature is reservoir layering leading to permeability heterogeneity parallel to flow. Because the origin of the shale-gas well data in Fig. 10 (provided by Stalgorova and Mattar, 2012) is unknown, this interpretation could not be confirmed. However, it is well-known that for low-permeability reservoirs within the Montney Formation, extensive layering can occur (**Fig. 12**) with resulting high contrasts in permeability. In Fig. 12, permeability contrasts were quantified for a Montney well with core measurements (using a profile permeameter). Contrast in bed-level permeabilities could be on the order of 100:1 in some cases, possibly enhanced by bedding-parallel fracturing (Becerra, 2022), leading to flow-regime signatures similar to that in Fig. 10. This requires further investigation.

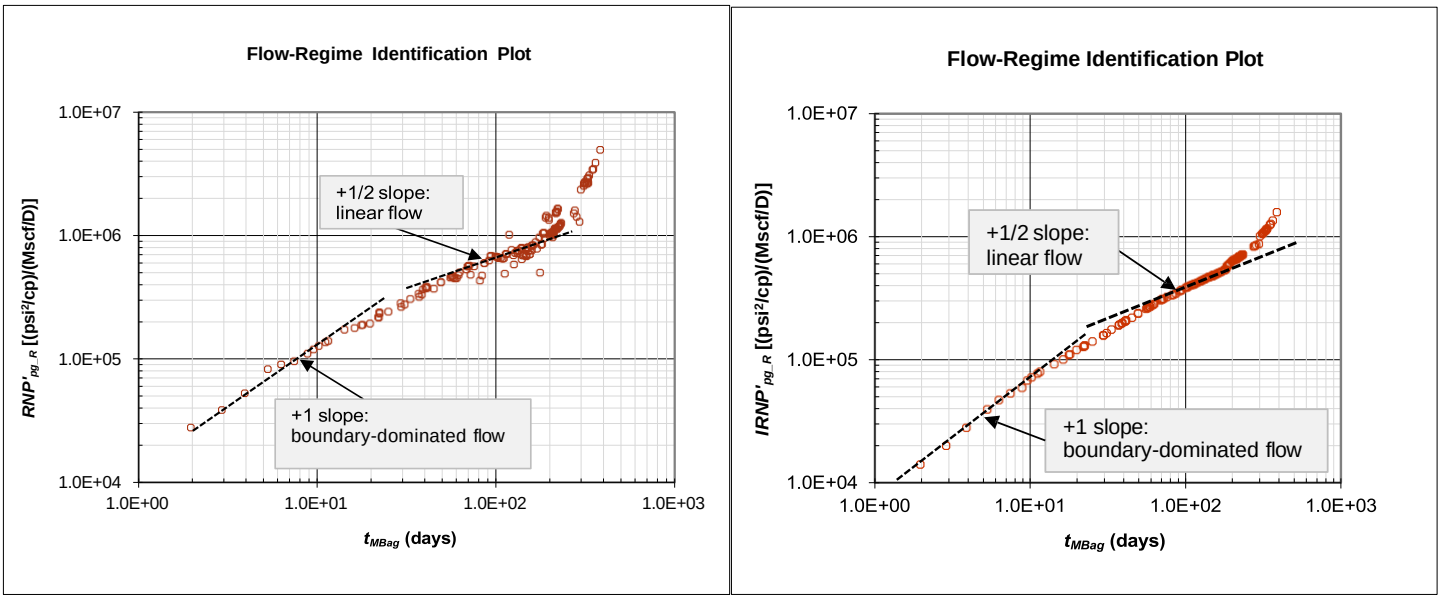


Figure 10: Flow-regime identification plot for multi-fractured horizontal well completed in a shale-gas well originally studied by Stalgorova and Mattar (2012). (Left) Plot generated using the derivative of rate-normalized pseudopressure. (Right) Plot generated using the derivative of the integral of rate-normalized pseudopressure. Plots modified from Clarkson (2021).

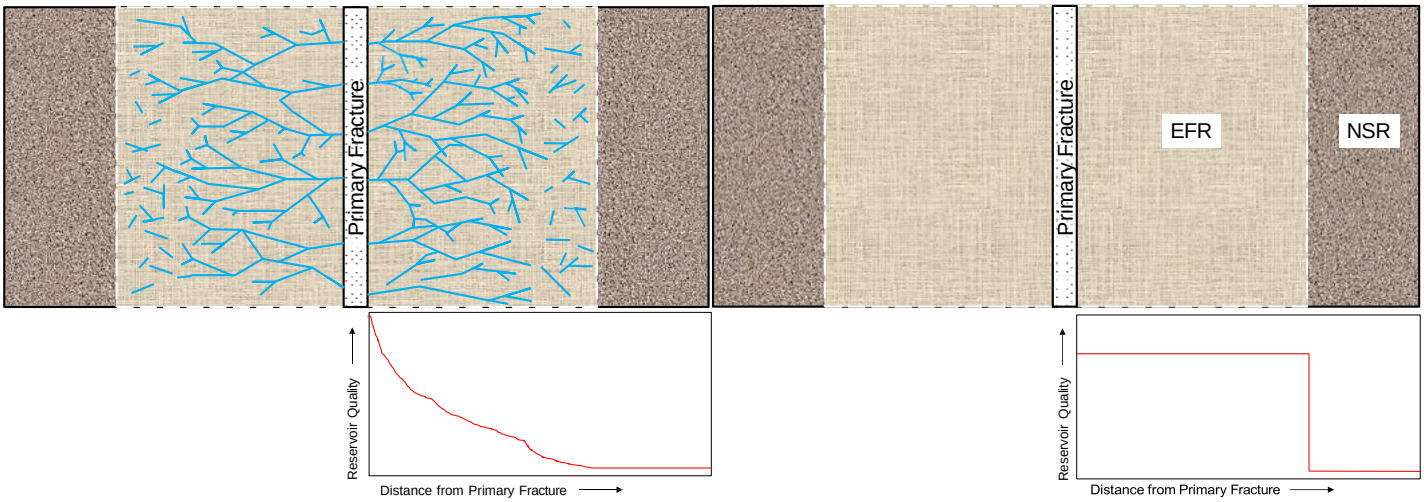

Figure 11: One possible conceptual model that can be used to interpret the flow-regime sequence observed for the shale-gas well in Fig. 10: enhanced fracture region (EFR). (Left) Conceptual model showing a single primary fracture (containing proppant) and branched fracturing occurring away from the primary fracture forming the enhanced fracture region. Branch fracturing is believed to be the result of reactivation of natural fractures during the stimulation treatment. Reservoir quality is assumed to degrade away from the primary hydraulic fracture due to a decrease in fracture density and connectivity. (Right) A simplified version of the EFR model where a composite-type reservoir is assumed with the EFR representing better reservoir quality and a non-stimulated reservoir (NSR) region representing the background (non-stimulated) reservoir. In this model, a step change in reservoir quality occurs from the EFR to the NSR. Modified from Clarkson (2021).

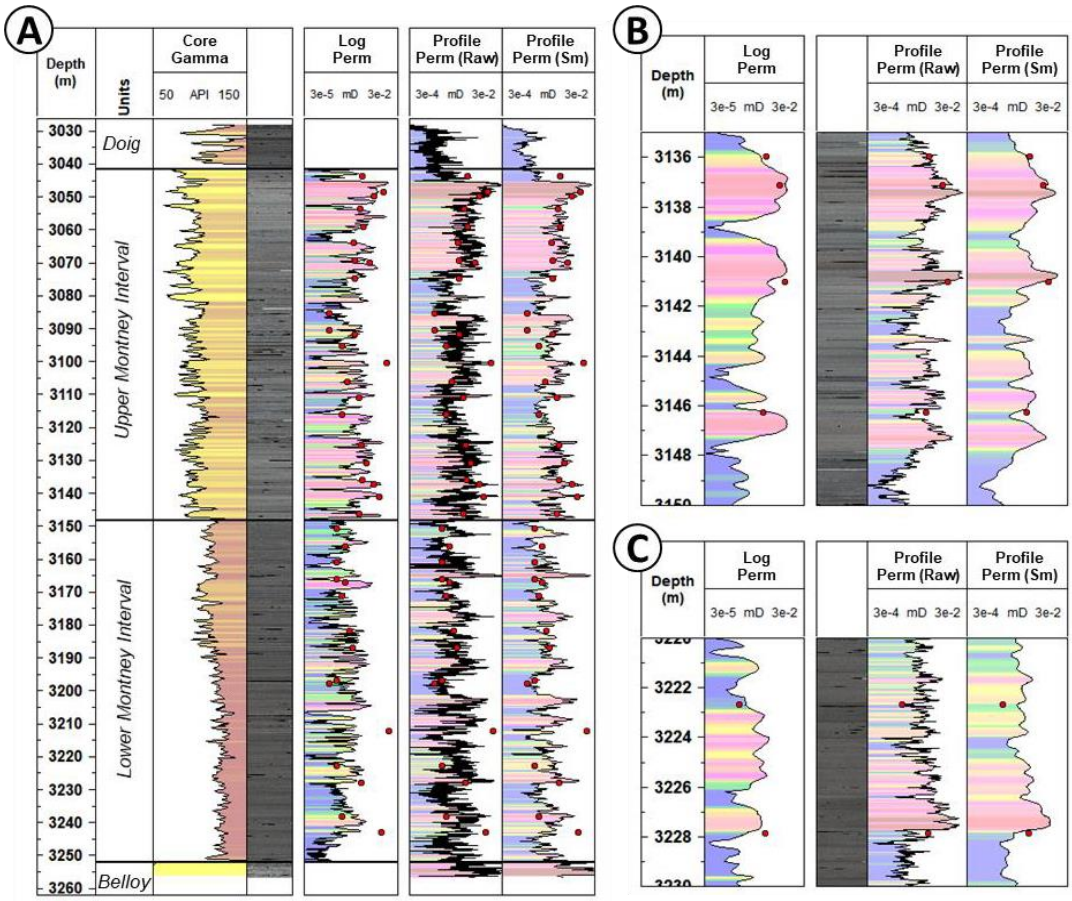


Figure 12. Illustration of permeability variation in the Montney. (A) A core gamma ray and core photograph are provided, and well-log-derived permeability, profile permeability (raw and smoothed data), and core plug permeability (CMS) are compared. (B and C) Zoom-in of log-derived permeability and profile permeability for selected intervals within the Upper (B) and Lower (C) Montney interval. From Becerra (2022).

*RTAPK Experiments: Inter-Well Communication*. The flow-regime identification plot for the "parent well" side of Sample 4 (Fig. 6), generated from RTAPK rate/pressure data, is provided in **Fig. 13** (left). After a brief transient linear flow period, the child well side starts to interfere with the parent side, causing a deviation upward from the half-slope line; this is followed by a transition, and boundary-dominated flow. The boundary-dominated flow is caused by a no-flow boundary that forms between the two producing sides, with the parent and child "wells" depleting their side of the core plug. Clarkson et al. (2024) recommended using the CFIP plot for the parent well to quantify the effects of inter-well interference between a parent and child well. The CFIP plot for the parent side of Sample 4 (Fig. 13, right) also illustrates the effect of the child side coming on production. As with the flow-regime identification plot, a short linear flow period is truncated by child side interference. After interference starts, the CFIP flattens (approaching boundary-dominated flow), then increases slightly. The late-time increase in CFIP is due to the rate of the parent side increasing relative to the child side, which causes the parent side to increase its share of the core pore volume, although boundary-dominated flow is the dominant flow regime.

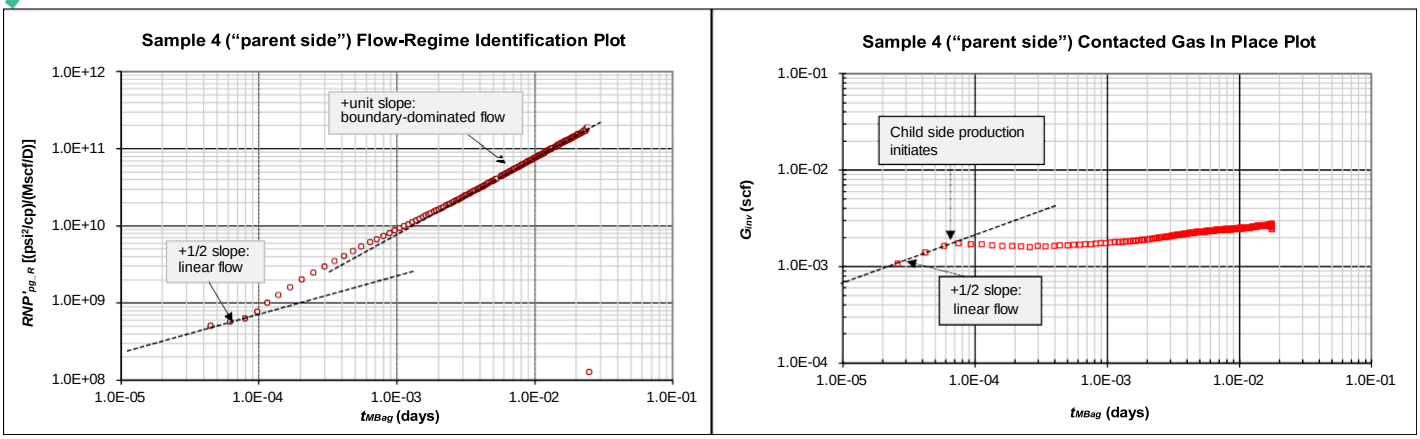


Figure 13: Results of the inter-well communication experiment using RTAPK. (Left) Flow-regime identification plot for parent well side of Sample 4. (Right) Contacted fluid-in-place plot for parent well side of Sample 4. Plot modified from Rahimof (2024).

*Comparison of RTAPK Results to Field Data*. The CFIP plot for a parent well (multi-fractured horizontal well completed in a low-permeability reservoir in western Canada) in communication with an offsetting child well, discussed in Clarkson et al. (2024), is provided in **Fig. 14**. The well started production ~ 40 days before the child well was placed on production, after which interference with the child well occurs. The CFIP plot, although noisy, suggests that the parent well CFIP increases until ~ 40 days (material balance time), after which child well interference causes the CFIP to drop sharply. Over time, the CFIP increases again and then follows a new trend. The communication between the wells is assumed to occur through hydraulic fractures, as illustrated on the right side of **Fig. 15**. This leads to relatively rapid communication between the wells after which an equilibrium is reached. Using the method described by Clarkson et al. (2024), the change in CFIP for the parent well caused by child well interference can be calculated; because the data is noisy, the estimate is somewhat subjective. The CFIP, and hence drainage volume of the parent well, is interpreted to decrease somewhat due to interference with the child well. Comparing this CFIP plot with the experimental results in Fig. 13 (right), some obvious differences are apparent. While the CFIP for the field case parent well exhibits a sharp drop and restabilization, the parent side for the experiment appears to drop only slightly after child side interference, and then exhibits a slight increase over time. The difference is due to the mechanism of interference. While the parent well for the field case is a multi-fractured horizontal well interpreted to be communicating with the child well through hydraulic fractures (Fig. 15, right), the parent side of Sample 4 communicates through the core matrix with the child side. This style of communication is more analogous to between-fracture communication through the reservoir matrix, as illustrated with the red dashed box in Fig. 15, where each side of the sample is the "fracture". In the future, attempts will be made to experimentally simulate communication through hydraulic fractures.

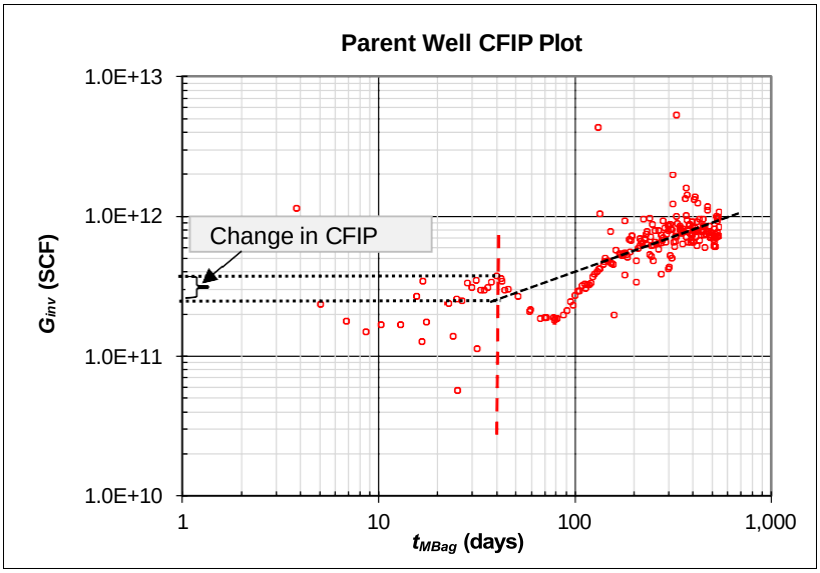


Figure 14: CFIP plot for the parent well of a parent-child pair. The vertical dashed line marks the time at which child well interference initiates, after which a steep drop in parent well CFIP occurs, followed by a transition and establishment of a new CFIP trend for the parent well. The change in CFIP caused by the child well is calculated using the procedure described by Clarkson et al. (2024). Modified from Clarkson et al. (2024).

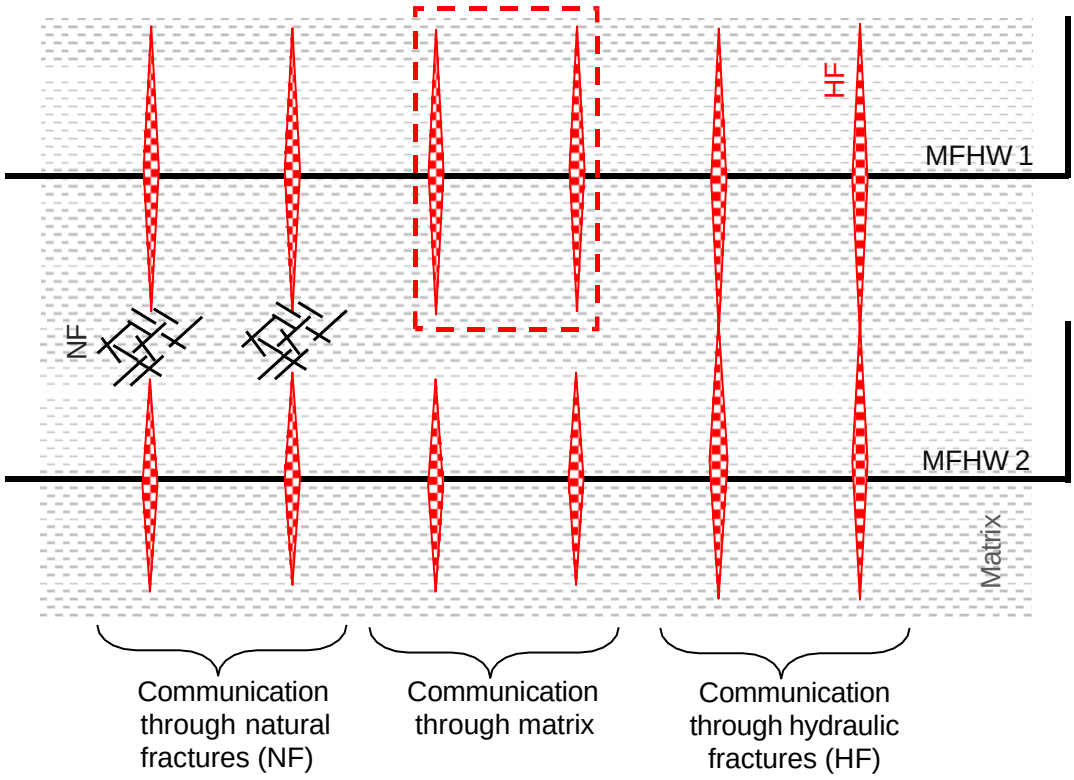


Figure 15: Illustration of possible mechanisms of communication between two offsetting multi-fractured horizontal wells. The parent well for the field case studied in Fig. 14 is interpreted to be communicating through hydraulic fractures with a child well. In contrast, communication between the parent and child sides of Sample 4 is interpreted to be analogous to between-fracture communication through the matrix illustrated with the red dashed box. Modified from Hamdi et al. (2021).

## Conclusions

RTAPK is a new core analysis method designed to not only obtain rapid estimates of permeability and porosity as a function of effective stress and pore pressure for tight rocks, but also to help solve problems related to the analysis of rate-transient analysis (RTA) data obtained in the field. The latter is enabled by the fact that RTAPK reproduces conditions under which wells produce in the field, and the data is analyzed the same way (i.e., using RTA methods).

In this work, RTAPK is used to evaluate the effect of permeability heterogeneity caused by bedding/laminations (aligned parallel to flow) on flow-regime signatures and permeability estimates. In addition, in a proof-of-concept study, an attempt is made to evaluate the effects of inter-well communication. For the heterogeneity study, three core plug samples (all from low-permeability intervals of the Montney Formation), with different levels of permeability heterogeneity as determined from profile permeability measurements performed on beds, are analyzed with RTAPK. In one case of a highly laminated core plug, the RTAPK-derived flow-regime signature resembled the flow-regime signature of a shale-gas well, which was previously interpreted to be related to fracture heterogeneity (using an enhanced fracture region model). The RTAPK results suggest that permeability heterogeneity caused by reservoir layering should be considered as a potential alternative to the interpretation of such field signatures.

The proof-of-concept inter-well communication experiment using RTAPK can be considered a success given that interference effects were observed, and could be quantified, by initiating flow from one side of a core plug (the “parent well”), followed by initiating flow from the other side (the “child well”). The flow-regime identification and contacted fluid-in-place (CFIP) plots for the parent side clearly show that the parent side drainage volume is affected by production from the child side. A CFIP plot for a field case reveals a more dramatic change in CFIP for the parent well caused by the child well. This is because, for the field case, communication with the offset well is interpreted to be through hydraulic fractures, whereas in the lab example, communication is through the rock matrix.

In future work, different field scenarios will be reproduced in the lab. Specifically, artificial and natural core plug samples will be used to evaluate the effects of fracture heterogeneity on flow-regime signatures and permeability estimates as well as to study the effect of through-fracture communication.

**Acknowledgements**

Chris Clarkson would like to acknowledge ARC Resources and Ovintiv for support of his Industrial Research Chair in the field of Subsurface Transitional Energy Pathways ('STEPs') at the University of Calgary, and Matt and Tara Brister for support of his Tamaratt Professorship in Transitional Energy Research. The sponsors of Tight Oil Consortium (TOC), hosted at the University of Calgary, are also gratefully acknowledged. Funding for this study was provided by Natural Sciences and Engineering Research Council (NSERC) Discovery Grant (RGPIN-2020-04541) and Discovery Accelerator Supplements Grant (RGPAS-2020-00116) to Clarkson.

**Nomenclature**

| | |
|---|---|
| BDF | acronym for boundary-dominated flow |
| BPR | acronym for backpressure regulator |
| CFIP | acronym for contacted fluid in place |
| EFR | acronym for enhanced fracture region |
| ELF | acronym for end of linear flow |
| FM | acronym for flowmeter |
| FMB | acronym for flowing material balance |
| $G$ | gas in place |
| $G_{inv}$ | contacted gas in place |
| $G_{pN}$ | normalized cumulative gas production |
| HF | acronym for hydraulic fractures |
| $IRNP$ | integral of $RNP$ for liquids |
| $IRNP'_R$ | radial derivative of $IRNP$ (for liquids, with respect to $\ln t_{MB}$) |
| $IRNP_{pg}$ | integral of $RNP_{pg}$ |
| $IRNP'_{pg\_R}$ | radial derivative of $IRNP_{pg}$ (for gases, with respect to $\ln t_{MBag}$) |
| $k$ | permeability |
| $k_a$ | apparent permeability to gas |
| $k_{a\_}C\ \ IP$ | apparent permeability to gas from contacted fluid-in-place plot |
| $k_{a\_}$ | apparent permeability to gas from the end of linear flow |
| $k_{a\_}$ | apparent permeability to gas from flowing material balance plot |
| $k_{a\_}SQRT$ | apparent permeability to gas from square-root of time plot |
| MFHW | acronym for multi-fractured horizontal well |
| MHM | acronym for model history matching |
| NF | acronym for natural fractures |
| NSR | acronym for non-stimulated reservoir |
| $P_{pg}NR$ | pseudopressure-normalized rate |
| PDP | acronym for pulse-decay permeability |
| PDPK | acronym for pressure-decay profile permeability |
| PT | acronym for pressure transducer |
| R | acronym for radial |
| $RNP$ | rate-normalized pressure for liquids |
| $RNP'_R$ | radial derivative of $RNP$ (for liquids, with respect to $\ln t_{MB}$) |
| $RNP_{pg}$ | rate-normalized gas pseudopressure |
| $RNP'_{pg\_R}$ | radial derivative of $RNP_{pg}$, (for gases, with respect to $\ln t_{MBag}$) |
| RTA | acronym for rate-transient analysis |
| RTAPK | acronym for rate-transient analysis, porosity and permeability |
| SLA | acronym for straight-line analysis |
| $t$ | time |
| $t_{MB}$ | material balance time for liquids |
| $t_{MBag}$ | material balance pseudotime for gas |
| TCA | acronym for type-curve analysis |

| | |
|---|---|
| TLF | acronym for transient linear flow |
| $V_p$ | pore volume |
| $V_{p\_}CGIP$ | pore volume from the contacted fluid-in-place plot |
| $V_{p\_}$ | pore volume from the end of linear flow |
| $V_{p\_}$ | pore volume from the flowing material balance plot |

**References**


Becerra, D., 2022. Geological Characterization and Evaluation of Reservoir Quality in The Montney Formation in West-Central Alberta. PhD thesis, Department of Geoscience, University of Calgary.

Clarkson, C. R., 2021. Unconventional Reservoir Rate-Transient Analysis. Gulf Professional Publishing.

Clarkson, C.R., Vahedian, A., Ghanizadeh, A., and Song, C., 2019. A New Low-Permeability Reservoir Core Analysis Method Based on Rate-Transient Analysis Theory. Fuel 235, p. 1530-1543.

Clarkson, C.R., Benson, A.-L.L., and Hamdi, H., 2024. Quantifying the Effects of Parent-Child Communication Using Dynamic Fluid-in-Place Calculations. SPE Hydraulic Fracturing Technology Conference and Exhibition, 6-8 February, 2024, The Woodlands, Texas.

Ghanizadeh, A., Clarkson, C.R., Vahedian, A., Ardakani, O.H., Sanei, H., and Wood, J.M., 2018. Laboratory-Based Characterization of Pore Network and Matrix Permeability in the Montney Formation: Implications for Methodology Comparisons. Bulletin of Canadian Petroleum Geology 66 (02), p. 1-27.

Hamdi, H., Behmanesh, H., and Clarkson, C.R., 2021. A Simple Method for Quantifying Inter-Well Communication Using Production Data from Single-phase Shale Gas Reservoirs. SPE Annual Technical Conference and Exhibition, 21-23 September, Dubai, UAE.

Jones, S. C., 1994. A New, Fast, Accurate Pressure-Decay Probe Permeameter. SPE Formation Evaluation 9(03), p. 193–199.

Jones, S. C., 1997. A Technique for Faster Pulse-Decay Permeability Measurements in Tight Rocks. SPE Formation Evaluation 12(01), p. 19–25.

Rahimof, N., 2024. Advancing the RTAPK (Rate-Transient Analysis, Porosity, and Permeability) Core Analysis Method. MSc thesis, submitted, Department of Chemical and Petroleum Engineering, University of Calgary.

Rahimof, N., Shabani, M., Ghanizadeh, A., Song, C., Clarkson, C.R., 2024. Use of the RTAPK Core Analysis Method to Evaluate the Impact of Matrix Heterogeneity on Flow-regime Signatures and Permeability Estimation. Unconventional Resources Technology Conference, June 17-19, 2024, Houston, Texas.

Stalgorova, E. and Mattar, L., 2012. Practical Analytical Model to Simulate Production of Horizontal Wells with Branch Fractures. SPE Canadian Unconventional Resources Conference, October 30 – November 1, 2012, Calgary, AB.

Yuan, B., Zhang, Z., and Clarkson, C.R., 2019. Generalized Analytical Model of Transient Linear Flow in Heterogeneous Fracture Liquid-rich Tight Reservoirs with Non-Static Properties. Applied Mathematical Modeling 76, p. 632-654.

GUSSOW 2024
Montney Subsurface Evaluation: Drive Towards Excellence
Banff, AB | October 2-4

# Relative Permeability of Low-Permeability Reservoirs: Montney Examples

Amin Ghanizadeh[1], Zhengru Yang[1], Mohammadebrahim Shabani[1], Chengyao Song[1], Niloufar Rahimof[1], Adnan Younis[1], Hamidreza Hamdi[1], and Christopher R. Clarkson[1]

1. University of Calgary

## Abstract

Evaluation of relative permeability is important for forecasting and optimizing production during primary and enhanced hydrocarbon recovery. Laboratory measurement of relative permeability in low-permeability rocks is time-consuming (weeks/months) and expensive (>10 times the cost of gas permeability tests). Conventional methods, such as steady-state and non-steady-state techniques, are often not practical for tight rocks due to low flow rates and long experimental times. Indirect methods of relative permeability determination, such as image analysis and pore-scale modeling, are simple and cost-effective. However, the application of indirect techniques to tight rocks is limited due to their inability to adequately account for fluid-rock interactions and the multiscale heterogeneity of tight rocks. Importantly, none of the conventional laboratory techniques can reproduce the boundary conditions under which wells are produced from (or injected into) in the field, and the data is not evaluated using the same methods as those used in the field. Additionally, routine laboratory techniques for measuring relative permeability typically require 'intact' core plugs and are not applicable to drill cuttings samples, which are often the only reservoir samples collected from multi-fractured horizontal wells. As a result of technical complexities and reservoir sample unavailability, sufficient relative permeability data is not available per formation to represent key rock types and flow units. Previous laboratory studies performed on low-permeability rocks, primarily focused on gas-water systems with only a few oil-water and gas-oil datasets. To date, only a few relative permeability datasets are available for low-permeability hydrocarbon reservoirs within the prolific Canadian Montney Formation, challenging field-scale modeling and optimization.

The objective of this study is to compare a series of conventional and advanced laboratory methods developed for relative permeability determination in tight rocks, with examples from the Montney Formation. A diverse sample suite of siltstones/sandstones from the Triassic Montney Formation was analyzed, covering a broad range of porosity (2-15%) and gas ($N_2$) permeability ($1.5 \cdot 10^{-5}$-$1.6 \cdot 10^{-1}$ md). The modified Dacy (m-Dacy) and the gas breakthrough (GBT) techniques, applicable to (relatively) high-permeability (>0.001 md) and low- permeability (<0.001 md) rocks, respectively, were used for core plug measurements. Importantly, gas relative permeability of select Montney core plugs was evaluated using the state-of-the-art RTAPK core analysis technique (based on rate-transient analysis, RTA). Proof-of-concept tests were also performed to evaluate whether gas-water relative permeability can be determined using artificial drill cuttings samples (core plugs crushed/sieved to 20-35 mesh size). The relative permeability values measured on the analyzed samples vary between 0.001 and 0.9, depending on methodology, sample type (core plug vs. artificial drill cuttings), water/oil saturation (10-75%), pore pressure (200-1000 psia), effective stress (500-4000 psia), and hysteresis path. The systematic experiments conducted herein extend the relative permeability datasets publicly available for the Montney Formation and provide new insights into the advantages and limitations of core-derived techniques for evaluation of relative permeability in low-permeability rocks.

## Background

The evaluation of relative permeability is essential for modeling and forecasting hydrocarbon recovery from low-permeability unconventional reservoirs such the Montney. However, measuring relative permeability in low- permeability rocks is technically challenging, time-consuming, and expensive due to the low flow rates and long experimental times. Conventional methods for evaluation of relative permeability using core plugs include 1) steady-state methods (i.e., gas and liquid are injected simultaneously with multiple fixed fractions), 2) unsteady- state methods (i.e., gas is injected to displace liquid), 3) stationary-liquid methods (i.e., effective gas permeability at variable wetting phase saturations held stationary by capillary retention; Dacy, m-Dacy). However, none of the routine laboratory techniques for measuring relative permeability using core plugs can reproduce the boundary conditions under which wells are produced from, or injected into, in the field. Additionally, drill cuttings are often the only reservoir samples collected from multi-fractured horizontal wells that are available for lab analysis. However, routine core-derived techniques for relative permeability analysis are not routinely applicable to drill cuttings samples.

## Objectives

The objectives of this study are to: 1) compare a series of conventional and advanced laboratory methods for relative permeability evaluation in the Montney Formation (**Table 1**), and 2) investigate the effect of fluid (water, oil) saturation and operational (e.g. pore pressure, differential pressure, hysteresis) controls on relative permeability.

Table 1: Summary of experimental studies focused on the evaluation of gas-liquid and liquid-liquid relative permeability in low-permeability Montney samples.

| Sample Type | Helium porosity (%) | Absolute Permeability (md) | Methods | Reference |
|---|---|---|---|---|
| Siltstones/Sandstones (Montney) | 4.3-7.7 | $k_{slip\text{-}corrected}$: $1.46 \cdot 10^{-5} – 3.4 \cdot 10^{-3}$ | Stationary-liquid Dacy (air/water) | Yassin et al. (2016) |
| Siltstones/Sandstones (Montney) | 2.9 – 8.8 | $k_{slip\text{-}corrected}$ ($N_2$): $2 \cdot 10^{-5}$ - $7 \cdot 10^{-3}$ | Stationary-liquid m-Dacy* ($N_2$/oil)<br>Gas breakthrough ($CH_4$/oil) | Ghanizadeh et al. (2021) |
| Siltstones/Sandstones (Montney) | 4.1-5.1 | $k_{slip\text{-}corrected}$ ($N_2$): $1 \cdot 10^{-4}$ - $1 \cdot 10^{-3}$ | RTAPK | Shabani et al. (2023) |
| Siltstones/Sandstones (Montney) | 6.5 | $k_{slip\text{-}corrected}$ ($N_2$): $5 \cdot 10^{-4}$ - $5 \cdot 10^{-3}$ | Crushed-rock analysis (rate-of-adsorption, $N_2$/water)<br>Stationary-liquid Dacy ($N_2$/water) | This summary (following Yang et al. 2021, 2023) |

* m-Dacy: Dacy method extended to lower permeability range using gas-flooding, with the possibility of measuring liquid relative permeability in addition to gas relative permeability.

## Materials and Methods

In total, 10 core plug samples (1,1.5” diameter; 1-2” length) and 2 crushed-rock material samples were investigated in this summary. Selected samples covered a broad range of helium porosity (2.9–13.8%) and slip- corrected gas ($N_2$, $CH_4$) permeability values, differing in mineralogy, and with total organic carbon content <1.5%. Silicates (69–71%) were the dominant minerals, followed by carbonates (24–25%) and clay minerals (4–5%, dominated by llite), as determined from X-ray diffraction (XRD) analysis. The analyzed Montney samples were classified as siltstones/sandstones with bioturbated and laminated fabrics. The tested core plug samples for RTAPK were drilled horizontally and vertically from low-permeability intervals of the Triassic Montney Formation in western Canada. The tested core plug samples for m-Dacy were drilled horizontally (parallel to bedding).

Four methods for measuring relative permeability were investigated including 1) m-Dacy (Dacy 2010, Ghanizadeh et al. 2021), 2) GBT (Amman-Hildenbrand 2012, Ghanizadeh 2021), 3) RTAPK (Shabani et al. 2023), and 4) crushed-rock relative permeability (Yang et al. 2023). The m-Dacy and GBT techniques are applicable to high-permeability (>0.001 md) and low-permeability (<0.001 md) rocks, respectively, and are performed on core plug samples (like RTAPK). For the first time, using the state-of-the-art RTAPK core analysis technique (based on RTA), Shabani et al. (2023) investigated gas relative permeability in the Montney. Conventional and new straight-line analysis methods, commonly applied to field production data, were used to evaluate effective gas permeability at variable stress and water saturations ($S_w$). The slope of the square root of time plot, time at the end of the linear flow, and contacted fluid-in-place plot were used to evaluate gas effective permeability values down to $1{\cdot}10^{-5}$ md. For crushed-rock relative permeability tests (Yang et al. 2023), the water vapor adsorption/desorption technique was employed to provide a wide range of water saturations. A numerical model developed previously (Yang et al. 2021, 2023) was used to estimate gas effective permeability at each saturation. A comprehensive suite of RTAPK, m-Dacy, gas breakthrough, and crushed-rock relative permeability tests were performed at varying pore pressures (400–1000 psia), confining pressures (900–5000 psia), and water saturations (0–53%) to investigate the effect of slip flow, effective stress, and water saturation on relative permeability. Repetitive drainage and imbibition GBT cycles were conducted on a select Montney sample to investigate the hysteresis in gas-oil relative permeability data.

## Results and discussion

*Dynamic range of relative permeability*

The measured relative permeability values range between 0.006 and 0.9, depending on methodology, fluid type (oil, water) saturation (10–75%), pore pressure (200–930 psia), effective stress (480–2800 psia), and hysteresis. Effective gas permeability values ranged between $5.4{\cdot}10^{-4}$ and $5.2{\cdot}10^{-3}$ md for RTAPK testing, between $5.4{\cdot}10^{-4}$ and $5.2{\cdot}10^{-3}$ md for m-Dacy, between $5.3{\cdot}10^{-5}$ and $7{\cdot}10^{-6}$ md for GBT, and between $1{\cdot}10^{-5}$ and $4{\cdot}10^{-7}$ md for crushed-rock analysis. The range of gas relative permeability values decreased in the order RTAPK > m-Dacy > GBT > crushed-rock analysis. The relative permeability values measured for the analyzed Montney samples were within the range previously reported for other Montney samples (Yassin et al. 2016, gas/water), tight rocks within the Western Canadian Sedimentary Basin (e.g. 0.0046-1.0; Bennion et al. 2002), caprocks (0.007-0.10; Amann-Hildenbrand et al. 2013) and tight sandstones (0.0003-0.10; Amann-Hildenbrand et al. 2016). The (maximum) gas effective permeability values measured with hydrocarbon/non-hydrocarbon gases ($CH_4$, $N_2$) were consistently (up to about two orders of magnitude) lower than slip-corrected gas and absolute (water, oil) permeability values under similar experimental conditions. The observed permeability reduction is attributed to reduced mobility to gas and liquid as a result of irreducible liquid saturation that, in turn, is governed by the characteristics of the pore throat system, wettability, and fluid-rock interactions. Consistency between gas and liquid relative permeability curves measured on sister Montney core plug samples was obtained, providing evidence of experimental repeatability and reproducibility. This consistency included S-shape behavior in oil relative permeability curves (using m-Dacy; **Fig. 1**, **left**).

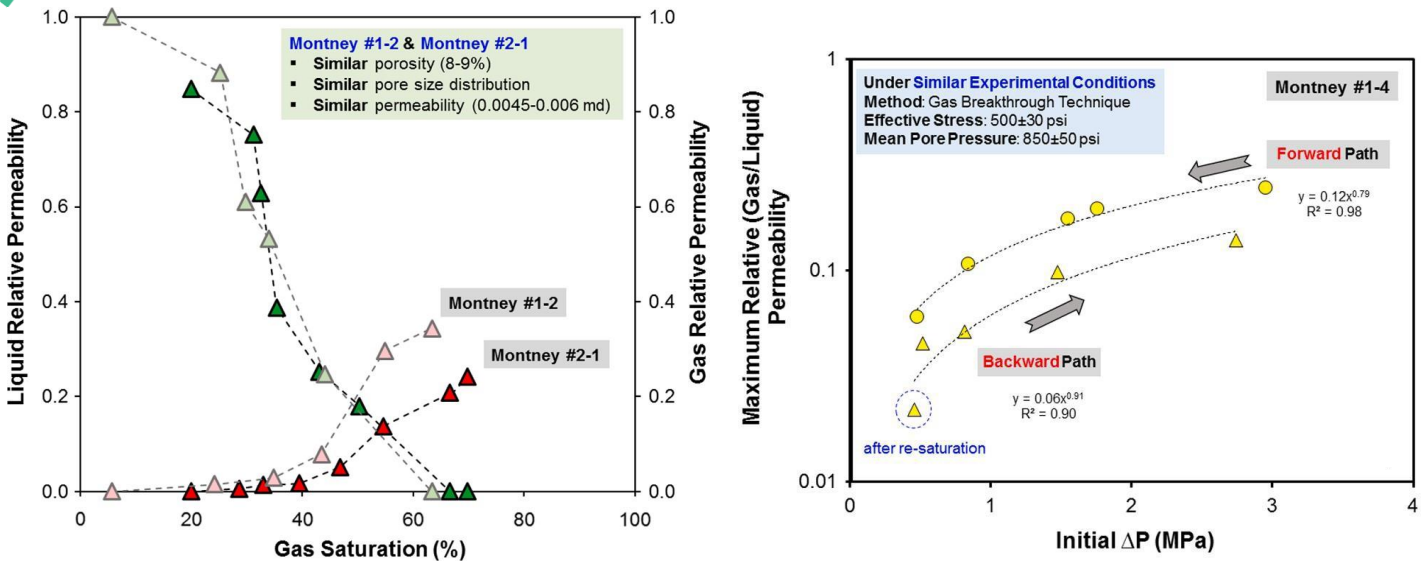


Fig. 1. Gas ($N_2$) and liquid (oil) relative permeability curves as a function of gas saturation for two sister Montney core plugs using m-Dacy method (left). Modified after Ghanizadeh et al. 2021. Impact of hysteresis and initial differential pressure on maximum gas relative permeability derived from GBT method (right). Modified after Ghanizadeh et al. 2021.

*Operational and geological controls on relative permeability*

Experimental data indicate that relative permeability is controlled by fluid saturation, pore/reservoir pressure, and hysteresis path, among others. Using the m-Dacy method, the gas relative permeability values measured for partially oil-saturated core plug samples increased (0.006–0.3) with decreasing oil saturation (75–30%). Using the GBT method, the gas ($CH_4$) relative permeability varied between 0.02 and 0.32, depending on pore pressure (191-640 psi), effective stress (482-2809 psi), and differential pressure (69-443 psi). Using RTAPK, effective gas permeability decreased, from $1.5 \cdot 10^{-3}$ to $7.8 \cdot 10^{-6}$ md, with increasing water saturation (0–53%). Effective gas permeability values measured using RTAPK decreased with increasing effective stress (500-4000 psia), likely due to reduced effective (transport) pore throat size and increased tortuosity. As a result of hysteresis, the maximum relative permeability values measured before re-saturation were consistently (up to about 60%) higher than those measured after re-saturation under similar experimental conditions (**Fig. 1**, **right**). The lower relative permeability values measured after re-saturation are attributed to gas phase trapping after drainage.

*Slip flow effect on relative permeability*

The presence of fluid (water, oil) within the pore network can affect the slip flow regime in low-permeability rocks. Laboratory-based gas relative permeability values are overestimated in the absence of gas slippage correction. Unlike single-phase gas flow, only a few studies have addressed the effect of gas slippage on two-phase (gas/liquid) flow in unconventional hydrocarbon reservoirs (e.g., Dullien 2012, Amann-Hildenbrand et al. 2013; Ghanizadeh et al. 2021, Shabani et al. 2023). Using RTAPK, slip factors decreased (from 715 to -286 $psia^{-1}$) with increasing water saturation (0–53%). The observed reduction is attributed to the decreasing contribution of the gas slip flow mechanism to overall gas transport. The reduction in slip factor with water saturation is likely due to the presence of water in smaller pores. Dullien (2012) introduced two different mechanisms, termed ‘channel flow’ and ‘funicular flow’, to describe the slip phenomenon in two-phase flow systems. Channel flow describes the independent flow of wetting and nonwetting phases in the interconnected network of pore throat capillaries. Funicular flow describes the simultaneous flow of wetting and nonwetting phases with the wetting phase surrounding the nonwetting phase. The gas slip factor for the funicular flow regime is expected to increase with liquid saturation. Channel flow, on the other hand, corresponds to flow of the non-wetting phase in larger, well-connected pores, with the wetting phase occupying smaller pores. The gas slip factor is expected to decrease with liquid saturation for channel flow, as observed previously (Dullien 2012, Ghanizadeh et al. 2021, Shabani et al. 2023). The ‘expected’ linear Klinkenberg trend may become reversed at the highest water saturations (45–53%) for some tight rocks, with close to zero and negative slip factors (**Fig. 2**). The close-to- zero and negative slip factors, determined from m-Dacy (Fig. 2, left) and RTAPK core analysis (Fig. 2, right) methods, can be explained by variable mechanisms of water drainage from the pore system (Shabani et al. 23).

Using the GBT technique, maximum gas ($CH_4$) relative permeability values decreased (up to about 50%) with increasing mean pore pressure (230–740 psia) likely due to the slip flow effect.

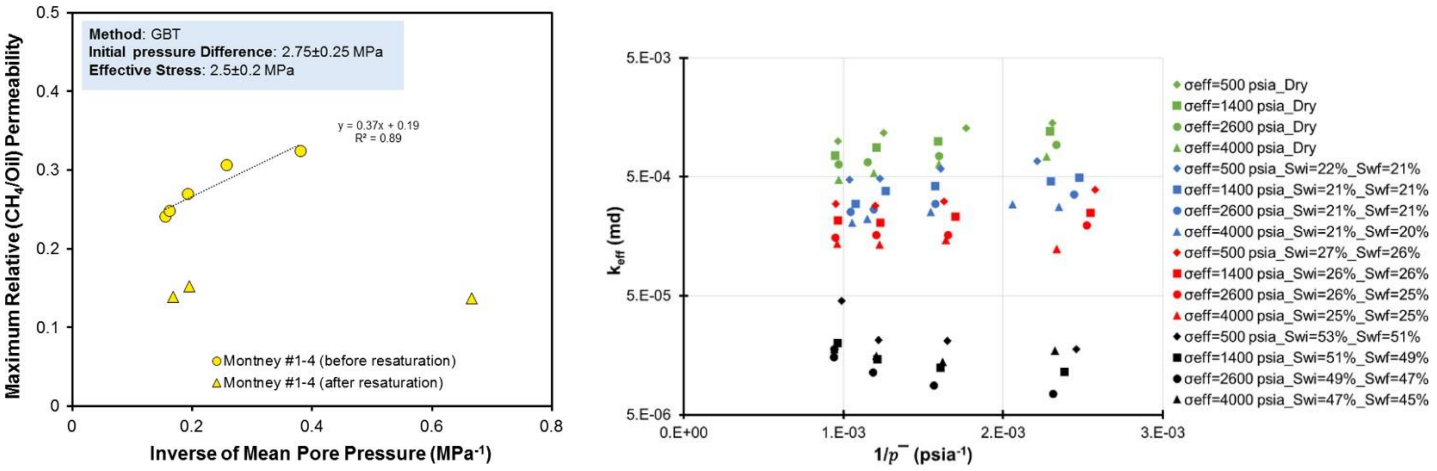


Fig. 2. Impact of water saturation on the trend of slip flow characteristics (Klinkenberg plot). Maximum gas ($CH_4$) relative permeability (derived by m-Dacy method) as a function of oil saturation and inverse of mean pore pressure (Montney example, left). The Klinkenberg trend flattened with increasing oil saturation. Modified after Ghanizadeh et al. (2021). Effective gas ($CH_4$) permeability (derived by RTAPK core analysis method) as a function of water saturation and inverse of mean pore pressure (Permian Basin example, left). Modified after Shabani et al. (2023).

*Modeling of core-derived relative permeability data*

The Corey (1954) model best fits *gas* relative permeability data measured using RTAPK (**Fig. 3**, **left**) while the LET (Lomeland et al. 2005) model best fits the combined *gas* and *liquid* relative permeability data measured using m-Dacy (**Fig. 3**, **right**). Notably, the gas relative permeability curves measured using the m-Dacy technique were suppressed at lower oil saturations, consistent with results of recent simulation studies in the Montney (Hamdi et al. 2020). Typically, gas effective permeability decreases rapidly in the matrix of tight rocks at liquid saturations above 40–50% due to the presence of immobile pore liquid. According to previous studies (Cluff and Byrnes 2010), there is a liquid (water) saturation region (between 55% and 89%) where neither liquid nor gas can flow effectively, corresponding to gas/liquid relative permeability values of less than 2%. This limiting liquid saturation region is referred to as 'permeability jail', primarily associated with rocks with absolute permeability values below 0.05 md.

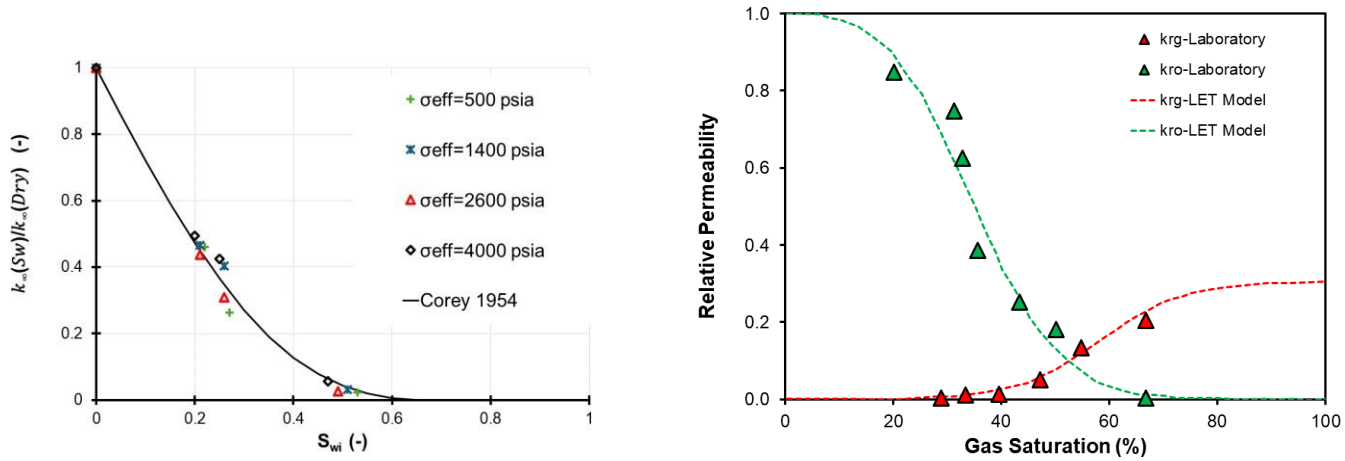


Fig. 3. Gas ($CH_4$) and liquid (water) relative permeability curves as a function of gas saturation and stress (500-4000 psia) using RTAPK method for a select tight rock sample (Permian Basin example, left). Modified after Shabani et al. 2023. Gas ($N_2$) and liquid (oil) relative permeability curves as a function of gas saturation using m-Dacy method for select Montney samples (right). Modified after Ghanizadeh et al. 2021.

Application of the Cory model was limited to modeling crushed-rock relative permeability data (**Fig. 4**). Dual- wettability models, as proposed previously (Yassin et al. 2016), may fit these data better due to the larger exposure of organic/inorganic matter in rock grains (yet to be tested/verified).

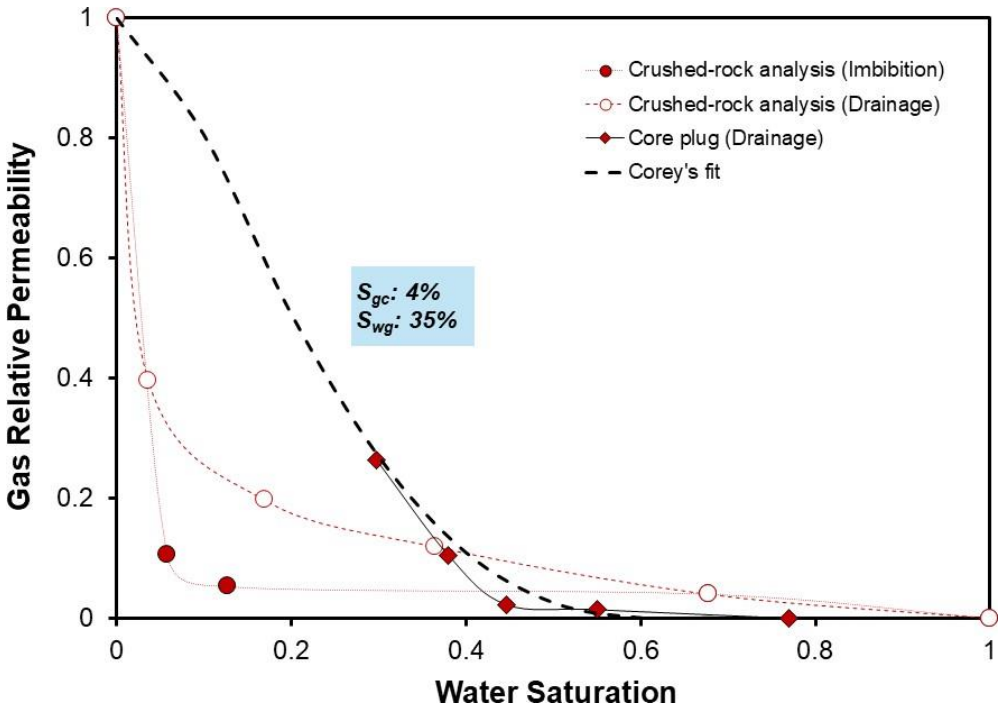


Fig. 4. Gas ($N_2$) relative permeability curves as a function of water saturation for select Montney crushed-rock and core plug samples. RTAPK core analysis method was used for measuring gas ($N_2$) relative permeability on the select core plug. As opposed to the analyzed core plug, application of the Cory model was limited to modeling crushed-rock gas (He) relative permeability data.

*Advantages and limitations of core-derived relative permeability methods*

The relative permeability measurement methods developed for tight rocks are based on different physical principles, sample preparation and experimental conditions, and therefore, have their own advantages and limitations. The Dacy, m-Dacy, and RTAPK methods are advantageous for their capability of generating relative permeability curves as a function of fluid saturation. However, accurate and reliable determination of the fluid (water, oil) saturation in the laboratory is an inherent challenge for low-permeability core plugs. For example, when applying the m-Dacy method, the “irreducible” oil saturation could not be reduced below 30% for Montney samples by Ghanizadeh et al. (2021), even after centrifuging under aggressive conditions (10,000 rpm; 1 week). Similar observations were reported for the microdarcy to millidarcy samples studied by Dacy (2010); liquid saturations below 20% could not be achieved with centrifuging. The GBT technique is advantageous because
1) it is applicable to low-permeability rocks within the nanodarcy range, 2) it provides a continues curve of relative permeability (as opposed to discrete datapoints generated using other core-pug-based methods), and 3) there is no need to disassemble/assemble core plugs in between testing for saturation alteration and determination (when combined a saturation detection method such as nuclear magnetic resonance, NMR). Relative permeability curves generated through other methods are established by collecting limited discrete datapoints, covering only a portion of the entire fluid saturation range. Using Dacy, m-Dacy, and RTAPK methods, the core plug samples are required to be disassembled/assembled frequently for determination of fluid saturation, which can potentially lead to the creation of micro/fractures, affecting the reliability of relative permeability data. The latter constraint can be potentially relived by coupling a continuous fluid saturation monitoring system (e.g. NMR) with Dacy, m-Dacy, and RTAPK core analysis methods, provided the degree of water saturation change (i.e. water drainage/imbibition) would be large enough so that a relative permeability curve could be generated from a single test. Another advantage of the GBT method is its speed (3–5 days per test; 100s of nanodarcy permeability) compared to the m-Dacy technique (3-4 weeks; 100s of nanodarcy permeability). However, the key limitation of the GBT technique is that the effective/relative permeability can be monitored as a function of pressure gradient only (not saturation, as opposed to other methods). As of now, liquid (oil, water) relative permeability can only be quantified using the m-Dacy technique. None of the other techniques is capable of evaluating the *liquid* (oil, water) relative permeability.

Satisfactory correlation between permeability estimates using different RTAPK approaches (average coefficient of variation <7%; Shabani et al. 2023) demonstrates the applicability of RTAPK method for effective and relative permeability assessment of partially-saturated ultra-tight reservoirs (down to less than $1 \cdot 10^{-5}$ md). Notably, test times after the start of the production were on the order of minutes, which is considerably shorter than those commonly achievable using routine methods (e.g., hours using Dacy/m-Dacy methods).

Using the gas breakthrough approach, it is possible to establish direct correlations between relative permeability and differential pressure, possibly mitigating the challenges of assessing liquid saturation in laboratory. The observed relationships between maximum gas relative permeability and initial pressure difference (Fig. 1, right), for instance, could potentially serve as a semi-quantitative tool for estimating relative permeability. These correlations could potentially provide a simple-yet-practical approach for predicting (maximum) gas effective permeability as a function of differential pressure without quantifying fluid saturation, which is notoriously challenging to determine for tight rocks in laboratory. The sequential drainage/imbibition cycles performed herein could have important implications for understanding the dynamics of oil and gas displacement in tight reservoirs such as the Montney during shut-in or cyclic gas injection (huff-n-puff) applications.

## Conclusions

Accurate determination and characterization of relative permeability is essential for reliable production forecasting and optimization purposes. There are significant uncertainties associated with estimating relative permeability curves from indirect techniques, resulting in uncertain reservoir simulation model outputs. In this summary, relative permeability values were reported for a diverse suite of Montney samples using hydrocarbon/non-hydrocarbon gases ($CH_4$, $N_2$) at variable experimental conditions. This study adds to the experimental relative permeability datasets, providing important information for constraining rate-transient analysis (RTA) models, and numerical models used to evaluate primary and enhanced oil recovery in tight hydrocarbon systems.

## Acknowledgements

The authors thank the sponsors of the Tight Oil Consortium hosted at the University of Calgary. Chris Clarkson would like to acknowledge Ovintiv Inc. (formerly Encana Corporation) and Shell for support of his Chair position in Unconventional Gas and Light Oil research at the University of Calgary. The authors thank Natural Sciences and Engineering Research Council of Canada (NSERC) for providing funding for this work through a Collaborative Research and Development (CRD) grant (CRDPJ 505339-16) and two Alliance grants (ALLRP 548652-19, ALLRP 586809-23).

## References

Amann-Hildenbrand, A., Dietrichs, J.P., Krooss, B.M., 2016. Effective gas permeability of tight gas sandstones as a function of capillary pressure – a non-steady-state approach. Geofluids, 16, 367-383.

Amann-Hildenbrand, A., Bertier, P, Busch, A., Krooss, B.M., 2013. Experimental investigation of the sealing capacity of generic clay-rich caprocks. International Journal of Greenhouse Gas Control, 19, 620-641.

Bennion, D.B., Thomas, F.B., Schulmeister, B.E., Ma, T., 2002. A correlation of water and gas-oil relative permeability properties for various Western Canadian sandstone and carbonate oil producing formations. Paper Number PETSOC-2002-066. Canadian International Petroleum Conference, Calgary, Alberta, 9-11 June.

Cluff, R.M., Byrnes, A.P., 2010. Relative permeability in tight gas sandstone reservoirs - the permeability jail model. Paper Number SPWLA-2010-58470. SPWLA 51st Annual Logging Symposium Society of Petrophysicists and Well-Log Analyst, Perth, Australia, June 19-23.

Corey, A.T., 1954. The interrelation between gas and oil relative permeabilities. Producers Monthly, 19, 38-41.

Dacy, J.M., 2010. Core tests for relative permeability of unconventional gas reservoirs. Paper Number SPE-135427-MS. SPE Annual Technical Conference and Exhibition, Florence, Italy, 20-22 September.

Dullien, F.A.L., 2012. Porous Media: Fluid Transport and Pore Structure. Academic press.

Ghanizadeh, A., Song, C., Clarkson, C.R., Younis, A., 2021. Relative permeability of tight hydrocarbon systems, An experimental study. Fuel, 294, 119487.

Hamdi, H., Clarkson, C.R., Esmail, A., Sousa, M.C., 2020. Importance of multiple-contact and swelling tests for huff-n-puff simulations: A Montney shale example. Paper Number: SPE-201557-MS. SPE Annual Technical Conference and Exhibition, Virtual, 27-29 October.

Lomeland, F., Ebeltoft, E., Thomas, W.H., 2005. A new versatile relative permeability correlation. Paper Number SCA2005-32. International Symposium of the Society of Core Analysts, Toronto, Canada, 21-25 August.

Shabani, M., Ghanizadeh, A., Clarkson, C.R., 2023. Gas relative permeability evaluation in tight rocks using rate-transient analysis (RTA) techniques. Marine and Petroleum Geology, 152, 106207.

Yang, Z., Yuan, B., Clarkson, C.R., Ghanizadeh, A., 2021. Experimental and numerical evaluation of surface diffusion in microporous/mesoporous media: Implications for improved gas permeability estimation in tight rocks using drill cuttings. Fuel, 285, 118974.

Yang, Z., Shabani, E., Solano, N., Ghanizadeh, A., Clarkson, C.R., 2023. Experimental determination of gas-water relative permeability for ultra low-permeability reservoirs using crushed-rock samples: Implications for drill cuttings characterization, Fuel, 347, 128331.

Yassin, M.R., Dehghanpour, H., Wood, J., Lan, Q., 2016. A theory for relative permeability of unconventional rocks with dual-wettability pore network. SPE Journal, 21:1970-1980.

GUSSOW 2024
Montney Subsurface Evaluation: Drive Towards Excellence
Banff, AB | October 2-4

# Calibrating downhole NMR logs – the Dos, Don'ts and Resonance! A Helpful Petrophysical Workflow and Example from the Montney Formation

Kristopher Farmer[1], Carolyn Currie[1,2*]

1.Core Laboratories, 2. Cenovus Energy (currently)

## Abstract

The Montney Formation remains one of the most important resource plays in the Canadian oil and gas market. It covers an extensive area, straddling Alberta and British Columbia, is over 300 meters thick in areas, all adding up to a whopping gas-in-place reserve of 1,965 trillion cubic feet (TCF) of gas, with recoverable estimates of more than 449 TCF (NEB, 2013). It contains a full spectrum of hydrocarbons, from dry gas on the western side of the basin to black oil in the east, with NGL's as a primary focus for operators, especially as key infrastructure and pipelines come online.

One of the main questions surrounding the Montney, especially on the Alberta side, is on water production. While overall lab derived residual water saturations remain on the low side, averaging 15-30%, the question becomes, where is all the water coming from? This question is partially answered by assessing and delineating where the water resides within the reservoir, both laterally and stratigraphically, whether that be in the free/mobile system, capillary-bound or clay-bound. More often than not, it's a combination of all three.

Core Laboratories Canada has spent the last 5-6 years investigating this water problem in the Montney Formation. Through extensive research on clay speciation's and total clay volumes using XRF, correcting calculated clay-bound water volumes which are compared to water-filled porosity, producing a 'desiccation curve', we have been able to delineate dehydrated/desiccated (clay-bound water only – not producible) and hydrated (mobile water + capillary-bound water) zones, with hydrated zones as potentially responsible for the water production. The question now becomes, how much of the hydrated zones is capillary-bound versus mobile, and this is where NMR can help. This presentation dives into the importance of core calibrating NMR logs and the effect that has on the T2 cutoffs for bound and mobile fluids when compared to industry standard T2 cutoffs based on expected lithologies.

In the case history presented, a review of the logging run yielded the following observations: NMR porosity lacked an oil and brine hydrogen index correction and, a T2 cutoff for carbonates (92ms) was applied, as well as a clay bound water cutoff of 3.3ms. To core calibrate these logs, a number of samples were selected for low frequency laboratory NMR T2 at 100% brine saturation for a total NMR T2 porosity followed by T2 at Swi to determine T2 cutoff. Total downhole NMR porosity was then hydrogen index corrected for bulk volume oil and water utilizing fluid saturations from a resistivity-based saturation model resulting in a core-calibrated NMR porosity model. This showed that the uncorrected NMR porosity from the vendor was an underestimation. The clay bound water T2 cutoff did not change much (3.0ms) but the bulk volume irreducible changed drastically to 21.3 ms. Using the refined NMR porosity and corrected fluid volumes, a more representative picture of the wellbore to formation fluid dynamics can be achieved. Furthermore, we can use these NMR parameters to calculate an NMR 'desiccation curve', which shows a strong correlation to the XRF 'desiccation curve', therefore paving the way to redefine the hydrated zones and water production in the Montney Formation.

## Statement of the background

With the increased use of NMR log being run in the Montney Formation, the value of core calibrating these logs provides benefits to help guide optimized reservoir targets. Wireline NMR porosity consists of hydrogen-bearing fluids within the volume of rock that the wireline tool is measuring (Appel, 2004). These NMR porosities are typically not corrected for

Hydrogen Index due to the uncertainty of fluid type and saturations during wireline logging. Generally, accepted industry standards T2 cutoffs of 33ms (sandstone) and 92ms (carbonates) have proven to be insufficient in characterizing bound versus free fluid in unconventional reservoirs. Furthermore, the application of the industry standard Coates coefficient of 10 can yield permeability models not representative of the reservoir.

## Materials and methods

In this example, wireline logs include a quad combo with an advanced wireline NMR log (Figure 1). Core testing consisted of basic properties (bulk density, porosity, grain density, saturations, permeability), XRD, XRF, and NMR. Prior to calibration of the NMR T2 logs, petrophysical properties including minerology, variable grain density, porosity, permeability, and saturations are modeled. These parameters provide a baseline for NMR core calibration. NMR T2 core testing consists of two measurements: NMR T2 at 100% Sw and NMR T2 at irreducible water saturation (Swi). These two measurements provide an NMR porosity, clay-bound water, and T2 cutoffs which defines the separation of Bulk Volume Irreducible (BVI) fluid and Free Fluid (FFI) (Figure 2).

For the porosity calibration, bulk volume (BV) fluid corrections for oil and water, generated from the saturation model were applied using a hydrogen index, resulting in a core calibrated NMR porosity. Downhole NMR clay-bound water was compared and adjusted to match core measured NMR and XRD calculated clay-bound water. To account for variations in T2 distributions from laboratory to downhole NMR, irreducible fluid saturations from NMR core measurements were used to calculate a T2 cutoff. The Coates permeability model is refined using core measured values by converting the equation into graphical form to solve for C (Figure 3).

Desiccation is assessed by comparing the water-filled porosity against clay-bound water. Water-filled porosity is simply the total porosity times the water saturation, whether that be modelled or measured. This presentation focuses on the clay-bound water, where we present two main methodologies for deriving that fraction. The first is calculated from XRD/XRF analysis, using detailed clay speciation's, which represents the theoretical amount of water that clays require to be in equilibrium. The second method is by utilizing the core calibrated NMR clay-bound water.

When compared to the physical water existing in the pore system – i.e. water-filled porosity – if that is less than the calculated clay-bound water, this means the clays are dehydrated, moreover the smaller the number, the more dehydrated the clays have become. Conversely, if the water-filled porosity is greater than the clay-bound water, this means the clays are fully hydrated and there is the potential for water to exist in the capillary-bound and free/mobile portions of the pore system. Comparison of the two desiccation curves, XRF/XRD vs. NMR clay-bound water, shows strong agreement (Figure 4).

## Results and discussion

Wireline NMR porosity increased by an average of 0.4 pu when hydrogen index corrected for bulk volume oil and water. NMR T2 clay-bound water cutoff was slightly adjusted from 3.3 ms to 3.0 ms. T2 cutoff defining bound vs free fluid was determined to change from 92ms to 21.3 ms increasing the free fluid present in the reservoir. The Coates coefficient C changed from 10 to 18.2 which resulted in refinement of the NMR permeability model.

With any logging suite, NMR logs come with their own set of limitations. Particularly the shallow depth of investigation of the wireline NMR tool complicates interpretation in areas of washout or badhole. Furthermore, resolution of the NMR logs are limited by logging speed and do not achieve the same resolution of the traditional quad combo logging suite.

## Conclusions

Correction of NMR porosity for hydrogen index and refinement of T2 cutoffs can be achieved through core calibration to maximize the value of the NMR logs. When core calibrated NMR wireline logs are integrated with standard petrophysical models, it can help guide optimization of the most perspective reservoir targets (Figure 5). Finally, in the absence of core, NMR clay-bound water is a good substitute for XRF clay-bound water inputs into calculating desiccation curves and delineating where the water exists in the reservoir.

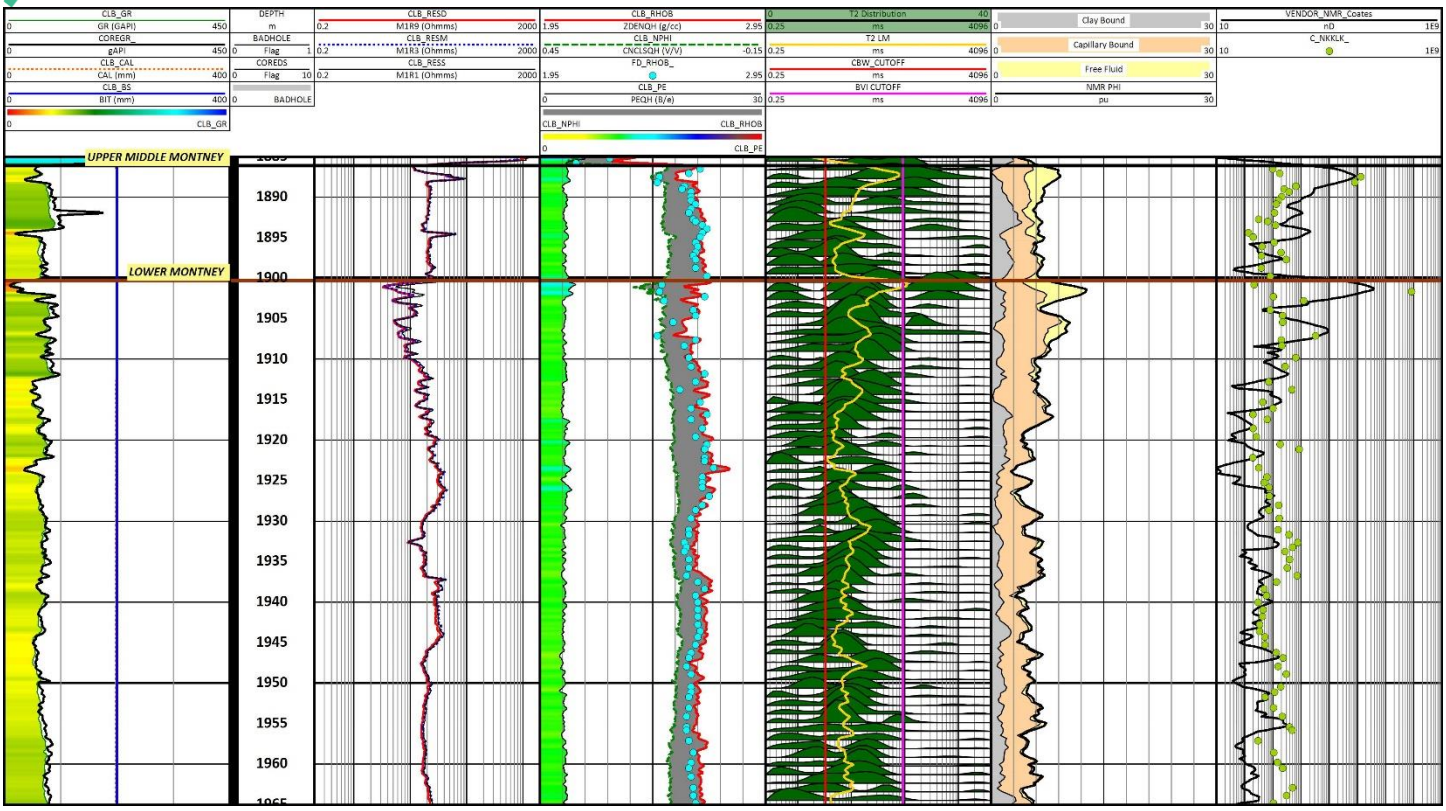


Figure 1

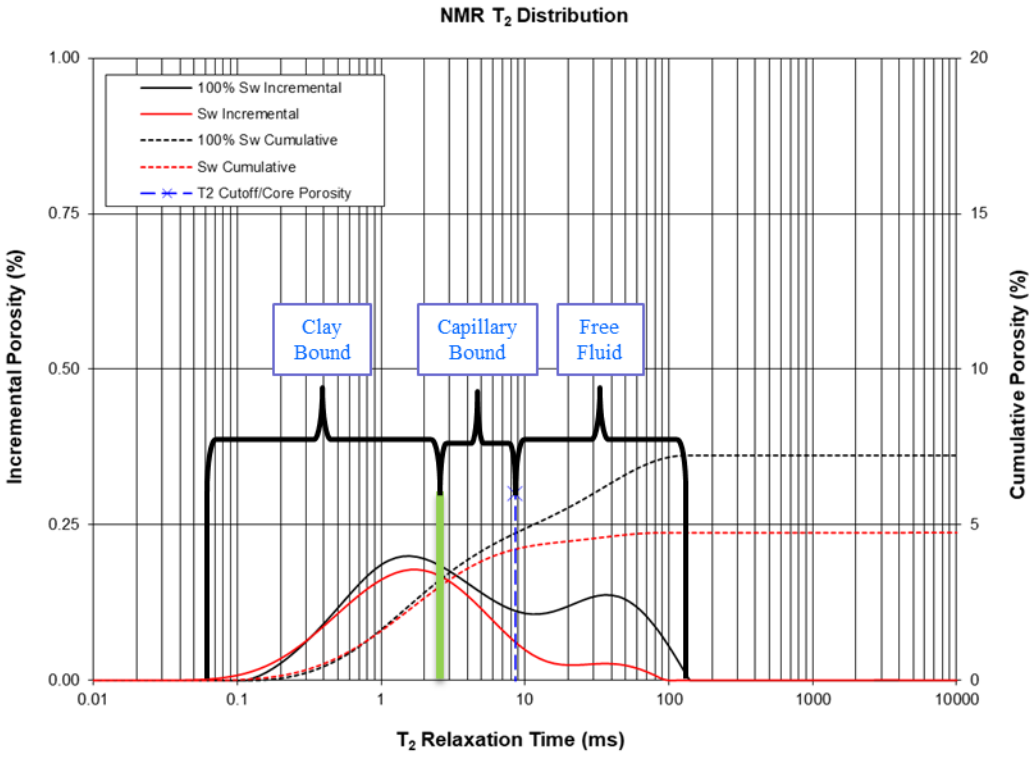


Figure 2

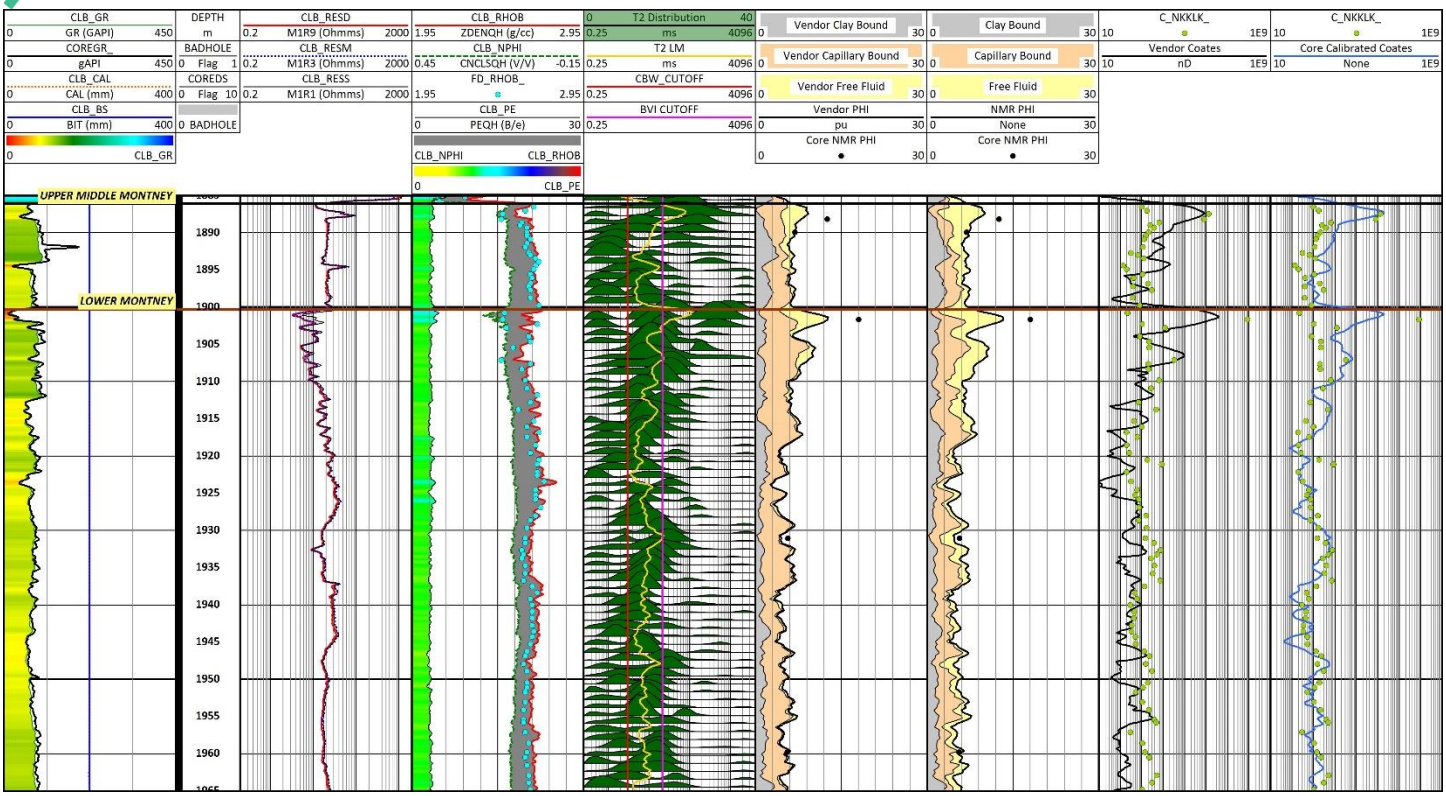


Figure 3

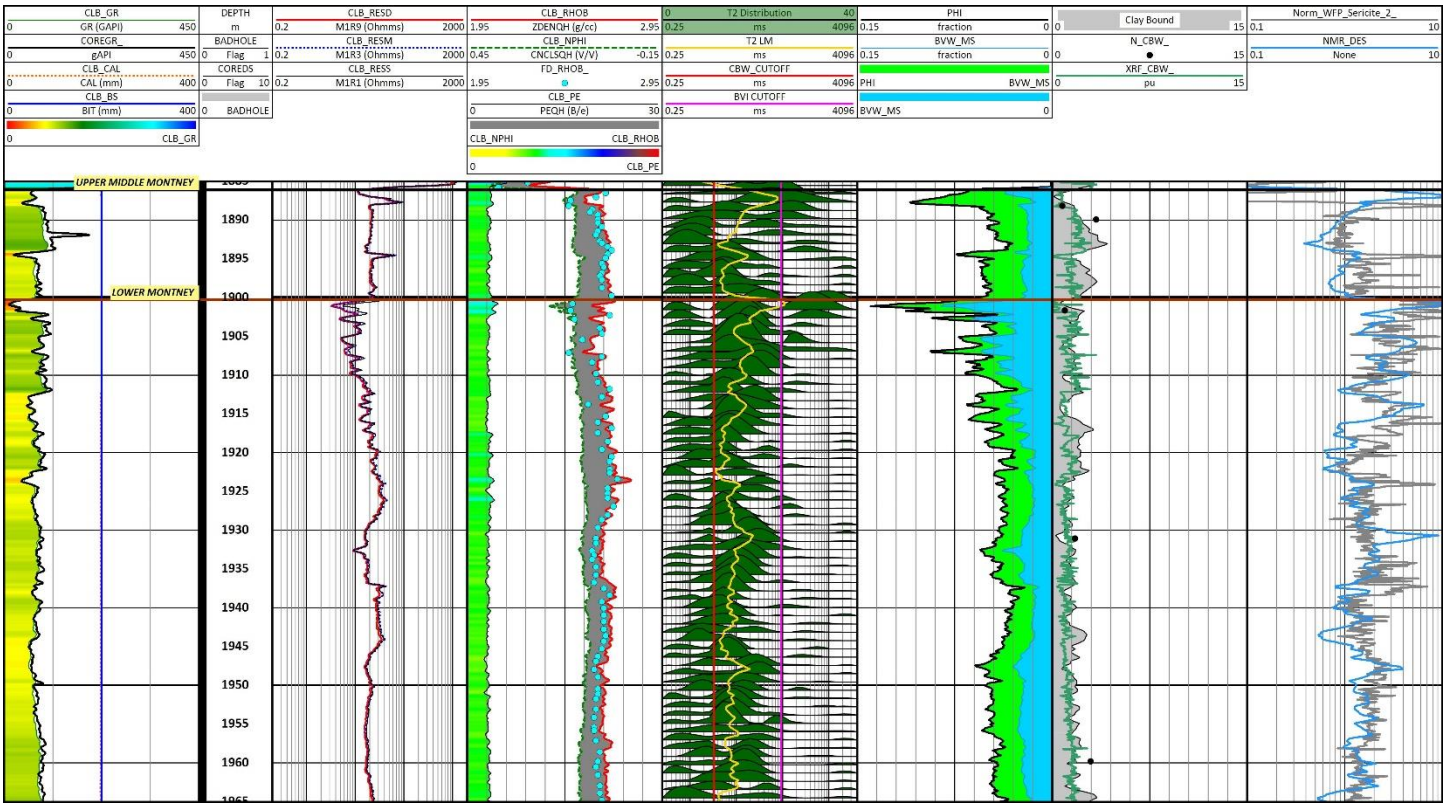


Figure 4

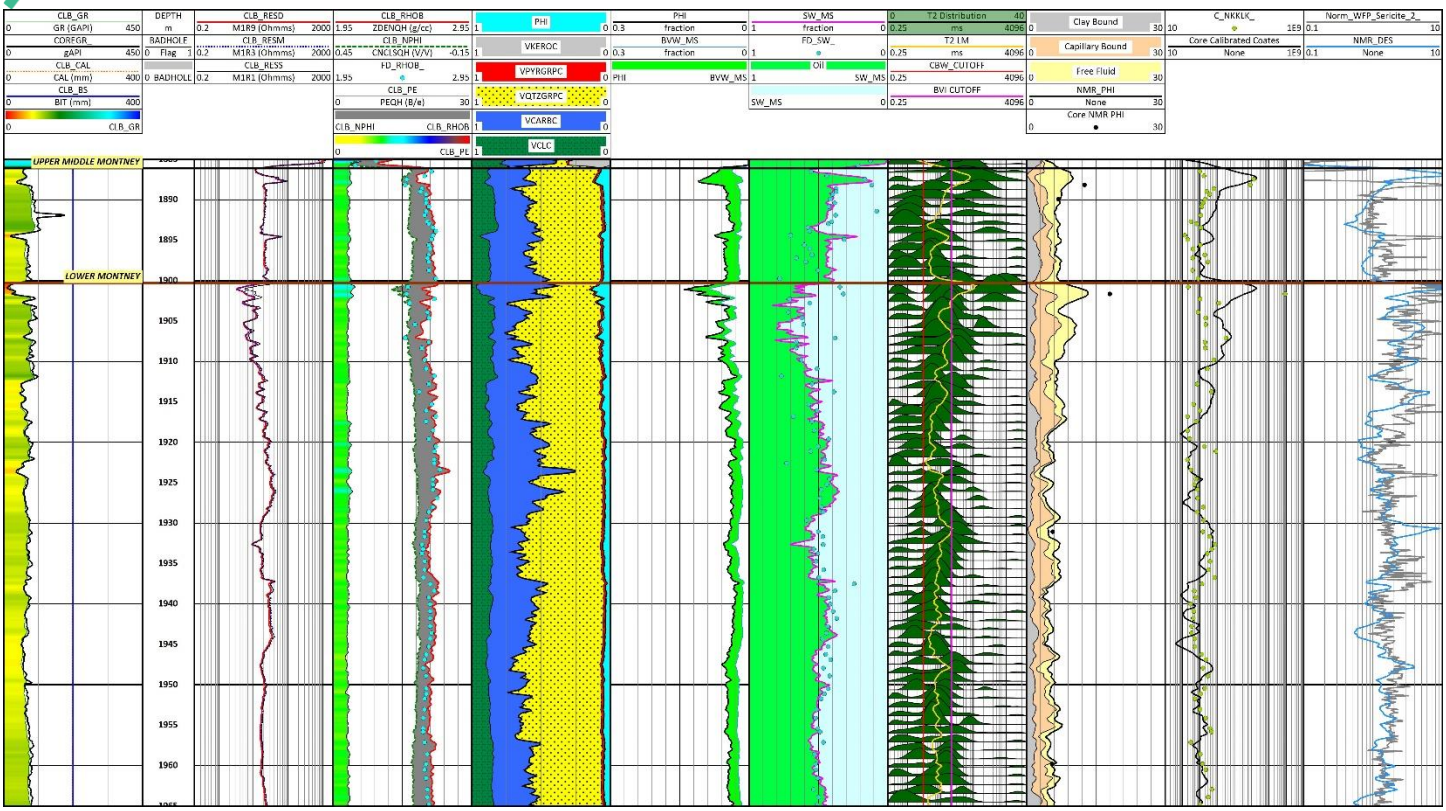


Figure 5

**References**

Appel, Matthias. Nuclear magnetic resonance and formation porosity. PETROPHYSICS-HOUSTON- 45, no. 3 (2004): 296-307.

NEB. Energy Briefing Note: The Ultimate Potential for Unconventional Petroleum from the Montney Formation of British Columbia and Alberta. November 2013. Available at: www.cer-rec.gc.ca.

GUSSOW 2024
Montney Subsurface Evaluation: Drive Towards Excellence
Banff, AB | October 2-4

# Developing a regional Montney mineral model solution and applications for well placement optimization: A case study from NEBC

Claire Woods[1], Patricia Rodrigues[2]

1. PETRONAS Energy Canada Ltd. 2. SeisPetro Geoconsulting, LLC

## Abstract

This study focuses on developing and applying a regional Montney mineral model solution to optimize target placement and understand production results in Northeastern British Columbia (NEBC). It details the model's calibration process, the inputs used, the minerals and fluid volumes solved, and addresses data limitations with recommendations for optimal calibration. The model specifically examines the role of calcite in production performance and identifies beneficial mineral associations. Using an AI-enabled multimineral software tool combined with petrophysical expertise significantly reduced the time required compared to traditional methods. Calibration utilized Elemental Capture Spectroscopy (ECS) logs and core data from ten wells, blind tested on five wells, and applied to 268 wells in the region. Uncertainty maps and curves were created to assess data reliability, factoring in proximity to logs and core samples, log normalization, and model non-uniqueness. These tools help flag areas of varying confidence levels, aiding the asset team in their workflow. The mineral model results are now routinely used by the asset team to refine landing zones and guide well placement decisions. A case study in NEBC demonstrates how the model improves reservoir characterization and optimizes well placement, enhancing hydrocarbon recovery and maximizing economic returns in the Montney play.

## Statement of the background

The mineral modelling work was undertaken in an effort to explain lower than expected production results in the Middle Montey. Core analysis and advanced petrophysical logs supported a negative correlation between increased calcite volume and lower EUR. Data coverage was limited to 20 control points across the study area, a regional mineral model was proposed to characterize mineral variability away from core and advanced log control.

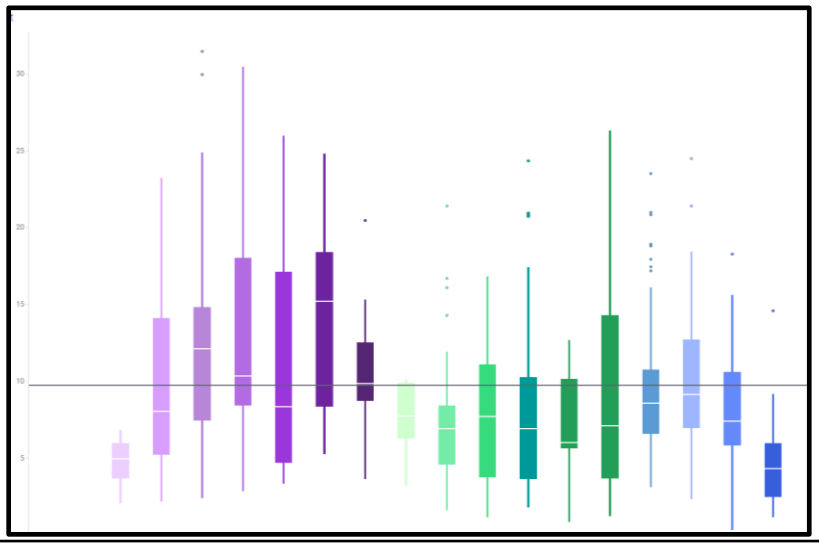

Figure 1 shows EUR against interval, the Middle Montney is shown in Green. EUR was lower than expected.

## Aims and Objectives

The aim was to better understand the regional variation in mineral volumes and the relationship to production, providing geologists with a tool to optimize landing zones. Standard petrophysical analysis of porosity and water saturation did not provide sufficient information to refine landing zone selection.

## Materials and methods

The area of interest counts with 268 wells with modern logs Gamma Ray (GR), density (RHOB), neutron (NPHI), photoelectric factor (PEF), and resistivity (RT). Ten of those wells count with Electron Capture Spectroscopy (ECS) logs which were inverted for mineralogy and calibrated using XRD results from four wells.

*Semi-automated log normalization and corrections*
Before the multimineral analysis was performed, a semi-automated log normalization was done to remove non-geologic features due to different vintages, drilling environment, and different logging companies. Due to drilling with heavy muds, the photoelectric factor required significant corrections to be used in the analysis. The photoelectric factor is a critical log when different carbonates (dolomite and calcite) are present and required to be solved for. Figures 2(a) and 2(b) show and example of the normalization process done to correct the PEF logs (2(a) before and 1(b)after).

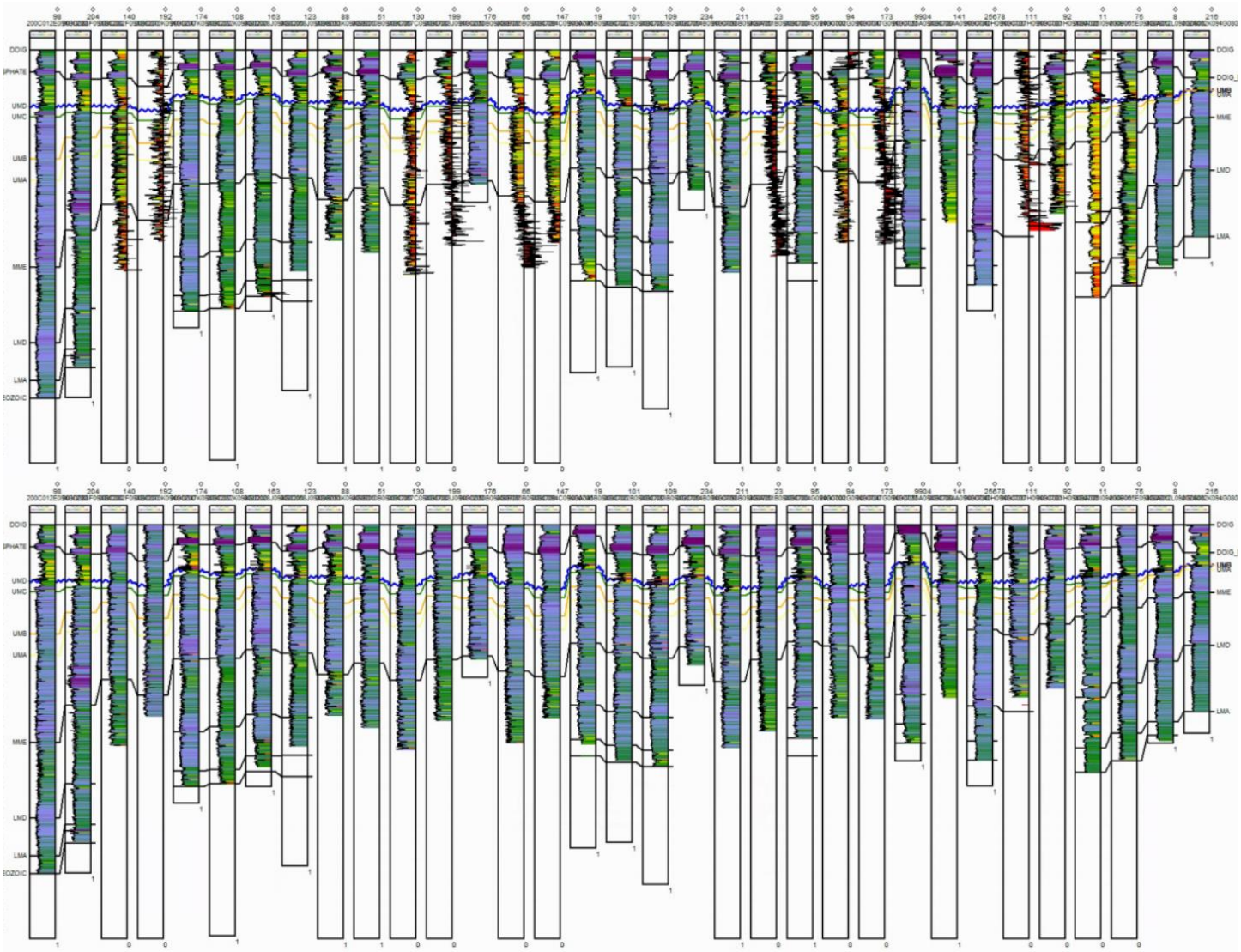

Figure 2 (a) before and (b) after

*Multimineral Analysis*

The complex mineralogy composition of the Montney formation, coupled with the limited number of logs in most wells, necessitates solving of mineral mixtures rather than individual minerals. Solving for mineral mixtures requires extensive refinement of mineral endpoints. To facilitate this process, the mineral model was developed utilizing an AI-enabled multimineral software tool that uses a genetic algorithm engineered to estimate minerology and fluid compositions in complex reservoirs (Michelena et.al. 2020).

Typical multimineral analysis requires the user to input the log properties (end-points) for each of the pure components of the rock. In complex reservoirs this task becomes difficult as there are many minerals present. In the area of the study, X-ray diffraction data (XRD) and total organic carbon analysis (TOC) of the Montney formation indicated the presence of at least twelve minerals (quartz, K-feldspar, plagioclase, calcite, dolomite, siderite, apatite, pyrite, chlorite, Illite, kaolinite, and kerogen). Calibration was achieved using results from Elemental Capture Spectroscopy (NEXT) logs and core data in ten wells, blind tested on five wells and applied to 268 wells in the area.

While the Elemental Capture Spectroscopy (NEXT) tool solves for mineral and kerogen components of the rock, its application was limited due to the small number of wells with this data. These wells were used for calibration points for the mineral model, enabling a robust regional multimineral solution.

The initial step involved analyzing the XRD data to determine which rock components to solve for based on their abundance and the project's objectives. Preliminary observations indicated that increased calcite volume was associated with lower EURs and impacted geomechanical behavior during completion. Given these relationships it was critical to solve explicitly for calcite in the mineral solution. Due to the high variability, quartz and dolomite were also important parts of the solution, similarly with clays and kerogen. The primary focus of the model was to predict the amount of calcite in the rock.

Although the remaining minerals were not explicitly solved for, they must be included within other minerals (as mineral mixes) because their presence affects the logs and needs to be accounted for. To achieve this, XRD analysis was conducted, and the relationships between minerals were corroborated to create mineral mixes. Figure 3(a) shows the relationship between quartz and total feldspars for one calibration well, while Figure 3(b) illustrates the relationship between clays and pyrite.

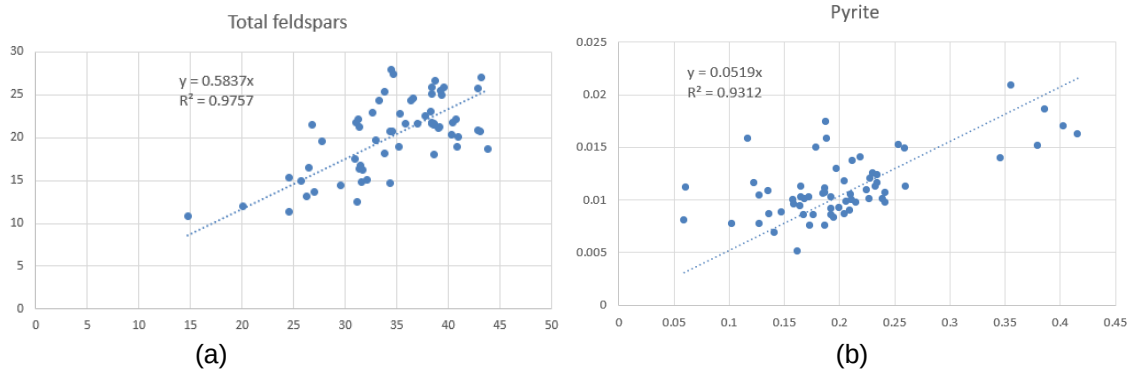


(a) (b)

Figure 3

Many combinations of minerals were explored and together with modeling observations the final rock components solved for were: QFMs (quartz, felsdspars, and mica), dolomite (which is mixed with other heavy components like siderite), clays and others (Illite, kaolinite, and pyrite), calcite, and kerogen. Reducing the problem to five rock components and two fluids (seven components in total). However, the number of logs available is five plus the unity equation we get six equations, therefore we require an additional restriction or log to be able to solve the problem. The preliminary work done in the area using a deterministic approach to predict porosity and kerogen showed a very good correlation with core data, so after several test we decided to incorporate the porosity from deterministic methods to add an equation to the solution.

The second step is to decide if/how to split the Montney formation. Based on the iMineralysis optimization results, the Montney formation was split into three subintervals for modeling purposes (Upper, middle and lower Montney).

The third step is to find adequate end-points for the new rock components. As explained above, since we are mixing some of the minerals, the default properties reported in the software are not adequate. iMineralysis® allows to set limits to the rock component properties to be used by the genetic algorithm as it searches for a solution. The software tests hundreds of combinations of endpoints within the specified user defined ranges. Petrophysical and regional knowledge were essential to define these ranges. This application of AI and petrophysical expertise significantly decreased the time required to

complete the study compared to a classical mineral modeling approach. Figure 4 shows the comparison of the mineral models from ECS vs multimineral analysis.

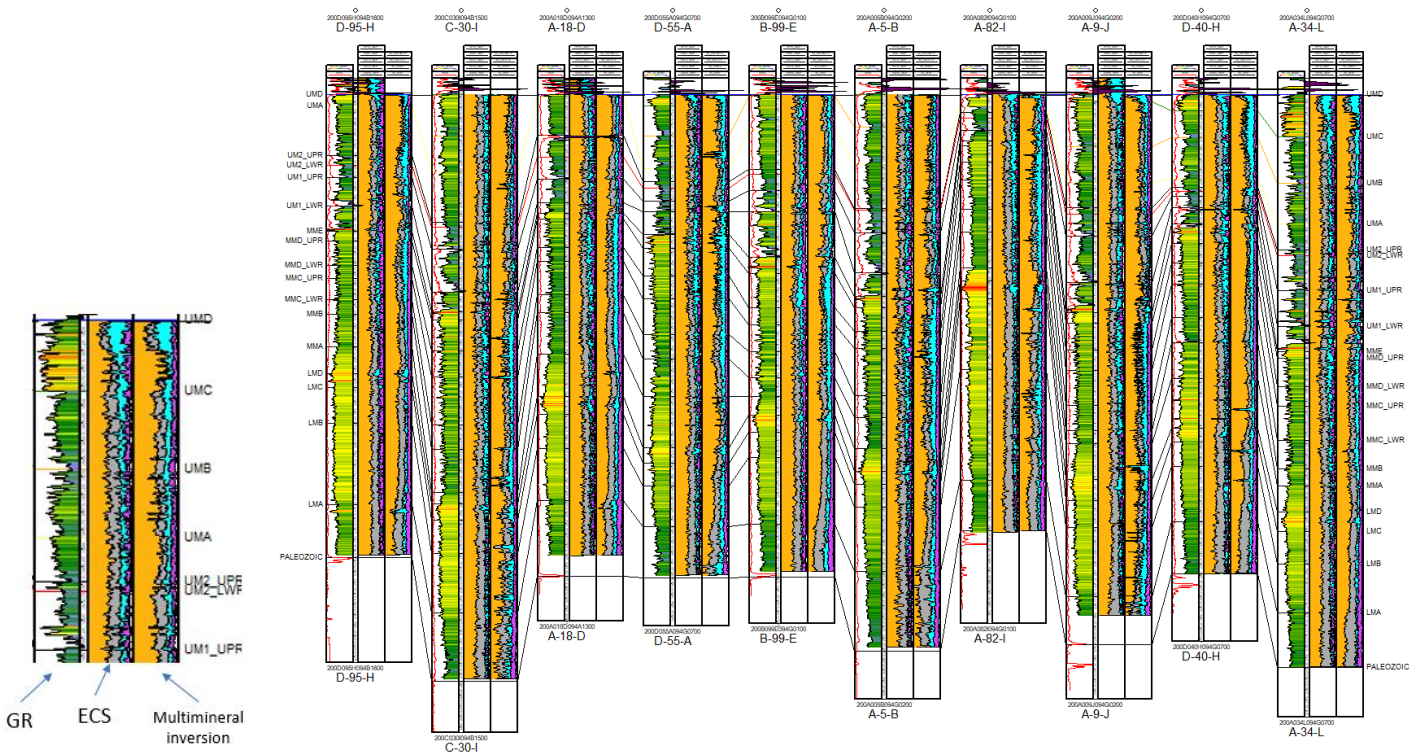


Figure 4

The fourth step was to determine a water saturation model for the area that statistically matched the water saturation measurements from core. For this area we used a modified Archie's model with m and n equal to 1.8 and salinity of 140 Kppm. We used a fixed temperature gradient model with depth to calculate water resistivity (Rw) from salinity.

The fifth and final step was to generate uncertainty maps and curves were generated, taking into account various factors such as proximity to well logs, proximity to calibration wells, degree of log normalization, and the inherent non-uniqueness of the multimineral model. The maps were constructed to evaluate the reliability of the mapped data across the area. The curves were created to flag areas of high, medium, and low confidence to complement the asset team workflow.

1) Proximity to calibration wells: distance to wells with core and/or ECS logs.
2) Level of log normalization: percent normalization of all logs with respect to the original log data. A global indicator was estimated using the average for all logs.
3) Inherent non-uniqueness of the multimineral model: end-points are calculated using five different seeds for the genetic algorithm and average and standard deviation of the realizations is estimated for each mineral output.

## Results and discussion

Mineral modelling results were generated in approximately 270 wells, producing regional mineral control across the study area. The results are now standard in the geologist tool kit for landing zone selection. Landing zones are selected on the basis in part on their mineral composition, well results have improved with targeted zone selection and geosteering to remain in zone. Full integration of the data is still ongoing and results to date show correlation between mineral composition and EUR. Initial results show the highest EUR wells correlate to highest QFM and lowest Calcite.

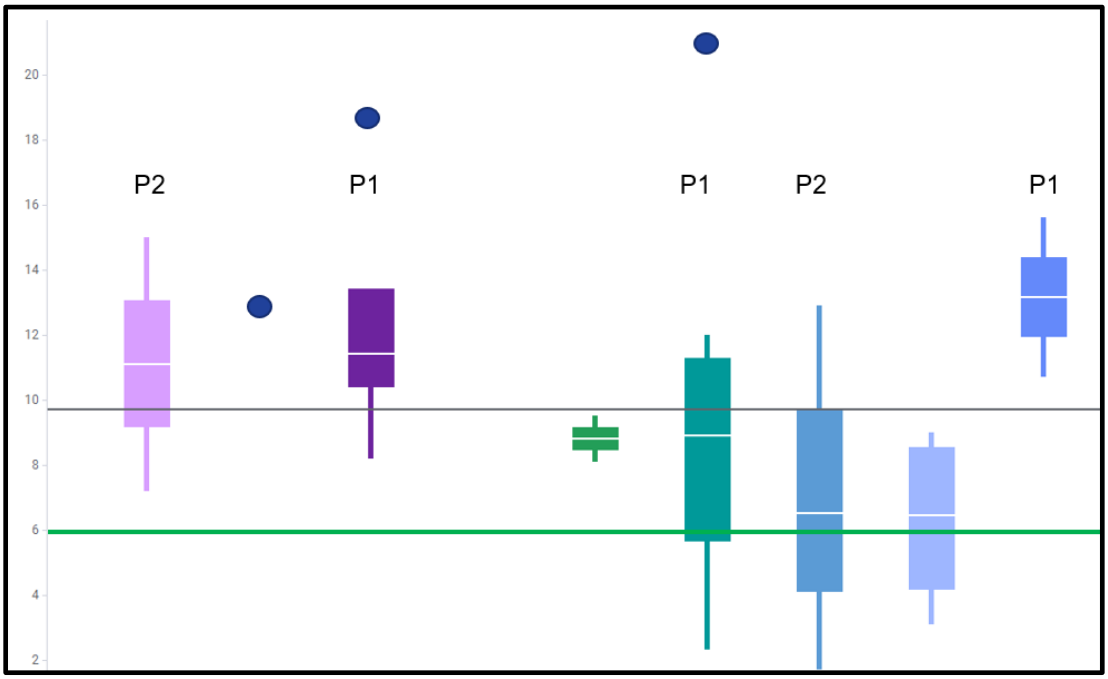


Figure 5 identifies 3 primary and 2 secondary targets within the area which correlate to low calcite and high QFM volumes.

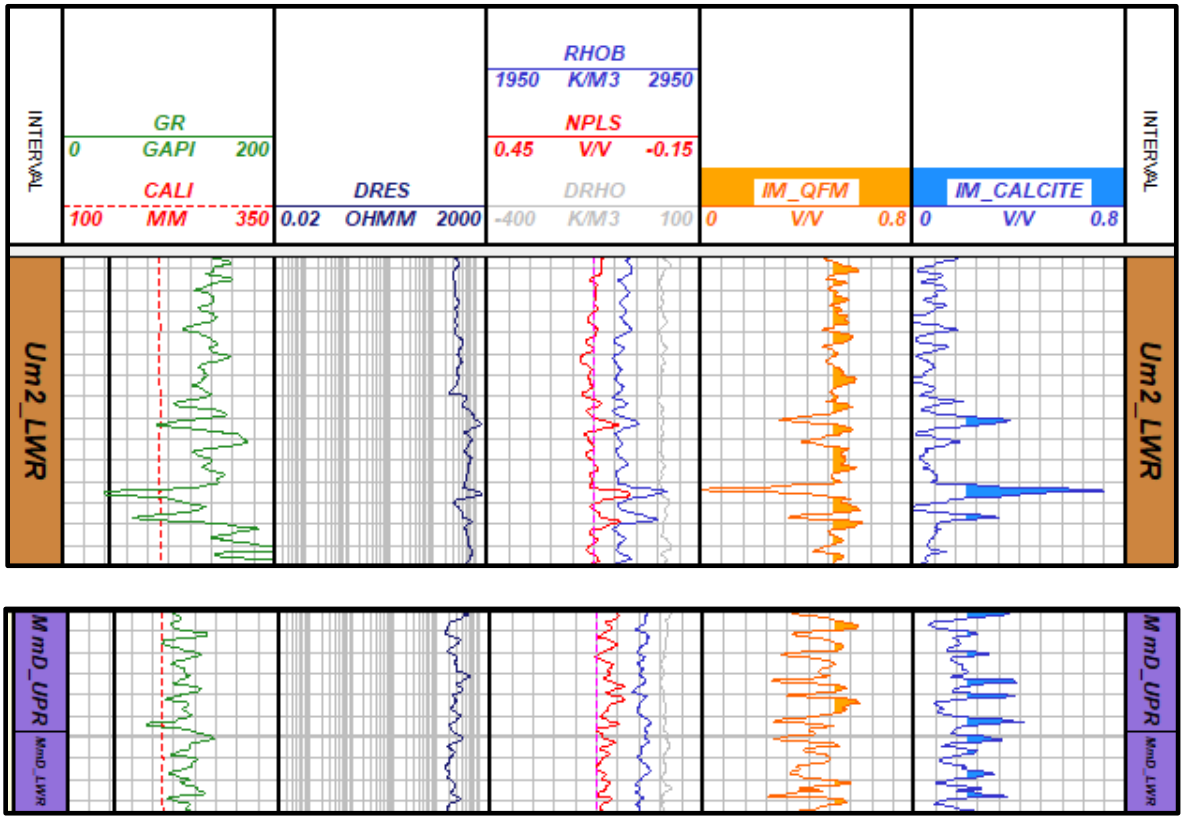


Figure 6. Primary targets have the highest EUR or lowest variability within their interval. Below is an example of a P1, high QFM low calcite log signature contrasted with a lower EUR interval with lower QFM and higher calcite.

Uncertainty results

Figure 7 (a), (b) and (c) shows the results of the three components of uncertainty studied (a) normalized distance to calibration wells, (b) degree of normalization of input logs and (c) average standard deviation of the minerals in the mineral model. In Figure Y, we show two possible combinations of the uncertainty maps to determine a global uncertainty map for the area. Figure Y (a) shows an equal weight combination and figure Y(b) shows 10% weight to the distance, 40% to normalization and 50% weight for the mineral model. These maps helped identify which areas have larger uncertainties in the model.

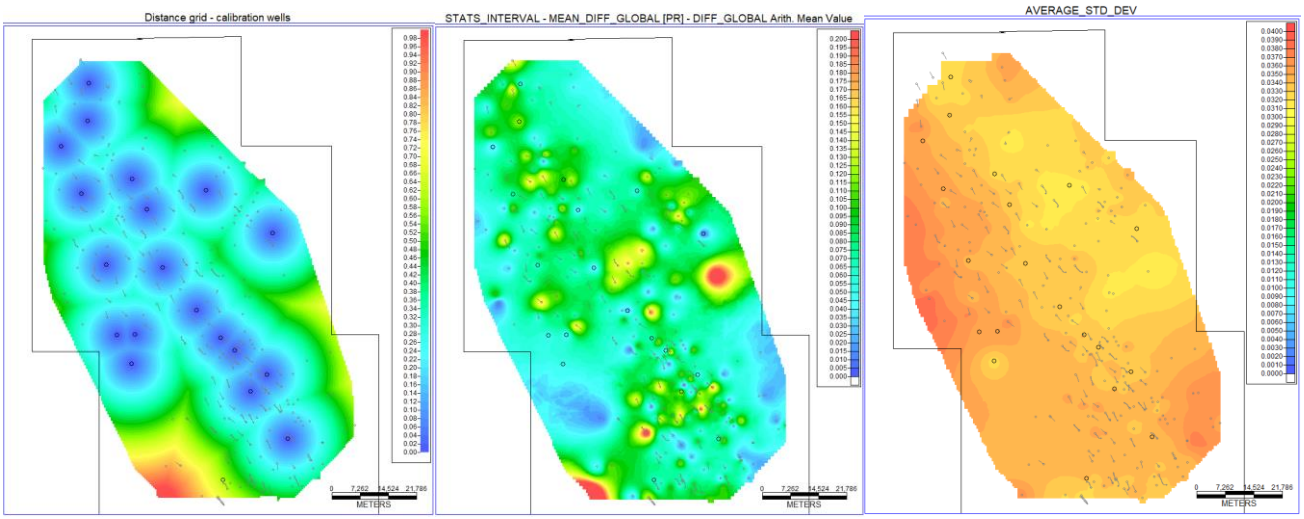


Figure 7 (a) Normalized distance to calibration wells (b) Degree of normalization (c) Average standard deviation

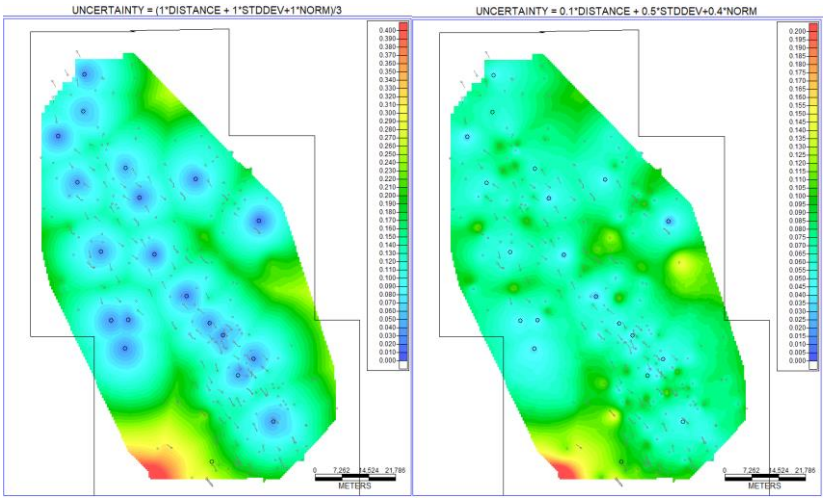


Figure 7 (a) Uncertainty = 1/3*Distance+1/3*norm+1/3*StdDev (b) Uncertainty = 0.1*Distance+0.4*norm +0.5*StdDev

## Conclusions

The work achieved the initial objective of modeling the regional variation in calcite and offered valuable insights into other mineral components impacting well success.This methodology enabled rapid evaluation and calibration, resulting in a model applied to approximately 270 wells within the study area. The results provided control for mapping, Although integration of the results is still ongoing, the results have already proven valuable for geoscientists in optimizing landing zones and better understanding EUR. Future efforts will incorporate geomechanical modeling to further enhance the geoscience toolkit

## References

Reinaldo J. Michelena; Kevin S. Godbey; Michael J. Uland; Patricia E. Rodrigues. Petrophysical multimineral analysis using genetic optimization to solve complex mineral composition in unconventional reservoirs. SEG International Exposition and Annual Meeting, Virtual, October 2020. SEG-2020-3425

GUSSOW 2024
Montney Subsurface Evaluation: Drive Towards Excellence
Banff, AB | October 2-4

# Machine Learning Application in Montney Petrophysics

Ramin Zamani

ConocoPhillips

## Abstract

Montney is an aerially extensive (130,000 Km2) lower Triassic formation with a thickness between 100m to 300m. Montney formation is predominantly fine to coarse grained siltstone. Since its beginning in 2005, unconventional development of the Montney formation has become the largest contributor to natural gas production in British Columbia (BC). Montney formation represents 93.2 per cent (81.4 Tcf) of BC's remaining raw gas reserves [1].

The focus of this study is on Petrophysical evaluation of the Montney formation in NE BC. A general approach to unconventional resource play Petrophysical evaluation is to calculate TOC and derive kerogen percentage. Pore space is divided into organic and inorganic, starting with an estimation on mineralogy the porosity and saturations are calculated. Some aspects of this approach and its application have been studied by researchers [2]. This general approach is more accurate where more advanced log data such as NMR or Neutron Spectroscopy are available in addition to standard logging suites. In the absence of advanced logs some approximations and assumptions are needed to build a Petrophysical model. These assumptions increase the uncertainty of calculated Petrophysical properties. There is an obvious tradeoff where selecting more types of log data in analysis reduces the number of available wells in any given area of interest (AOI). An alternative Petrophysical interpretation workflow based on Machine Learning (ML) is used in this work, to calculate the end products (porosity and saturation) directly from input raw log data and without intermediary steps or having to solve a complex mineralogy framework first.

Machine ~~L~~earning is a powerful tool that has been used in Energy and other industries to solve challenging problems. In this work we demonstrate how ML techniques can be used as an alternative approach to provide a Petrophysical model for reservoir characterization. In the case of Montney formation, it is shown a careful application of ML practices can lead to a much more representative Petrophysical model compared to deterministic and/or multi mineral methods when analyzing large group of wells with only a basic suite of logs available.

This study goes through a step-by-step approach to build an ML model for Montney Formation. The work begins with log and core data collection, preparation, and exploration. Harmonizing sampling rate is performed and considering the physics of each measurement, data is selected and validated. Bad data is either flagged and removed or corrected where possible. Non log, categorical data is introduced as an input to the model followed by selection and implementation of these data. A ML process for semi supervised electrofacies is built and is added to environmentally corrected logs. Finally, the main ML model pipeline is built, and hyper parameters are optimized. Model validation is performed, and limitations are explored. Model performance metrics are shown, and overfitting and generalization are discussed.

At the end a comparison is made between performances of a deterministic and ML Petrophysical model. Out of sample tests are shown.

## Statement of the background

Challenges to Petrophysical evaluation of Montney formation and other unconventional plays can be broadly categorized into the following:

1) Organic matter effect. In Montney formation, organic carbon can be found in kerogen and bitumen in addition to fluids in pores space. These additional sources of Carbon affect the logging tool responses that need to be accounted for.
2) Petrophysical models. Montney rock formations are more complex than conventional reservoirs and the Petrophysical models required to describe Montney have more components to solve for. In order to solve for a model with more components, some advanced logging measurements such as geochemical or NMR logs are needed in addition to the basic suite of logs. In the absence of said advanced logs, unconventional models become undetermined in a sense of not having a unique solution (fig 1).
3) The limitations of different core analysis methods. The core analysis methods can be broadly divided into whole rock and crushed rock analysis. Some methods are standardized while many innovative methods have been tried by various labs and operating companies. The lack of a single standard method presents a challenge to integrate core analysis from different sources with log responses.

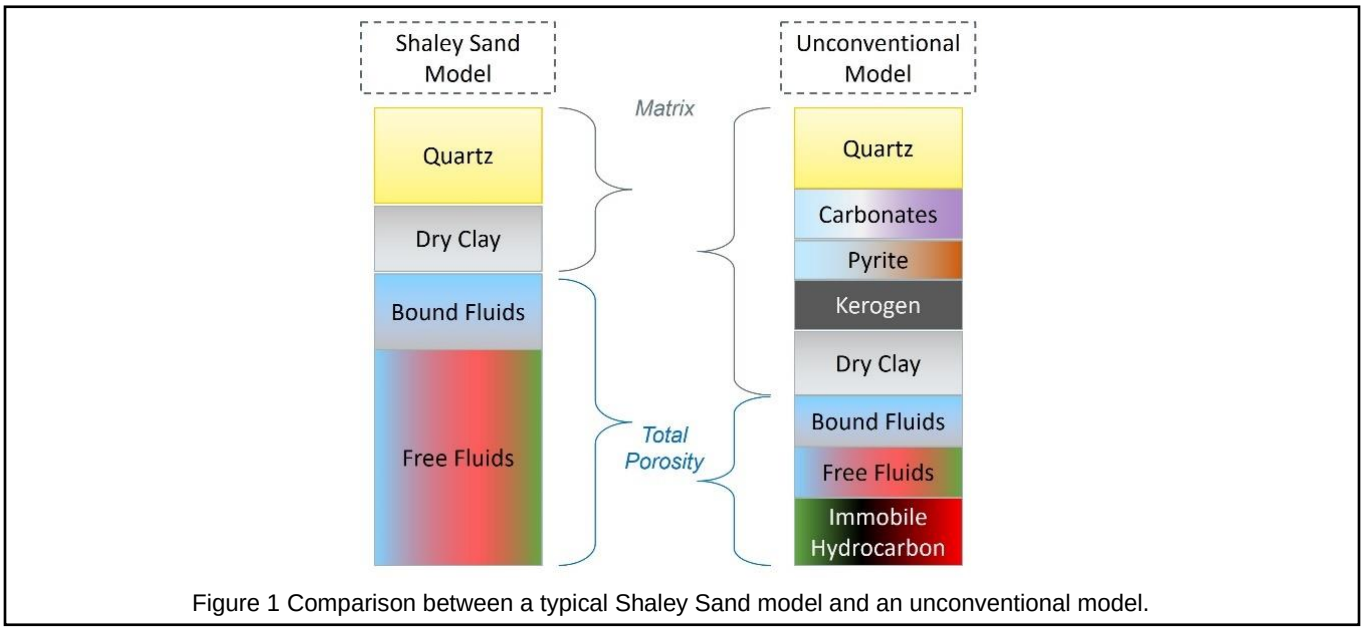


Figure 1 Comparison between a typical Shaley Sand model and an unconventional model.

4) Heterogeneity and its effect on log to core calibration efforts. There is a significant difference between the volume of rock measured by logging tools and core analysis. For example, a LECO carbon analyzer for TOC determination needs only 100 milligram of sample which is about 0.038 cm3 in volume whereas a typical wireline density tool measures about 2,000 cm3 of rock depending on rock type and assuming maximum depth of detection of 10 cm [3]. It is easy to understand the degree of difficulty calibrating a log calculated TOC to core measurement where variability of TOC within the volume of investigation by logging tool is high.

One practical solution to address the complexity of unconventional reservoirs in Petrophysical analysis is the use of a key-well concept [4]. The key-well(s) are wells with rather comprehensive log and core data sets. The idea is to make a thorough analysis on key-wells and apply the parameters and correlations to a development area. The inherent risk associated with this approach is not having the whole area of interest sampled thus treating a variable parameter as a constant and propagating computational errors with unknown consequences throughout the AOI.

This ML study is designed to address the above-mentioned problem of a key-well approach. Application of ML methods to Montney formation evaluation can reduce impact of the above-mentioned challenges (1) and (2) but cannot help much with challenges (3) and (4).

Another problem with deterministic models is the issue of solution stability. For example, in many deterministic workflows, the formation water saturation (Sw) can become erratic in very low porosities. One common workaround is to use a set of constraints to force Sw to a set value once a threshold of porosity is passed. Once applied to many wells, these hard coded constraints make the property distribution unrealistic and difficult to work with (fig 2).

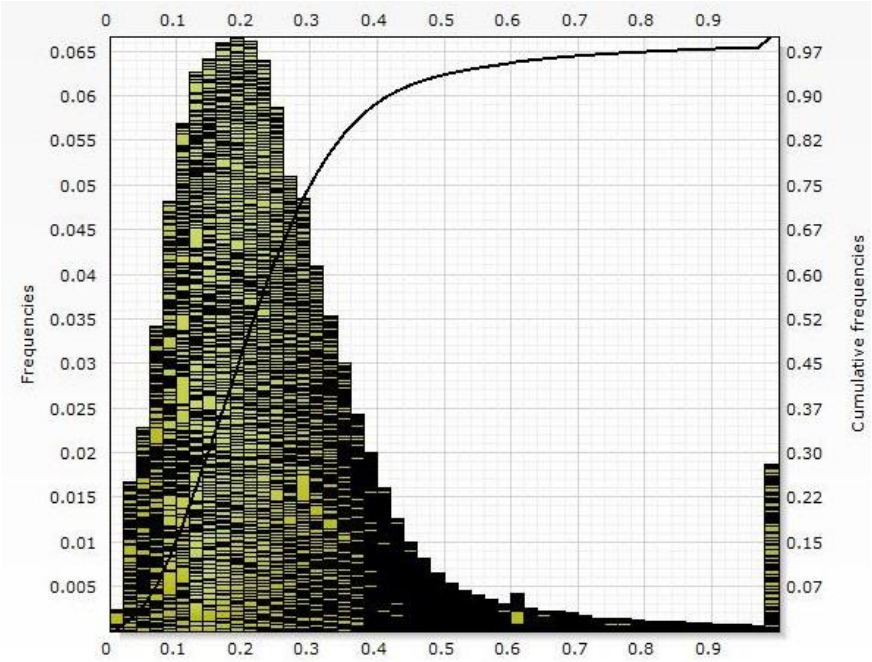


Figure 2 An example of deterministic Sw model generating an unrealistic distribution near the far end of the Sw scale.

## Aims and Objectives

The aim of this study is to capture as much rock variability as possible for Montney formation evaluation while avoiding the need for complex models through the use of ML techniques. The specific goal of this formation evaluation is to calculate basic rock properties like porosity and water saturation needed as input to Geo models over a defined AOI without having a need to solve for some intermediary variables such as detailed mineralogy.
This study demonstrates the use of feature engineering as a tool to enhance ML models' performance and apply natural constraints without needing to impose any hard coded scheme to keep output curve distributions within bounds.

## Materials and methods

The focus of this study is ConocoPhillips Montney acreage Northeast of province of British Columbia, Canada. The Lithology of Montney formation over the AOI is siltstone composed dominantly of Quartz/Feldspar with low clay content. Average depth of Montney formation in this area is about 1900m TVD and average thickness is around 250m. Log data from some 227 wells within the AOI were used as input to the model. Five basic logging curves selected for study are Natural Gamma Ray, Sonic Compressional Slowness, Bulk Density, Thermal Neutron Porosity and Deep Resistivity; these logs provide a total of 5 x 559,155 log sample points. Auxiliary curves such as caliper and bulk density correction are used for environmental corrections and bad hole identification. From core analyses, 2944 core porosity sample measurements, and 2703 core Sw measurements were used. The relatively large amount of data made ML techniques practical for this study.

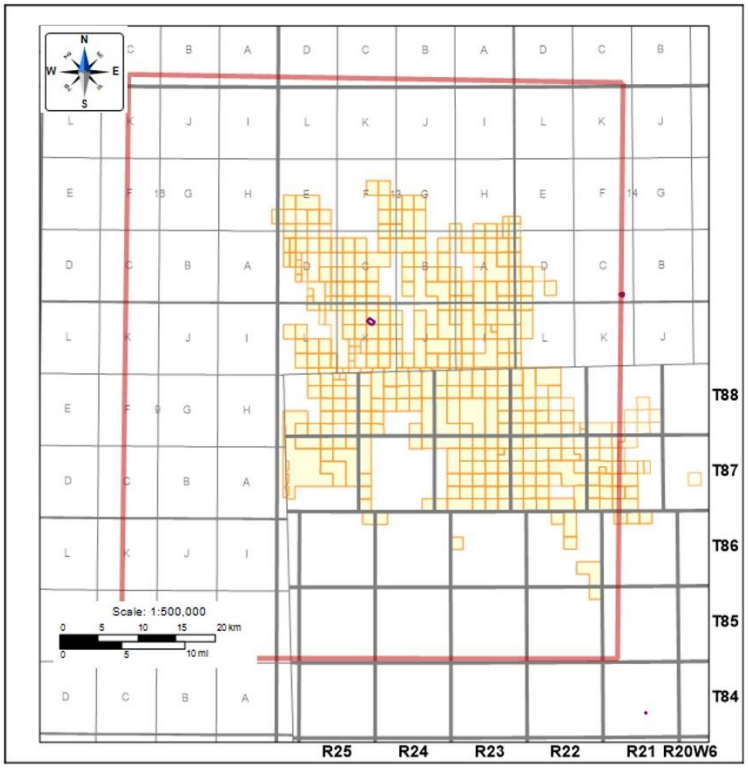


Figure 3 Study area of interest (AOI).

## Results and discussion

In general, the ConocoPhillips Montney AOI study shows a ML approach to Montney Petrophysical evaluation provides better results in comparison to deterministic methods in both matching the core analyses and capturing the variability correctly (fig 4). For this purpose, multiple deterministic and ML models were built. It is not in the scope of this abstract and presentation to cover all models but highlight the major aspects of the ML workflow and provide a comparison with competing methods.

This study found in almost all cases a decision tree type model worked better than a neural net.

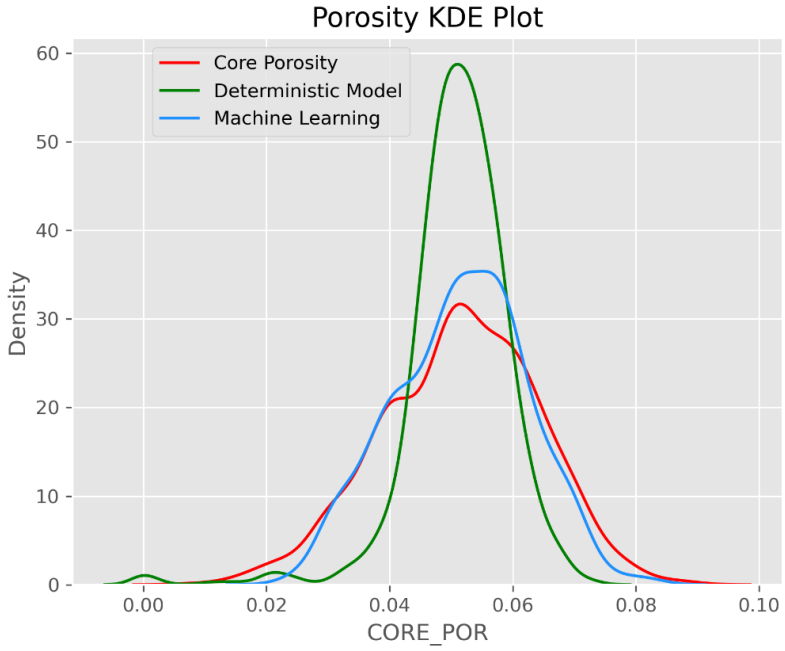


Figure 4 Kernel density plot compares Core analysis porosity distribution to modelled porosity

**Machine Learning application limitation**

One limitation of ML workflows is their ability to maintain predictability when applied to unseen data or data with input ranges different from the training set. In this context the issue of overfitting and underfitting is quite important. In building ML Petrophysical models, there is a need to ensure the right balance between Bias and Variance is achieved [5]. In this study we use k-fold cross validation for most ML models to reduce the possibility of over fitting. There are other options available to Petrophysicists and there is no suggestion here that k-fold cross validation is the most suitable but simply emphasizing the issue of overfitting needs to be considered in ML pipeline construct. In addition to built-in steps, a test case was built with data far away from the study AOI. For this test case a preserved porosity model was applied to different wells in the test area far away from the AOI. The result was a good match showing the ML porosity has retained some predictive ability away from the AOI and therefore has not been over fitted. The distance between the centre of the study AOI and the test well shown in figure 5 is about 90 Km to the South.

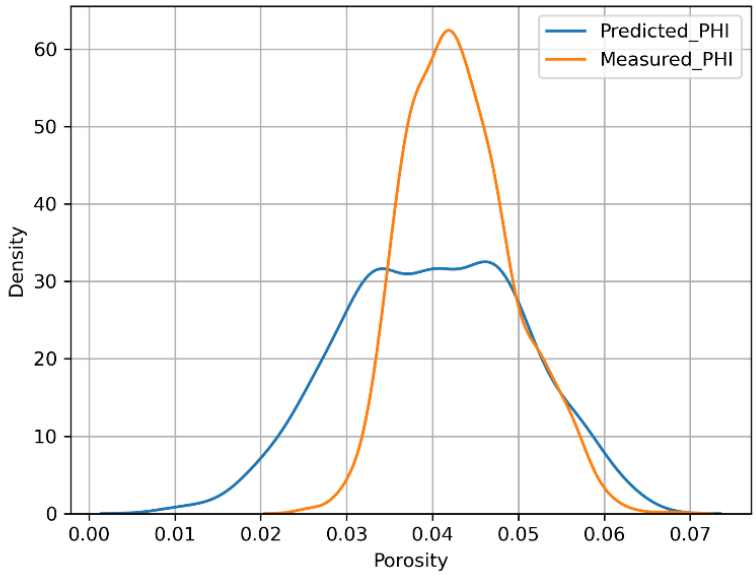


Figure 5 Machine Learning Porosity applied to a test case 90 Km from the AOI compared to measured porosity

## Conclusions

The new era of digital transformation has already made a significant impact on various industries and the Energy Industry's Geosciences is no exception. Machine Learning methods have a potential to make a major contribution to advancement in all aspects of the Geosciences. This study did not include dynamic or 3D data. A natural progression is to include afore mentioned types like production data or seismic data in the data model. There are also challenges to any ML application. The state of the input data is important as correcting and vetting the data remains to be a major bottleneck for ML workflows. Although there exists standardization in some data types for example LAS or DLIS for log data, the Energy Industry suffers from a lack of data standards for many other data types, for example core data. Improved application of ML techniques going forward will require more deliberate focus on data standardization across vendors and data tools.

## References

BC Energy regulator | 2022 Oil and Gas Reserves and Production Report.

Thaimar R. Ramirez, Jim D. Klein, Ron J. M. Bonnie | Comparative Study of Formation Evaluation Methods for Unconventional Shale-Gas Reservoirs: Application to the Haynesville Shale (Texas), SPE 144062

Gordon L. Moake | What is the Depth of Investigation of Open hole Nuclear Tools. SPWLA 55th Annual Logging Symposium, Abu Dhabi, United Arab Emirates, May 2014. Paper Number: SPWLA-2014-MMM

Vivian K. Bust, SPE, Azlan A. Majid, SPE, Joshua U. Oletu, SPE, and Paul F. Worthington, SPE, Gaffney, Cline & Associates | The Petrophysics of Shale Gas Reservoirs: Technical Challenges and
Pragmatic Solutions. Copyright 2011, International Petroleum Technology Conference IPTC 14631

Mikhail Belkin, Daniel Hsu, Siyuan Ma, Soumik Mandal | Reconciling modern machine-learning practice and the classical bias–variance trade-off. Proceedings of the National Academy of Sciences (PNAS) Vol. 116 | No. 32

GUSSOW 2024
Montney Subsurface Evaluation: Drive Towards Excellence
Banff, AB | October 2-4

# Gas Cycling Enhanced Oil Recovery (EOR) in Unconventional Reserves

F. Brent Thomas[1], Michael S. Piwowar[1], William M. Gibb[1], Carter D.W. Clarkson[1]

AGAT Laboratories Ltd.

## Abstract

For the last fifteen years, oil and gas production from unconventional reserves has provided the potential for energy independence in North America. For example, in 2010, oil production from the unconventional reserves of the Permian basin, in West Texas, was 600,000 Barrels of Oil per day (BOPD). In 2019, oil production from the same Permian resource was 3.6 million BOPD. Comparable unconventional contributions have occurred in Canada. Unconventional oil production has approximately quadrupled over the last fifteen years in Alberta. However, field decline rates are such that capital investment must be very significant in order to keep up with the steep decline rates. Indeed, production rates often decrease by 70% during the first year.

Gas injection EOR has been used for decades in conventional reservoirs in order to extend the production life and improve recover factor. The approach in conventional reservoirs is to continuously inject gas to establish improved interfacial tension (IFT) and mobility control and then mobilize and drive residual oil from the injection wells to the producing wells. However, in the Montney, for example, where the permeability is 4 to 5 orders of magnitude lower than conventional porous media, continuous injection of gas is impractical if not impossible. Huff and Puff gas injection, or gas cycling EOR (GCEOR), has been used in many unconventional reservoirs in the USA; benefits of GCEOR have been reported in the literature. No commercial GCEOR applications have been implemented in the Montney to date. The authors have patented laboratory procedures for testing nano-Darcy porous media for GCEOR and have run more than 70 primary depletions followed by GCEOR in porous media ranging from 10 nD to 2400 nD. Results of this testing are summarized in this paper along with lessons learned in the context of these and other questions:

1. How efficient is GCEOR relative to gas utilization?
2. Is GCEOR performance a function of degree of depletion during primary production?
3. Will GCEOR be effective for sequestration?
4. Do geological characteristics matter in GCEOR applications?
5. Does GCEOR perform better in oils than gas condensate systems?

## Background

Many researchers have modeled GCEOR in unconventionals. Hoffman et al. (1), Carlsen et al.(2), Nohavitza et al. (3), Malo et al. (4), Ganjdanesh et al. (5), Cronin et al. (6) and Sheng (7) provide examples of published work where GCEOR has been modeled mathematically. There are many unknowns and experimentation would be beneficial in order to combine fluid phase behavior with geological properties without having to assume relationships without any physical data. In order to conduct fluid displacements in nano-Darcy rock, traditional axial flow testing is not practical. The flow path is long in order to provide sufficiently large hydrocarbon pore volumes (HCPV) and the cross-sectional area is small. This combination results in experimental run times that are on the order of years. By using radial flow very large HCPV is possible with short flow path and high superficial area for flow. Moreover, since unconventional production is achieved by hydraulic fracturing it was desired to create an experimental design that would include matrix drainage into the fracture and then flow within the fracture to the well. Figure 1 shows the patented design that was developed for this work.

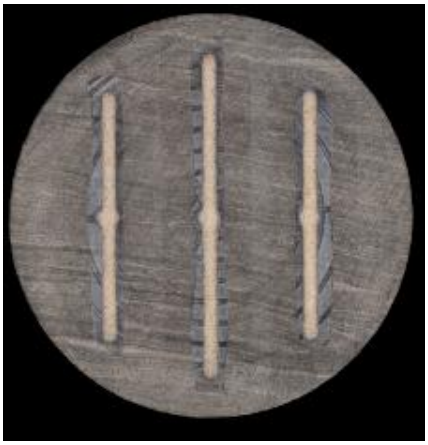

Figure 1: Cross-sectional Preparation

The photograph is of the end of a full-diameter section of Montney vertical core. The slots were created with water jet technology and then packed with 40 mesh frac sand which was the proppant used in the field completions. Even though for the photograph shown in Figure 1, there were three slots created, only one slot was used for almost all the testing in this work – a center-line slot. Similar work was also done with slabbed core as is shown in Figure 2. Slabs are aligned so that the center slot is continuous from one end to the other; with a peripheral screen, high pressure oil is injected radially into the matrix and then, with the slot pressure (frac pressure) low, flow is induced radially inward. Reversing the flow is easily accomplished by maintaining the slot pressure at injection pressure and then achieving invasion of the injection gas into the tight matrix. Thus, Huff and Puff operations are easily performed.

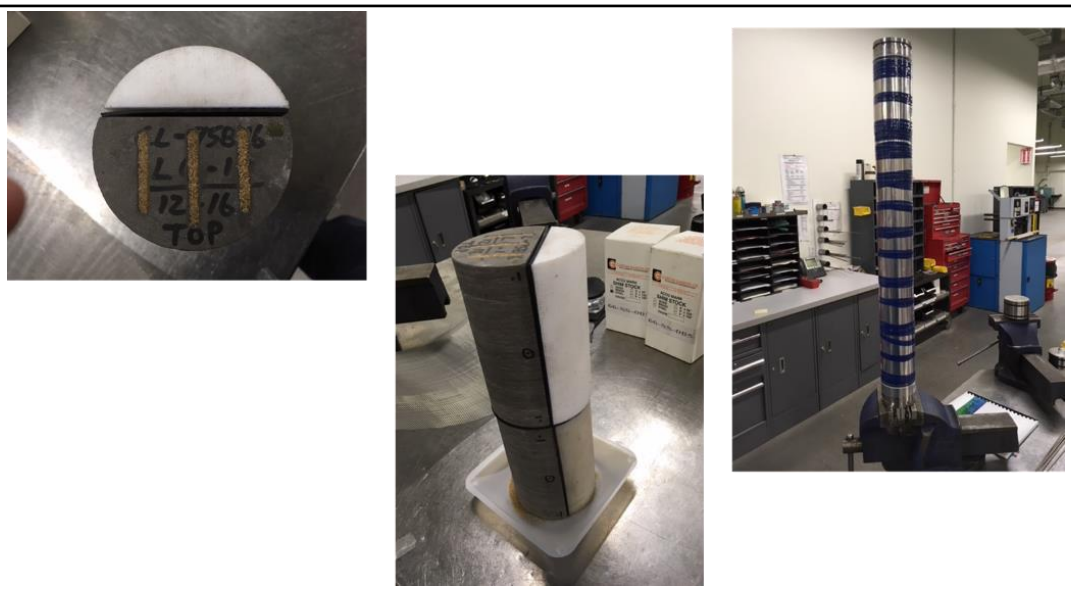


Figure 2 – Slabbed Core and Stacks created

By creating differential pressures, from the periphery into the slot (production cycle), or from the slot outward (Injection cycle), fluid flow can be induced as desired; using vertical core combined with radial flow creates flow in the direction consistent with the horizontal reservoir that describes the Montney – the Montney always exhibits stimulated rock volumes that are thin compared to areal extent. The field situation is shown in an idealized way in between hydraulic fractures. Figure 3 suggests an axis of symmetry in between the half lengths; from the axis of symmetry to the frac is what is represented from the periphery of the full-diameter core sample to the slot in the experiment. A more detailed discussion of the experiments is found in Thomas et al. (8-12).

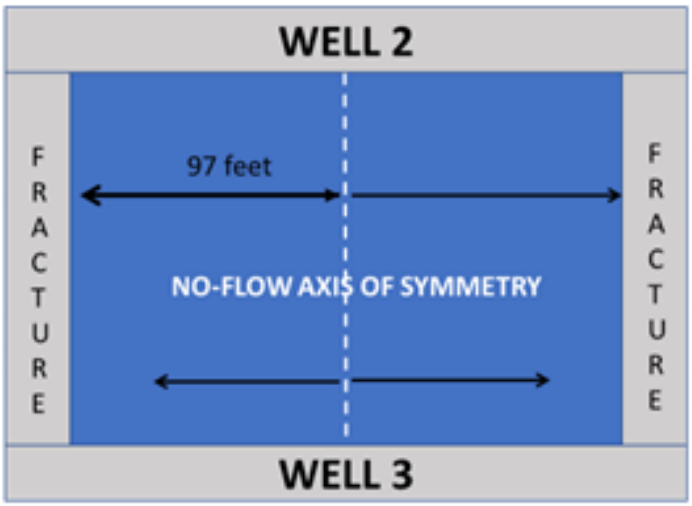


Figure 3 – Idealized Field Scenario Between Hydraulic Fracs

Implementing the reservoir pressures in the lab would be the equivalent of examining the differential pressures in the region of the matrix close to the fracs. If GCEOR is efficient in the region proximate to the frac, then GCEOR in the whole SRV would proceed as the high-pressure gas interface propagates further into the matrix. Indeed, some researchers conceptualize Huff and Puff operations in the following manner: Jacobs (13) indicates, speaking of GCEOR: ". . . any new barrels of oil that make it to the surface are likely sourced from only a few inches into the rock, at most. We say production comes from the near-fracture areas and that's it. . ." The net effect in the field is the propagation of this high-mass transfer zone away from the hydraulic fracture, reaching deeper into the matrix, towards the no-flow axis of symmetry.

In this work, the GCEOR experiments are conducted on only 10 cm diameter core, as the independent variables are changed performance optimization can be evaluated leading towards pressure optimization, injection gas composition sensitivity, effect of the degree of primary depletion on GCEOR performance, gas utilization quantification and the relative importance of geology compared to gas composition and pressure.

One of the first Montney systems that was analyzed exhibited in situ reservoir fluid permeability of 832 nD. It contained 41 API oil with a Gor of 870 scf/BBL. Table 1 presents a summary of the different experiments conducted on this system. The best performance was observed from the 25 and 50% depletion scenarios during primary production followed by GCEOR Huff and Puff cycles at reservoir pressure with primary gas (a process gas stream comprised of hydrocarbon components only). For clarity, percentage depletion refers to the final pressure at the completion of the end of primary production divided by the initial reservoir pressure. This system appeared to benefit from leaving more energy in the reservoir at commencement of the Huff and Puff cycles – higher pressure at the end of primary depletion when GCEOR is commenced.

| SUMMARY OF PERFORMANCE - PROJECT 4 | | | | | | | | |
|---|---|---|---|---|---|---|---|---|
| | | RECOVERY (%OOIP) | | | | | | GCEOR |
| RUN # | GAS INJECTED (HCPV) | PRIMARY | TOTAL | GCEOR | GAS | HUFF PRESSURE (PSIG) | % DEPLETION | % PD |
| 1 | 3.8 | 52.5 | 89.4 | 36.9 | PRIMARY | 3000 | 75 | 70.2 |
| 2 | 1.9 | 53.4 | 55.6 | 2.2 | LEAN | 3000 | 75 | 4.1 |
| 3 | 3.1 | 21.9 | 94.7 | 72.9 | PRIMARY | 3000 | 50 | 333.2 |
| 4 | 4.4 | 23.6 | 99.9 | 76.3 | PRIMARY | 3000 | 50 | 323.1 |
| 5 | 4.1 | 25.8 | 77.4 | 51.7 | LEAN | 4000 | 50 | 200.6 |
| 6 | 6.5 | 5.1 | 99.9 | 94.8 | PRIMARY | 3000 | 25 | 1870.4 |

Table 1- Summary of Montney System 2 Performance

Figure 4 shows a summary of total oil recovery and gas utilization as a function of gas injected during GCEOR cycles. The best GCEOR tests show very low gas consumption values indicating that GCEOR, when properly designed, behaves like a gas storage operation; the operator foregoes gas sales while using the gas to recover residual oil and then eventually recovers the gas on the last Puff cycles. If $CO_2$ were to be used, then rather than producing the gas on the last production cycle, the operator would leave the $CO_2$ in situ for sequestration. As oil recovery increases during GCEOR, more void volume is available for sequestration.

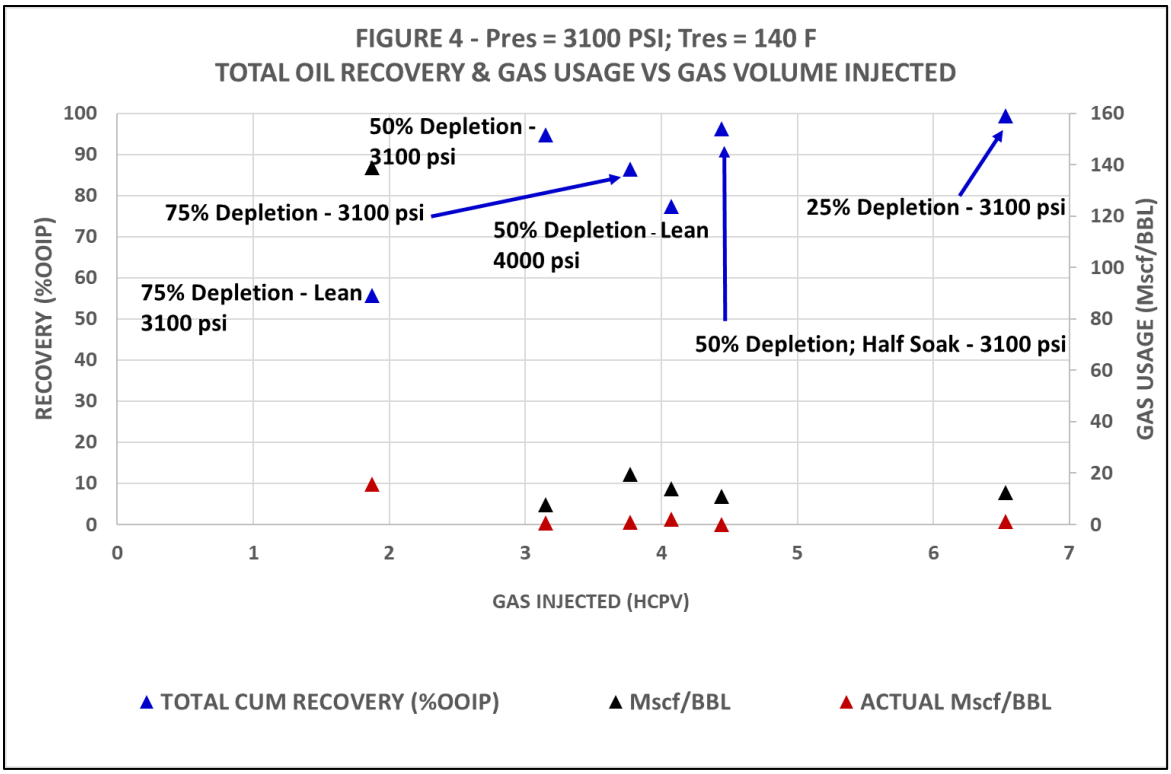


Figure 5 shows a chart of peak field oil flowrates as a function of the different GCEOR operations. The peak field rates are calculated from the experiments using the approximate superficial fracture area of contact between the frac and the matrix. The hydraulic frac half length, the vertical height, two sides and two wings of the same half-length multiplied by the number of frac stages (in an idealized model) provides the total area. From the experiment, the oil flux is determined directly from the different stages of the test – primary depletion and Huff and Puff cycles (oil volume produced divided by the cycle time divided by the experimental area of flow (slot height and length x two sides)). The experimental oil flux is then multiplied by the total approximate field hydraulic fracture area in order to obtain the peak oil rates shown in Figure 5. Figure 5 also shows maximum differential pressure observed in the experiment. Brown et al. (14) report a mathematical description of the pressure field in unconventional production.

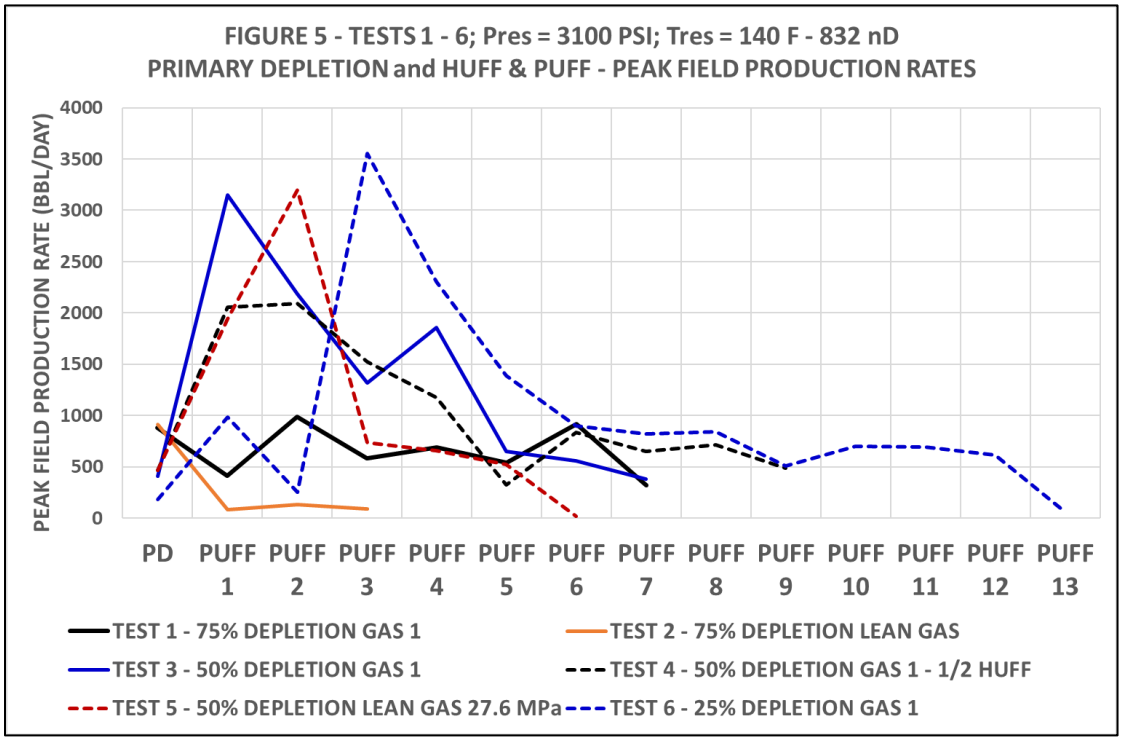

Figure 6 presents the oil recovery history for the last run from Table 1. Primary production was only 25% depletion (P primary depletion final = (1-0.25) x 20.6 MPa) followed by 13 Huff and Puff cycles with maximum Huff pressure at 20.6 MPa. The process gas used during the Huff cycles was very effective at recovering residual oil and this sixth test was the most efficient of the six runs that were performed on this system. Comparing the six runs, the sixth run had the least primary depletion, leaving more energy in the reservoir for the commencement of GCEOR. With very high recovery, by ceasing GCEOR operation at the end of the last Huff cycle, significant sequestration opportunity is evident. It should be emphasized that the experiments access approximately 5 centimeters of matrix adjacent to the slot (frac representation). The recovery is therefore very high. As was mentioned above, referring to the field scenario, as quoted by Jacobs(13) : ". . . any new barrels of oil that make it to the surface are likely sourced from only a few inches into the rock, at most. We say production comes from the near-fracture areas and that's it. . .". Therefore, a few inches adjacent to the fracs in situ would correspond to significant reservoir oil volumes in light of the millions of square feet of superficial area of contact between the matrix and the hydraulic fracs. This volume of oil recovered corresponds to the sequestration volume that will be available.

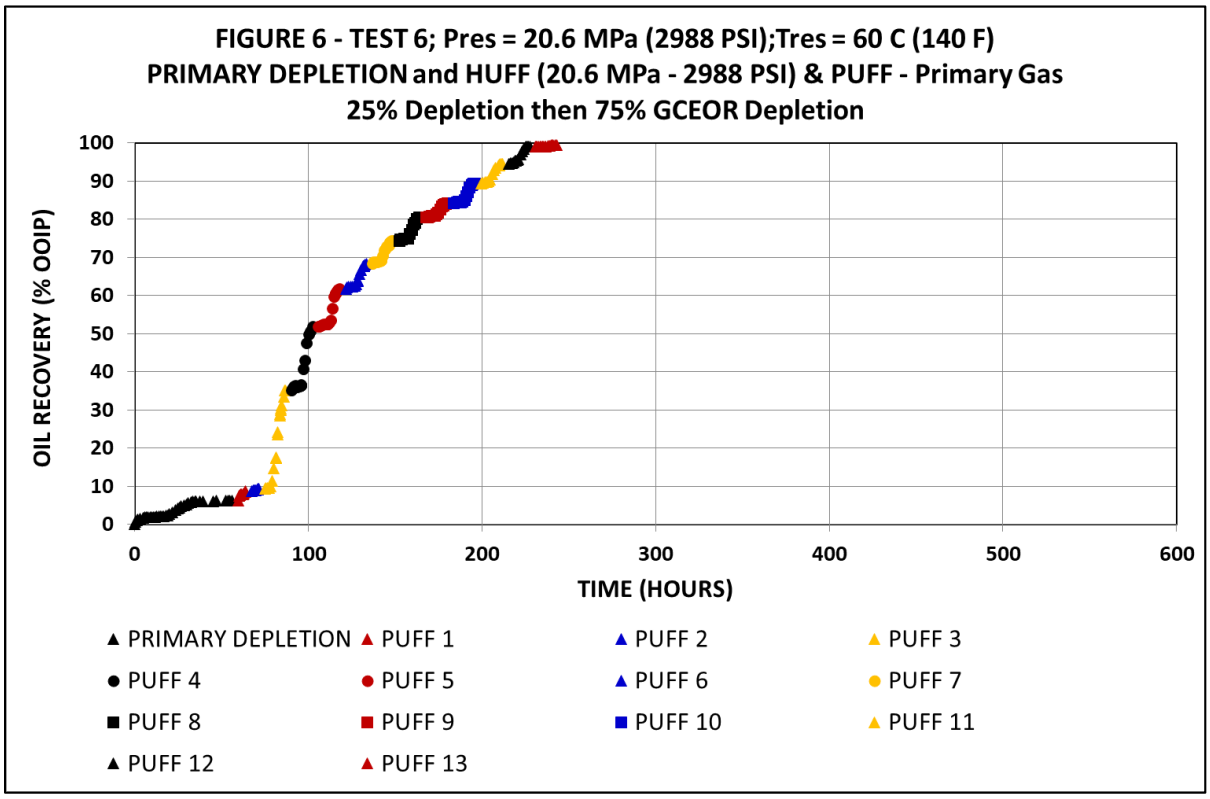


**Summation**

Table 2 summarizes the multiple Montney and Duvernay systems that were analyzed as part of the work discussed herein.

**TABLE 2 - RANGE OF ROCK AND FLUID PROPERTIES**

| PROJECT # | Oil Permeability (nD) | Fluid GOR (scf/BBL) | STO API | Viscosity (cP) | T (F) | Pres (PSI) | Pb (PSI) |
|---|---|---|---|---|---|---|---|
| **MONTNEY 1** | 2400 | 1460 | 43 | 0.247 | 189.0 | 3800 | 3750 |
| **MONTNEY 2** | 1500 | 1404 | 43 | 0.522 | 197.0 | 4410 | 4400 |
| **MONTNEY 3** | 1350 | 1581 | 44 | 0.202 | 172.0 | 3640 | 3600 |
| **MONTNEY 4** | 832 | 870 | 41 | 0.458 | 140.0 | 3100 | 3000 |
| **MONTNEY 5** | 400 | 2650 | 47 | 0.205 | 161.0 | 4450 | 4300 |
| **MONTNEY 6** | 319 | 1182 | 45 | 0.588 | 156.0 | 4000 | 3900 |
| **DUVERNAY 1** | 13 | 840 | 40 | 0.277 | 192.0 | 5250 | 2000 |

One of the questions with which the work was begun was to determine if geology mattered in GCEOR Huff and Puff operations. In order to evaluate if the geology was limiting the performance, the fluid system from project 4 (832 nD) was used to saturate the porous media from project 5. Primary depletion and GCEOR at conditions used in the project 4 GCEOR work were then performed. After that, the fluid from Montney 1 (exhibiting natural fractures) was also used to saturate the porous media from project 5. If the fluids were the dominant influence, then no matter what the rock, the performance under GCEOR should be the same. In other words, if the geology were to be the same, but the fluids were changed then the performance would be expected to change. Figure 7 shows the results. The GCEOR response, with fluids from project 4 when utilized in the porous media from project 5, was almost exactly that of project 5. As shown in Table 2, project 4 fluids were close to the least volatile (41 API, 870 scf/BBL), whereas the fluids from project 5 were the second-most volatile (47 API, 2650 scf/BBL). Project 4 was performed with injection gas exhibiting an FCM pressure of 5624 psia at a maximum Huff pressure of 3100 psig and resulted in a total recovery (primary and GCEOR) of approximately 87% OOIP. Project 5, even though maximum Huff pressure was well above FCM pressures, showed a total recovery of approximately 50% OOIP

(primary plus GCEOR). The system exhibiting some natural fractures showed excellent primary depletion recovery whereas when that same fluid was used in the porous media from project 5 the recovery signature was very close to that of project 5 and fluid from project 4 in project 5 rock. That is, whatever the fluid system, the recovery signature for both primary and GCEOR operations, was very similar. It is concluded from these experiments that the fluids are not controlling and that the geology is governing the primary depletion and GCEOR response.

FIGURE 7 - THE EFFECT OF POROUS MEDIA ON GCEOR PERFORMANCE

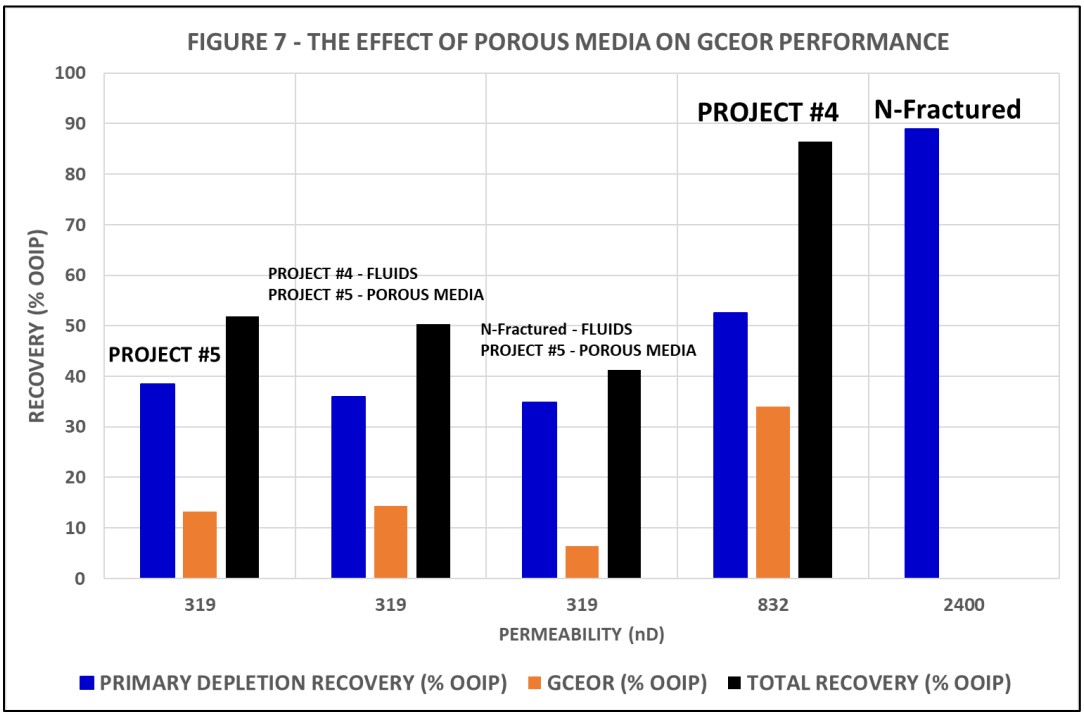


Another question to which an answer was sought was whether GCEOR performs better in gas condensate systems than in oils. Figure 8 shows the results of Primary depletion and GCEOR performed on two porous media, each one saturated with gas condensate fluid and subsequently with oil. Primary depletion performed better in the two oil systems than in the two gas condensate systems. GCEOR performed better in the gas condensate systems than in the oils.

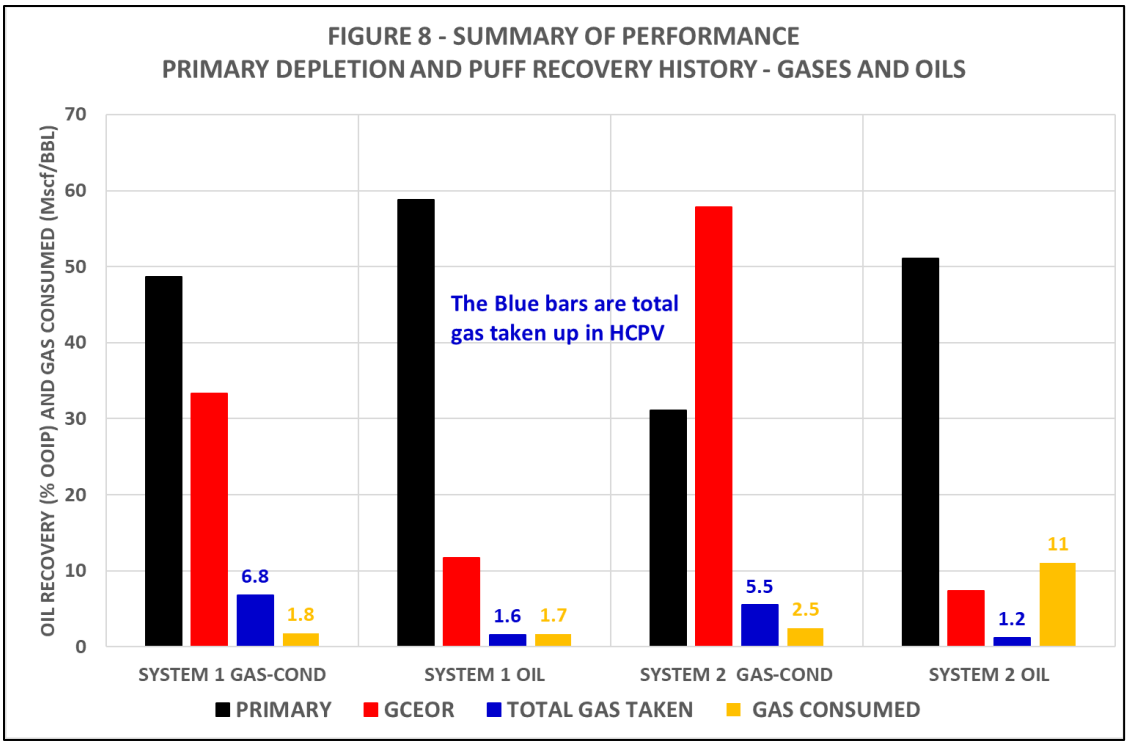


Figure 9 shows expected relative permeability relationships for a gas condensate and for an oil system. Figure 9A suggests that the condensate becomes mobile (critical condensate saturation - Scc) at a condensate saturation of approximately 0.3 (that is, a gas saturation of 0.58 when starting at a gas saturation of 0.88 – 12% initial water saturation). The maximum liquid drop out was less than 30% and so the condensate would not be mobile; the only liquid produced would be carried as the gas phase which would then be condensed in the atmospheric separator.

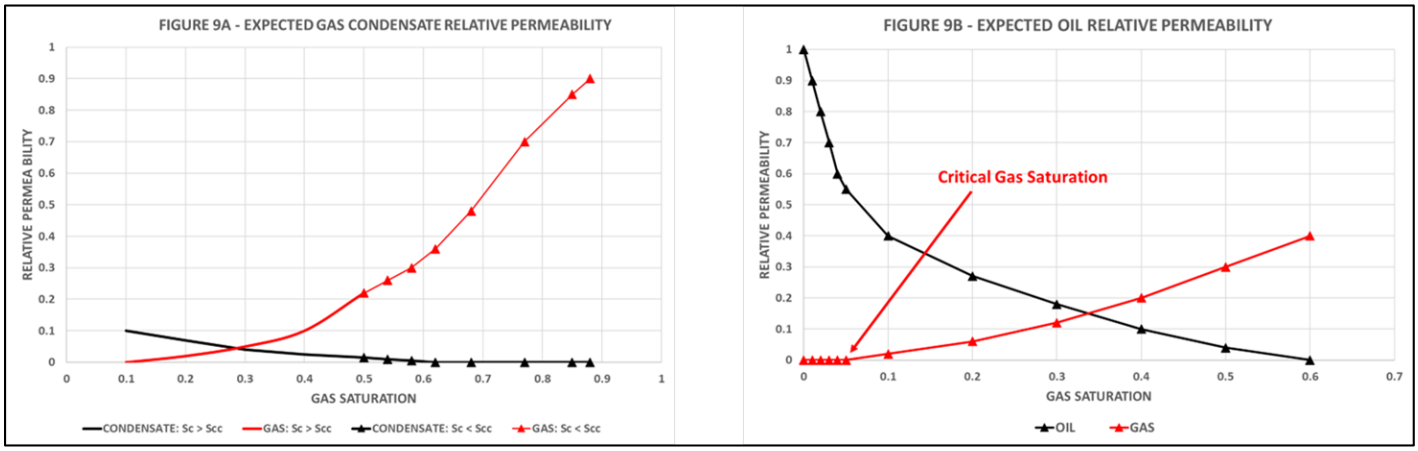


As the liquid condenses from the gas phase in situ the liquid would be trapped in the rock since the critical condensate saturation is greater than the maximum liquid dropout. Liquid production on primary depletion would therefore be expected to be less than with an oil where the liquid is always mobile at gas saturations less than that corresponding to the residual oil saturation. Thus, primary depletion liquids recovery would be expected to be better with an oil. GCEOR would be expected to have superior performance with a condensate since interfacial tension was superior with the condensate compared to the oil. Total liquid recoveries for the gas condensate systems were approximately 81% and 89% whereas for the oils the hydrocarbon liquid recoveries were approximately 70% and 59%. In light of this, the evidence suggests that GCEOR performs better in gas condensate systems than in oils, where the porous media are the same.

## References


B. Todd Hoffman, David Reichhardt, 2019. Quan Eval Rec Mech for Huff-n-puff Gas Inj in Uncon Res, Uncon Res Tech Conf (URTeC), DOI 10.15530/urtec-2019-147

M.L. Carlsen, C.H. Whitson, M.M. Dahouk, B. Younus, I. Yusra, E. Kerr, J.

Nohavitza, M. Thuesen, J.H. Drozd, R. Ambrose, S. Mydland, 2019. Comp Tracking of a Huff-n-Puff Proj in the Eagle Ford, Uncon Res Tech Conf (URTeC), DOI 10.15530/urtec-2019-539

Scott Malo, Jimmy McNamara, Nick Volkmer; Ehsan Amirian, 2019. Eagle Ford – Intro Big Bad Wolf, Uncon Res Tech Conf (URTeC), DOI 10.15530/urtec-2019-624

Reza Ganjdanesh, Wei Yu, Mauricio Xavier Fiallos, Erich Kerr, Kamy Sepehrnoori,

Raymond Ambrose,2019. Gas Inj EOR in Eagle Ford Shale Gas Cond Res, Uncon Res Tech Conf (URTeC), DOI 10.15530/urtec-2019-987

Michael Cronin, Hamid Emami-Meybodi, Russell Johns, 2019. Multicomp Diff Model of Cyc Solv Inj in Ultratight Res, SPE-196008-MS

Sheng, J. J. 2015. EOR in Shale Res by Gas Inj *Journal of Natural Gas Science and Engineering* **22:** 252–259.
F. Brent Thomas, Michael Piwowar, Hongmei Zhang, William Gibb, 2019. Gas-Cyc EOR in Liq-Rich Prod, SPE-197099-MS

F. Brent Thomas, Michael Piwowar, Mehdi Noroozi, Juan Marin, William Gibb, Hongmei Zhang, 2020. Exp Meas of Montney and Duvernay Gas-Cycl EOR (GCEOR), SPE-199994-MS

F. Brent Thomas, Michael Piwowar, Mehdi Noroozi, William Gibb, Juan Marin, Hongmei Zhang 2020. Insight Gained fr Exp Gas-Cyc EOR in the Unconv Montney and Duvernay Forms, SPE-200359-MS.

F. Brent Thomas, Michael Piwowar, Mehdi Noroozi, Ronnel Apil, Juan Marin[2], William Gibb, Carter Clarkson, Hongmei Zhang, Stan Swacha, Insights gained fr fifty lg-vol prim dep - gas cyc huff and puff exps in the Montney and Duvernay forms, Uncon Ress Techs Confs (URTeC) DOI 10.15530/urtec-2020-3228

F. Brent Thomas, Farhad Qanbari, Aaron White, Michael Piwowar, Mehdi Noroozi, Ronnel Apil, Juan Marin, William Gibb, Carter Clarkson, Hongmei Zhang, Stan Swacha, a comp of prim dep and GCEOR in the Montney form; volat oil and rich gas conden, Unconv Res Tech Conf (URTeC) DOI 10.15530/urtec-2020-3266

Ahmadi as quoted in Jacobs, T., “How Tight-Oil Wells Grow Old”, Journal of Pet Tech, February, 2020, pg. 32

M. Brown, E. Ozkan, R. Raghavan, H. Kazemi, Practical Solutions for Pressure Trans Resp of Frac Wells in Unconventional Shale Reservoirs, SPERE 14(06), 663-676, 13, December, 2011.

GUSSOW 2024
Montney Subsurface Evaluation: Drive Towards Excellence
Banff, AB | October 2-4

# Failure and recovery of marine productivity following the Early Triassic hothouse

Stephen Grasby

Geological Survey of Canada

## Abstract

The Early Triassic represents a period of prolonged recovery following the most severe extinction of the Phanerozoic. Records show this to be a period of extremely high global temperatures, likely driven by Siberian Traps eruption induced global warming. How this hothouse impacted marine ecosystems and prolonged the recovery process remains uncertain. Across northwestern Pangea, Early Triassic marine sediments are characterized by low organic matter content, despite recurrent anoxia which would create conditions more suitable for preservation and being located on the western continental margins were the majority of primary productivity in the Panthalassa Ocean would occur. Geochemical proxies suggest the paucity of organic matter reflects a productivity collapse rather than changes in preservation. Nitrogen isotopes show a progressive negative shift starting at the Permian/Triassic extinction and continuing through to the Smithian, indicating progressively growing nutrient limitation. High ocean temperatures likely deepened the thermocline, limiting nutrient recycling and upwelling into the photic zone driving nutrient stress. Final ocean cooling in the Anisian is marked by widespread deposition of phosphate and organic rich black shales across NW Pangea (including the Doig Formation of western Canada) and return of N isotopes to values consistent with active nutrient upwelling. A hyperthermal driven nutrient-limited Early Triassic Ocean was likely a key inhibiter of marine recovery.

## Statement of the background

What prolonged the Early Triassic recovery and marine productivity has been under active debate. Examination of nitrogen isotope records can help elucidate nutrient availability, and thus constraints on primary productivity in Early Triassic oceans. Heterotrophic denitrification and/or anaerobic ammonia oxidation are the principal mechanism for loss of ocean nitrogen, returning to the atmosphere as $N_2$ (Ward et al., 2009). Regions of significant denitrification (i.e., the reduction of $NO_3$/$NO_2$ to $N_2$) leave subsurface waters highly enriched in $^{15}N$. In contrast, atmospheric nitrogen fixation produces organic matter relatively depleted in $^{15}N$, with $\delta^{15}N$ values close to that of the atmosphere (0‰). As such, the $\delta^{15}N$ of organic matter (OM) in modern oceans is highly variable, but relatable to biogeochemical processes of different marine environments

## Aims and Objectives

We examined the Early to Late Triassic geochemical record of the Sverdrup Basin, Canadian High Arctic to elucidate the impacts of the global hothouse on marine productivity at that time.

## Materials and methods

Samples were collected from fresh exposures in outcrop. In the laboratory, any remaining weathered surfaces were removed and fresh samples were powdered by agate mortar and pestle. Total N and $\delta^{15}N$ were analyzed by using an elemental analyzer connected to an isotope ratio mass spectrometer. Approximately 20% of the samples were analyzed in duplicate with a mean standard deviation of 0.16‰. Results are reported as standard δ-values in per mil (‰ versus air). The reference material used during analysis of the samples (IA-R001 wheat flour, Iso-Analytical Ltd.) had a $\delta 1^5N$ value of 2.55‰ versus air and contained 1.88% N (w/w). Control samples were analyzed to check the accuracy of the measurements, with precision better than ± 0.2‰.

## Results and discussion

Late Permian high $\delta^{15}N$ values (>9‰) are consistent with water-column denitrification in continental margin upwelling zones, suggesting that changes in oxygenation are largely controlled by recycling of nutrients and high organic productivity. An initial ~1‰ drop in $\delta^{15}N$ in the earliest Triassic represents nitrogen loss counterbalanced by advected light nitrate derived from large changes in $N_2$ fixation. $\delta^{15}N$ progressively declined through the Early Triassic to values varying between +1‰ and –1‰, within the $\delta^{15}N$ range of marine diazotrophs (0.5‰ to –2‰) that directly fix nitrogen from atmospheric $N^2$ under nutrient stressed conditions. At that time, global oceans had greatly expanded oxygen minimum zones and reduced ecological diversity and highly elevated sea surface temperatures. Predictions for modern global warming suggest that deepening thermoclines would cause a net reduction of nutrient supply even in active upwelling regions. Therefore, along with decreased upwelling, nutrient-rich waters may have been further trapped in anoxic waters below a deepened Early Triassic thermocline. Such anoxic conditions would have driven significant P liberation and increased denitrification, generating the observed drop in N/P and the Early Triassic phosphate gap. Therefore, both reduced upwelling and trapping of nutrient-rich waters could have created an overall Early Triassic nutrient gap, marked by low δ15N and N/P values, that would have stressed primary productivity along the northwest margin of Pangea.

Reduced primary productivity in northwest Pangea is supported by the parallel drop in TOC and N/P from the end Permian extinction until at least Spathian time. Strongly anoxic to euxinic Early Triassic conditions would have favored organic matter preservation, suggesting that this progressive decrease in TOC reflects declining primary productivity. This is further supported by proxies for primary productivity (Ba, Ni, Cu) that show enrichment factors >1 before the extinction, consistent with a highly productive continental margin supported by upwelling, that abruptly dropped at the LPE, and remained low to very low (<1) throughout the Early Triassic, consistent with a switch to low primary productivity.

Nitrogen isotope values return to pre-extinction values in the late Anisian accompanied by deposition of major organic rich petroleum source rocks across northwestern Pangea that are characterized by phosphatic rich deposition. This is time with final decline of sea surface temperatures and cooling of terrestrial environments. Such cooling likely lead to renewed upwelling of nutrient rich waters leading to deposition of phosphatic units globally.

## Conclusions

Results suggest that that the global hothouse event of the Early Triassic had significant impact on marine primary productivity influencing deposition of Early Triassic strata. Final amelioration lead to formation of major petroleum source rocks and phosphate deposits across western North American and the circum-Arctic region.

GUSSOW 2024
Montney Subsurface Evaluation: Drive Towards Excellence
Banff, AB | October 2-4

# Hydrocarbon migration dynamics through burial and uplift history of the Montney Formation

James M. Wood

Calaber1 Resources

## Abstract

Hydrocarbon migration, driven by the dynamically changing pressure-volume-temperature (PVT) conditions that accompany burial and uplift, is gaining increased recognition as a common phenomenon within unconventional low-permeability petroleum accumulations. The Lower Triassic Montney Formation in western Canada hosts a major unconventional hybrid petroleum accumulation with a complex history of hydrocarbon migration from both external and internal source rocks. A review of recent geochemical studies highlights evidence of three main widespread episodes of intraformational hydrocarbon migration within this siltstone-dominated formation. These episodes include (1) initial migration of early-generated mobile bitumen and oil from internal Montney organic-rich source rocks during rapid burial, followed by (2) gas-condensate migration during deep burial and over-pressuring, and finally (3) late-stage methane-enriched gas migration, mainly during basin uplift and depressurization. Temporal relationships of these three migration episodes fit a dynamic model of hydrocarbon generation and migration tied to basin subsidence and uplift history. Recognizing multiple episodes of hydrocarbon migration is important for technical and economic evaluations of the Montney unconventional resource play because it provides a basis for understanding the intricate geographic and stratigraphic distribution of condensate-gas ratio (CGR) in terms of a first-order trend controlled by thermal maturity and second-order trends due to hydrocarbon migration. The dynamic migration and mixing history of gas and condensate can directly impact Montney well performance, with economic consequences. These impacts commonly include lower CGR and higher gas content than expected from routine thermal maturity proxies. The Montney Formation has abundant publicly available subsurface data, and thus serves as a well-documented analogue for understanding other unconventional petroleum accumulations that may have had multiple episodes of intraformational hydrocarbon migration.

## Statement of the background

The Lower Triassic Montney Formation hosts a major unconventional hybrid petroleum accumulation (Jarvie, 2012; Euzen et al., 2021) with a complex history of hydrocarbon migration from both external and internal source rocks (Rudra et al., 2024). Organic geochemistry and PVT studies conducted since 2012 have significantly advanced our knowledge about the intraformational migration of oil, condensate, gas and supercritical fluid in the Montney Formation. However, the timing of discrete hydrocarbon migration modes and episodes with respect to the dynamically changing PVT conditions that accompanied burial and uplift is still inadequately understood. Recently, the main hydrocarbon migration episodes identified in previous studies were integrated into a simple overall model of hydrocarbon generation, hydrocarbon migration and pressure evolution tied to burial and uplift history (Wood, 2023). Here, this model of evolving hydrocarbon dynamics within the Montney Formation is reviewed and revised.

## Aims and Objectives

The aims of this investigation on the Montney unconventional hybrid petroleum accumulation are to (1) evaluate and summarize key evidence from previously published geological and geochemical research on the intraformational hydrocarbon migration of oil, gas-condensate and methane-enriched gas, and (2) integrate the key findings into a dynamic model of hydrocarbon generation, hydrocarbon migration and pressure evolution tied to burial-uplift history.

## Materials and methods

The key Montney geochemical studies reviewed and evaluated (Kuppe et al., 2012; Wood and Sanei, 2016; Laycock et al., 2021; Wood et al. 2021a; Watt et al., 2022; Wood et al., 2022) used a range of methods including stable carbon isotope analysis of core extracts, stable carbon isotope and compositional analysis of produced gas, compound-specific isotope analysis of co-produced gas and liquid samples, LECO TOC measurements, Rock-Eval pyrolysis measurements, PVT studies, and well production data. Geologic context in these studies was provided by regional mapping of gas composition and well production CGR, as well as measurements and observations from core analysis, organic and thin-section petrography, and scanning electron microscopy. The independently recognized intraformational migration episodes of oil, gas-condensate and methane-enriched gas were integrated into an overall model of hydrocarbon migration dynamics (Wood, 2023) tied to the Montney's burial and uplift history.

## Results and discussion

A review of previous geochemical investigations of the Montney unconventional petroleum accumulation revealed evidence of three main widespread episodes of intraformational hydrocarbon migration (Wood, 2023). The inferred timing of these migration episodes with respect to the burial and uplift history of the Montney Formation is shown schematically in Figure 1. The first episode was characterized by the initial migration of early-generated mobile bitumen and oil from internal Montney organic-rich source rocks during rapid burial (Laycock et al., 2021; Watt et al., 2022; Ardakani et al., 2022). The second episode consisted of gas-condensate migration during deep burial and over-pressuring (Kuppe et al., 2012; Wood et al., 2022). The final episode involved late-stage methane-enriched gas migration, mainly during basin uplift and depressurization (Wood and Sanei, 2016; Wood et al., 2021a). A review and summary of the key geological and geochemical evidence for the three main episodes of intraformational hydrocarbon migration is provided by Wood (2023). Here, these migration episodes are discussed in the integrated context of a simple hydrocarbon fluid and pressure evolution model tied to burial and uplift history.

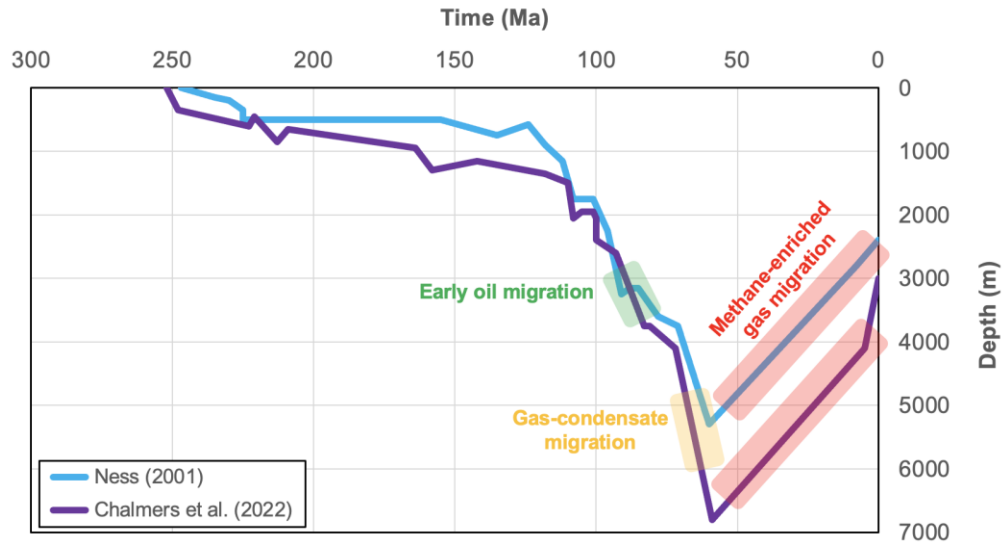


Figure 1: Modeled burial and uplift history of the Montney Formation for a NW Alberta well (blue line; Ness, 2001) and a BC well close to the Cordilleran deformation front (purple line; Chalmers et al., 2022). Rapid burial began at ~110–120 Ma in response to thrust sheet loading of the Cordilleran Orogeny. Maximum burial was at ~60 Ma. Basin uplift and removal of overburden occurred from ~60 Ma to the present-day. Colour-filled rectangles indicate approximate timing of intraformational migration of early oil (green), gas-condensate (yellow) and methane-enriched gas (red).

**Generation-migration model with burial.** The burial phase of the model is shown in Figure 2. The model begins at Burial Time 1 when the deeper southwest part of the Montney Formation enters the oil window. Highly viscous, mobile petroleum is initially generated (Curiale, 1986; Hackley et al., 2022; Sanei, 2020) from dominantly Type II oil-prone sedimentary organic matter within organic-rich shale laminae and migrates at a local-scale (mm to m) into adjacent reservoir siltstone beds (Ardakani et al., 2022). Stable carbon isotope trends associated with the original environmental conditions of the sedimentary organic matter (Laycock et al., 2021; Watt et al., 2022) are minimally disturbed by the short migration distance of the early-generated mobile petroleum. With thermal progression through the oil window, the highly viscous mobile petroleum thermally cracks to light oil and residual solid bitumen. The light oil migrates farther and accesses tighter pore structures than the early-generated mobile petroleum due to its lower viscosity (Jacob, 1989). Charging by mobile bitumen and oil displaces free water from siltstone pores (Wood, 2013; Wood, 2015; Wood et al., 2021b). Slight over-pressuring commences at the transition from the black oil to the volatile light oil windows. The introduction of early generated light n-

alkanes induces dissociation of oil into asphalt and paraffin-rich fractions (Wood et al., 2018b). Asphalt precipitates or adsorbs onto pore walls, locally altering the wettability from uniform water-wet conditions to variable water-wet and hydrocarbon-wet conditions (i.e., dual-wettability) at the micro-scale (Lan et al., 2015; Yassin et al., 2016; Wood et al., 2018a). Local biodegradation of oil occurs until a formation temperature of ~80$^{O}$C is exceeded with progressive burial (Sanei et al., 2015; Cesar et al., 2023).

With further subsidence to Burial Time 2, the southwest part of the Montney Formation, which was previously in the oil window, now enters the wet gas-condensate window. Wet gas-condensate is generated by the thermal cracking of oil, and undergoes short-range up-dip migration driven by pressure gradient (Wood et al., 2022). Hybrid gas-condensate forms with the introduction of gas-condensate to *in-situ* hydrocarbon liquid (Thompson, 2016; Wood et al., 2022). Thermal degradation of oil produces solid bitumen (Chalmers and Bustin, 2012; Freeman, 2012; Sanei et al., 2015; Wood et al., 2015, 2018a, 2018b, 2020), which occludes pore space and substantially decreases the permeability of reservoir siltstone beds (Wood et al., 2015; Akai and Wood, 2018; Akihisa et al., 2018; Ghanizadeh et al., 2018). The onset of significant gas generation causes increased over-pressuring. Gas charging induces water displacement and vaporization, resulting in additional removal of free water from siltstone pores and culminates in pervasive saturation by gas (Wood, 2015; Wood et al., 2021b). Further up-dip during Burial Time 2, a part of the Montney Formation that was previously in the normally pressured, pervasively water saturated section now enters the oil window.

With additional subsidence, culminating in maximum burial (approximately 60 Ma, Fig. 1) at Burial Time 3, the southwest part of the Montney Formation, which was previously in the wet gas-condensate window, now enters the dry gas window. Dry gas is generated by the thermal cracking of wet gas and condensate, and undergoes moderate-range migration driven by pressure gradient (Kuppe et al., 2012). Solid bitumen matures to pyrobitumen (Sanei et al., 2015; Wood et al., 2018b). Peak gas generation intensifies the degree of over-pressuring. Further up-dip during Burial Time 3, the Montney section that was previously in the oil window now enters the wet gas-condensate window, and a part of the Montney Formation that was previously in the normally pressured, pervasively water saturated section enters the oil window.

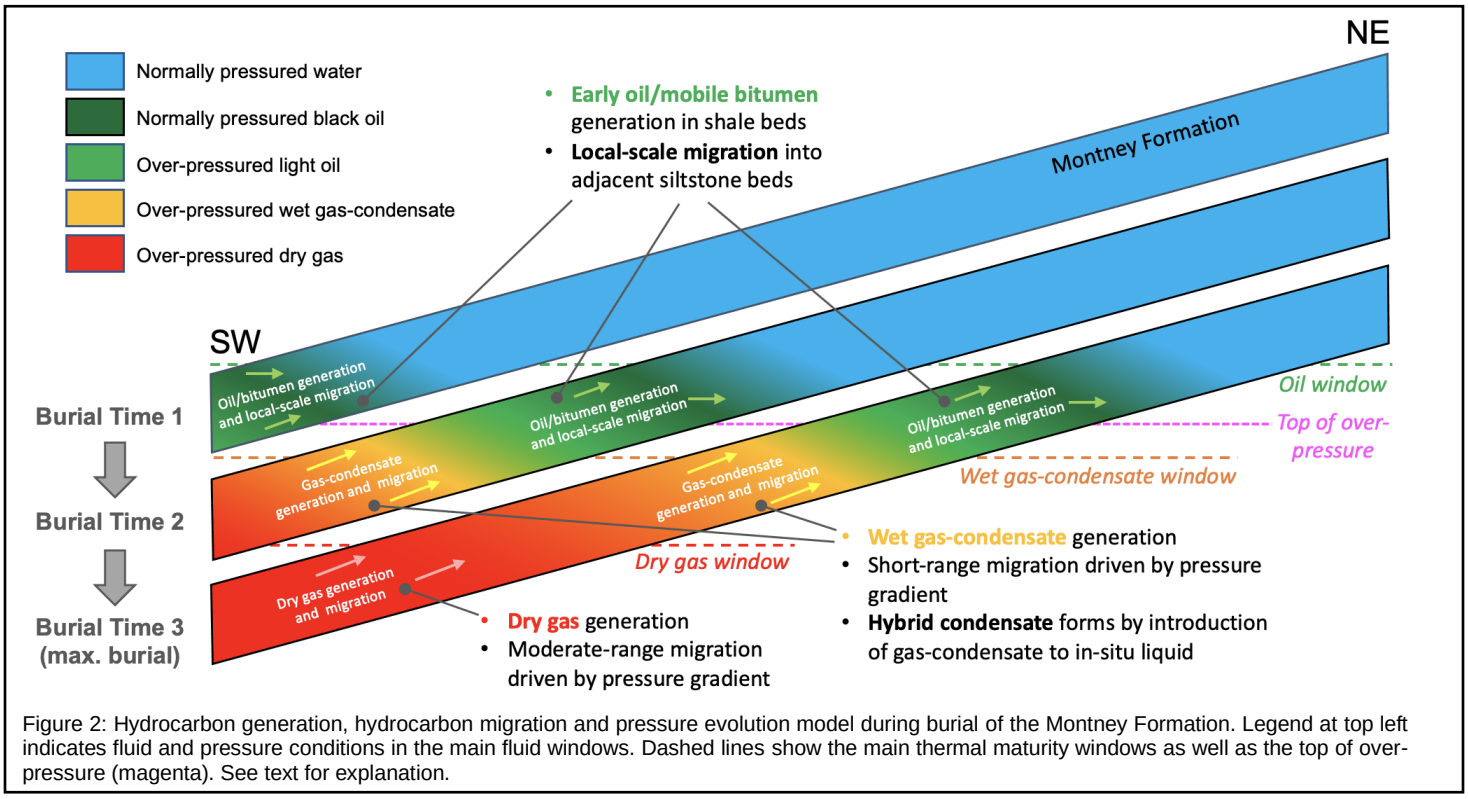


Figure 2: Hydrocarbon generation, hydrocarbon migration and pressure evolution model during burial of the Montney Formation. Legend at top left indicates fluid and pressure conditions in the main fluid windows. Dashed lines show the main thermal maturity windows as well as the top of over-pressure (magenta). See text for explanation.

**Migration model with uplift.** The uplift phase of the model, from approximately 60 Ma to the present day (Fig. 1), is shown in Figure 3. The uplift model begins with the state at maximum burial depth from the burial model (Burial Time 3, Fig. 2). With uplift and accompanying reduction in pressure and temperature, supercritical single-phase hydrocarbon fluids separate into liquid and methane-enriched gas phases (Wood et al., 2021a). The separated methane-enriched gas migrates up-dip (red arrows, Fig. 3), driven by regional pressure gradient, buoyancy and gas expansion (Wood and Sanei, 2016; Wood et al., 2021a). The migration rate is minimal to low across most of the Montney unconventional petroleum accumulation, but significantly higher along suitably oriented trends of enhanced permeability and positive local structure, forming long-range migration pathways for methane-enriched gas (Wood and Sanei, 2016; Wood et al., 2021a). Faults influence migration

pathways by acting as barriers and baffles to the up-dip transmission of methane-enriched gas (Euzen et al., 2018, 2019; 2021; Wood et al., 2021a; Chalmers et al., 2022; Wood et al., 2024). Supercritical methane-rich fluids deeper in the Montney Formation also migrate up-dip along favorable permeability trends, responding dynamically to progressive pressure reduction in the shallower portions of methane-rich gas migration pathways (Wood et al., 2021a). In the light oil window, migration and loss of exsolved gas (Wood et al., 2021a) leads to a change from slightly over-pressured to slightly under-pressured conditions (Gibbs and Rakhit, 2019). Temperature reduction and hydrocarbon volume expansion during uplift also prompt reservoir pressure reduction in a manner consistent with the equation of state for reservoir fluids (Xia et al., 2020). Migration of undersaturated dry gas causes further vaporization and removal of formation water from siltstone pores (Wood, 2015; Wood et al., 2021b). Intraformational gas migration to the up-dip margin of the unconventional petroleum accumulation leads to gas leakage and massive depressurization (Wood and Sanei, 2016). Depressurization promotes desorption of methane from organic matter, particularly in shallower portions (oil window) of the Montney unconventional petroleum accumulation (unpublished data). Kilometer-scale uplift (Fig. 1) results in the depths of the present-day hydrocarbon fluid windows no longer matching those of the corresponding thermal maturity windows at maximum burial (Fig. 3).

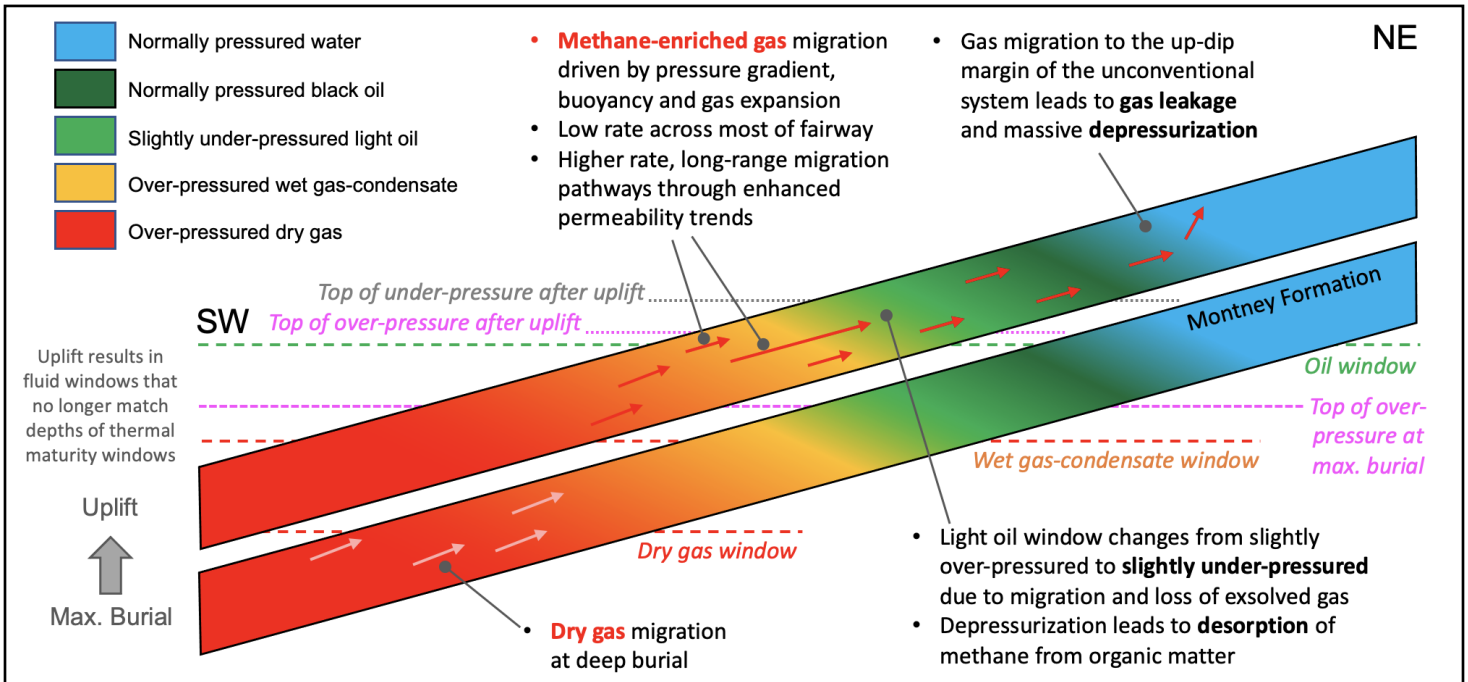


Figure 3: Hydrocarbon migration and pressure evolution model during uplift of the Montney Formation. Legend at top left indicates fluid and pressure conditions in the main fluid windows after uplift. Long-dash lines show the main thermal maturity windows. Short-dash magenta lines indicate the top of over-pressure at maximum burial and after uplift. Short-dash grey line shows the top of under-pressure after uplift. See text for explanation.

**Economic significance.** Recognizing multiple episodes of hydrocarbon migration, and their geographic and stratigraphic variability (e.g., Wood et al., 2024), is important for technical and economic evaluations of the Montney unconventional resource play. This is because it provides a basis for understanding the intricate geographic and stratigraphic distribution of CGR in terms of a first-order trend controlled by thermal maturity and second-order trends due to hydrocarbon migration (Wood and Sanei, 2016, 2017). The dynamic migration and mixing history of gas and condensate can directly impact Montney well performance, with economic consequences. These impacts commonly include lower CGR and higher gas content than expected from routine thermal maturity proxies.

## Conclusions

A review of previous key geochemical investigations revealed evidence of three main widespread episodes of intraformational hydrocarbon migration in the Montney unconventional petroleum accumulation. The first episode was characterized by the migration of early-generated mobile bitumen and oil from internal organic-rich source rocks during rapid burial. The second episode consisted of gas-condensate migration during deep burial and over-pressuring. The final episode involved late-stage methane-enriched gas migration, mainly during basin uplift and depressurization. Temporal relationships of these three migration episodes fit a dynamic model of hydrocarbon generation, hydrocarbon migration and pressure evolution tied to basin subsidence and uplift history. Advanced organic geochemical studies conducted at the basin scale are needed to test this simple model of hydrocarbon migration dynamics and to more fully resolve the complex history of hydrocarbon migration and mixing in the Montney Formation. Recognizing multiple episodes of hydrocarbon

migration is important for technical and economic evaluations of the Montney unconventional resource play because it provides a basis for understanding the intricate geographic and stratigraphic distribution of CGR in terms of a first-order trend controlled by thermal maturity and second-order trends due to hydrocarbon migration. The dynamic migration and mixing history of gas and condensate can directly impact Montney well performance, with economic consequences. These impacts commonly include lower CGR and higher gas content than expected from routine thermal maturity proxies. The Montney Formation, with abundant publicly available subsurface data, provides a well-documented analogue for understanding other unconventional petroleum accumulations that may have had multiple episodes of intraformational hydrocarbon migration.

## Acknowledgements

I gratefully thank the following colleagues for sharing their insights during previous collaborative research projects on hydrocarbon migration in the Montney Formation: Omid Ardakani, Victoria Biersteker, Jaime Cesar, Tristan Euzen, Scott Leroux, Arka Rudra, Hamed Sanei and Lana Sharp.

## References

Akai, T. and Wood, J.M. 2018. Application of pore throat size distribution data to petrophysical characterization of Montney tight gas siltstones. Bulletin of Canadian Petroleum Geology, v. 66, p. 425–435.

Akihisa, K., Knapp, L.J., Sekine, K., Akai, T., Uchida, S., Wood, J.M., Ardakani, O.H. and Sanei, H. 2018. Integrating mud gas and cuttings analyses to understand local CGR variation in the Montney tight gas reservoir. International Journal of Coal Geology, v. 197, p. 42-52.

Ardakani, O.H., Cesar, J., Pedersen, P.K., Mackie, S.J., Reyes J. and Wood, J.M. 2022. Occurrence and preservation of primary organic matter in a hybrid unconventional reservoir: Montney Formation, Western Canada sedimentary basin. International Journal of Coal Geology, v. 261, 104096.

Cesar, J., Ardakani, O.H., Watt, E., Song, Y., Kingston A. and Ahad, J.M. 2023. Paleo-biodegradation and hydrocarbon mixing in a major hybrid petroleum reservoir. Scientific Reports, 13, 4357.

Chalmers, G.R.L. and Bustin, R.M. 2012. Geological evaluation of Halfway–Doig–Montney hybrid gas shale–tight gas reservoir, northeastern British Columbia. Marine and Petroleum Geology, v. 38, p. 53–72.

Chalmers, G.R., Lacerda Silva, P., Bustin A.A., Sanlorenzo, A. and Bustin, R.M. 2022. Geology and geochemistry of the hydrocarbon compositional changes in the Triassic Montney Formation, Western Canada. Energies, v. 15, 8677.

Curiale, J.A., 1986. Origin of solid bitumens, with emphasis on biological marker results. Organic Geochemistry, v. 10, p. 559-580.

Euzen, T., Chatellier J.-Y. and Mort, A. 2018. Geological controls on fluid compositional variations in unconventional hybrid plays: Insight from gas geochemistry (Montney play, western Canada). Unconventional Resources Technology Conference, July 23–25, 2018, Houston, Texas, USA.

Euzen, T., Watson, N., Chatellier, J.-Y., Mort, A. and Mangenot, X. 2019. Petroleum system analysis using unconventional gas geochemistry: Examples from the Montney play of western Canada. Unconventional Resources Technology Conference, July 22–24, 2019, Denver, Colorado, USA.

Euzen, T., Watson, N., Fowler, M., Mort, A. and Moslow, T.F. 2021. Petroleum distribution in the Montney hybrid play: Source, carrier bed and structural controls. AAPG Bulletin, v. 105, p. 1867–1892.

Freeman, M.J. 2012. Lithological, diagenetic, and organic controls on reservoir quality in the Lower Triassic Montney Formation, Pouce Coupe, Alberta. Master's thesis, University of Calgary, Calgary, Alberta, Canada, 291 p.

Ghanizadeh, A., Clarkson, C.R., Vahedian, A., Ardakani, O.H., Wood, J.M. and Sanei, H. 2018. Laboratory-based characterization of pore network and matrix permeability in the Montney Formation: Insights from methodology comparisons. Bulletin of Canadian Petroleum Geology, v. 66, p. 472-498.

Gibbs, A. and Rakhit, K. 2019. Hydrodynamics, geothermics and spatial variations in hydrocarbon fluid distribution within the Montney Formation, Alberta and British Columbia, Canada. SPE Annual Technical Conference and Exhibition, September 30–October 2, 2019, Calgary, Alberta, Canada.

Hackley, P.C., Zhang, T., Jubb, A.M., Valentine, B.J., Dulong, F.T. and Hatcherian, J.J. 2020. Organic petrography of Leonardian (Wolfcamp A) mudrocks and carbonates, Midland Basin, Texas: the fate of oil-prone sedimentary organic matter in the oil window. Marine and Petroleum Geology, v. 112, 104086.

Jacob, H. 1989. Classification, structure, genesis and practical importance of natural solid oil bitumen ("migrabitumen"). International Journal of Coal Geology, v. 11, p. 65-79.

Jarvie, D.M. 2012. Shale resource systems for oil and gas: Part 1 - Shale-gas resource systems. AAPG Memoir 97, p. 69–87.

Kuppe, F.C., Haysom, S. and Nevokshonoff, G. 2012. Liquids rich unconventional Montney reservoir: The geology and the forecast. SPE Canadian Unconventional Resources Conference, October 30–November 1, 2012, Calgary, Alberta, Canada.

Lan, Q., Dehghanpour, H., Wood, J. and Sanei, H. 2015. Wettability of the Montney tight gas formation. SPE Reservoir Evaluation & Engineering, v. 18, p. 417-431.

Laycock, D., Watt, E., Tobin, R., Kelly, S., Johnston, M. and Michael, E. 2021. Examining the origins and yield impact of a stratified oil column in the Montney Formation, NE BC. Unconventional Resources Technology Conference, July 26-28, 2021, Houston, Texas, USA.

Ness, S. 2001. The application of basin analysis to the Triassic succession, Alberta Basin: An investigation of burial and thermal history and evolution of hydrocarbons in Triassic rocks. Master's thesis, University of Calgary, Calgary, Alberta, Canada, 179 p.

Rudra, A., Wood, J.M., Biersteker, V. and Sanei, H., 2024. Oil migration from internal and external source rocks in an unconventional hybrid petroleum system, Montney Formation, western Canada. International Journal of Coal Geology, v. 285, 104473.

Sanei, H. 2020. Genesis of solid bitumen. Scientific Reports, v. 10, 15595.

Sanei, H., Wood, J.M., Ardakani, O.H., Clarkson, C.R. and Jiang, C. 2015. Characterization of organic matter fractions in an unconventional tight gas siltstone reservoir. International Journal of Coal Geology, v. 150, p. 296-305.

Thompson, K.F.M. 2016. Hybrid gas condensates and the evolution of their volatile light hydrocarbons. Organic Geochemistry, v. 93, p. 32–50.

Watt, E.A., Laycock, D.P., Michael, E., Tobin, R.C., Kelly, S. and Johnston, M.N. 2022. Hydrocarbon charge and petroleum system evolution of the Montney Formation: A multidisciplinary case study of the Blueberry sub-play in Northeast British Columbia, Canada. Bulletin of Canadian Energy Geoscience, v. 69, p. 21-50.

Wood, J.M. 2013. Water distribution in the Montney tight gas play of the western Canadian sedimentary basin: significance for resource evaluation. SPE Reservoir Evaluation & Engineering, v. 16, p. 290-302.

Wood, J.M. 2015. Crushed-rock vs. full-diameter core samples for water-saturation determination in a tight-gas siltstone play. SPE Reservoir Evaluation & Engineering, v. 18, p. 407-416.

Wood, J.M., 2023. Intraformational migration of oil, gas-condensate and methane-rich gas in a major unconventional petroleum accumulation: Montney Formation, Western Canada. Latin America Unconventional Resources Technology Conference, December 4-6, 2023, Buenos Aires, Argentina.

Wood, J.M. and H. Sanei, H. 2016. Secondary migration and leakage of methane from a major tight-gas system. Nature Communications, v. 7, 13614.

Wood, J.M. and Sanei, H. 2017. Secondary migration of methane as a modifier of hydrocarbon fluid distribution in the Montney tight-gas fairway. GeoConvention, May 15-19, 2017, Calgary, Alberta, Canada.

Wood, J.M., Sanei, H., Curtis, M.E. and Clarkson, C.R. 2015. Solid bitumen as a determinant of reservoir quality in an unconventional tight gas siltstone play. International Journal of Coal Geology, v. 150–151, p. 287–295.

Wood, J.M., Sanei, H., Ardakani, O.H., Curtis, M.E., Akai, T. and Currie, C. 2018a. Solid bitumen in the Montney Formation: Diagnostic petrographic characteristics and significance for hydrocarbon migration. International Journal of Coal Geology, v. 198, p. 48-62.

Wood, J.M., Sanei, H., Ardakani, O.H., Curtis, M.E. and Akai, T. 2018b. Organic petrography and scanning electron microscopy imaging of a thermal maturity series from the Montney tight-gas and hydrocarbon liquids fairway. Bulletin of Canadian Petroleum Geology, v. 66, p. 499–515.

Wood, J.M., Ardakani, O.H., Sanei, H., Curtis, M.E. and Royer, D. 2020. Application of paleoporosity and bitumen saturation concepts to tight-gas accumulations containing solid bitumen. International Journal of Coal Geology, v. 228, 103547.

Wood, J.M., Euzen T., Sharp, L. and Leroux, S. 2021a. Phase separation and secondary migration of methane-rich gas accompanying uplift of an unconventional tight-hydrocarbon system, Montney Formation, western Canada. Marine and Petroleum Geology, v. 124, 104808.

Wood, J.M., Curtis, M.E., Ardakani, O.H. and Sanei, H. 2021b. Movement of native fluids during scanning electron microscopy imaging of petroliferous siltstones: Evidence from the Montney Formation, western Canada. Fuel, v. 290, 120020.

Wood, J.M., Cesar, J., Ardakani, O.H., Rudra, A. and Sanei, H. 2022. Geochemical evidence for the internal migration of gas condensate in a major unconventional tight petroleum system. Scientific Reports, v. 12, 7931.

Wood, J.M., Euzen, T. and Cesar, J., 2024. Influence of faults on late-stage migration of methane-rich gas in a major unconventional hydrocarbon accumulation: Montney Formation, western Canada. Marine and Petroleum Geology, v. 164, 106857.

Xia, X., Michael, E. and Gao, Y. 2020. Preservation of lateral pressure disequilibrium during the uplift of shale reservoirs. AAPG Bulletin, v. 104, p. 825-843.

Yassin, M.R., Dehghanpour, H., Wood, J.M. and Lan, Q. 2016. A theory for relative permeability of unconventional rocks with dual-wettability pore network. SPE Journal, 21, p.1970-1980.

GUSSOW 2024
Montney Subsurface Evaluation: Drive Towards Excellence
Banff, AB | October 2-4

# Montney carbonate diagenesis: a tool to track down fluid flow and water/rock interaction during the Early Triassic evolution of the Western Canada sedimentary basin

Mastaneh H. Liseroudi[1], Omid H. Ardakani[1,2], Per K. Pedersen[2], Hamed Sanei[3]

1.Natural Resources Canada, Geological Survey of Canada, 2. Department of Geoscience, University of Calgary, 3. Department of Geoscience, Aarhus University

## Abstract

Fluid influx most commonly linked to regional tectonic and hydrogeologic setting of sedimentary basins, plays a critical role in diagenetic evolution of these basins. The regional history of paleofluid flow and their respective driving mechanisms can be reconstructed employing petrographic and geochemical studies coupled with geodynamics of sedimentary basins and flow and transport hydrodynamics. The current study examines carbonate diagenesis in the siltstone-dominated Early Triassic Montney Formation of the Western Canadian Sedimentary Basin (WCSB) and addresses the origin of diagenetic fluids, their major flow systems, and association with tectonic and hydrogeology of the Montney Formation in the WCSB.

Several generations of non-ferroan to ferroan calcite ($C_1$-$C_3$) and dolomite ($D_1$-$D_4$) cement formed during early to late stages of diagenesis and burial were observed in petrographic studies. Bulk $\delta^{13}C$ and $\delta^{18}O$ values of carbonate cements range from -7.1 to +0.4‰ and -9.5 to -2.8‰ (VPDB), respectively, noticeably lower than the estimated $\delta^{13}C$ and $\delta^{18}O$ values of Early Triassic seawater. The $^{87}Sr/^{86}Sr$ isotope ratio of these samples are also significantly more radiogenic than Early Triassic seawater, ranging from 0.7108 to 0.7128.

The isotopic values ($\delta^{18}O$ and $^{87}Sr/^{86}Sr$) support mixing of the Montney Formation pore water through extensive interaction with hot basinal brines derived either from Precambrian metasediments or interacted with siliciclastic strata in the basin. Influx of hydrothermal fluids in western Alberta and deeper burial depth and higher temperature in northeastern British Columbia were also influential in carbonate cementation in the Montney Formation. Calcite and dolomite cements with $^{13}C$-depleted signature validate the role of organic carbon, possibly stemmed from breakdown and oxidation of organic matter and hydrocarbons via microbial and thermochemical sulfate reduction processes.

According to the results of this study, in addition to the Montney Formation pore water, the fluids responsible for the diagenetic evolution of the Montney Formation were partially sourced from metasediments of the Cordillera thrust belt and topography-driven fluids resulted from Jurassic to Cretaceous Columbian and Laramide tectonism. This study highlights the significance of an integrated approach for a better understanding of diagenetic history of sedimentary basins, that has implications for resource exploration and development, and carbon storage.

## Statement of the background

Carbonate cementation is an important diagenetic process that exerts a strong control on the reservoir properties and heterogeneity of siliciclastic rocks (e.g., Mansurbeg et al., 2008; Wang et al., 2016; Lai et al., 2017), and evaluation of their potential for carbon capture, utilization, and storage (CCUS) (e.g., Lindner 2017; Orr, 2018; Raza et al., 2019; Paluszny et al., 2020).

The Lower Triassic Montney Formation of the Western Canadian Sedimentary Basin (WCSB) is a siltstone-dominated siliciclastic unit with a complex geological and geochemical history (Figs. 1 and 2). Investigating the depositional and diagenetic evolution of the Montney Formation is of particular interest due to its deposition after the end-

Permian mass extinction, the Earth's largest bio-crisis (e.g., Schoepfer et al., 2013; Zhang et al., 2019) and its world-class unconventional tight gas and hydrocarbon liquids reserves (National Energy Board, 2013; USGS, 2019). Additionally, the sedimentological and diagenetic development of the formation has significantly aroused interest in this formation as the potential target for future CCUS (e.g., Bachu and Stewart, 2002; Heller and Zoback, 2014; Rajkumar et al., 2021) and $CO_2$ Enhanced Oil and Gas Recovery (EOGR; e.g., Ghanizadeh et al., 2020; Eghbalvala et al., 2020; Thomas et al., 2020) in the WCSB, contributing to reduce greenhouse gas emissions.

Carbonate cementation (calcite and dolomite) is a significant diagenetic event that affected the reservoir quality and fluid flow of the Montney Formation by occlusion of porosity, and accordingly permeability (Liseroudi et al., 2022b). Hence, constraining the controls on carbonate cement formation, the origin of fluid flow events, and its timing has substantial implications for hydrocarbon exploration and establishing the evolution of the basin-scale fluid flow system within a geological time scale. Furthermore, carbonate diagenesis in fine to very-fine-grained sedimentary rocks, like the Montney Formation, is one of the essential elements controlling both storage potential and caprock integrity of these rocks for CCUS (e.g., Mouzakis et al., 2016; Miller et al., 2016; Lindner, 2017; Fatah et al., 2022).

## Aims and Objectives

Studies performed on the origin of carbonate diagenetic fluids and their precipitation conditions in the Montney Formation are limited and local in scale, both geographically and stratigraphically. Based on limited petrographic and stable isotope geochemical data, Wiebe, (1991), Barber, (2002) and Egbobawaye, (2017) suggested that formational fluids diluted by meteoric water contributed to the formation of carbonate cement in the Montney Formation. In contrast, Vaisblat et al., (2021) based on petrographic evidence, proposed that carbonate cementation mostly occurred in the shallow burial realm through reflux of brines from nearshore saltpans. In those studies, however, minimal attention has been devoted to the nature of diagenetic fluids, major geological and geochemical processes, and water/rock interactions incorporating isotope

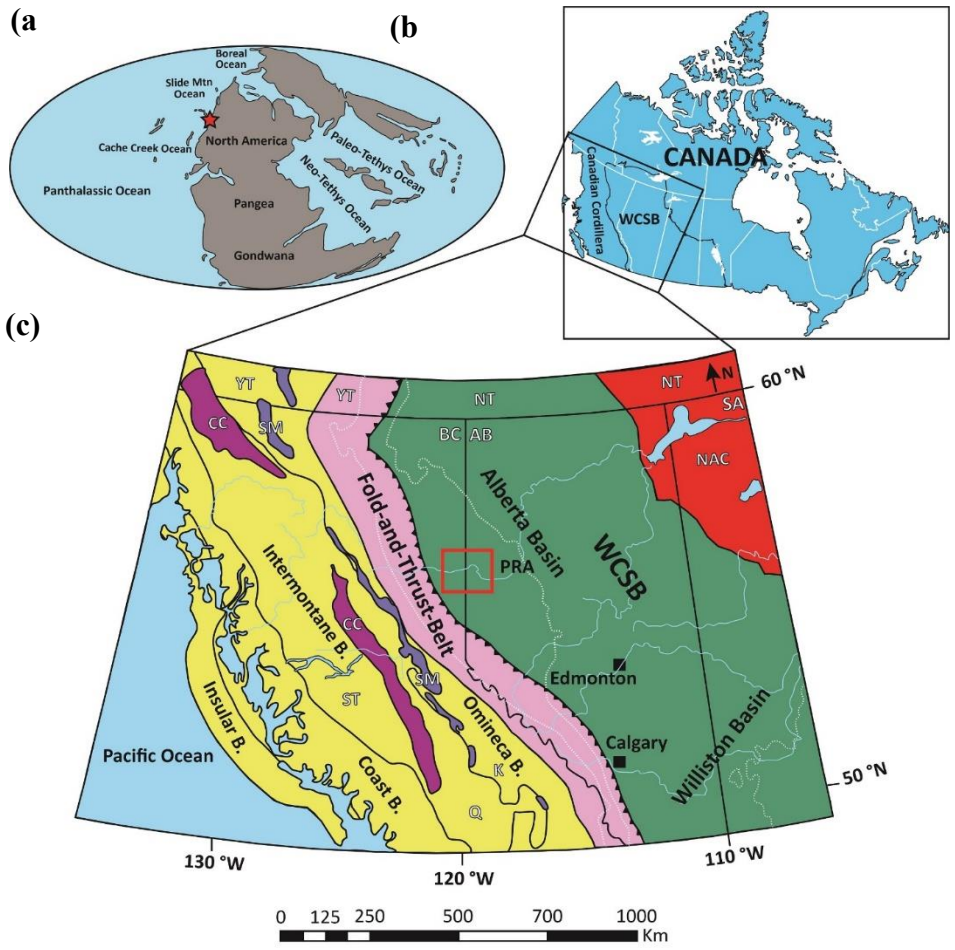


Figure 1: (a) Paleogeographic map of the world during Early Triassic (modified after Colorado Plateau Geosystems image, 2016). The red star shows the location of the WCSB during Early Triassic. (b) Location of the WCSB and Canadian Cordillera on Canada's map. (c) Geological map of the Canadian Cordillera with the main belts and accreted terranes and the WCSB with the location of Peace River Arch (PRA), and Alberta and Williston basins (modified after Rohais et al., 2018). The white dashed line shows preserved Triassic strata. The red rectangle shows the location of the present study. Abbreviations: Terranes: CC: Cache Creek; ST: Stikini; Q: Quesnellia; K: Kootney; SM: Slide Mountain; Provinces and Territories: AB: Alberta; BC: British Columbia; SA: Saskatchewan; YT: Yukon; NT; Northwest; NAC: North America craton. B stands for the belt as Omineca Belt and others.

geochemistry. Most importantly, none of those studies have addressed the regional formation- and basin-scale fluid flow mechanism(s) and the role of the tectonic evolution of the Canadian Cordillera and the WCSB.
In the current research, we aim to evaluate the source of diagenetic fluids responsible for carbonate cementation and their regional basin-scale pathways in the foreland basin of western Canada. Transmitted light petrography, high resolution backscattered scanning electron microscopy (SE, BSE), energy dispersive X-ray spectroscopy (SEM-EDXS) and SEM-Cathodoluminescence (SEM-CL) imaging techniques, bulk stable carbon and oxygen isotope analysis, as well as bulk strontium isotope geochemistry of a regional Montney Formation core sample set in western Alberta (WAB) and northeast British Columbia (NEBC; Fig. 2a) were employed to examine the source of carbonate diagenetic fluids in the Montney Formation.

## Materials and methods

The study area is located in the subsurface of WAB and NEBC in the Peace River region in the WCSB (Fig. 2a). The WCSB is a westward-thickening sedimentary wedge with up to 6 km thickness in front of the fold-and-thrust belt of the present-day Canadian Rocky Mountains and zero thickness at the eastern erosional edge near the Canadian Shield, divided into the Alberta and Williston basins by the Bow Island Arch (Fig. 1a-c; Price, 1994; Wright, 1994; Tufano and Pietras, 2017).

The Montney Formation of the WCSB consists of shoreface to offshore and turbidite deposits (Fig. 2a; Davies et al., 1997; Moslow and Davies, 1997; Zonneveld and Moslow, 2018), with a mixed siliciclastic-carbonate depositional environment. Stratigraphically, the Permian Belloy Formation and the phosphatic shales of the Doig Formation unconformably underlies and overlie the Montney Formation in the Peace River region, respectively (Fig. 2b; Davies et al., 1997, 2018; Zonneveld and Moslow, 2018).

Normal faults, including the Carboniferous to Permian Dawson Creek Graben Complex and precursor Precambrian basement normal and strike-slip faults, are abundant in the Peace River region (Barclay et al., 1990; Davies et al., 1997; Hope et al., 1999; Berger et al., 2008). It is seismically and structurally demonstrated that extensional normal faulting was episodically reactivated from the Devonian until the Cretaceous (Hope et al., 1999; Mei, 2009), particularly by loading of compressional thrust faults associated with the Jurassic Colombian and Cretaceous Laramide orogenies (O'Connell et al., 1990).

Diagenetic evolution and compositional modifications in the mineral assemblages of the Montney Formation occurred significantly from Early Triassic (early diagenetic stage corresponding to shallow burial) to Late Cretaceous (late diagenetic stage corresponding to deep burial (Liseroudi et al., 2022b, 2021, 2020; Vaisblat et al., 2021) and prior to maximum burial (80-60 Ma, Ness, 2001; Ducros et al., 2017; Rohais et al., 2018; Watt et al., 2022).

Paleogeographically, the Montney Formation was deposited on a clastic ramp along the northwestern margin of the Pangea Supercontinent (Golonka, 2007) in a collisional retro-foreland basin (Rohais et al., 2018). Subsequently, it is possible to establish a close link between the formation of thrust sheets of the Canadian Cordillera, the induced rising

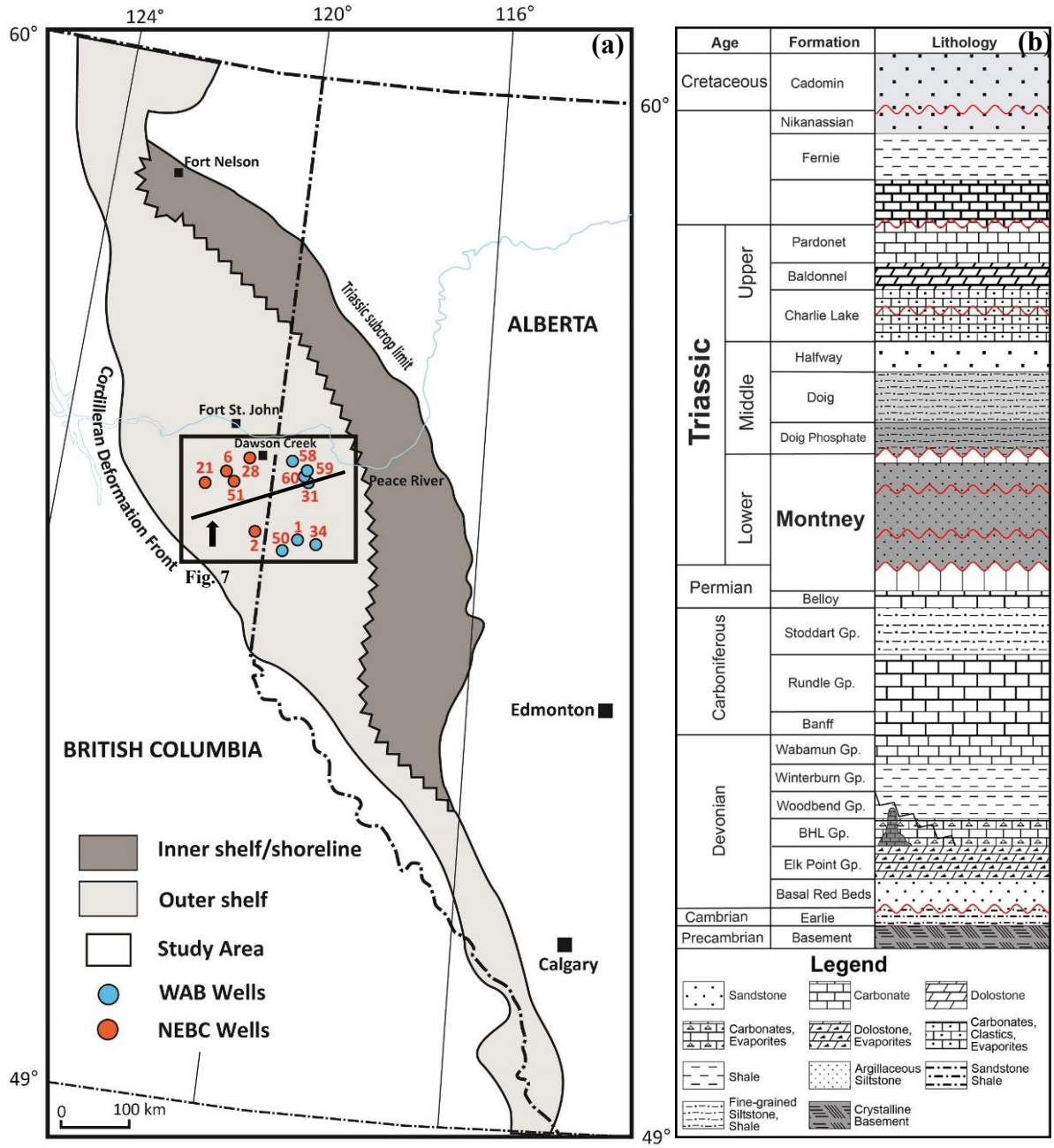


Figure 2: (a) Montney subcrop and outcrop map (modified after Edwards et al., 1994) with the location of the studied wells in NEBC (orange circles) and WAB (blue circles). The black line shows the location of the cross-section in Fig. 7. (b) Lithostratigraphic column of the WCSB in WAB and NEBC (modified after Mossop and Shetsen, 1994; Davies et al., 1997, 2018; Zonneveld and Moslow, 2018).

topography and the foreland basin, and the burial diagenetic and fluid flow evolution of the Montney Formation that occurred mainly from the Late Jurassic to Late Cretaceous (Liseroudi et al., 2022b).

One hundred and ten core samples from twelve wells located in NEBC and WAB were used for transmitted light petrography, bulk carbon and oxygen stable isotope, and $^{87}Sr/^{86}Sr$ isotope ratio analysis of calcite and dolomite. Ninety thin sections were prepared and used for petrographic studies at the Geological Survey of Canada, Calgary. Nine representative samples were later examined in more detail by scanning electron microscopy (SEM) and energy-dispersive X-ray spectroscopy (SEM-EDXS) at the University of Calgary. SEM-Cathodoluminescence (CL) petrography was also carried out on six representative samples.

Thirty-three bulk samples from eleven wells with calcite and dolomite cement were analyzed by Continuous Flow Isotope Ratio Mass Spectrometry (CF-IRMS) at the University of Calgary for carbon ($\delta^{13}C$) and oxygen ($\delta^{18}O$) isotopes. Thirty-seven individual dolomite-bearing samples from six wells in WAB were also selected for $\delta^{13}C$ and $\delta^{18}O$ isotopes measurement of dolomite. All results are reported in the per mil notation (‰) relative to the international V-PDB scales for $\delta^{13}C$ and $\delta^{18}O$.

The $^{87}Sr/^{86}Sr$ isotope ratios were measured in six bulk carbonate (mixed calcite and dolomite) and two bulk dolomite samples using a Thermo-Fisher Scientific Triton Thermal Ionization Mass Spectrometer (TIMS) at the University of Calgary. Since $^{87}Sr$ can be leached from Rb-bearing minerals (most likely illite, K-feldspar, and detrital mica in the Montney Formation) as a result of the decay of $^{87}Rb$ to $^{87}Sr$, or from the dissolution of $^{87}Sr$-enriched evaporite minerals (Chaudhuri and Clauer, 1992), bulk carbonate samples were treated using a set of sequential leaching experiments with nitric acid ($HNO_3$) and the variations of $^{87}Sr/^{86}Sr$ isotope ratios versus reaction time were assessed (four-step leaching experiment; Spencer et al., 2018).

## Results and Discussion

### Dolomite and calcite petrography

Dolomite occurs mostly as pore-filling or replacive cement and exhibits spatial variations in morphology and chemical composition in NEBC and WAB (Figs. 3a-g.). In NEBC, it is mainly present as euhedral planar-e, ferroan rhombic crystals (Fig. 3a-d) which under SEM-CL, exhibit different phases of overgrowth zones ($D_1$, dull blue-luminescent and $D_2$, non-luminescent) mostly nucleated on rounded and corroded non-ferroan detrital dolomite grains (Dd-bright blue luminescent; Fig. 3a-b). In WAB, dolomite type noticeably changes to subhedral to anhedral planar-s to non-planar pore-filling cement ($D_3$; Fig. 3e-f) that is less ferroan than the NEBC dolomite. $D_4$ occurs locally in some wells in both NEBC and WAB as euhedral planar-e, ferroan rhombic crystals and replaces anhydrite cement (Fig. 3g).

Calcite was mainly observed in NEBC and occurs as three types of non-ferroan to ferroan pore-filling ($C_1$), replacive ($C_2$) and non-ferroan pore-filling cement ($C_3$) (Figs. 3c, h-j). Under SEM-CL, it is present as authigenic cement without detrital cores. The $C_1$ cement in NEBC is subhedral to anhedral in shape. Non-ferroan to ferroan replacive calcite ($C_2$) occasionally has overgrown pore-filling calcite cement ($C_1$) and partially replaced zoned dolomite crystals ($D_1$ and $D_2$) in some samples in NEBC (Fig. 3h). In WAB, calcite was only observed in one well (well 50) as non-ferroan pore-filling cement ($C_3$; Fig. 3i-j). Under SEM-CL, this calcite phase shows a uniform dull blue CL with a minor relic of likely earlier calcite cement featured by brighter blue CL (Fig. 3j).

### Isotope geochemistry

Separation of distinct calcite and dolomite cement phases was not possible due to the very-fine crystalline nature of the cements in the Montney Formation, therefore, bulk isotopic data were measured in this study that theoretically is representative of the latest carbonate cements precipitated ($C_2$, $D_2$, and $D_3$), and diagenetic events/processes controlled carbonate cementation. The localized last calcite ($C_3$) and dolomite ($D_4$) cements were difficult to sample, therefore, their $\delta^{13}C$ and $\delta^{18}O$ values were not measured.

The $\delta^{13}C$ and $\delta^{18}O$ values of dolomite range from -6.5 to +0.4‰ (mean = -3.1 ± 1.8‰ VPDB; n = 70) and -7.8 to -2.8‰ (mean = -5.1 ± 1.2‰ VPDB; n = 70), respectively (Fig. 4). The $\delta^{13}C$ values of pore-filling dolomite ($D_3$) in WAB ranges from -5.9 to +0.4‰ (mean = -3.1± 2.2‰ VPDB; n = 37), which is almost similar to the $\delta^{13}C$ values of zoned dolomite ($D_2$) in NEBC (-6.5 to -0.5‰; mean = -3.0 ± 1.2‰ VPDB; n = 33).

The $\delta^{18}O$ values of dolomite in WAB and NEBC varies over a narrow range; however, they exhibit two distinct clusters. The $\delta^{18}O$ values of $D_3$ cement in WAB vary from -6.1 to -2.8‰ (mean = -4.1 ± 0.7‰ VPDB; n = 37), which are approximately 2‰ more enriched than $\delta^{18}O$ values of $D_2$ in NEBC (-7.8 to -4.8‰; mean = -6.1 ± 0.7‰ VPDB; n = 33; Fig. 4). Calcite ($C_2$) in NEBC shows similar $\delta^{13}C$ values to dolomite ranging from -7.1 to -0.1‰ (mean = -3.1 ± 1.4‰ VPDB; n = 33) with a narrower range of $\delta^{18}O$ values varying from -9.5 to -6.0‰ (mean = -8.2 ± 0.8‰ VPDB; n = 33; Fig. 4).

The $^{87}Sr/^{86}Sr$ ratios of six mixed calcite and dolomite samples after 0.5 hours of reaction with nitric acid (four-step leaching test) range from 0.7104 to 0.7116. After 3 hours of reaction with nitric acid, the $^{87}Sr/^{86}Sr$ isotope varies from 0.7114 to 0.7136. The range of the $^{87}Sr/^{86}Sr$ isotope ratios after 48 and 192 hours of reaction varies from 0.7128 to 0.7252 and 0.7131 to 0.7550, respectively. These samples also yield $^{87}Sr/^{86}Sr$ isotope ratios ranging from 0.7105 to 0.7117 after eight days of full leaching. The $^{87}Sr/^{86}Sr$ isotope values of two bulk dolomite samples are almost similar, ranging from 0.7108 to 0.7114 after eight days of full leaching (Figs. 5 and 6a-b).

### Source of carbonate cement: inferences from carbon and oxygen isotope geochemistry

The $\delta^{13}C$ and $\delta^{18}O$ values of the best-preserved marine carbonates during the Early Triassic range from -2.0 to +4.3‰ V-PDB and -5.2 to -0.7‰ V-PDB, respectively (Fig. 4; Veizer et al., 1999; Korte et al., 2005; Stebbins et al., 2019). Therefore, theoretically, any carbonate cement precipitated from Early Triassic pore water should reflect this isotopic signature. The calcite cement ($C_2$) of the Montney Formation ($\delta^{13}C$ = -7.1 to -0.1‰ VPDB with 91% of data points ranging from -4.9 to -1.4‰ V-PDB and $\delta^{18}O$ = -6.0 to -9.5‰ VPDB) exhibits lower $\delta^{13}C$ and $\delta^{18}O$ values than Early Triassic pore water (Fig. 4). The $\delta^{13}C$ value of dolomite cement is believed to be similar to or slightly enriched (*ca* 1‰) than its contemporaneous calcite (Sheppard and Schwarcz, 1970). The lower $\delta^{13}C$ values of calcite and dolomite may suggest contribution from $^{12}C$-enriched sources (e.g., Hitchon and Krouse, 1972; Machel et al., 1995; Swart, 2015; Lai et al., 2017).

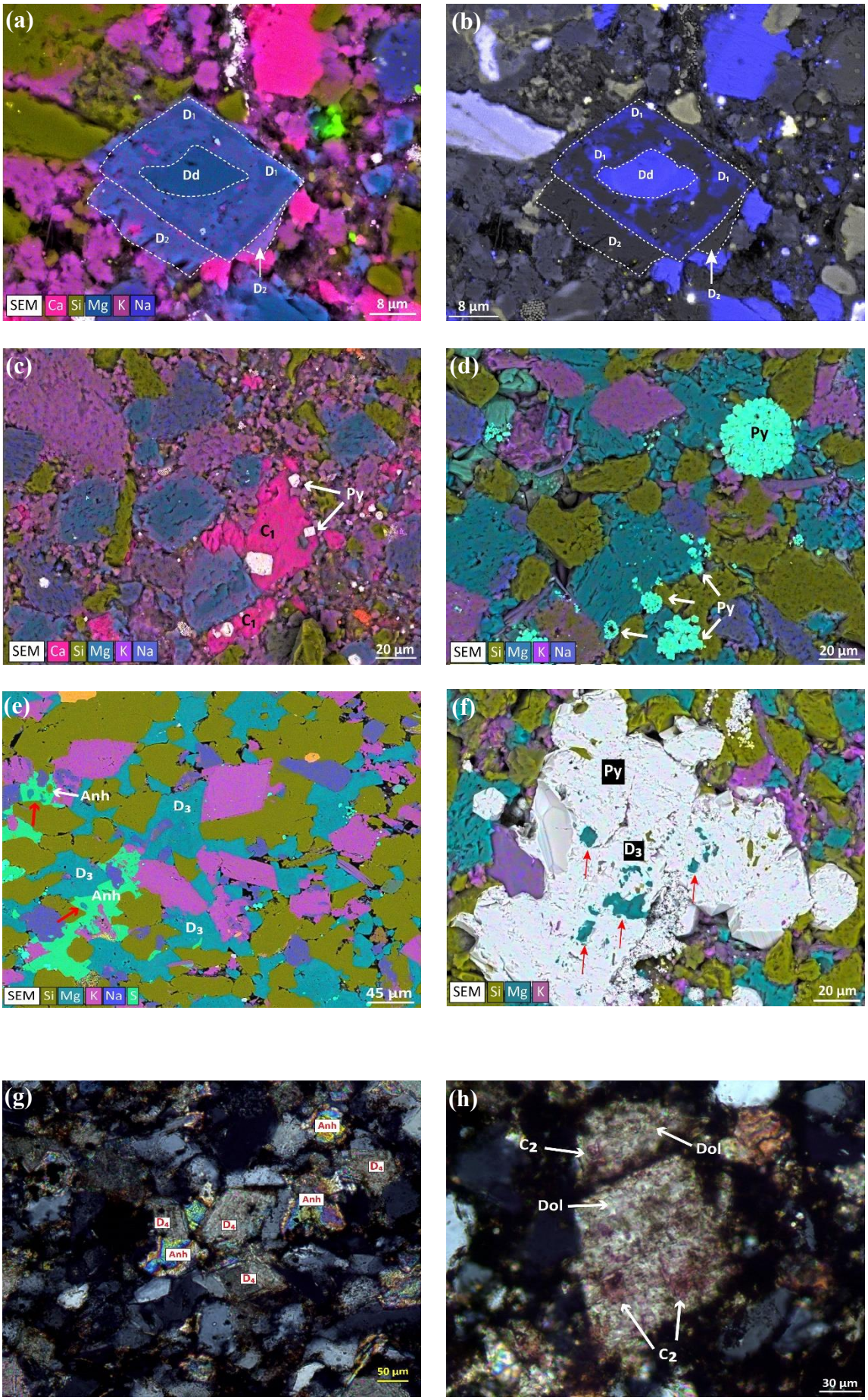
(a)
D1
Dd
D1
D2
D2
SEM Ca Si Mg K Na
8 µm
(b)
D1
D1
Dd
D1
D2
D2
8 µm
(c)
Py
C1
C1
SEM Ca Si Mg K Na
20 µm
(d)
Py
Py
SEM Si Mg K Na
20 µm
(e)
Anh
D3
D3
Anh
D3
SEM Si Mg K Na S
45 µm
(f)
Py
D3
SEM Si Mg K
20 µm
(g)
Anh
D4
Anh
D4
D4
Anh
D4
50 µm
(h)
C2
Dol
Dol
C2
30 µm

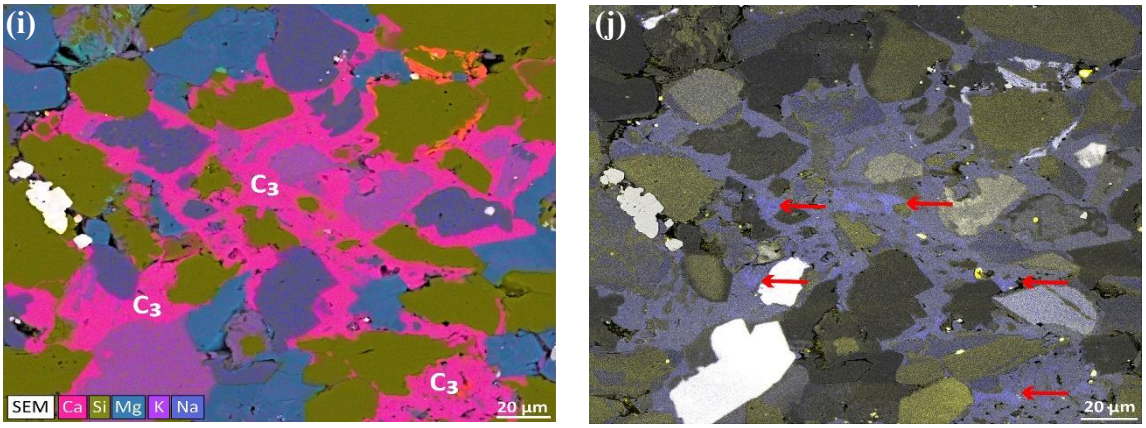


Figure 3: (a) SEM-EDXS image and (b) SEM-CL image of a planar-e zoned dolomite in NEBC with detrital core (Dd) and two generations of cement ($D_1$ & $D_2$). The first cement generation ($D_1$) is partially replaced by the second ferroan generation ($D_2$, non-luminescent; UWI: B-052-I/093-P-06/2, 4038.36 m). (c) SEM-EDXS image of zoned dolomite crystals ($D_1$ & $D_2$) and their paragenetic relationship with non-ferroan to ferroan pore-filling calcite cement ($C_1$). Note the location of cubic pyrite microcrystals (Py) on the periphery of $C_1$ cement (UWI: B-052-I/093-P-06/2, 4038.36 m). (d) SEM-EDXS image of zoned dolomite ($D_1$ & $D_2$) surrounded or superimposed by framboidal pyrite (UWI: A-036-G/093-P-01/0, 3418.70 m). (e) SEM-EDXS image of planar-s to non-planar pore-filling dolomite cement ($D_3$) in WAB. This dolomite is dissolved and replaced by later anhydrite cement (Anh-red arrow; UWI: 01-32-070-09W6/0, 2549.03 m). (f) SEM-EDXS image of pyrite clusters (coalesced pyrite, Liseroudi et al., 2021) enclosing $D_3$ cement in WAB (red arrow; UWI: 01-32-070-09W6/0, 2531.94 m). (g) Photomicrograph of the zoned dolomite cement ($D_4$) replacing earlier anhydrite cement (UWI: 14-13-078-16W6/0, 2887.70 m). (h) Photomicrograph of non-ferroan to ferroan replacive calcite cement ($C_2$) replacing dolomite crystals ($D_1$ & $D_2$) in NEBC (UWI: B-052-I/093-P-06/2, 4010.29 m). (i) SEM-EDXS image and (j) SEM-CL image of non-ferroan pore-filling cement ($C_3$) observed only in WAB. It shows a uniform dull blue luminescence with negligible remnants of a potentially earlier generation of calcite (red arrow; UWI; 16-29-069-10W6/0, 2868.72 m). Ca, Si, Mg, K, Na, S elements are superimposed X-ray responses.

The oxygen isotopic fractionation between dolomite and its precursor calcite ($\Delta\delta^{18}O_{Dolomite\text{-}Calcite}$) at 25°C is estimated to be 3 ± 1‰ (Land, 1980). Assuming a 3‰ fractionation and using the assumed Early Triassic seawater isotopic composition (Veizer et al., 1999; Korte et al., 2005; Stebbins et al., 2019), the estimated $\delta^{18}O$ value of dolomite precipitated from Early Triassic pore water should range between -2.2 to +2.3‰ (V-PDB) (Fig. 4). The $\delta^{18}O$ values of pore-filling dolomite ($D_3$; -6.1 to -2.8‰ V-PDB) in WAB and zoned dolomite ($D_2$; -7.8 to -4.8‰ V-PDB) in NEBC, together with their $\delta^{13}C$ values (-6.5 to +0.4‰ V-PDB) are noticeably lower than carbon and oxygen isotopic signatures of dolomite cement derived from Early Triassic pore water (Fig. 4).

Consequently, the high $^{18}O$-depleted signatures of the Montney Formation carbonate cements demonstrate the diagenetically-controlled isotopic modification of these phases governed by evolved Montney pore waters through water/rock interaction with deep circulated meteoric waters or hot basinal brines, the incursion of hydrothermal fluids and/or elevated temperature during later stages of burial (Morad et al., 1990; Mansurbeg et al., 2009; Mansour et al., 2014; Lai et al., 2017). The low $\delta^{13}C$ values of the calcite and dolomite phases could be attributed to meteoric waters (carrying soil $CO_2$), pore waters containing organically-derived $CO_2$ resulting from breakdown and thermal maturation, and microbial and thermochemical sulfate reduction (MSR-TSR) of organic matter and/or hydrocarbons in oil field brines during burial (Machel et al., 1995; Mansurbeg et al., 2008; Cao et al., 2017; Morad et al., 2019).

The high TDS values of the Montney Formation pore water (Hitchon et al., 1971; Kirste et al., 1997; Osselin et al., 2018, 2019), paucity of K-feldspar or mica replacement by kaolinite (Worden and Burley, 2003; Mansurbeg et al., 2020), and iron oxides or hydroxide coating around carbonate cement phases (Worden and Burley, 2003; Ulmer-Scholle et al., 2014), along with highly radiogenic $^{87}Sr/^{86}Sr$ isotope ratios of calcite and dolomite cement (discussed below; Figs. 5 and 6a-b) rule out the contribution of deep-flushed meteoric waters to burial diagenesis and the low $\delta^{13}C$ and $\delta^{18}O$ values of carbonate cement in the Montney Formation.

Dolomite cement, particularly in WAB ($D_3$) is coarser in crystal size, planar-s to non-planar in fabric, and lacks crystal zonation ($D_3$; Figs. 3e), suggesting its potential recrystallization from an earlier-formed dolomite cement during the progressive burial at higher temperatures or the influx of later hydrothermal fluids (e.g., Machel, 1997; Al-Aasm, 2000; Machel, 2004; Gregg et al., 2015). This interpretation is in good agreement with the timing (late early to intermediate diagenetic stage) and paragenetic relationship of $D_3$ cement with the latest crystalline pyrite (coalesced pyrite) and anhydrite phase (Liseroudi et al., 2020, 2021, 2022a), characterizing its recrystallization through the elevated temperature of deeper burial setting (20 to 170°C; Ness, 2001; Ducros et al., 2017; Gasparrini et al., 2021) and interaction of the Montney pore waters with structurally-controlled hydrothermal brines in WAB (Liseroudi et al., 2020, 2021, 2022a).

The low $\delta^{13}C$ values of $D_2$ and $C_2$ cements formed during shallow burial may have been controlled by oxidation of local primary organic matter (Beaton et al., 2010a,b; Rokosh et al., 2012; Romero-Sarmiento et al., 2016) through MSR and/or

thermal degradation of organic matter during progressive burial (Liseroudi et al., 2021). The deeper burial setting of the Montney Formation is dominated by solid bitumen/pyrobitumen resulting from late migration and the thermal cracking of hydrocarbons into this formation (Ejezie, 2007; Sanei et al., 2015; Wood et al., 2018a,b, 2020). The $^{13}C$-depleted composition of $D_3$, therefore, can be associated with TSR of organic matter and/or migrated hydrocarbons (Liseroudi et al., 2021) incorporating $^{13}C$-depleted $CO_2$ into the Montney Formation pore waters and dolomite precipitation.

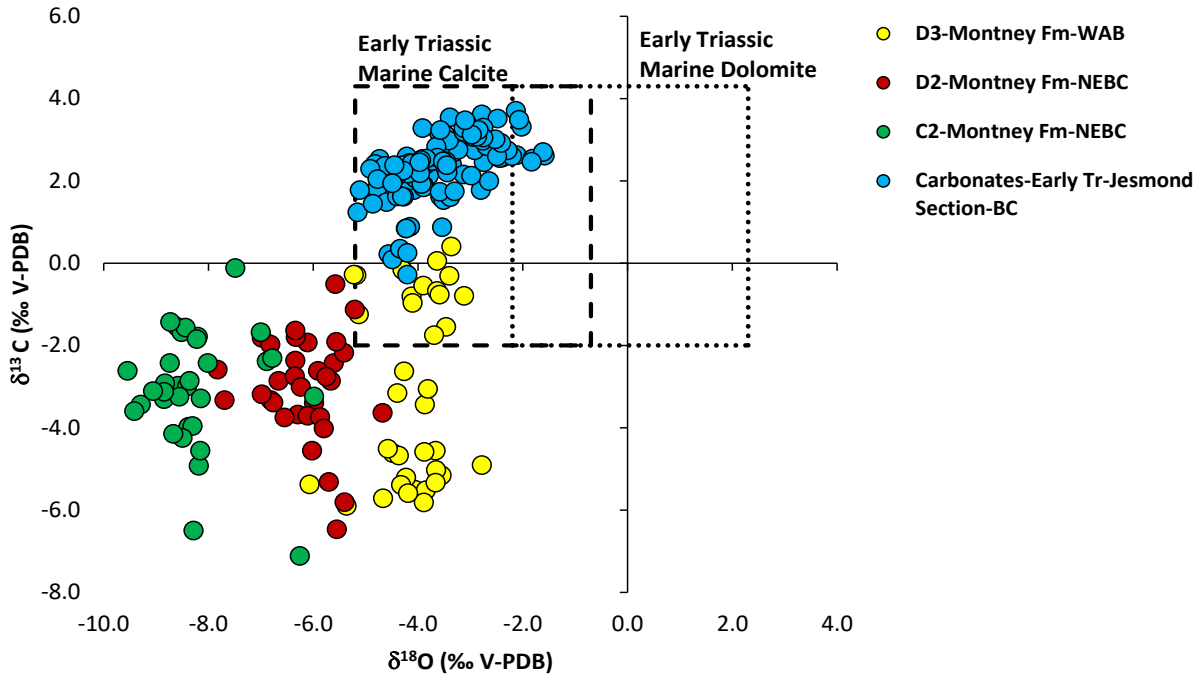


Figure 4: The $\delta^{13}C$ and $\delta^{18}O$ values of studied carbonate samples ($C_2$, $D_2$ and $D_3$) in NEBC and WAB. Estimated $\delta^{13}C$ and $\delta^{18}O$ values of Early Triassic marine calcite (dashed square) are from Veizer et al., (1999); Korte et al., (2005) and Stebbins et al., (2019). The dotted square represents calculated $\delta^{13}C$ and $\delta^{18}O$ values for dolomites precipitated from Early Triassic seawater (Land, 1980). The $\delta^{13}C$ and $\delta^{18}O$ values of Jesmond carbonate section in BC (blue circles; Stebbins et al., 2019), representative of the isotopic signature of Early Triassic seawater in the WCSB, are presented for comparison.

**Origin of paleofluids: inferences from strontium isotope geochemistry**

Considering the fine crystalline texture of carbonate cement phases in the present study, the $^{87}Sr/^{86}Sr$ isotope ratios were also measured from bulk carbonate fraction, supporting the hypothesis of potential $^{87}Sr$ contribution from Rb-bearing minerals in the host rock. The $^{87}Sr/^{86}Sr$ values of the Montney bulk carbonate (mixed calcite and dolomite) and bulk dolomite cement vary over a wide range of 0.7104 to 0.7550 during the four-step leaching experiment (Fig. 5). These Sr isotope values are more radiogenic than the estimated $^{87}Sr/^{86}Sr$ isotope ratios of coeval Triassic seawater (Figs. 5 and 6a-b; 0.7072 - 0.7082; Veizer et al., 1999; McArthur et al., 2020).

As it is shown in Fig. 5, the $^{87}Sr/^{86}Sr$ ratios of studied samples increased through time and the eight day (192 hours) leachate exhibits the highest $^{87}Sr/^{86}Sr$ ratio (0.7131 to 0.7550), suggesting potential incorporation of radiogenic strontium potentially from the decay of illite, k-feldspar and detrital mica in the mixed carbonate samples. However, a linear extrapolation of the measured $^{87}Sr/^{86}Sr$ isotope ratios to zero reaction time yields $^{87}Sr/^{86}Sr$ isotope values ranging from 0.7108 to 0.7128 (mean = 0.7119, n = 6), similar to $^{87}Sr/^{86}Sr$ ratio of dolomite samples (0.7108 to 0.7114, mean = 0.7111, n = 2) measured via the eight-day full leaching method and dolomite samples with $^{87}Sr/^{86}Sr$ isotope ratios of 0.7106 to 0.7127 from the Montney Formation (Spencer et al., 2018). These Sr isotope values are still highly radiogenic compared to the assumed 0.7072-0.7082 values of Triassic seawater (Figs. 5 and 6a-b; Veizer et al., 1999; McArthur et al., 2020).

This extrapolation confirms that highly radiogenic Sr isotope values are not internally sourced from the decay of Rb-bearing mineral phases through time within the Montney siltstone. Rather, they are representative of diagenetic modification and the addition of radiogenic Sr to the Montney Formation pore waters from external sources. These external sources could be deep basinal brines controlled topographically and tectonically by the Canadian Cordillera (discussed below; Fig. 7; e.g., Qing and Mountjoy, 1992, 1994; Garven, 1995; Machel and Cavell, 1999).

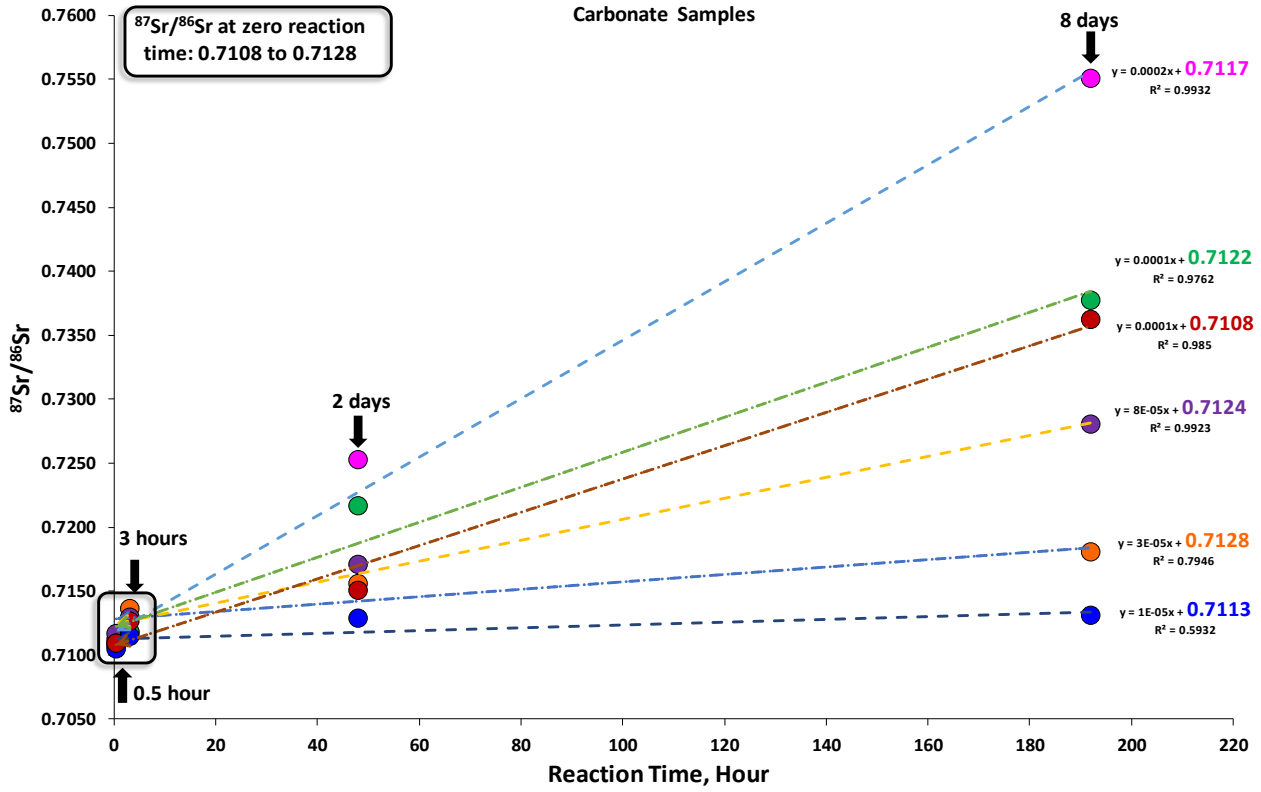


Figure 5: $^{87}Sr/^{86}Sr$ isotope ratios of bulk carbonate (mixed calcite and dolomite) samples through four steps of sequential leaching test (0.5, 3, 48, 192 hours) and reaction with nitric acid. Note the extrapolated values (y-intercept) at zero reaction time (black rectangle). The linear extrapolation of the measured $^{87}Sr/^{86}Sr$ isotope values to zero reaction time yields $^{87}Sr/^{86}Sr$ isotope values ranging from 0.7108 to 0.7128 that is highly radiogenic.

**Montney Formation paleohydrogeology; tectonically-induced or topography-driven?**

Fluid movement in sedimentary basins can be both intraformational or basin-scale (cross-formational; Worden and Burley, 2003; Worden et al., 2016). Two major driving mechanisms for basin-scale fluid migration in sedimentary basins are: 1) topography-driven fluid flow in foreland basins and 2) tectonically-induced fluid flow in foreland fold-and-thrust belts (Garven, 1995). In the former, the topographic relief associated with the emplacement of thrust sheets leads to the circulation of groundwaters through the deepest underlying strata in the adjacent foreland basin and interaction with hot deep basinal fluids of the basin. The latter is related to the expulsion of fluids from thrust sheets resulting from tectonic compression in orogenic belts (Garven, 1995).

Evidence from petrographic examinations (optical and SEM), paragenetic relationships between different diagenetic phases, and carbon, oxygen, and Sr isotopes confirm that the diagenetic evolution of the Montney Formation was controlled by both intraformational (Montney Formation pore water) and basin-scale cross-formational fluid flow. Burial diagenetic fluid flow of the formation is associated with the inception of the North America Cordillera (during Jurassic time) and subsequent development of the retro-foreland basin in the WCSB (Price, 1994; DeCelles, 2004; Miall and Blakey, 2008; Rohais et al., 2018). Basin modelling suggests that shallow to deep burial of the Montney Formation coincides with the occurrence of Columbian (Jurassic-Early Cretaceous) and Laramide (Late Cretaceous to Early Tertiary) orogenies (Ness, 2001; Ducros et al., 2017; Rohais et al., 2018), and three pulses of tectonic thrusting of the Rocky Mountain fold-and-thrust belt (Pană and van der Pluijm, 2015).

The regional background strontium isotope ratio of basinal shales in the WCSB is 0.7120 (Machel and Cavell, 1999; Buschkuehle and Machel, 2002). This suggests $^{87}Sr/^{86}Sr$ isotope values of > 0.7120 (up to 0.7320) of carbonate or sulfate cement can be representative of cross-formational fluids expelled from Precambrian metasediments of the Cordillera deformed belt or structurally-controlled interaction of hydrothermal fluids with metasediments of Precambrian basement (Machel and Cavell, 1999; Buschkuehle and Machel, 2002; Lonnee and Machel, 2006; Gromek et al., 2012).

The strontium isotope ratios of the Montney carbonate cement (0.7108 to 0.7128, mean = 0.7117, n = 8; Figs. 5 and 6a-b), however are similar to both basinal shales and Precambrian metasediments. They are also comparable to Sr isotope values of Upper Devonian to Lower Cretaceous brines in the Alberta Basin (Group I formation waters = 0.7076 to 0.7129; Connolly et al., 1990), the majority of Paleozoic hydrothermal saddle dolomites of the WCSB and eastern United States (Davies and Smith, 2006) or Devonian hydrothermal saddle dolomites of southeastern Alberta to northwestern British Columbia (0.7082

to 0.7159; Al-Aasm et al., 2019), that were proposed to have been sourced from structurally-controlled warm (~ 75-200 °C) and saline (~ 8 to 27 wt. % NaCl eq.) basinal hydrothermal fluids interacted with underlying Devonian

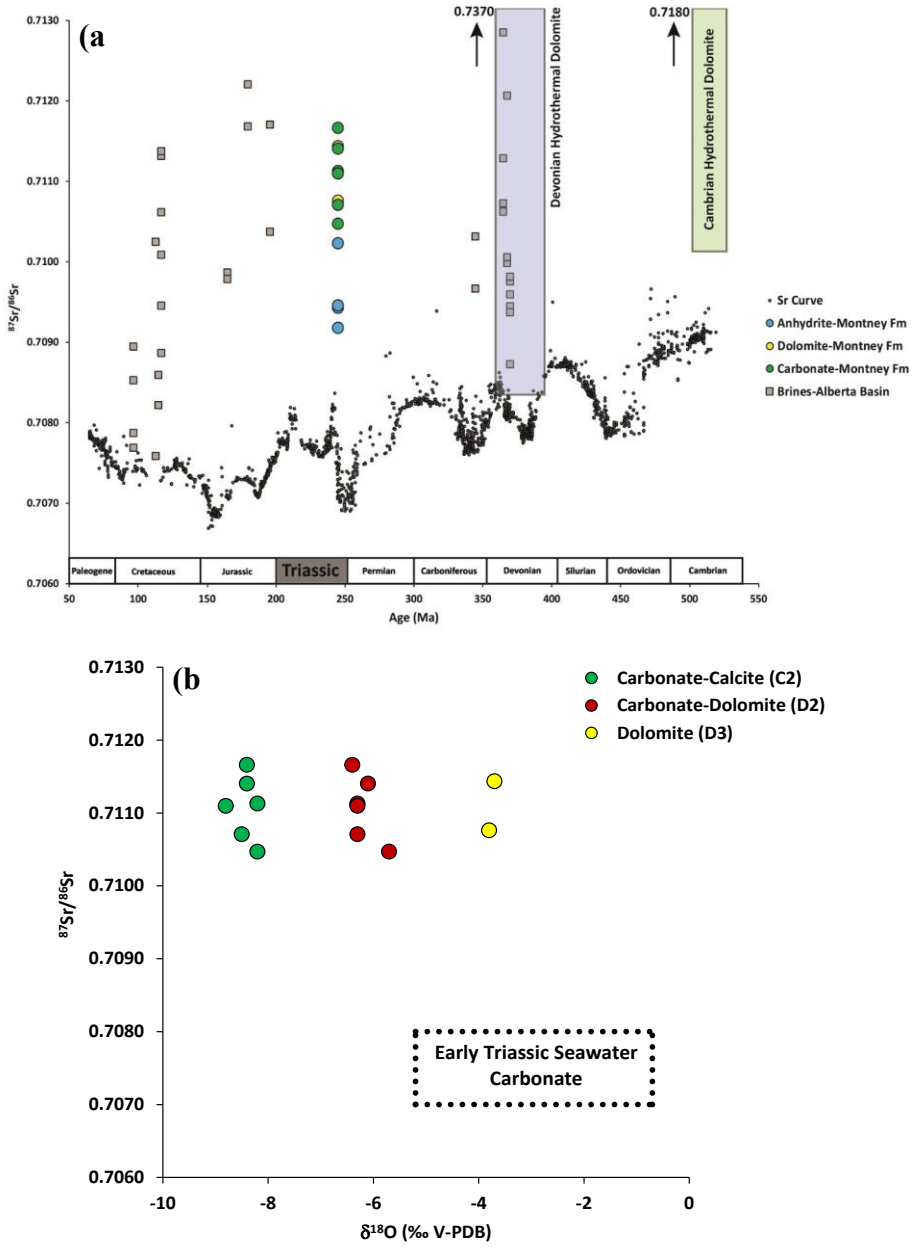


Figure 6: (a) Secular $^{87}Sr/^{86}Sr$ curve of Paleogene to Cambrian seawater (Veizer et al., 1999; McArthur et al., 2020) and $^{87}Sr/^{86}Sr$ isotope ratios of dolomite and bulk carbonate (mixed calcite and dolomite) samples measured in this study. $^{87}Sr/^{86}Sr$ isotope values of fracture- and vug-filling anhydrite phases from WAB (Liseroudi et al., 2020) are also shown for comparison. $^{87}Sr/^{86}Sr$ isotope ratios of brines in Alberta are from Connolly et al., (1990). Blue and green rectangles show $^{87}Sr/^{86}Sr$ isotope values of Devonian hydrothermal dolomite (Davies and Smith, 2006; Al-Aasm et al., 2019) and Cambrian hydrothermal dolomite (Davies and Smith, 2006), respectively. (b) $^{87}Sr/^{86}Sr$ isotope values vs. $\delta^{18}O$ values of bulk carbonate and dolomite samples in the Montney Formation. The dotted rectangle is representative of estimated $^{87}Sr/^{86}Sr$ isotope ratios and $\delta^{18}O$ values of Early Triassic seawater (Veizer et al., 1999; Korte et al., 2005; Stebbins et al., 2019; McArthur et al., 2020).

and Cambrian clastics and metasediments of Precambrian basement (Fig. 6a; Davies and Smith, 2006; Al-Aasm et al., 2019).

Three out of six NEBC carbonate samples that are geographically closer to the Cordillera deformation belt exhibit $^{87}Sr/^{86}Sr$ isotope ratios of > 0.7120 (Fig. 5). The WAB dolomite samples (0.7113 ± 0.0005) were taken from wells away from the deformation front (Figs. 1c and 2a); however, they are still significantly more radiogenic than the assumed values of coeval Triassic seawater (0.7072-0.7082; Veizer et al., 1999; McArthur et al., 2020; Fig. 6a-b). The $^{87}Sr/^{86}Sr$ isotope ratios of fracture- and vug-filling anhydrite in WAB were also reported to be highly radiogenic (0.7092 to 0.7102; Fig. 6a), and to have

originated from Devonian-sourced sulfate-rich hydrothermal brines interacted with Precambrian crystalline rocks and other siliciclastic strata in the basin and migrated upward through deep-rooted fault networks to the Montney Formation (Liseroudi et al., 2020).

As previously discussed, the $\delta^{18}O$ values of carbonate cement are also $^{18}O$-depleted and lower than the assumed $\delta^{18}O$ values of Early Triassic seawater (Figs. 4 and 6b; Veizer et al., 1999; Korte et al., 2005; Stebbins et al., 2019). The $\delta^{18}O$ values of $C_2$ calcite in NEBC range from -9.5 to -6.0‰ (mean = -8.2 ± 0.8‰ V-PDB). NEBC $D_2$ cement is also more $^{18}O$-depleted ($\delta^{18}O$ = -7.8 to -4.8‰ V-PDB; mean = -6.1 ± 0.7‰ VPDB) than WAB $D_3$ cement (-6.1 to -2.8‰ V-PDB; mean = -4.1 ± 0.7‰ VPDB).

However, the juxtaposition of NEBC with the Cordillera deformed belt along with more negative $\delta^{18}O$ values and radiogenic $^{87}Sr/^{86}Sr$ isotope values suggest the contribution of both topography-driven and tectonically-induced fluid incursions to the diagenetic evolution of the Montney Formation (Fig. 7). Based on the observed geochemical evidence explained above, a portion of fluids could have potentially been driven out of metasediments of the Cordillera thrust belt and also topography-controlled and flushed through the basin and the Montney Formation in NEBC as a result of the Jurassic to Cretaceous Columbian and Laramide tectonism (Fig. 7). The elevated topography adjacent to the thrust belt forced the basin groundwaters to flow deep into the underlying high and low permeable formations and interact with hot and radiogenic basinal fluids leading to lower $\delta^{18}O$ values and more radiogenic strontium isotope signatures of $D_2$ cement in NEBC (Fig. 7).

The geochemical evidence of earlier tectonically- and topography-driven fluid flow models (Qing and Mountjoy, 1992, 1994; Machel and Cavell, 1999; Buschkuehle and Machel, 2002), however, suggested that basinal fluids moving updip and away from the compressed belt and elevated topography (here towards Alberta) should be more $^{18}O$-enriched and less radiogenic due to their interaction and mixing with cooler formation waters of shallower strata. This may be the case for WAB $D_3$ cement with slight enrichment in $^{18}O$ values (2‰, Fig. 4), and general depletion in radiogenic strontium signals (Fig. 6a-b). Nonetheless, $D_3$ cement is $^{18}O$-depleted ($\delta^{18}O$ = -6.1 to -2.8‰ V-PDB), considerably radiogenic (0.7108 to 0.7114) and recrystallized.

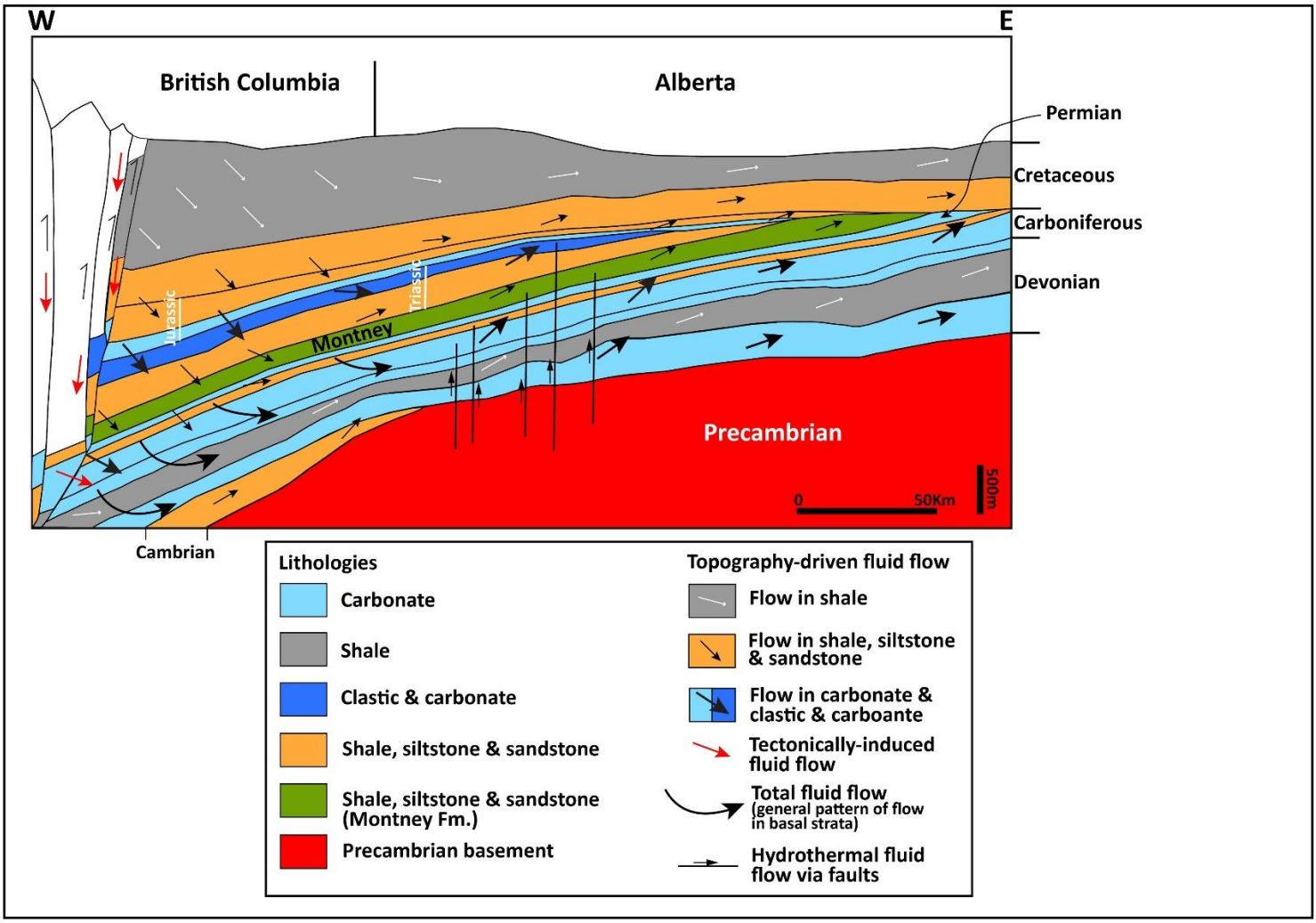

Figure 7: Schematic cross-section of the study area in WAB and NEBC (shown on Fig. 2a) with the illustration of potential fluid flow systems (tectonically-induced and topography-driven; e.g., Garven, 1995; Machel and Cavell, 1999), and faults-controlled hydrothermal fluid flow (Liseroudi et al., 2020) contributed to the diagenetic fluid evolution of the Montney Formation. For the purpose of simplicity, fluid flow driven by erosional rebound is not shown on this cross-section. Details in text.

The $\delta^{18}O$ values of pore waters and brines in the Montney Formation and underlying formations in Alberta (Devonian Woodbend to Wabamun groups and Carboniferous Banff and Rundle and Stoddart groups) vary from -15.9 to +10.7‰ SMOW (n = 153), with 93% of samples ranging from -8.0 to +9.0‰ SMOW (n = 142; Hitchon and Friedman, 1969; Connolly et al., 1990; Simpson, 1999; Osselin et al., 2018; Owen et al., 2020). Some of these formations consist of shale or sandy shales (Mossop and Shetsen, 1994) with higher radiogenic strontium content. Hence, it is possible for tectonically- and topography-driven diagenetic fluids migrating updip towards Alberta to have interacted with clastics and formation waters of these strata with lower $\delta^{18}O$ values and more radiogenic strontium signals.

The WAB hydrogeology is predominantly governed by late hydrothermal fluids derived from Precambrian basement and Devonian evaporites via deep-seated normal fault networks (Liseroudi et al., 2020, 2021, 2022a). These networks of deep faults in Alberta propagate upward into Triassic strata or even Cretaceous rocks (Eaton et al., 1999; Hope et al., 1999; Mei, 2009) and facilitated the incursion of hydrothermally-controlled basinal brines into the Montney Formation (Fig. 7). Hence, we suggest that diagenetic evolution, including carbonate diagenesis of the Montney Formation in WAB was controlled by the Montney pore waters mixed with the basin-scale tectonically- and topography-driven diagenetic fluids, and hydrothermal fluid flow (Liseroudi et al., 2020, 2021; 2022a,b).

## Conclusions

Carbonate diagenesis, the origin of diagenetic paleofluids, and the main fluid flow mechanisms in the siltstone-dominated Montney Formation of the WCSB was investigated using petrography and isotope geochemistry coupled with regional tectonic and hydrogeology studies. Following are the main results of the study:

1) Carbonate diagenesis in the Montney Formation consists of non-ferroan to ferroan calcite ($C_1$-$C_3$) and dolomite ($D_1$-$D_4$) cement formed during early to late stages of diagenesis. Progressive carbonate cementation is evident from the morphology of carbonate crystals, the presence of overgrowth cement, and their paragenetic relationship with other authigenic minerals in the samples.

2) Both calcite and dolomite are $^{13}C$- and $^{18}O$-depleted relative to the assumed $\delta^{13}C$ and $\delta^{18}O$ values of Early Triassic seawater. Their $^{87}Sr/^{86}Sr$ isotope values are also highly radiogenic than the Early Triassic seawater implying that the Montney Formation is diagenetically altered by fluids other than the Montney pore water.

3) The low $\delta^{18}O$ values along with radiogenic $^{87}Sr/^{86}Sr$ isotope values of dolomite and calcite cement are aligned with the contribution of deep basinal brines sourced either from metasediments of Precambrian or interacted with siliciclastic units of the basin. These isotope geochemical signatures also suggest the involvement of hydrothermal fluids in WAB and elevated burial temperature in NEBC in the diagenetic fluid evolution of the Montney Formation.

4) The low $\delta^{13}C$ values of the studied carbonate cement support the incorporation of organically-derived $CO_2$ resulting from MSR- and TSR-induced oxidation of organic matter and hydrocarbons in the Montney Formation.

5) The burial diagenetic setting of the Montney Formation was influenced by the Montney Formation pore water mixed with fluids expelled from metasediments of the Canadian Cordillera and deep circulated topography-driven fluids associated with Jurassic to Cretaceous Columbian and Laramide tectonic evolution.

## References

Al-Aasm, I.S., 2000. Chemical and isotopic constraints for recrystallization of sedimentary dolomites from the Western Canada Sedimentary Basin. Aquatic Geochemistry 6, 227–248. https://doi.org/10.1023/A:1009611224589.

Al-Aasm, I.S., Mrad, C., Packard, J., 2019. Fluid compartmentalization of Devonian and Mississippian dolostones, Western Canada Sedimentary Basin: petrologic and geochemical evidence from fracture mineralization. Canadian Journal of Earth Sciences 56, 265–305. https://doi.org/10.1139/cjes-2018-0226.

Bachu, S., Stewart, S., 2002. Geological Sequestration of Anthropogenic Carbon Dioxide in the Western Canada Sedimentary Basin: Suitability Analysis. Journal of Canadian Petroleum Technology 41, 32-40. https://doi.org/10.2118/02-02-01.

Barber, L.M., 2002. Sedimentology, Diagenesis and Reservoir Caharacterization o f the Montney Formation at Sturgeon Lake South' F' Pool West-Central Alberta, Unpublished M.Sc. thesis. University of Calgary, 563 pp.

Barclay, J.E., Krause, F.F, Campbell, R.I, Utting, J., 1990. Dynamic casting of growth faulting: Dawson Creek Graben Complex, Carboniferous-Permian Peace River Embayment, Western Bulletin of Canadian Petroleum Geology 38A, 115-145.

Beaton, A.P., Pawlowicz, J.G., Anderson, S.D.A., Berhane, H., Rokosh, C.D., 2010a. Organic Petrography of the Montney Formation in Alberta: Shale Gas Data Release. Energy Resources Conservation Board, ERCB/AGS Open File Report 2010-07.

Beaton, A.P., Pawlowicz, J.G., Anderson, S.D.A., Berhane, H., Rokosh, C.D., 2010b. Rock EvalTM, total organic carbon, and adsorption isotherms of the Montney Formation in Alberta: shale gas data release. Energy Resources Conservation Board, ERCB/AGS Open File Report 2010-05.

Berger, Z., Boast, M., Mushayandebvu, M., 2008. The contribution of integrated HRAM studies to exploration and exploitation of

unconventional plays in North America Part 1: The Peace River Arch. Reservoir 35, 42–47.
Buschkuehle, B.E., Machel, H.G., 2002. Diagenesis and paleofluid flow in the Devonian Southesk-Cairn carbonate complex in Alberta, Canada. Marine and Petroleum Geology 19, 219–227. https://doi.org/10.1016/S0264-8172(02)00014-4.
Cao, B., Luo, X., Zhang, L., Sui, F., Lin, H., Lei, Y., 2017. Diagenetic evolution of deep sandstones and multiple-stage oil entrapment: A case study from the Lower Jurassic Sangonghe Formation in the Fukang Sag, central Junggar Basin (NW China). Journal of Petroleum Science and Engineering 152, 136–155. https://doi.org/10.1016/j.petrol.2017.02.019.
Chaudhuri, S. and Clauer, N., 1992. Signatures of radiogenic isotopes in deep subsurface waters in continents. In: Clauer, N., Chaudhuri, S., (Eds.), Isotopic Signatures and Sedimentary Records. Lecture Notes in Earth Sciences 43, pp. 497–529.
Connolly, C.A., Walter, L.M., Baadsgaard, H., Longstaffe, F.J., 1990. Origin and Evolution of Formation Waters, Alberta Basin, Western Canada Sedimentary Basin. II. Isotope systematics and water mixing. Appllied Geochemistry 5, 397–413.
Davies, G.R., Moslow, T.F., Sherwin, M.D., 1997. The Lower Triassic Montney Formation, west-central Alberta, Bulletin of Canadian Petroleum Geology 45, 474-505.
Davies, G.R., Smith, L.B., 2006. Structurally controlled hydrothermal dolomite reservoir facies: An overview. American Association of Petroleum Geologists Bulletin 90, 1641–1690. https://doi.org/10.1306/05220605164.
Davies, G.R., Watson, N., Moslow, T.F., Maceachern, J.A., 2018. Regional subdivisions, sequences, correlations and facies relationships of the lower triassic montney formation, west-central Alberta to northeastern British Columbia, Canada-With emphasis on role of paleostructure. Bulletin of Canadian Petroleum Geology 66, 23–92.
DeCelles, P.G., 2004. Late Jurassic to Eocene evolution of the Cordilleran thrust belt and foreland basin system, western U.S.A. American Journal of Science 304, 105–168. https://doi.org/10.2475/ajs.304.2.105.
Ducros, M., Sassi, W., Vially, R., Euzen, T., Crombez, V., 2017. 2-D basin modeling of the Western Canada sedimentary basin across the Montney-Doig system: Implications for hydrocarbon migration pathways and unconventional resources potential. AAPG Memoir 114, 117–134. https://doi.org/10.1306/13602027M1143703.
Dutton, S.P., 2008. Calcite cement in Permian deep-water sandstones, Delaware Basin, west Texas: Origin, distribution, and effect on reservoir properties. American Association of Petroleum Geologists Bulletin 92, 765–787. https://doi.org/10.1306/01280807107
Eaton, D.W., Ross, G.M., Hope, J., 1999. The rise and fall of a cratonic arch: A regional seismic perspective on the Peace River Arch, Alberta. Bulletin of Canadian Petroleum Geology 47, 346–361.
Edwards, D.E., Barclay, J.E., Gibson, D.W., Kvill, G.E., Halton, E., 1994. Triassic Strata of the Western Canada Sedimentary Basin, In: Mossop, G.D., Shesten, I. (Eds.), Geological Atlas of the Western Canadian Sedimentary Basin. Canadian Society of Petroleum Geologists, Calgary, pp. 259–275.
Egbobawaye, E.I., 2017. Isotopes ($^{13}C$ and $^{18}O$) Geochemistry of Lower Triassic Montney Formation, Northeastern British Columbia, Western Canada. Natural Science 9, 355–376. https://doi.org/10.4236/ns.2017.910034.
Eghbalvala, M., Habibi, A., Dehghanpour, H., 2020. A Laboratory Protocol for Evaluating Microemulsions for Enhanced Oil Recovery while Fracturing, SPE Canada Unconventional Resources Conference, SPE-200002-MS. https://doi.org/10.2118/200002-MS.
Ejezie, N., 2007. Triassic Oil Families and Possible Source Rocks, Peace River Embayment Area, Alberta, Canada, Unpublished M.SC. thesis, University of Calgary, 408 pp.
Fatah, A., Mahmud, H.B., Bennour, Z., Golami, R., Hossain, M., 2022. The impact of supercritical CO2 on the pore structure and storage capacity of shales. Journal of Natural Gas Science and Engineering 98, 104394. https://doi.org/10.1016/j.jngse.2021.104394.
Garven, G., 1995. Continental-scale ground water flow and geologic processes. Annual Reviews of Earth and Planetary Sciences 23, 89-117.
Gasparrini, M., Lacombe, O., Rohais, S., Belkacemi, M., Euzen, T., 2021. Natural mineralized fractures from the Montney-Doig unconventional reservoirs (Western Canada Sedimentary Basin): Timing and controlling factors. Marine and Petroleum Geology 124, 140826. https://doi.org/10.1016/j.marpetgeo.2020.104826.
Ghanizadeh, A., Song, C., Clarkson, C.R., Younis, A., 2020. Experimental Evaluation of Relative Permeability in Tight Oil Systems: Examples from North American Tight Oil Plays. SPE/AAPG/SEG Unconventional Resources Technology Conference. URTEC-2020-3052-MS. https://doi.org/10.15530/urtec-2020-3052.
Golonka, J., 2007. Late Triassic and Early Jurassic palaeogeography of the world. Palaeogeography, Palaeoclimatology, Palaeoecology 244, 297–307. https://doi.org/10.1016/j.palaeo.2006.06.041.
Gregg, J.M., Bish, D.L., Kaczmarek, S.E., Machel, H.G., 2015. Mineralogy, nucleation and growth of dolomite in the laboratory and sedimentary environment: A review. Sedimentology 62, 1749–1769. https://doi.org/10.1111/sed.12202.
Gromek, P., Gleeson, S.A., Simonetti, A., 2012. A basement-interacted fluid in the N81 deposit, Pine Point Pb-Zn District, Canada: Sr isotopic analyses of single dolomite crystals. Mineralium Deposita 47, 749–754. https://doi.org/10.1007/s00126-012-0435-2.
Heller, R., Zoback, M., 2014. Adsorption of Methane and Carbon Dioxide on Gas Shale and Pure Mineral Samples. Journal of Unconventional Oil and Gas Resources 8, 14–24. http://dx.doi.org/10.1016/j.juogr.2014.06.001.
Hitchon, B., Billings, G.K., Klovan, J.E., 1971. Geochemistry and origin of formation waters in the western Canada sedimentary basin-III. Factors controlling chemical composition. Geochimica et Cosmochimica Acta 35, 567–598. https://doi.org/10.1016/0016-7037(71)90088-3.
Hitchon, B., Friedman, I., 1969. Geochemistry and origin of formation waters in the western Canada sedimentary basin-I. Stable isotopes of hydrogen and oxygen. Geochimica et Cosmochimica Acta 33, 1321–1349. https://doi.org/10.1016/0016-7037(69)90178-1.
Hitchon, B., Krouse, H.R., 1972. Hydrogeochemistry of the surface waters of the Mackenzie River drainage basin, Canada. III. Stable isotopes of oxygen, carbon and sulfur. Geochimica et Cosmochimica Acta 36, 1337–1357.
Hope, J., Eaton, D.W., Ross, G.M., 1999. Lithoprobe seismic transect of the Alberta Basin: Compilation and overview. Bulletin of Canadian Petroleum Geology 47, 331–345.
Kirste, D., Desrocher, S., Spence, B., Hoyne, B., Tsang, B. Hutcheon, I. 1997. Fluid flow, water chemistry, gas chemistry and diagenesis in the subsurface Triassic in Alberta and British Columbia. Bulletin of Canadian Petroleum Geology 45, 742–764.
Korte, C., Kozur, H.W., Veizer, J., 2005. $\delta^{13}C$ and $\delta^{18}O$ values of Triassic brachiopods and carbonate rocks as proxies for coeval

seawater and palaeotemperature. Palaeogeography, Palaeoclimatology, Palaeoecology 226, 287–306. https://doi.org/10.1016/j.palaeo.2005.05.018.
Lai, J., Wang, G., Chen, J., Wang, S., Zhou, Z., Fan, X., 2017. Origin and distribution of carbonate cement in tight sandstones: The upper triassic yanchang formation chang 8 oil layer in West Ordos Basin, China. Geofluids 2017, 1–14. https://doi.org/10.1155/2018/8650963.
Land, L.S., 1980. The isotopic and trace element geochemistry of dolomite: The state of the art. In: Zenger, D.H., Dunham, J.B., Ethington, R.L., (Eds.), Concepts and Models of Dolomitization. SEPM Special Publication 28, pp. 87–110.
Lindner, E.N., 2016. Review of the Effects of CO2 on Very-Fine-Grained Sedimentary Rock/Shale - Part II: Clay Mineral & Shale Response to Hydration; NETL- TRS-10-2016; NETL Technical Report Series; U.S. Department of Energy, National EnergyTechnology Laboratory: Morgantown, WV, p 68.
Liseroudi, M.H., Ardakani, O.H., Pedersen, P.K., Sanei, H., 2022b. Fluid flow and water/rock interaction during the Early Triassic evolution of the Western Canada Sedimentary Basin as revealed by carbonate diagenesis. Marine and Petroleum Geology 142, 105765. https://doi.org/10.1016/j.marpetgeo.2022.105765.
Liseroudi, M.H., Ardakani, O.H., Pedersen, P.K., Sanei, H., 2022a. Diagenetic and geochemical controls on H2S distribution in the Montney Formation, Peace River Region, Western Canada. In: O.H., Ardakani and P.K., Pedersen (Eds.): Hydrogen sulfide (H2S) in the Montney Formation - investigating a complex issue. The Geological Survey of Canada open file report # 8878, 14-24.
Liseroudi, M.H., Ardakani, O.H., Pedersen, P.K., Stern, R.A., Wood, J.M., Sanei, H., 2021. Microbial and thermochemical controlled sulfur cycle in the Early Triassic sediments of the Western Canadian Sedimentary Basin. Journal of Geological Society of London, jgs2020-175. https://doi.org/10.1144/jgs2020-175.
Liseroudi, M.H., Ardakani, O.H., Sanei, H., Pedersen, P.K., Stern, R.A., Wood, J.M., 2020. Origin of sulfate-rich fluids in the Early Triassic Montney Formation, Western Canadian Sedimentary Basin. Marine and Petroleum Geology 114, 104236. https://doi.org/10.1016/j.marpetgeo.2020.104236.
Lonnee, J., Machel, H.G., 2006. Pervasive dolomitization with subsequent hydrothermal alteration in the Clarke Lake gas field, Middle Devonian Slave Point Formation, British Columbia, Canada. American Association of Petroleum Geologists Bulletin 90, 1739–1761. https://doi.org/10.1306/03060605069
Machel, H.G., 1997. Recrystallization versus neomorphism, and the concept of "significant recrystallization" in dolomite research. Sedimentary Geology 113, 161–168. https://doi.org/10.1016/S0037-0738(97)00078-X.
Machel, H.G., Buschkuehle, B.E., Michael, K., 2001. Squeegee flow in Devonian carbonate aquifers in Alberta , Canada. In; Cidu, R., (Ed.), Water-Rock-Interaction, Proceedings of the Tenth Interntional Symposium on Water-Rock Interaction, WRI-10, Villasimius, Italy, pp. 631–634.
Machel, H.G., Cavell, P.A., 1999. Low-flux, tectonically-induced squeegee fluid flow ("hot flash") into the Rocky Mountain Foreland Basin. Bulletin of Canadian Petroleum Geology 47, 510–533. https://doi.org/10.35767/gscpgbull.47.4.510.
Machel, H.G., Krouse, H.R., Sassen, R., 1995. Products and distinguishing criteria of bacterial and thermochemical sulfate reduction. Appllied Geochemistry 10, 373–389. https://doi.org/10.1016/0883-2927(95)00008-8.
Machel, H.G., 2004. Concepts and models of dolomitization: A critical reappraisal. In: Braithwaite,C.J.R., Rizzi, G., Darke, G., (Eds.). The Geometry and Petrogenesis of Dolomite Hydrocarbon Reservoirs. Geological Society Special Publication 245, pp. 7-63.
Mansour, A.S., Rifai, R.I., Shaaban, M.N., 2014. Geochemical constraint on the origin of the multi-mineralogic carbonate cements in the subsurface Middle Jurassic sandstones, Central Sinai, Egypt. Journal of Geochemical Exploration 143, 163–173. https://doi.org/10.1016/j.gexplo.2014.04.009.
Mansurbeg, H., Caja, M.A., Marfil, R., Morad, S., Remacha, E., Garcia, D., Martín-Crespo, T., El-Ghali, M.A.K., Nystuen, J.P., 2009. Diagenetic evolution and porosity destruction of turbiditic hybrid arenites and siliciclastic sandstones of foreland basins: Evidence from the Eocene Hecho Group, Pyrenees, Spain. Journal of Sedimentary Research 79, 711–735. https://doi.org/10.2110/jsr.2009.060.
Mansurbeg, H., Morad, S., Al Suwaidi, M., Qurtas, S., Tveiten, O.G., Shahrokhizadeh, S., Harchegani, F.K., 2020. Meteoric-water incursion into marine turbditic sandstones: Evidence from the Andrew Formation (Paleocene), UK Central Graben, North sea. Marine and Petroleum Geology 118, 104428. https://doi.org/10.1016/j.marpetgeo.2020.104428.
Mansurbeg, H., Morad, S., Salem, A., Marfil, R., El-ghali, M.A.K., Nystuen, J.P., Caja, M.A., Amorosi, A., Garcia, D., La Iglesia, A., 2008. Diagenesis and reservoir quality evolution of palaeocene deep-water, marine sandstones, the Shetland-Faroes Basin, British continental shelf. Marine and Petroleum Geology 25, 514–543. https://doi.org/10.1016/j.marpetgeo.2007.07.012.
McArthur, J.M., Howarth, R.J., Shields, G.A., Zhou, Y., 2020. Strontium Isotope Stratigraphy. In: Grastein, F.M., Ogg. J.G., Schmitz, M.D., Ogg, G.M., (Eds.), Geologic Time Scale 2020. Volume 1, Elsevier B.V., pp. 211-238. https://doi.org/10.1016/b978-0-12-824360-2.00007-3.
Mei, S., 2009. New insights on faults in the Peace River Arch region, northwest Alberta, based on existing well-log data and refined trend surface analysis. Canadian Journal of Earth Sciences 46, 41–65. https://doi.org/10.1139/E09-006.
Miall, A.D., Blakey, R.C., 2008. The Phanerozoic tectonic and sedimentary evolution of North America. In: Miall, A.D., (Ed.), the Sedimentary Basins of the United States and Canada. Sedimentary Basins of the World 5, Elsevier Science, Amsterdam, pp. 1–29.
Miller, Q.R.S., Wang, X., Kaszuba, J.P., Mouzakis, K.M., Navarre-Sitchler, A.K., Alvarado, V., McCray, J.E., Rother, G., Bañuelos, J.L., Heath, J.E., 2016. Experimental Study of Porosity Changes in Shale Caprocks Exposed to Carbon Dioxide-Saturated Brine II: Insights from Aqueous Geochemistry. Environmental Engineering Science 33, 736–744. https://doi.org/10.1089/ees.2015.0592.
Monger, J.W.H. Price, R.A. 1979. Geodynamic evolution of the Canadian Cordillera- progress and problems. Canadian Journal of Earth Sciences 16, 770-791.
Morad, D., Nader, F.H., Morad, S., Rossi, C., Gasparrini, M., Alsuwaidi, M., Al Darmaki, F., Hellevang, H., 2019. Limited thermochemical sulfate reduction in hot, anhydritic, sour gas carbonate reservoirs: The Upper Jurassic Arab Formation, United Arab Emirates. Marine and Petroleum Geology 106, 30-41. https://doi.org/10.1016/j.marpetgeo.2019.04.023.
Morad, S., Al-Aasm, I.S., Ramseyer, K., Marfil, R., Aldahan, A.A., 1990. Diagenesis of carbonate cements in Permo-Triassic sandstones from the Iberian Range, Spain: evidence from chemical composition and stable isotopes. Sedimentary Geology 67, 281–295.

https://doi.org/10.1016/0037-0738(90)90039-V.
Moslow, T.F., Davies, G.R., 1997. Turbidite reservoir facies in the lower triassic montney formation, west-central Alberta. Bulletin of Canadian Petroleum Geology 45, 507–536.
Mossop, G.D., Shetsen, I., compilers, 1994. Geological Atlas of the Western Canadian Sedimentary Basin: Calgary, Alberta, Canadian Society of Petroleum Geologists and Alberta Research Council, 510 pp.
Mouzakis, K.M., Navarre-Sitchler, A.K., Rother, G., Bañuelos, J.L., Wang, X., Kaszuba, J.P., Heath, J.E., Miller, Q.R.S., Alvarado, V., McCray, J.E., 2016. An Experimental Study of Porosity Changes in Shale Caprocks Exposed to CO2-Saturated Brines I: Evolution of Mineralogy, Pore Connectivity, Pore Size Distribution, and Surface Area. Environmental Engineering Science 33, 725–735. https://doi.org/10.1089/ees.2015.0588.
National Energy Board (NEB), 2013. Canada's Energy Future 2013, Energy Supply and Demand Projections to 2035, An Energy Market Assessment November 2013, 87 p., https://www.neb-one.gc.ca/ nrg/ntgrtd/ftr/2013/2013nrgftr-eng.pdf.
Ness, S.M., 2001. The Application of Basin Analysis to the Triassic Succession, Alberta Basin: an Investigation of Burial and Thermal History and Evolution of Hydrocarbons in Triassic Rocks, Unpublished M.Sc. thesis, University of Calgary, 192 pp.
O'Connell, S.C., Dixon, G.R., Barclay, J.E., 1990. The origin, history, and regional structural development of the Peace River Arch, Western Canada. Bulletin of Canadian Petroleum Geology 38A, 4–24.
Orr, F.M., Jr. 2018. Carbon Capture, Utilization, and Storage: An Update. SPE Journal 94190, 2444-2455. https://doi.org/10.2118/194190-PA.
Osselin, F., Nightingale, M., Hearn, G., Kloppmann, W., Gaucher, E., Clarkson, C.R., Mayer, B., 2018. Quantifying the extent of flowback of hydraulic fracturing fluids using chemical and isotopic tracer approaches. Applied Geochemistry 93, 20-29. https://doi.org/10.1016/j.apgeochem.2018.03.008
Osselin, F., Saad, S., Nightingale, M., Hearn, G., Desaulty, A.M., Gaucher, E.C., Clarkson, C.R., Kloppmann, W., Mayer, B., 2019. Geochemical and sulfate isotopic evolution of flowback and produced waters reveals water-rock interactions following hydraulic fracturing of a tight hydrocarbon reservoir. Science of the Total Environment 687, 1389–1400. https://doi.org/10.1016/j.scitotenv.2019.07.066.
Owen , J., Bustin, R.M., Bustin, A.M.M., 2020. Insights from mixing calculations and geochemical modeling of Montney Formation post hydraulic fracturing flowback water chemistry. Journal of Petroleum Science and Engineering 195, 107589. https://doi.org/10.1016/j.petrol.2020.107589.
Pană, D.I., van der Pluijm, B.A., 2014. Orogenic pulses in the Alberta Rocky Mountains: Radiometric dating of major faults and comparison with the regional tectono-stratigraphic record. GSA Bulletin 127, 480–502. https://doi.org/10.1130/B31069.1.
Paluszny, A., Graham, C.C., Daniels, K.A., Tsaparli, V., Xenias, D., Salimzadeh, S., Whitmarsh, L., Harrington, J.F., Zimmerman, R.W., 2020. Caprock integrity and public perception studies of carbon storage in depleted hydrocarbon reservoirs. International Journal of Greenhouse Gas Control 98, 103057. https://doi.org/10.1016/j.ijggc.2020.103057.
Price, R., 1994. Cordilleran tectonics and the evolution of the Western Canada sedimentary basin. In: Mossop, G.D., Shetsen, I., (Comps.). Geological Atlas of Western Canada. Canadian Society of Petroleum Geologists, pp. 13–24.
Qing, H., Mountjoy, E., 1992. Large-scale fluid flow in the Middle Devonian Presqu'ile barrier, western Canada sedimentary basin. Geology 20, 903–906.
Qing, H., Mountjoy, E.W., 1994. Formation of coarsely crystalline, hydrothermal dolomite reservoirs in the Presqu'ile Barrier, Western Canada Sedimentary Basin. American Association of Petroleum Geologists Bulletin 78, 55–77. https://doi.org/10.1306/bdff9014-1718-11d7-8645000102c1865d.
Rajkumar, P., Pranesh, V., Kesavakumar, R., 2021. Influence of CO2 retention mechanism storage in Alberta tight oil and gas reservoirs at Western Canadian Sedimentary Basin, Canada: hysteresis modeling and appraisal. Journal of Petroleum Exploration and Production Technology 11, 327–345. https ://doi.org/10.1007/s1320 2-020-01052 -7.
Raza, A., Gholami, R., Rezaee, R., Rasouli, V., Rabiei, M., 2019. Significant aspects of carbon capture and storage – A review. Petroleum 5, 335-340. https://doi.org/10.1016/j.petlm.2018.12.007.
Rohais, S., Crombez, V., Euzen, T., Zonneveld, J.P., 2018. Subsidence dynamics of the montney formation (Early triassic, western Canada sedimentary basin): Insights for its geodynamic setting and wider implications. Bulletin of Canadian Petroleum Geology 66, 128–160.
Rokosh, C.D., Lyster, S., Anderson, S.D.A., Beaton, A.P., Berhane, H., Brazzoni, T., Chen, D., Cheng, Y., Mack, T., Pana, C., Pawlowicz, J.G., 2012. Summary of Alberta's Shale- and Siltstone-Hosted Hydrocarbon Resource Potential, ERCB/AGS Open File Report 2012-06, 339 p.
Romero-Sarmiento, M.F., Euzen, T., Rohais, S., Jiang, C., Littke, R., 2016. Artificial thermal maturation of source rocks at different thermal maturity levels: Application to the Triassic Montney and Doig formations in the Western Canada Sedimentary Basin. Organic Geochemistry 97, 148–162. https://doi.org/10.1016/j.orggeochem.2016.05.002.
Sanei, H., Wood, J.M., Ardakani, O.H., Clarkson, C.R., Jiang, C., 2015. Characterization of organic matter fractions in an unconventional tight gas siltstone reservoir. International Journal of Coal Geology 150–151, 296–305. https://doi.org/10.1016/j.coal.2015.04.004.
Schoepfer, S.D., Henderson, C.M., Garrison, G.H., Foriel, J., Ward, P.D., Selby, D., Hower, J.C., Algeo, T.J., Shen, Y., 2013. Termination of a continent-margin upwelling system at the Permian-Triassic boundary (Opal Creek, Alberta, Canada). Global and Planetary Change 105, 21–35. https://doi.org/10.1016/j.gloplacha.2012.07.005.
Sheppard, S.M.F., Schwarcz, H.P., 1970. Fractionation of carbon and oxygen isotopes and magnesium between coexisting metamorphic calcite and dolomite. Contribution to Mineralogy and Petrology 26, 161–198. https://doi.org/10.1007/BF00373200.
Simpson, G.P., 1999, Sulfate reduction and fluid chemistry of the Devonian Leduc and Nisku Formations in southcentral Alberta, unpublished Ph.D. thesis, University of Calgary, 228 pp.
Spencer, R., Weedmark, T., Besplug, J., Wright, H., Behr, J.M., Corp, D.E., 2018. SEM Fabric Analyses of the Montney Formation : An Aid to Determination of Reservoir Properties. GeoConvention 2018 Extended Abstract, Calgary, Canada, pp 1-5.
Spencer, R.J., 1987. Origin of Ca-Cl brines in Devonian formations , western Canada sedimentary basin. Applied Geochemistry 2, 373–384.

Stebbins, A., Algeo, T.J., Olsen, C., Sano, H., Rowe, H., Hannigan, R., 2019. Sulfur-isotope evidence for recovery of seawater sulfate concentrations from a PTB minimum by the Smithian-Spathian transition. Earth-Science Reviews 195, 83–95. https://doi.org/10.1016/j.earscirev.2018.08.010.

Swart, P.K., 2015. The geochemistry of carbonate diagenesis: the past, present and future. Sedimentology 62, 1233-1304. doi: 10.1111/sed.12205.

Thomas, F.B., Piwowar, M., Noroozi, M., Gibb, W., Marin, J., Zhnag, H., 2020. Experimental Measurements of Montney and Duvernay Gas-Cycling Enhanced Oil Recovery GCEOR. SPE Canada Unconventional Resources Conference, SPE-199994-MS. https://doi.org/10.2118/199994-MS.

Tufano, B.C., Pietras, J.T., 2017. Coupled flexural-dynamic subsidence modeling approach for retro-foreland basins: Example from the Western Canada Sedimentary Basin. GSA Bulletin 1622-1635. https://doi.org/10.1130/b31646.1.

Ulmer-Scholle, D.S., Scholle, P.A., Schieber, J., Raine, R.J., 2014. A Color guide to the petrography of sandstones, siltstones, shales and associated rocks. AAPG Memoir 109, 526 p.

USGS, 2018. Assessment of Continuous Gas Resources in the Montney and Doig Formations, Alberta Basin Province, Canada, 2018. National and Global Petroleum Assessment. Fact Sheet 2018-3071, pp 2.

Vaisblat, N., Harris, N.B., Ayranci, K., Power, M., Debhur, C., Bish, D.L., Chalatunyk, R., Krause, F., Crombez, V., Euzen, T., Rohais, S., 2021. Compositional and diagenetic evolution of a siltstone, with implications for reservoir quality; an example from the Lower Triassic Montney Formation in western Canada. Marine and Petroleum Geology 105066, https://doi.org/10.1016/j.marpetgeo.2021.105066.

Veizer, J., Ala, D., Azmy, K., Bruckschen, P., Buhl, D., Bruhn, F., Carden, G.A.F., Diener, A., Ebneth, S., Godderis, Y., Jasper, T., Korte, C., Pawellek, F., Podlaha, O.G., Strauss, H., 1999. 87Sr/86Sr, δ13C and δ18O evolution of Phanerozoic seawater. Chemical Geology 161, 59–88. https://doi.org/10.1016/S0009-2541(99)00081-9.

Wang, J., Cao, Y., Liu, K., Liu, J., Xue, X., Xu, Q., 2016. Pore fluid evolution, distribution and water-rock interactions of carbonate cements in red-bed sandstone reservoirs in the Dongying Depression, China. Marinea and Petroleum Geology 72, 279–294. https://doi.org/10.1016/j.marpetgeo.2016.02.018.

Watt, E.A., Laycock, D.P., Michael., E., Tobin, R.C., Kelly, S., Johnston, M.N., 2022. Hydrocarbon charge and petroleum system evolution of the Montney Formation: A multidisciplinary case study of the Blueberry sub-play in Northeast British Columbia, Canada. Bulletin of Canadian Energy Geoscience 69, 21-50.

Wiebe, C.G., 1991. Diagenetic changes with depth of the Triassic Montney Formation coquina lithofacies. Unpublished B.Sc. Honors thesis, University of Calgary, 75 p.

Wood, J.M., Sanei, H., Haeri-Ardakani, O., Curtis, M.E., Akai, T., 2018a. Organic petrography and scanning electron microscopy imaging of a thermal maturity series from the montney tight-gas and hydrocarbon liquids fairway. Bulletin of Canadian Petroleum Geology 66, 499–515.

Wood, J.M., Sanei, H., Haeri-Ardakani, O., Curtis, M.E., Akai, T., Currie, C., 2018b. Solid bitumen in the Montney Formation: Diagnostic petrographic characteristics and significance for hydrocarbon migration. International Journal of Coal Geology 198, 48–62. https://doi.org/10.1016/j.coal.2018.09.004.

Worden, R.H., Benshatwan, M.S., Potts, G.J., Elgarmadi, S.M., 2016. Basin-scale fluid movement patterns revealed by veins: Wessex Basin, UK. Geofluids 16, 149–174. https://doi.org/10.1111/gfl.12141.

Worden, R.H., Burley, S.D., 2003. Sandstone Diagenesis: The Evolution of Sand to Stone. In: Burley, S.D., Worden, R.H., (Eds.), Sandstone Diagenesis: Recent to Ancient, Blackwell Publishing, pp. 3-44. https://doi.org/10.1002/9781444304459.ch.

Wright, G.N., McMechan, M.E., Potter, D.E.G., 1994. Structure and Architecture of the Western Canada Sedimentary Basin. In: Mossop, G.D., Shetsen, I., (Comps.). Geological Atlas of Western Canada. Canadian Society of Petroleum Geologists, pp. 25–40.

Zhang, L., Orchard, M.J., Brayard, A., Algeo, T.J., Zhao, L., Chen, Z.Q., Lyu, Z., 2019. The Smithian/Spathian boundary (late Early Triassic): A review of ammonoid, conodont, and carbon-isotopic criteria. Earth-Science Reviews 195, 7–36. https://doi.org/10.1016/j.earscirev.2019.02.014.

Zonneveld, J.P., Moslow, T.F., 2018. Palaeogeographic setting, lithostratigraphy, and sedimentary framework of the lower triassic montney formation of western Alberta and northeastern British Columbia. Bulletin of Canadian Petroleum Geology 66, 93–127.

GUSSOW 2024
Montney Subsurface Evaluation: Drive Towards Excellence
Banff, AB | October 2-4

# High-resolution isotope geochemistry of sulfur-bearing compounds in the Montney Formation: Implications for the source and mobility of $H_2S$

Andrew Kingston

AGAT Laboratories

## Introduction

Hydrogen sulfide ($H_2S$) is a naturally occurring highly toxic and corrosive gas, found at varying concentrations throughout the Montney Formation; however, its origin is not fully understood. Despite several recent sulfur isotope studies into the origin of $H_2S$, there is a lack of consensus as to the processes and origin(s) of $H_2S$ in produced fluids. Part of the reason for this is the Montney Formation's diverse array of sulfate and sulfide minerals, along with various mineralization phases, stemming from its complex diagenetic history. Therefore, to accurately utilize sulfur isotope fingerprinting to assess the origin of the sulfur-bearing compounds responsible for $H_2S$ generation a comprehensive evaluation of all sulfur containing minerals is required.

Sulfur cycling within sediments is complex and controlled by depositional environment (Pasquier et al., 2017; 2021a); early and late diagenetic processes (Riciputi et al., 1996), variable redox history (Pasquier et al., 2021b), and post-depositional inputs of sulfur-bearing species (e.g., hydrocarbons, sulfate-rich hydrothermal fluids, etc.) (Liseroudi et al., 2020). Sulfur isotope records derived from bulk sampling of sediments leads to the mixing of multiple sulfur-bearing phases/compounds derived from this complex history and as such represent inaccurate archives of either paleoenvironmental conditions during deposition, early diagenesis, or late diagenetic features. Therefore, to accurately assess the origin of different sulfide phases it is first necessary to characterize all forms of sulfide mineralization in the context of both depositional and diagenetic history. This is accomplished using a combination of petrographic, mineralogical, and geochemical tools at the micro-scale. In this study, we combine Secondary Ion Mass Spectrometry (SIMS) with Laser Raman Spectroscopy to evaluate both grain-specific sulfur isotope composition with *in situ* mineralogy mapping within a 200m full Montney core from Alberta.

## Methods

*In situ sulfur isotope analysis (Secondary Ion Mass Spectrometry)*

Doubly polished thick sections (100 µm) were prepared from 12 depths in the core. Following petrographic analysis, 33 regions of interest (ROI) were selected encompassing the full range of pyrite textures and mineral associations observed in the core. ROIs were cored from thick sections using a 1.5 mm diamond drill bit and arranged alongside pre-polished fragments of internal reference materials in an epoxy mount. Detailed images of ROIs were collected with backscatter electrons via scanning electron microscopy for SIMS spot selection. Sulfur isotope ratios ($^{34}S/^{32}S$) were analyzed on an IMS-1280 multi-collector ion microprobe housed in the Canadian Centre for Isotopic Microanalysis at the University of Alberta. All sulfur isotope data is reported in standard per mil (‰) notation relative to Canyon Diablo Troilite (VCDT). Total uncertainty for pyrite $\delta^{34}S$ measurements is ± 0.20 ‰ (2σ).

*In situ mineralogical analysis (Raman Spectroscopy)*

Raman spectroscopy was acquire using a Renishaw inVia Confocal Raman microscope housed in the Organic Geochemistry and Petrology Lab at the Geologic Survey of Canada in Calgary, Alberta. The Raman microscope is equipped with a 2,400 line/mm grating, Leica ×100 and ×20 objectives (N.A. = 0.9; 0.4 respectively) and a motorized stage. Excitation was via a 532 nm green laser providing up to 20 mW of power, which was reduced to 2 mW for analysis in this study. All

spectra were collected in high confocality mode to limit the excitation volume for each measurement resulting in a minimum spot size of 0.76 um at a focal length of 2 um. Mineral identification used a combination of Renishaw inorganic spectral libraries and RRUFF database (Lafuente et al., 2015).

## Results and Discussion

### *Sulfide Mineralogy and Sulfur Isotope Geochemistry*

Three main sulfide minerals were identified using Raman spectroscopy. The dominant sulfide phase is pyrite followed by marcasite and lastly minor amounts of diagenetic sphalerite. Sulfides are overwhelmingly dominated by pyrite however marcasite occurs in the basal portion of the Montney and within the underlying Belloy Formation (Fig. 1). Pyrite grain morphology is classified into four main groups including: framboidal, euhedral, coalesced, and replacive; consistent with the groups defined by Liseroudi et al. (2021). Marcasite textures vary depending on occurrence (e.g., radiating growth or replacive).

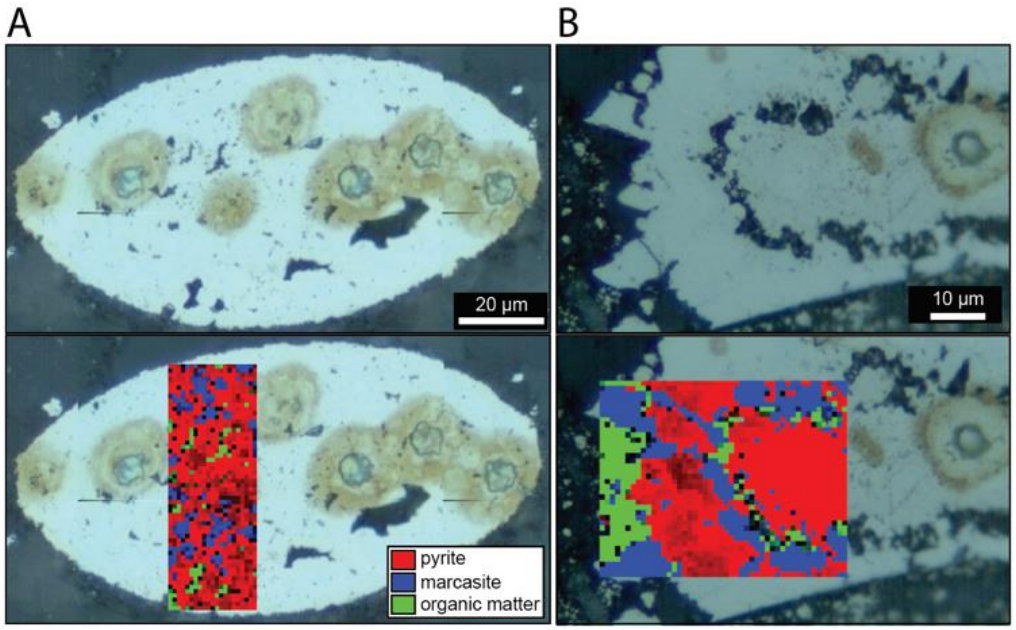


***Figure 1:*** *Raman spectroscopy map of sulfide mineralization at the boundary between the Montney and underlying Belloy Formations illustrating the co-occurrence of pyrite and marcasite. Circular structures are related to SIMS in situ isotope analysis.*

Co-occurring pyrite and marcasite grains have similarly low sulfur isotope compositions (Fig. 2) potentially reflecting similar sulfur sources (related to microbial activity), however different mineralogy reflects different environmental conditions during precipitation. Marcasite is known to form in acidic conditions, which may have been pervasive in Late Permian-Early Triassic bottom waters (Li et al., 2023). Late diagenetic pyrite is generally represented by euhedral, coalesced or replacive textures and has higher $\delta^{34}S$ values. Overall, all pyrite $\delta^{34}S$ values are lower than co-existing sulfate $\delta^{34}S$ values (i.e., co-occurring $\delta^{34}S_{SO4}$ values or Triassic seawater $\delta^{34}S_{SO4}$ curve) suggesting that it is unlikely that sedimentary sulfide minerals were precipitated from $H_2S$ generated via thermochemical sulfate reduction or anaerobic oxidation of methane associated sulfate reduction.

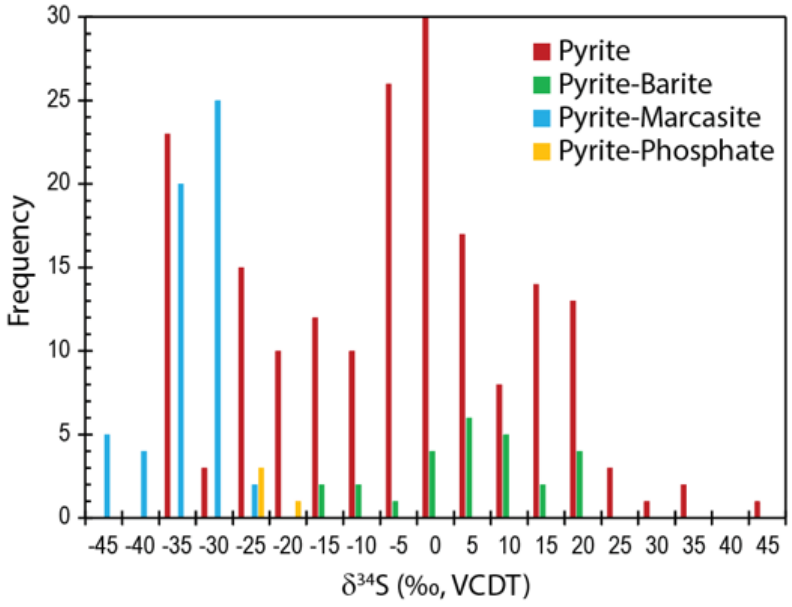


***Figure 2:*** *Distribution of sulfur isotope data with respect to host sulfide mineralogy*.

*Sulfate Mineralization*

Three phases of sulfates minerals were observed including anhydrite, gypsum, and barite. The dominant phase is anhydrite followed by gypsum and some isolated occurrences of barite. Anhydrite occurs within nodules associated with biogenic material and along with gypsum as pore-filling cements. Barite is observed in close association with pyrite where it appears to represent late diagenetic oxidation of pyrite.

Despite observing different anhydrite textures there is a small range in $\delta^{34}S_{SO4}$ values. Furthermore, anhydrite generally reflect global Triassic seawater $\delta^{34}S_{SO4}$ composition (Claypool et al., 1980; Strauss, 1999; Bernasconi et al., 2017) although slightly lower values are found at the top of the Montney section, potentially related to the incursion of later sulfate-rich fluids into this more porous section. Barite-pyrite sulfur isotope equilibrium fractionation suggests precipitation at elevated temperatures around 90°C and based on burial history implies a late diagenetic origin.

## Conclusions

Results indicate the main sulfate minerals include anhydrite, gypsum, and barite occurring as cements or nodules. The dominant sulfide mineral is pyrite, however notable occurrences of both marcasite and pyrite in the Lower Montney indicates multiple generations of sulfide mineralization occurred. Sulfur isotope composition of pyrite is highly dependent on its mineral associations with marcasite-pyrite grains exhibiting the lowest sulfur isotope values and pyrite associated with anhydrite and barite cements having the highest sulfur isotope values. Together these results suggest the Montney Formation experienced multiple phases of sulfide and sulfate mineralization implying the potential for multiple phases of $H_2S$ generation. Despite this, $H_2S$ produced from the Montney Formation has a very narrow range in sulfur isotope values (Fig. 3) indicating either $H_2S$ in the Montney is well mixed or can be attributed to a limited number of sources. The $\delta^{34}S$ values of Montney $H_2S$ are closer in composition to late forming diagenetic sulfide minerals and therefore likely relate to late-stage diagenetic processes and/or the introduction of externally derived sulfur-bearing compounds (e.g., sulfate, $H_2S$) during fluid mobilization.

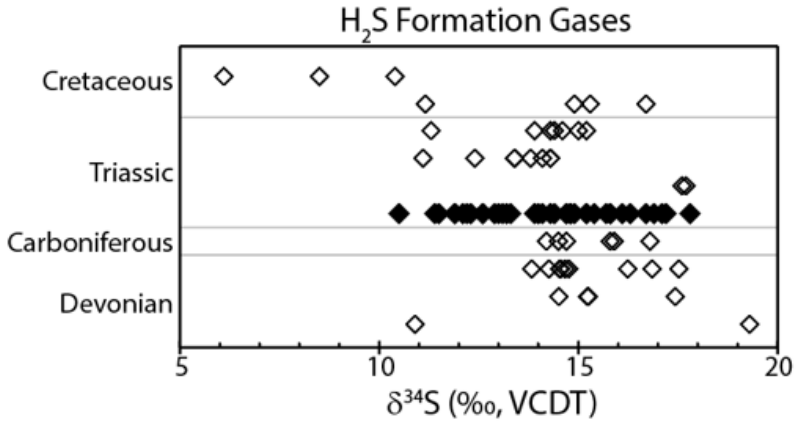


***Figure 3:*** *Sulfur isotope composition of hydrogen sulfide gas from various formations in the Western Canadian Sedimentary Basin. Montney Samples are represented by filled symbols.*

## References

Bernasconi, S. M., Meier, I., Wohlwend, S., Brack, P., Hochuli, P. A., Bläsi, H., ... & Ramseyer, K. (2017). An evaporite-based high-resolution sulfur isotope record of Late Permian and Triassic seawater sulfate. Geochimica et Cosmochimica Acta, 204, 331-349.

Claypool, G. E., Holser, W. T., Kaplan, I. R., Sakai, H., & Zak, I. (1980). The age curves of sulfur and oxygen isotopes in marine sulfate and their mutual interpretation. Chemical geology, 28, 199-260.

Lafuente B, Downs R T, Yang H, Stone N (2015). The power of databases: the RRUFF project. In: Highlights in Mineralogical Crystallography, T Armbruster and R M Danisi, eds. Berlin, Germany, W. De Gruyter, pp 1-30

Li, R., Wu, N., Shen, S. Z., Wang, X. L., Chen, H., Algeo, T. J., ... & Zhang, F. (2023). A rapid onset of ocean acidification associated with the end-Permian mass extinction. Global and Planetary Change, 225, 104130.

Liseroudi, M. H., Ardakani, O. H., Sanei, H., Pedersen, P. K., Stern, R. A., & Wood, J. M. (2020). Origin of sulfate-rich fluids in the Early Triassic Montney Formation, Western Canadian Sedimentary Basin. Marine and Petroleum Geology, 114, 104236.

Liseroudi, M. H., Ardakani, O. H., Pedersen, P. K., Stern, R. A., Wood, J. M., & Sanei, H. (2021). Microbial and thermochemical controlled sulfur cycle in the Early Triassic sediments of the Western Canadian Sedimentary Basin. Journal of the Geological Society, 178(4), jgs2020-175.

Pasquier, V., Sansjofre, P., Rabineau, M., Revillon, S., Houghton, J., & Fike, D. A. (2017). Pyrite sulfur isotopes reveal glacial− interglacial environmental changes. Proceedings of the National Academy of Sciences, 114(23), 5941-5945.

Pasquier, V., Fike, D. A., & Halevy, I. (2021). Sedimentary pyrite sulfur isotopes track the local dynamics of the Peruvian oxygen minimum zone. Nature communications, 12(1), 4403.

Pasquier, V., Bryant, R. N., Fike, D. A., & Halevy, I. (2021). Strong local, not global, controls on marine pyrite sulfur isotopes. Science advances, 7(9), eabb7403.

Riciputi, L. R., Cole, D. R., & Machel, H. G. (1996). Sulfide formation in reservoir carbonates of the Devonian Nisku Formation, Alberta, Canada: An ion microprobe study. Geochimica et Cosmochimica Acta, 60(2), 325-336.

Strauss, H. (1999). Geological evolution from isotope proxy signals—sulfur. Chemical Geology, 161(1-3), 89-101.

GUSSOW 2024
Montney Subsurface Evaluation: Drive Towards Excellence
Banff, AB | October 2-4

# Assessing in-situ organic sulfur content with drill cuttings to predict organic sulfur content in produced fluids via empirical correlation and machine learning in the Montney Blueberry sub-play

Elizabeth Watt[1], Yishu Song[2]

1. ConocoPhillips Canada, 2. ConocoPhillips

## Abstract

In an unconventional play $H_2S$ and organic sulfur content greatly impact development plans, facility designs, and product offtake decisions. A workflow was developed and successfully applied to assess in-situ organic sulfur content with drill cuttings and predict the $H_2S$ risk on production prior to hydraulic fracturing.

Drill cuttings taken with water-based mud were collected in the build and lateral sections of multiple wells across the area of study. Using a chemical solvent, oil was extracted from the drill cuttings. These extracts, along with produced oils were systematically characterized for total sulfur content, SARA fractions, detailed high-resolution gas chromatography (GC) and gas chromatography mass spectrometry (GCMS) compositions. Produced gases were analyzed for $H_2S$ content and detailed gas composition. A subset of samples were analyzed for sulfur isotopes, $\delta^{34}S$.

Substantial changes of in-situ organic sulfur content, both vertically and laterally, were observed in the study area. The produced oils have lower total sulfur content than the associated drill cuttings extracts, due to production fractionation as evidenced by both SARA and GC compositional differences. However, a strong correlation between the sulfur content in extracts and produced oils was observed. As expected, $H_2S$ content in produced gases showed a strong correlation with the sulfur content in produced oils across the area of study. These empirical correlations enable a fast turnaround $H_2S$ risk assessment during drilling or immediately after, but before well completion.

Key learnings resulting from this project include:

1. Reliable assessment of in-situ organic sulfur content in the Montney formation prior to hydraulic fracturing
2. Strong correlation between in-situ organic sulfur content and total sulfur content in produced oils
3. Strong correlation between $H_2S$ content in produced gases and total sulfur content in produced oils

Mapping the variability of in-situ organic sulfur content in the Montney rocks will hopefully lead to a better understanding of the controls on $H_2S$ distribution.

## Statement of the background

$H_2S$ and organic sulfur contents in produced fluids heavily impacts production, processing facility designs and sales specifications. Accurately predicting produced fluid quality is important to ensure these considerations are met. Organic sulfur and produced $H_2S$ in gas are highly variable and have a very complex distribution in the Montney. Utilizing the collection of drill cuttings to understand the quantity in-situ and tie to produced fluids is one potential way to estimate the produced gas $H_2S$ and produced organic sulfur weight percent.

## Aims and Objectives

The primary goal of this work is to better understand the distribution of organic sulfur in the rocks prior to completion and flowback, to characterize the variability both vertically in build sections and laterally along the horizontal wells and tie that to what is produced at surface. Secondly, this work attempts to elucidate the origin and mechanisms responsible for the produced $H_2S$ from the Montney formation. This project is specific to the Blueberry sub-play; however, it may be insightful for the overall understanding of the Montney play.

## Materials and methods

This study area is in northeast British Columbia, in the Blueberry Montney sub-play. Across the acreage the $H_2S$ content in the gas ranges from 0 to ~2% measured from produced separator gases via a Tutwiler, Draeger or Gastec, while the total sulfur content in the separator oil is between 0 to >7.5 g/kg, determined with ASTM D4294.

Cuttings from wells drilled with water-based muds are utilized to assess the in-situ organic sulfur content across the target reservoir. The drill cutting samples are collected as wet cuttings with IsoJars© and sent to the laboratory to be extracted using dichloromethane, DCM, via Soxhlet extractor. The extracted oils are then measured for total sulfur content with ASTM D1552 via a LECO S-144DR. Approximately 100 mg oil sample is analyzed with a detection limit of 0.01%.

Medium Performance Liquid Chromatography (MPLC) was used to determine the SARA (Saturate, Aromatic, Resin and Asphaltene) composition of both cutting extracts and produced oils.

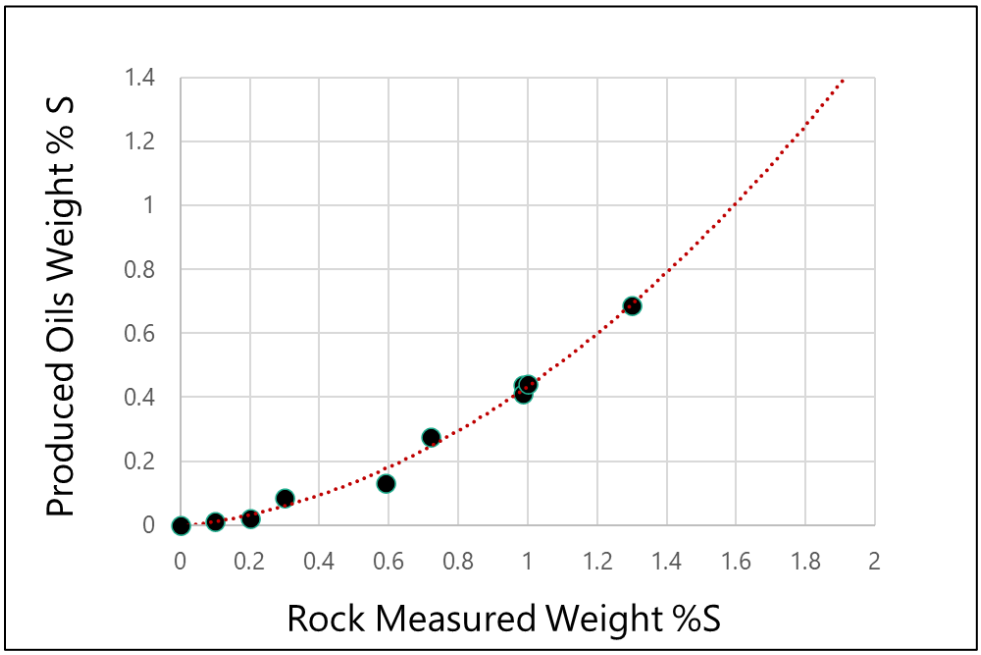


**Figure 1**: Correlation between total sulfur content in cutting extracts and total sulfur content in produced oils at the same location.

## Results and Discussion

The Montney was deposited during a unique time in history, after the Permian-Triassic mass extinction event. Slowed biotic recovery (Woods et al, 2023), Smithian thermal maximum (Lyu et al., 2019), and changes to the global carbon-sulfur cycle (Stebbins et al, 2018b) contribute to the variability that is seen throughout the ~300m section. The increasing seawater sulfate through Smithian-Spathian boundary supports the observed increase in the total sulfur content and sulfur-containing biomarkers in the extracted oils, of the Upper Montney compared to the Middle/Lower Montney, (Figure 2). The Upper Montney also shows continued vertical increase in sulfur content up through the Spathian and into the uncomfortably overlying Doig Phosphate. These observations align with an increase in available sulfate due to global climatic events during deposition and subsequent preservation of organic matter. This does not account for any additional sulfate due to migrating sulfate rich brines from either stratigraphically above or below in subsequent time.

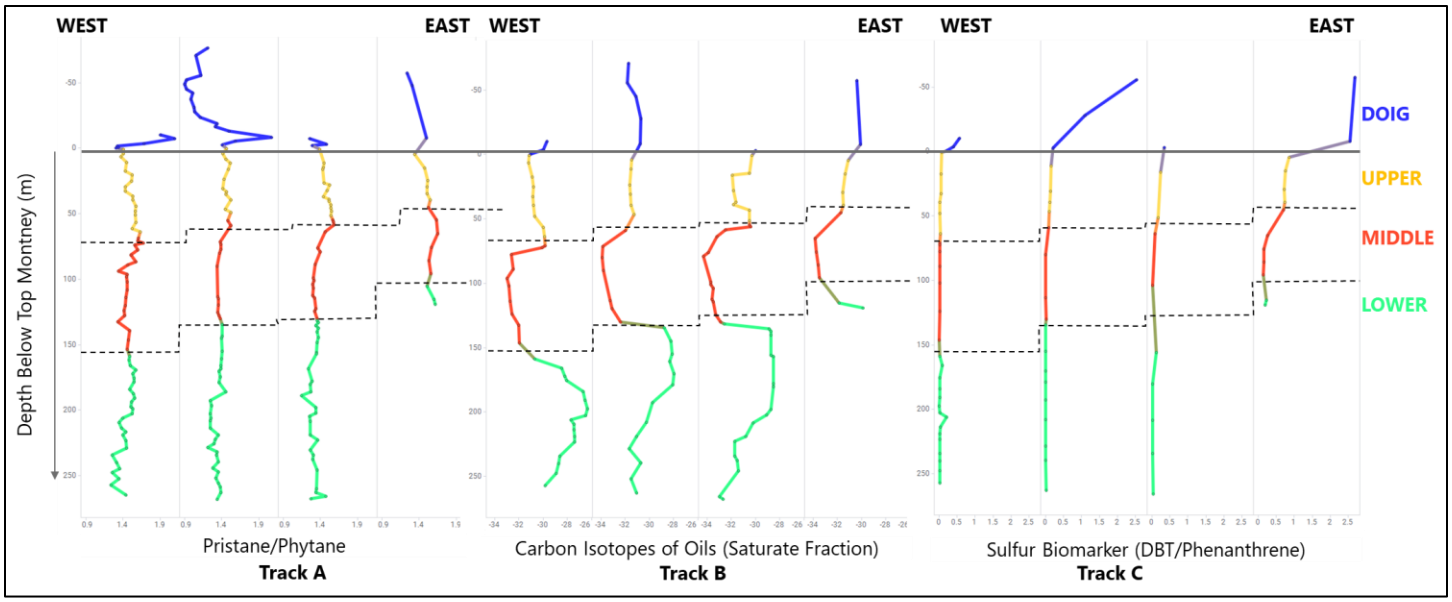


**Figure 2**: Extracted oils from core or cuttings illustrate the different depositional conditions, **Track A**, utilizing Pristane/Phytane to understand environment and oxidation conditions, the carbon isotope signature of the Saturate fraction ($\delta^{13}C$ in ‰), **Track B**, and a sulfur biomarker DBT/Phenanthrene is **Track C**. The carbon isotope excursions (CIE) are tied with global climatic events and are present today in the in-situ oils.

The Montney formation has considerable variability in produced fluids sulfur content across Alberta and British Columbia. In the north Montney Blueberry sub-play the sulfur content in the produced oils correlates overall with fluids maturity (from basin model and/or vitrinite reflectance equivalent from biomarkers and gas isotopes), as shown in Figure 3. There are notable exceptions to this correlation, including an area around the Hay River Fracture Zone, HRFZ, where despite lower maturity fluids, the produced oils and gases are sulfur poor and low $H_2S$. The mechanisms behind this are out of scope of this paper.

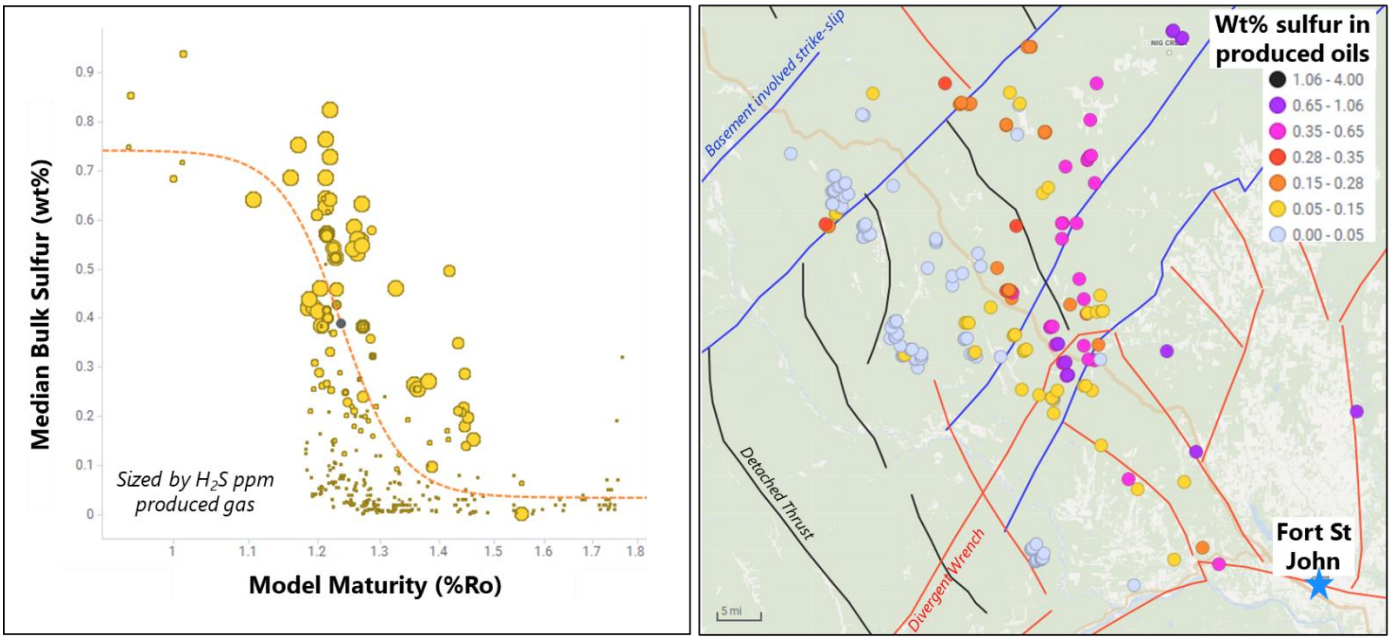


**Figure 3**: Correlation between organic sulfur in produced oils and modelled vitrinite reflectance maturity equivalent, left; Map illustrating the distribution of weight percent sulfur in produced oils both by color and size. Faults from Wood et al, 2024.

Strong correlation between total sulfur content (weight %) in rock extracts and total sulfur content in corresponding produced oil was observed, as shown in, Figure 1. This correlation, a nonlinear relationship via curve fitting, enables prediction of total sulfur content in the produced oils based on total sulfur content in the cutting extracts from a new well prior to completion and flowback. This dataset is still in its infancy and will continue to expand, to improve understanding of the impact of the completion, drilling mud contaminants and data bias on the range of expected outcomes.

The total sulfur content in the produced oils also correlates to the $H_2S$ content in the produced gases, as shown in Figure 4, which is captured with a non-linear curve fit. This enables predicting $H_2S$ content in produced gas with total sulfur content in produced oil, from the total sulfur content in drill cutting extracts. With this workflow, an assessment of $H_2S$ content in produced gas is available, post drilling but before hydraulic fracturing.

The maturity of the produced oils from Montney is consistent with its SARA compositions. Generally, for oil generated from the same source rock, its asphaltenes and resin contents decrease as oil maturity increases, and vice versa. This was observed in both produced oils and rock extracts in the Montney, where fluids of lower maturity from the east have higher asphaltenes and resin content than fluids of higher maturity from the west. At a given well location, produced oil has lower asphaltene and resin content than the corresponding cutting extracts. This is a widely observed phenomenon, termed as production fractionation, in which heavy and polar petroleum fractions are left behind in formation rock as production proceeds. For low permeability rock like Montney, production fractionation is expected to be more pronounced. Some heavy and polar components that are solvent extractable, may not be producible at all. Organic sulfur in oil mainly resides as heteroatoms in asphaltenes and resins, to a lesser extent in aromatics, and least in saturates. This nicely explains the observed correlation of total sulfur content between produced oils and corresponding cutting extracts, as shown in Figure 1.

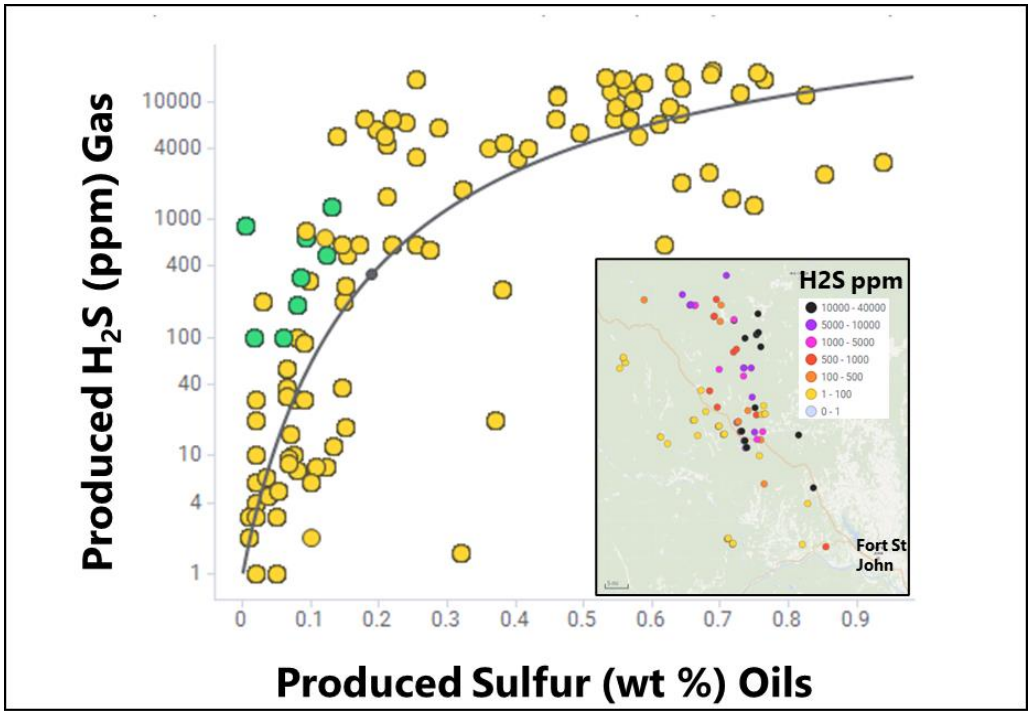


**Figure 4**: The correlation between produced sulfur in oils and produced $H_2S$ in gas. The inset map shows the range of data plotted.

The data collected from build sections across this acreage illustrates a general trend of increasing organic sulfur content from west to east, as well as stratigraphically from Middle Montney up through the Doig Phosphate. A change in organic sulfur content occurs across the Hay River Fracture zone, but the measured organic sulfur in cuttings remains correlated to produced sulfur in oils. Despite sub-regionally consistent organic sulfur trends, variability has been observed in cuttings collected along the laterals, even in wells landed within a 10-20 m stratigraphic window.

## Conclusions

There is a strong correlation between measured in-situ organic sulfur in the drill cuttings and the organic sulfur in the produced fluids. The produced gases $H_2S$ is also correlated to the organic sulfur in the oils. This study has produced the following observations:

1. Reliable assessment of in-situ organic sulfur content in the Montney formation prior to hydraulic fracturing
2. Strong correlation between in-situ organic sulfur content and total sulfur content in produced oils
3. Strong correlation between $H_2S$ content in produced gases and total sulfur content in produced oils

Mapping the variability of in-situ organic sulfur content in the Montney rocks will hopefully lead to a better understanding of the controls on $H_2S$ distribution.

### References


Azzam Barham, Mohd Suhaili Ismail, Maman Hermana N.S Zaninal Abidin. Biomarker characteristics of Montney source rock, British Columbia, Canada. Heliyon 7, e08395, 2021.

Shane D. Schoepfer, Charles M. Henderson, Thomas F. Moslow, Chen Shen. Extremely high resolution XRF core scanning reveals the Early Triassic depositional history of the Montney Formation in northeastern British Columbia, Canada. Paleogeography, Paleoclimate, Paleoecology, v. 637, 2024, 112019.

Alan Stebbins, Thomas J. Algeo, Christian Olsen, Hiroyoshi Sano, Harold Rowe, Robyn Hannigan,
Sulfur-isotope evidence for recovery of seawater sulfate concentrations from a PTB minimum by the Smithian-Spathian transition, Earth-Science Reviews, Volume 195, 2019, Pages 83-95.

Adam D. Woods, John-Paul Zonneveld, Ryan Wakefield, Hyperthermal-driven anoxia and reduced productivity in the aftermath of the Permian-Triassic mass extinction: a case study from Western Canada, Fontiers Earth Science, Volume 11, 2023.

Zhengyi Lyu, Lei Zhang, Thomas J. Algeo, Laishi Zhao, Zhong-Qiang Chen, Chao Li, Biao Ma, Feihong Ye,
Global-ocean circulation changes during the Smithian–Spathian transition inferred from carbon-sulfur cycle records, Earth-Science Reviews, Volume 195, 2019, Pages 114-132.

Peirce, John & Cordsen, Andreas & Glenn, Ted. The Great Slave Lake Shear Zone - Implications for Exploration in NW Alberta and NEBC. Research Gate.

James M. Wood, Tristan Euzen, Jaime Cesar, Influence of faults on late-stage migration of methane-rich gas in a major unconventional hydrocarbon accumulation: Montney Formation, western Canada, Marine and Petroleum Geology, Volume 164, 2024.

GUSSOW 2024
Montney Subsurface Evaluation: Drive Towards Excellence
Banff, AB | October 2-4

# Montney Microbiome: Provenance and persistence of shale microorganisms encountered during different stages of hydraulic fracturing

Gabrielle Scheffer[1], Carmen Li[1], Andrew Kingston[2], Jayne Rattray[1], Nicole Taylor[3], Omid Adarkani[2], Casey R.J. Hubert[1*]

[1]Geomicrobiology Group, Department of Biological Sciences, University of Calgary, Calgary, Canada

[2]Geological Survey of Canada, Calgary, Alberta, Canada

[3]OSP Microcheck, Calgary, Alberta, Canada

## Abstract

Microbial populations in hydraulically fractured tight unconventional reservoirs have been extensively studied in order to better understand and optimize industrial operations. Microbiological investigations typically involve analysis of injection and flowback water samples that pass through these environments, based on the assumption that relevant microorganisms are introduced from the surface. In this study, subsurface core material was additionally investigated to allow a more complete examination of the provenance of microbiome constituents in Montney subsurface reservoir systems. Accordingly, samples included cores, cuttings and drilling muds obtained during initial drilling as well as the fluids involved in eventual hydraulic fracturing (injection fluids and produced water). Distinct microbial populations identified in subsurface cores and drill cuttings that were absent from all other sample types included *Desulfallas-Sporotomaculum, Nocardioides, Paeniglutamicibacter*, *Granulicatella* and *Pseudomonas*, suggesting these groups may be part of a pre-existing subsurface microbiome in Montney shale. Metagenomic analysis of these populations highlighted metabolisms suited to extreme subsurface reservoir conditions, notably adaptations to high temperature (90°C downhole), high salinity and the presence of toxic metals (arsenic, cadmium, lead and mercury). Despite evidence suggesting subsurface origins of these populations, they were not prevalent in the microbiome analysis of produced water sampled at regular intervals over the course of one year of production, which instead highlighted surface-derived bacterial populations similar to those observed in drilling mud samples. By delineating pre-existing deep tight reservoir microbiomes and surface-derived microbial populations that are introduced this study highlights potential sources, causes and dynamics of microbiological impacts when engineering interventions like hydraulic fracturing interact with the deep subsurface biosphere.

## Statement of the background

Shale oil reservoirs and hydraulic fracturing have been studied extensively to understand roles and impacts of microbial communities active during oil and gas production operations, with sampling programs often extending over a year in Marcellus and Permian Basin formations in the United States [1-6]. Hydraulic fracturing has been shown to promote microbial growth *in situ*, notably following the addition of microbial growth substrates in the fracturing fluid (e.g., guar gum or other polymers) that can be broken down by microbial communities [7]. There have been limited hydraulic fracturing microbiology studies in Canada, where the Montney formation is the most prolific shale resource. As part of the Western Canadian Sedimentary Basin, the Montney formation spans 130,000 km$^2$ from northeast British-Columbia to northwest Alberta [8]. Compared to other shale reservoirs, the Montney formation is considered low-permeability (10 μD, 3% porosity) with water saturation of around 30% [9-11]. This raises questions about the potential habitability of resident microbiomes in a shale-hosted deep biosphere that exists prior to hydraulic fracturing and the introduction of surface-derived fluids and microbes.

## Aims and Objectives

This study aims to understand the source of different microbial constituents identified Montney shale reservoir systems. Knowing whether microbiomes associated with hydraulic fracturing are long-standing residents of deep biosphere shales, or rather being introduced from surface environments with incoming fracturing fluids will help to understand microbial problems such as souring and corrosion and inform strategies for their control. Microbiological comparison of core, cuttings, drilling muds, injection water and produced water were undertaken using modern DNA sequencing tools with and without high temperature incubations in order to establish the provenance (subsurface derived vs surface derived) of different microbial populations encountered in tight rock unconventional shale reservoirs and production fluids.

## Materials and methods

Prior to hydraulic fracturing, Montney reservoir samples from subsurface core plugs were obtained at 3302 m depth and preserved for further analyses. These samples were required for separate petrographic studies prior to production and represent the pristine shale environment and were also able to be used for microbiological characterisation. During subsequent drilling of the production well, cuttings mixed with oil-based drilling muds from 3302 m, 3350 m, 3400 m, 3450 m and 3517 m were collected. Corresponding drilling mud-only samples for these depths were also collected for comparison. During subsequent hydraulic fracturing, flowback water samples were collected every 20-100 $m^3$ of water produced initially, followed by monthly sampling over the course of one year. Injection water was also collected. Samples were used in high temperature incubation at 90°C to test for microbial metabolism, and in direct DNA sequencing analysis that used both 16S rRNA gene PCR amplification for biodiversity screening as well as PCR-independent shotgun metagenomic sequencing for assessing metabolic genes and metabolic potential in each of the resulting microbiome libraries.

## Results and discussion

Among the 55 different samples analyzed, produced waters gave rise to the most biodiversity, in particular in the early days of the 1-year monitoring period. Produced waters gave rise to 16S rRNA gene amplicon libraries featuring between 3,562 to 100,368 sequence reads per sample. Far fewer reads were recovered in samples of oil-based drilling muds (157 to 16,417), likely due to bentonite clays providing a charged matrix causing absorption of DNA and interfering with molecular workflows. Importantly, pristine core plugs and shale cuttings (rinsed from drilling muds) also gave rise to successful DNA sequencing, with libraries featuring 148 to 73,663 reads.

To enrich organisms from shale, cuttings from 3302, 3350 and 3400 m were thoroughly rinsed (repeated 5x) to remove drilling muds prior to being incubated in triplicate under conditions similar those reported in the shale formations (high salinity, high temperature, similar geochemistry and amended with glucose and guar gum). Parallel incubations of drilling muds corresponding to the same depths provided controls (also in triplicate) to enable more confidently highlighting microbial signatures unique to the shale. Guar gum and glucose amendments stimulated microbial activity at 90°C following inoculation with shale cuttings rinsed from drilling muds. Concentrations of the degradation intermediates mannose and galactose exhibited different dynamics in incubations with rinsed shale cuttings compared to drilling mud-only, suggesting a different microbial response in these two sets of conditions. Indeed, DNA sequencing revealed that certain microbial groups increased in relative abundance in the shale-only incubations but were completely absent from parallel incubations with only drilling muds. Different *Pseudomonas* were found only in the 3302 m and 3400 m rinsed shale incubations, including one that was also observed in incubations of pristine core. Similarly, for both the 3350 m and 3400 m depths clear increases in members of the *Desulfallas-Sporotomaculum* family were observed in the rinsed shale incubations. Other apparently shale-specific groups of bacteria were affiliated with *Granulicatella* and *Nocardioides*. Overall, different subsurface samples (pristine shale core plugs, shale cuttings rinsed from drilling muds) gave rise to 493 amplicon sequence variants (an approximation for different species) that were not detected in drilling mud or produced fluids (i.e., samples associated with surface environments).

Metabolic responses in incubations of different samples, together with amplicon sequencing biodiversity patterns suggest certain microbial lineages are present in shale as part of a pre-existing subsurface microbiome. This was investigated further through metagenomic sequencing of 16 different samples (incubations, injection fluid and produced fluids). Out of the 18 resulting genomes, three were highlighted as being organisms likely originating from deep biosphere shale environments based on contig coverage profiles (two *Pseudomonas* and one *Paeniglutamicibacter*). These genomes include genes for tolerance to high salinity and toxic metals, consistent with a subsurface lifestyle. To assess high temperature adaptation, GC content of tRNA coding genes were used to infer optimal temperatures for growth suggesting all three shale-associated genomes correspond to thermophiles (average GC content 62%) compared to lower estimates for a genome associated with fracturing fluids (45%). Similarly, genes related to lignin and hydrocarbon metabolism were observed in the shale-associated genomes but are absent from the drilling mud- and fracturing fluid-associated genomes.

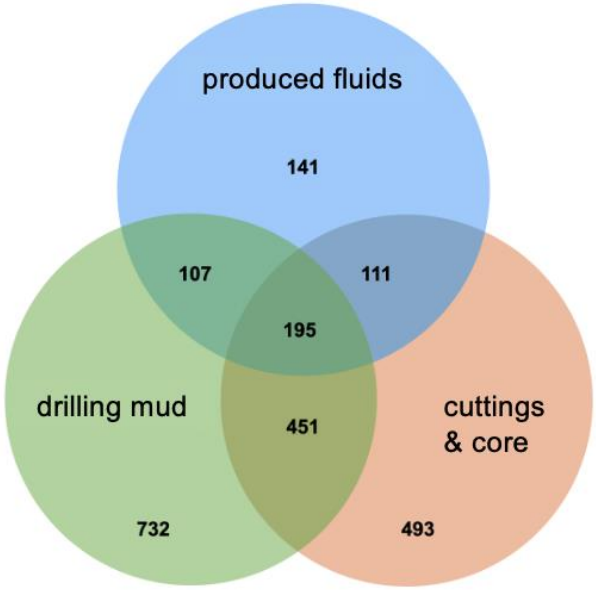


**Figure 1.** Overall microbial diversity detected in 16S rRNA gene amplicon sequencing libraries of different sampling types, indicated as the number of amplicon sequence variants (ASVs). While some overlap is observed, 493 distinct ASVs are unique to subsurface derived core or cuttings from Montney shale. ASVs are approximately equivalent to unique microbial species.

## Conclusions

Patterns of microbial metabolism, biodiversity measurements using 16S rRNA gene sequencing, and metagenomic analysis all point to a pre-existing subsurface microbiome in Montney shale that is independent from surface-derived microbes that are introduced during hydraulic fracturing. The 493 species-level groups unique to subsurface samples feature notable groups like *Desulfallas-Sporotomaculum* and *Pseudomonas*, with the latter also highlighted in genomic reconstruction that points to genetic adaptations to subsurface life. On the other hand, many microbial groups that were detected are not unique to subsurface samples and are likely surface derived (i.e., from drilling muds or water sources used in hydraulic fracturing). Delineating different microbial groups, their potential activities in these oil and gas fields, and their likely sources, will enable more tailored microbial control strategies to be designed and implemented.

### References

Cluff MA, Hartsock A, MacRae JD, Carter K, Mouser PJ. Temporal Changes in Microbial Ecology and Geochemistry in Produced Water from Hydraulically Fractured Marcellus Shale Gas Wells. *Environ Sci Technol* 2014; 48: 6508-6517.

Corrin E, Harless M, Rodriguez C, Degner DL, Archibeque R. Evaluation of a More Environmentally Sensitive Approach to Microbiological Control Programs for Hydraulic Fracturing Operations in the Marcellus Shale Using a Nitrate-Reducing Bacteria and Nitrate-Based Treatment System. 2014. Society of Petroleum Engineers.

Lipus D, Vikram A, Ross D, Bain D, Gulliver D, et al. Predominance and Metabolic Potential of Halanaerobium spp. in Produced Water from Hydraulically Fractured Marcellus Shale Wells. *Appl Environ Microbiol* 2017; 83.

Tucker YT, Mroz T. Microbes in Marcellus Shale: Extremophiles living more than two kilometers inside the Earth? *Fuel* 2018; 234: 1205-1211.

Daly RA, Borton MA, Wilkins MJ, Hoyt DW, Kountz DJ, Wolfe RA, et al. Microbial metabolisms in a 2.5-km-deep ecosystem created by hydraulic fracturing in shales. *Nature Microbiology* 2016; 1: 16146.

Amundson KK, Borton MA, Daly RA, Hoyt DW, Wong A, Eder E, et al. Microbial colonization and persistence in deep fractured shales is guided by metabolic exchanges and viral predation. *Microbiome* 2022; 10: 5.

Liang R, Davidova IA, Marks CR, Stamps BW, Harriman BH, Stevenson BS, et al. Metabolic Capability of a Predominant Halanaerobium sp. in Hydraulically Fractured Gas Wells and Its Implication in Pipeline Corrosion. *Frontiers in Microbiology* 2016; 7.

Yaghoubi A, Dusseault MB, Leonenko Y. Injection-induced fault slip assessment in Montney Formation in Western Canada. *Sci Rep* 2022; 12: 11551.

Osselin F, Saad S, Nightingale M, Hearn G, Desaulty A-M, Gaucher EC, et al. Geochemical and sulfate isotopic evolution of flowback and produced waters reveals water-rock interactions following hydraulic fracturing of a tight hydrocarbon reservoir. *Sci Total Environ* 2019; 687: 1389-1400.

Clarkson CR, Ghaderi SM, Kanfar MS, Iwuoha CS, Pedersen PK, Nightingale M, et al. Estimation of fracture height growth in layered tight/shale gas reservoirs using flowback gas rates and compositions–Part II: Field application in a liquid-rich tight reservoir. *Journal of Natural Gas Science and Engineering* 2016; 36: 1031-1049.

Riazi N, Clarkson CR, Ghanizadeh A, Vahedian A, Aquino S, Wood JM. Determination of elastic properties of tight rocks from ultrasonic measurements: Examples from the Montney Formation (Alberta, Canada). *Fuel* 2017; 196: 442-457.

GUSSOW 2024
Montney Subsurface Evaluation: Drive Towards Excellence
Banff, AB | October 2-4

# Measuring Fracture Efficiency, Propagation and Variability in Limited Entry Completion Design using Open Hole and Cased hole Diagnostic Technologies. A Montney Case Study from the Heritage Area NEBC

Ryan Simpson*, Dallas Gara, Grant Wagner, Nathan Tsang, and Farhan Alimahomed

ARC Resources Ltd.

## ABSTRACT

ARC Resources Ltd., “ARC” operates a prolific natural gas project within their Dawson Creek Montney asset located in Northeast British Columbia. As a result of the continuous pad development employed by ARC, a unique opportunity was presented to evaluate the nature of induced hydraulic fractures from a recently completed offsetting pad that targeted the lower Montney. The existing, completed pad deployed cased-hole ultrasonic diagnostic technology to quantitatively measure cluster efficiency, distribution and perforation erosion after completion operations. The new development pad possessed a well with a planned close approach to the existing pad, with variable offset distance, and was drilled in the same target horizon. An open-hole Formation Micro Imager, “FMI” log was deployed on the new pad to evaluate the nature of induced hydraulic fractures, their interaction with the regional stress conditions, and existing geological features. Combining downhole diagnostic technologies, between two temporally spaced development pads, provided insight on the propped half-length, far-field fracture propagation characteristics and allowed evaluation of multi-cluster stage design. It is essential to characterize hydraulic stimulation, proppant transport and cluster efficiency to effectively develop unconventional resources. Observational, quantitative diagnostic methods to gain insight into optimizing well spacing, tonnage, water intensity and completion design is an underutilized technology. Combining these technologies expedites the analysis and learning products and timelines. The ability to limit ineffective expenditure, whether through reduced well interference, or diminishing returns on pumped volumes, is necessary to maximize resource development value.

### Statement of the background

How completion induced hydraulic fractures propagate, prop, grow, distribute and interact with the Montney formation, including existing natural fractures/faults, is poorly understood. Fracture modeling, geomechanical modeling and rate transient analysis “RTA” provide numerical insights into this problem, but uncertainty remains due to the inherent upscaling and averaging of input data. ARC was presented with an opportunity to physically measure resultant completion induced fractures from a completed parent well, using a subsequent child well drilled to within ~107m of the parent.

### Aims and Objectives

By physically measuring the resultant parent well fractures, within the open-hole section of the child well, ARC intended to better understand propped half-length, whether induced fractures propagated as single planar fractures or as multiple complex fractures, or “swarms, as well as whether the presence of natural geological features/fractures affected the growth of the induced fractures including the nature of their subsurface interactions. The project also allowed for validation of the post-completion cluster erosion measurements, and resultant near-field created fractures of the parent well.

## Materials and methods

The parent and child well's target the same interval in the middle lower Montney, within the Heritage area of NEBC. Post-completion ultrasonic completion evaluation technology, "UCET," was conducted on the parent well. Which supplied measurements of casing erosion at every perf cluster. Cluster erosion is interpreted to be proportional to the amount of water/sand/slurry that exited any one perforation cluster in a multi-cluster frac stage. An open-hole formation micro image log, "FMI" was run on the child well, over the area of close approach. The FMI provided precise measurements of fractures, whether induced or natural, as well as their aperture, azimuth and dip. The diagnostic technologies that were employed, when interpreted in tandem, allowed for 3D spatial empirical measurements over several completion stages and existing geological features/faults.

## Results and discussion

The ability to combine these diagnostic technologies provided a unique opportunity to see "both" sides of the problem. The initiation points, cluster-by-cluster/stage-by-stage at the parent well with the coincident created fractures at the child well. The FMI identified 169 fractures over the logged interval, 92 of which occurred as part of a swarm, 77 of which occurred as a single planar fracture. All fractures were interpreted as either natural or induced. Induced fractures have a very steep dip, >84°, while natural fractures were sub-vertical and dipped less steeply. The azimuth of induced fractures were all within + or – 7.5° of the regional SHmax direction. Larger cluster erosion was associated with an increased number of fractures as well as higher average aperture. However, induced fracture aperture only exceeded the width of 100 mesh proppant in six instances. >90% of measured frac apertures were roughly equivalent to the grainsize of lower Montney silt; thus, implying an element of self-propping fractures. This observation runs counter to commonly modeled propped fracture half-length.
Natural fracture azimuth had a much wider distribution at + or - 35° of SHmax. It was observationally apparent that naturally occurring fractures were reactivated by the offsetting completions. In one instance 15 fractures were identified to have interacted with a fault feature. These observed fractures once projected along measured azimuth, indicated a wide point of origin. Projected to the offsetting parent well, it would equate to ~125m or more than one stage in length. This implies that there is profound interaction between completion "frac-energy," with naturally occurring geological features. These interactions are postulated to be a result of lower tensile strength, or variance of the local stress conditions, intrinsic to the natural features.

## Conclusions

This diagnostic field trial observing, measuring, and characterizing the created hydraulic fractures resulting from a cased-hole completion design has provided a unique opportunity to quantify the nature of stimulated rock volume. The near absence of fracture aperture wider than the pumped proppant, at just over 110m away, implies an element of "self-propping" and fracture conductivity without far-field proppant transport. Large cluster erosion was associated with a higher number of created fractures. The created hydraulic fractures also showed multiple initiations, or "swarms," to be common in the lower Montney. Naturally occurring faults/fractures were observed to interact with the offset completions which implies frac-energy, or propagation, was attracted/directed towards the features. Perforation clusters that were offset with natural features, in the SHmax direction, showed higher average erosion and influenced the proppant distribution across the stage. The methods employed in this study proved to be enlightening with respect to the nature of fracturing stimulation. The prospect of tailoring completion design to the local geological conditions, or evaluating proppant loading/water intensity, is paramount to reducing unproductive expenditure and improving capital efficiency.

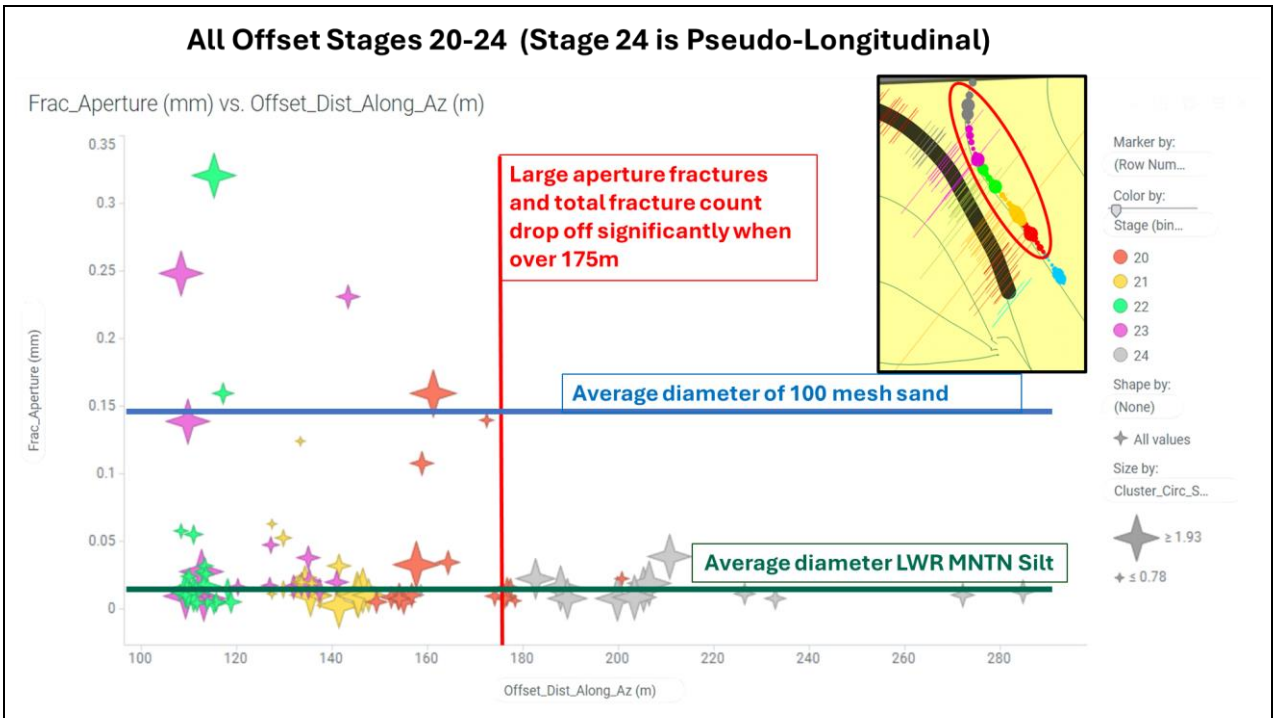


## References

Ghanizadeh, A., Clarkson, C.R., Deglint, H., Vahedian, A., Aquino, S., Department of Geoscience, University of Calgary; Wood, J.M., Encana Corporation, Unpropped/Propped Fracture Permeability and Proppant Embedment Evaluation: A Rigorous Core-Analysis/Imaging Methodology

GUSSOW 2024
Montney Subsurface Evaluation: Drive Towards Excellence
Banff, AB | October 2-4

# Integrating 3D Subsurface Modeling and Completion Data: A Demonstration of Improving Modeled Attributes and Integrating Hydraulic Fracturing Data and Analytics

Chris Bird[1], Nathan Tsang[1], Matt Torriero[1], Conor MacLean[1]

1.ARC Resources

## Abstract

In recent years ARC Resources Geosciences team has increased efforts to: build and utilize 3D subsurface Geomodels, develop and implement Analytics technology, and integrate datasets across petro-technical disciplines. The goal of this strategy is to improve development and operational decisions on our extensive Montney assets. Integrating subsurface geoscience interpretation with observed well completion data in the field affords an opportunity to improve development decisions over traditional workflows where data typically remain in silos by discipline.

We discuss enhancements and improvements made to the 3D Geomodel over one of ARC's Montney assets through seismic integration and well log normalization. The benefit of these enhancements become clear in the second section where we examine a workflow to bring digital well completion data into the 3D model, leverage in-house analytical tools, and to provide geologic context to well completion observations and data. This resulted in an ability to synthesize multidisciplinary data effortlessly in a unique 3-dimensional space in ways that would have been onerous, or near impossible, several years prior.

## Statement of the background

In order to improve subsurface recommendations for Montney development, the geoscience team at ARC is confronted with some data problems that need to be overcome. These problems include data fidelity, and data integration. In this presentation we will explore how ARC assessed, and improved, the data quality of its well log and seismic data for input into a Montney 3D cellular geomodel. Then we will see how ARC can then integrate geo data, as encapsulated in the geomodel, and operations data with the goal to improve the geoscience inputs into Montney development decisions; these include spacking/stacking (i.e. should we drop/add a development bench?), well placement (should our landing zone in a given bench be adjusted due to subsurface considerations?), completion intensity (are upcoming pads in an area expected to be more, or less, difficult on the frac?).

## Materials and methods

This section should provide a brief summary the field area / geological setting / material being investigated, why they are suitable to address the problem at hand and the proposed methods to achieve the aims and objectives. The focus area of this presentation is a Montney asset in ARC's portfolio which has exhibited variance on key completions KPI's and production. Using Petrel, we integrate all our available geoscience data, including well logs, core measurements, seismic inversion products, and well tests such as DFITs, into a 3D petrophysical and geomechanical model.

The novelty of this work, however, is the integration of this 3D geomodel with the digital completions data in a data analytics environment as well as an interpretation environment.

## Results and discussion

Some key observations from this work are that data fidelity must be interrogated, and improved, in order that integrating the 3D geomechanical model with operations data yield fruitful observations. Curves unedited for noise or requiring normalization and poor seismic inversion products are shown to render this type of integrated analysis to be ineffectual. Further, integration of a high fidelity geomodel with completions KPIs in a data analytics environment is shown to boost confidence in the subsurface interpretation, and is more efficient. This is shown in Figure 1 where horizontal wells with a frac KPI (hot colours indicate tougher frac'ing) is plotted in section view against the Young's Modulus model. Figure 2 shows a crossplot of this KPI with young's modulus. Both figures boost confidence that elevated elastic stiffness increases frac difficulty.

## Conclusions

The intention of this presentation is not to deep dive on any specific problem ARC has encountered. Rather it is to demonstrate our evolving workflows in which building high-fidelity 3D geomodels, integrating with digitized operations data, and leveraging data analytics tools are driving our ability to make observations in the data that would have been extremely difficult prior.

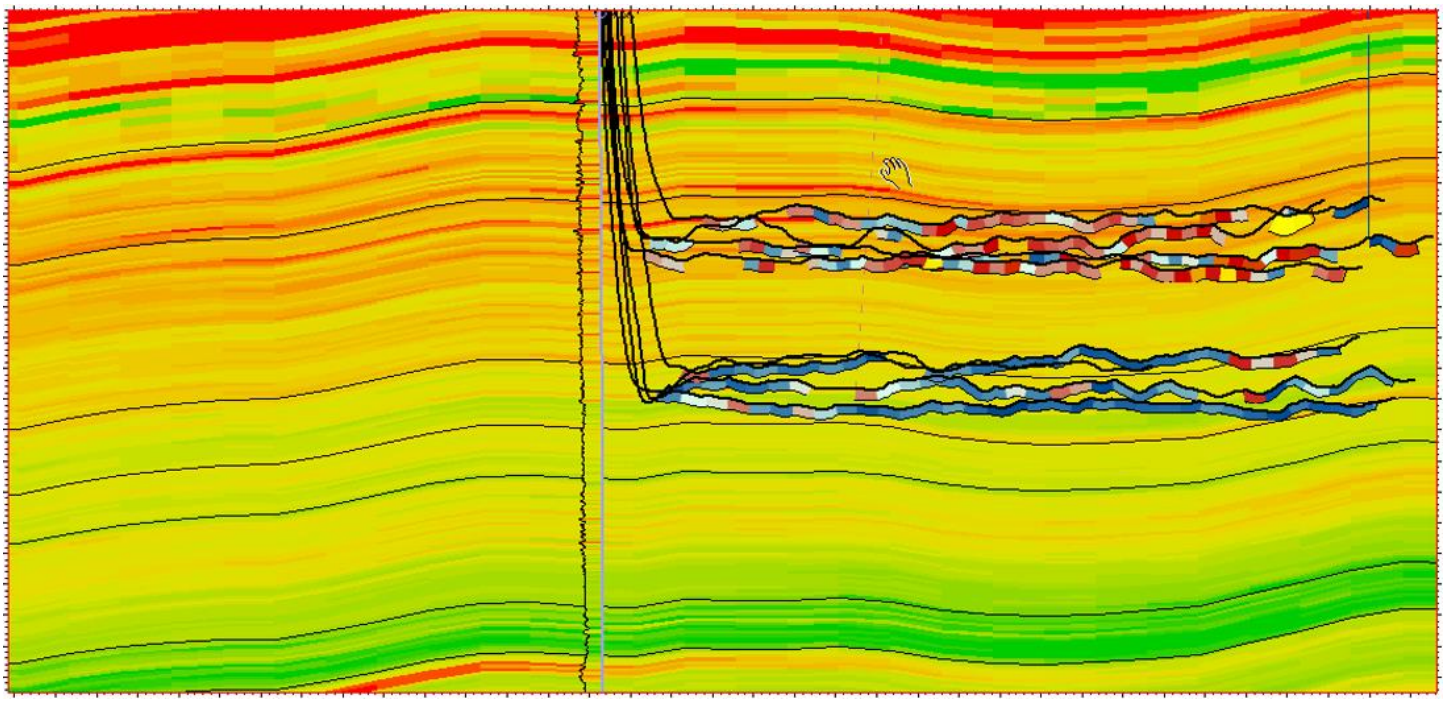

Figure 1. Montney horizontal producer wells plotted on a section of young's modulus pulled from the geomodel. Hot colours (reds) of Young's Modulus indicate high rock stiffness and green is low stiffness. A completion KPI is digitized and plotted along the horizontal wells as a well log. Hot colours of this frac KPI log indicate stages of difficult treating. Cold colours indicate easier treating. As can be seen the higher stiffness upper bench is associated with many more difficult stages to complete. Seismic by permission of Pulse Seismic.

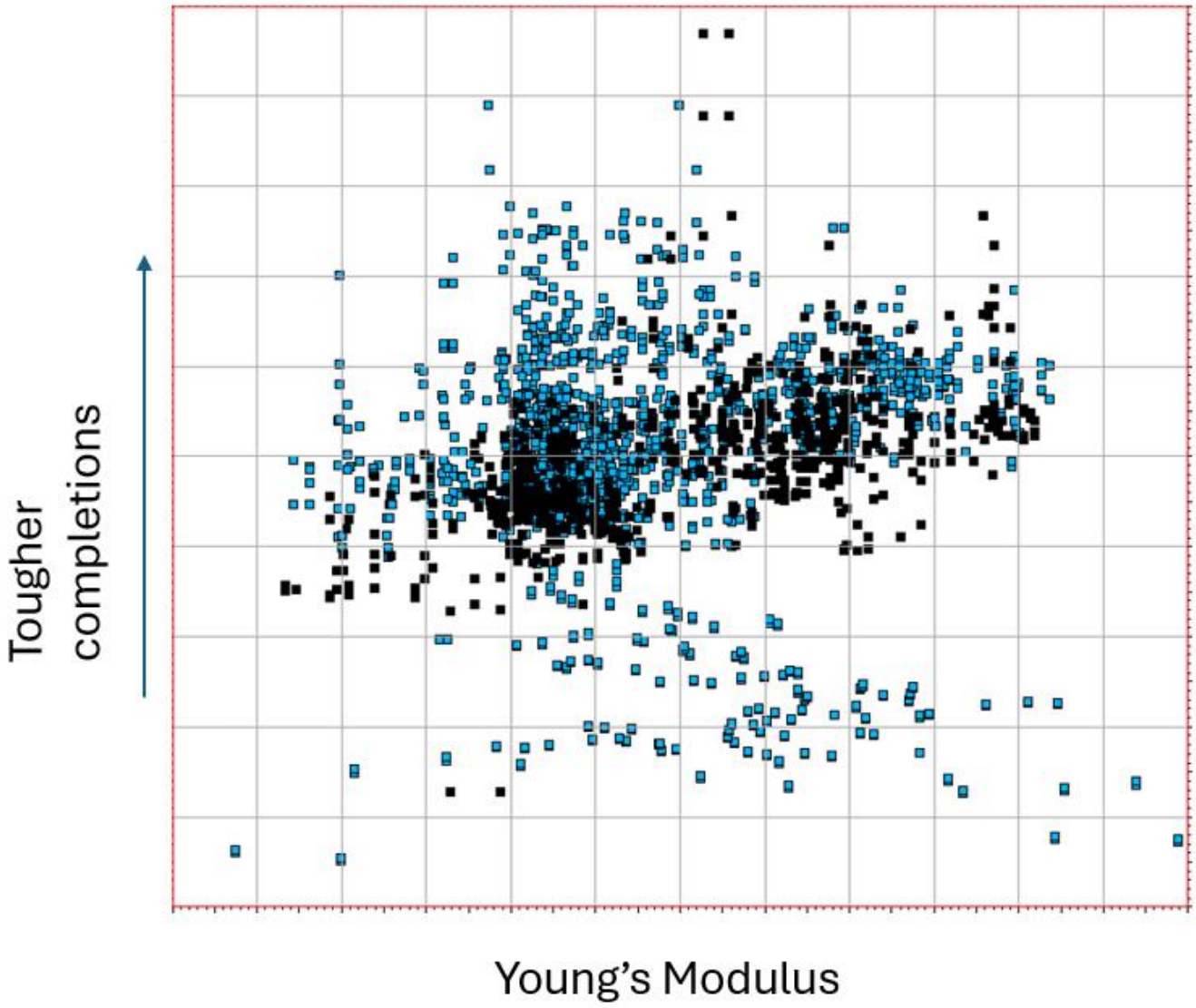


Figure 2. Crossplot demonstrating the relationship between rock stiffness and more difficult completions suggested in Figure 1. Seismic by permission of Pulse Seismic

GUSSOW 2024
Montney Subsurface Evaluation: Drive Towards Excellence
Banff, AB | October 2-4

# Montney – As polar as it can get

Jaime Cesar[1,2] Omid, H. Ardakani[2,]

1. AGAT Laboratories, 2. Geological Survey of Canada

## Abstract

Petroleum systems within the Montney Formation continue offer multiple interrogations about source, mixing and alteration processes of hydrocarbons. Addressing these questions using organic geochemistry represents a challenge due to low biomarker concentration in the liquids and frequent mixing of gas/condensate hydrocarbons. Since common biomarkers were not available, this study has focused on a different group of molecules, the resin fraction of soluble bitumen. These polar compounds were derivatized and subsequently resolved using chromatographic techniques at the Geological Survey of Canada. Identified compounds include *n*-fatty acids and alkan-2-ones, which did not have an apparent association with *n*-alkanes. In addition, this study is the first report of 1,13-, 1,14- and 1,15-diols in fossil organic matter; and in carbon number ranges of $C_{15}$-$C_{29}$, $C_{16}$-$C_{29}$ and $C_{17}$-$C_{29}$ respectively. The similar distributions of 1,14- 1,15-diols suggests a common origin for these compound classes, whereas 1,13-diols seem to derive from a different source or mechanism. Similarly, a series of alkan-3-ols was identified in the $C_{12}$-$C_{28}$ range, sharing a common distribution pattern with the *n*-fatty acids. The large variability detected in the molecular distribution of oxygen-containing aliphatic compounds introduces the question whether they may record a geochemical signature that precedes thermal degradation and hydrocarbon migration events within Montney reservoirs.

## Statement of the background

The largest percentage of hydrocarbons in the Montney Formation are thought to originate from thermal degradation of migrated oil (Sanei et al., 2015; Wood and Sanei, 2016). Maximum burial and thermal maturity in the Late Cretaceous/Early Paleogene implied thermal cracking of hydrocarbons which led to the petroleum accumulations we know today (Wood and Sanei, 2016; Ducros et al., 2017; Euzen et al., 2021). Geochemical assessment has then been limited by the low abundance of biomarkers (e.g., hopanes and steranes) in the condensates and light oils that resulted from thermal degradation.
In contrast to molecules in the gas-condensate range, there is a group of compounds that have not been analyzed in Montney samples; these are polar compounds from the resin fraction of soluble bitumen. It is known that resins are scarce (or absent) in the produced condensates and light oils. However, they are preserved in the solid bitumen residue within the reservoir, and may record a fingerprint of the original source of migrated hydrocarbon. In addition, these polar compounds can be a source of gas/condensate, particularly when thermal alteration (cracking) takes place (e.g., Michels et al., 2000) as is the case of the Montney Formation. Investigating the polar fraction of extracted bitumen may open a new series of geochemical tools for resource assessment in Montney and similar plays where thermal degradation of oil has taken place.

## Aims and Objectives

This study aims to investigate the presence of polar organic compounds in bitumen extracts from the Montney Formation. Specifically, it targets the identification of oxygenated molecules in Montney samples from different locations within the Western Canadian Sedimentary Basin. Potential sources for these compounds are discussed as well. Research findings presented herein are an expansion of the work by Cesar et al. (2023).

## Materials and methods

Homogenized rock samples were solvent-extracted using dichloromethane (DCM) in a Soxhlet apparatus for 24 h. The samples correspond to core intervals from the different stratigraphic Members (Lower, Middle, and Upper), different locations, and different thermal maturity levels. Polar fractions were obtained from the extracted bitumen using column chromatography by elution with methanol once saturate and aromatic hydrocarbon fractions had been eluted with *n*-pentane and DCM:*n*-pentane, respectively. Aliquots of the polar fractions (0.5–1 mg) were derivatized in 200 µL of pyridine and 300µL of N,O-Bis(trimethylsilyl) trifluoroacetamide (BSTFA) at 70°C for 1h. Then, the derivatized fractions were dried under a gentle stream of nitrogen at 35°C and re-dissolved in *n*-hexane for molecular analysis using gas chromatography – mass spectrometry (GC-MS). For GC-MS, derivatized fractions were analyzed via gas chromatography time of- flight mass spectrometry (GC–QTOF-MS) on an Agilent 7890BGC - 7200 QTOF mass spectrometer equipped with a DB5-ms column (60 m × 0.25 µm i.d. × 0.25 mm f.t.), using splitless injection and helium as carrier gas (1.3 mL/min). The temperature program of the GC oven started at 80°C for 1min, then ramped at 5°C/min to 325°Cand held at the final temperature for 30min.

## Results and discussion

A large variety of preserved oxygenated compounds were detected including *n*-fatty acids and alkan-2-ones, which did not have an apparent association with *n*-alkanes (Figure 1). Based on their distinctive distribution pattern, fatty acids have not been degraded to *n*-alkanes (e.g., via decarboxylation). Likewise, the alkan-2-ones do not represent oxidation products of the *n*-alkanes. Mechanisms to explain the preference for even numbered carbon chain of alkan-2-ones remain unknown though even-chain ketones have been identified in Australian torbanites (Zhang and Volkman, 2020).

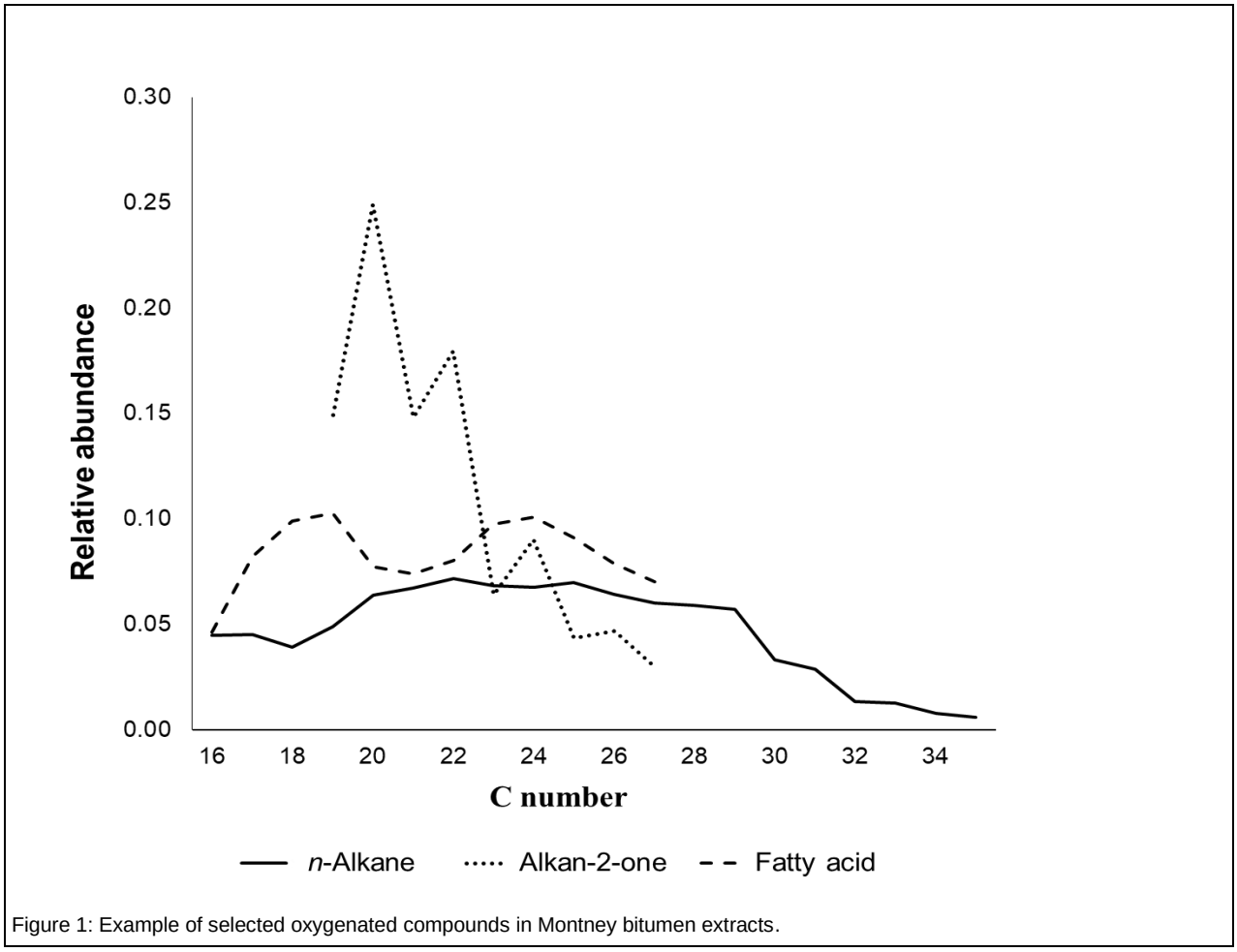


Figure 1: Example of selected oxygenated compounds in Montney bitumen extracts.

This study reports 1,13-, 1,14- and 1,15-diols in the extracted organic matter; and in carbon number ranges of $C_{15}$-$C_{29}$, $C_{16}$-$C_{29}$ and $C_{17}$-$C_{29}$ respectively. The similar distributions of 1,14- 1,15-diols suggests a common origin for these compound classes, whereas 1,13-diols seem to derive from a different source or mechanism. These diols could be breakdown products of their longer-chain counterparts or have otherwise precursors that have not been identified to this date. A series of alkan-3-ols was also identified in the $C_{12}$-$C_{28}$ range, sharing a common distribution pattern with the *n*-fatty acids.

We must also highlight that the molecular characteristics of the samples did not seem to be specific of a particular Montney Member. The lack of differentiation among Montney Members might have resulted from hydrocarbons migrating from the same source or variable combinations of two or more sources.

## Conclusions

The large variability detected in the molecular distribution of oxygen-containing aliphatic compounds introduces the question whether they may record a geochemical signature that precedes thermal degradation and hydrocarbon migration events within Montney reservoirs. Additionally, several avenues are yet to explore; polar sulfur- and nitrogen-containing compounds can be studied in the future, which might provide light on depositional environment of the original organic matter, and alteration processes such as biodegradation. If polar fractions are potential sources of gas condensates within Montney, stable carbon isotopes could also be a path to follow in order to stablish fluid to source correlations.

## References

Cesar, J., Robinson, R., Naeher, S., Milovic, M., Ardakani, O.H. (2023). Fatty acids, alkanones and alcohols from a major lower Triassic low-permeability petroleum reservoir. Front. Earth Sci. 11:1137026. doi: 10.3389/feart.2023.1137026

Ducros, M., Sassi, W., Vially, R., Euzen, T., and Crombez, V. (2017). “2-D basin modeling of the Western Canada sedimentary basin across the Montney-Doig system. implications for hydrocarbon migration pathways and unconventional resources potential,”. Petroleum systems analysis—case studies. Editors M. A. AbuAli, I. Moretti, and H. M. Nordgård Bolås. Tulsa: (AAPG Memoir), 114, 117–134.

Michels, R., Burkle, V.,Mansuy, L., Langlois, E., Ruau, O., and Landais, P. (2000). Role of polar compounds as source of hydrocarbons and reactive medium during the artificial maturation of Mahakam Coal. ENERG FUEL 14, 1059–1071. doi:10.1021/ ef000046d

Sanei, H., Wood, J. M., Ardakani, O. H., Clarkson, C. R., and Jiang, C. (2015). Characterization of organic matter fractions in an unconventional tight gas siltstone reservoir. Int. J. Coal Geol. 150–151, 296–305. doi:10.1016/j.coal.2015.04.004

Wood, J., and Sanei, H. (2016). Secondary migration and leakage of methane from a major tight-gas system. Nat. Commun. 7 (13614), 13614–13619. doi:10.1038/ncomms13614

Zhang, Z., and Volkman, J. K. (2020). Isotopically enriched n-alkan-2-ones with even chain predominance in a torbanite from the Sydney Basin, Australia. Org. Geochem. 144, 104018. doi:10.1016/j.orggeochem.2020.104018

GUSSOW 2024
Montney Subsurface Evaluation: Drive Towards Excellence
Banff, AB | October 2-4

# Unveiling the Depths: Mapping and Modeling the Montney Formation for Enhanced Resource Evaluation

Mary Minnett[1], David Jenkinson[1],

1. McDaniel & Associates

## Abstract

Over the course of the last fifteen years, McDaniel has dedicated extensive effort and expertise to map the geological features of the Montney Formation. Initially focusing on a comprehensive two-dimensional analysis, McDaniel's work has been instrumental in providing a basin-wide perspective essential for evaluating client reserves within this prolific hydrocarbon reservoir.

Building upon this foundational mapping, McDaniel has undertaken a significant advancement in the past three years: the conversion of the 2D reservoir maps into a sophisticated three-dimensional geological model. This transformative process has enabled the calculation of in-place volumes with increased accuracy and granularity, offering a deeper understanding of the complex spatial distribution of hydrocarbon resources within the Montney Formation.

By leveraging the 3D geological model, well performance can be tied back to the rock properties, for any given Montney zone. This capability not only enhances McDaniel's ability to optimise production strategies but also facilitates informed decision-making regarding resource allocation and reservoir development.

Furthermore, by integrating machine learning processes McDaniel can predict future well results using the geological model as an input. This innovative approach not only streamlines decision-making processes but also empowers clients with insights into the potential productivity of prospective drilling locations. McDaniel will provide examples of where reservoir parameters are a driving factor and directly influencing production, focusing on keys areas such as Gold Creek, Altares, Wapiti, and others.

## Statement of the background

Initiated in 2008, the project began with patchwork two-dimensional geological mapping and interpretations for client land bases. As the Montney development expanded and McDaniel's market share in the region grew, the need for a comprehensive basin-wide geological interpretation became evident. Over the past few years, McDaniel has transitioned from localised 2D reservoir parameter mapping to a broader basin-wide approach, integrating these 2D maps into Petrel to develop a comprehensive 3D model of the Montney basin.

Previously, reservoir maps for the Montney were updated on a client-by-client basis, requiring weekly or monthly revisions to incorporate new vertical wells, core data, and other inputs. This method proved to be labour-intensive and inefficient. The shift to a 'master map' approach, which encompassed the entire Montney basin streamlined the process. This approach involved a substantial initial investment in data integration—including loading vertical wells, downloading LAS files, and performing quality control checks on all data—but enabled biannual updates with new data or significant workflow enhancements. This reduced the need for frequent ad hoc updates and minimises the impact on in-place volumes. This paper will detail the transition from 2D mapping to a 3D model and discuss how a basin-wide interpretation has enhanced McDaniel's ability to achieve precise reserves and consulting interpretations.

## Aims and Objectives

The primary aim is to develop a comprehensive basin-wide interpretation of the Montney Formation to explain regional trends in reservoir parameters. This approach enhances McDaniel's geologists and engineers' ability to evaluate current and prospective land bases, reserves, consulting projects, and integrate data into multivariate machine learning workflows. By establishing a master map from the outset, the aim is to streamline the initiation of new client projects, in contrast to previous ad hoc interpretations.

The mapping work encompasses all necessary parameters for calculating in-place volumes, including structural surfaces, isopachs, net pay, porosity, water saturation, pressure, condensate-to-gas ratio (CGR), reservoir solution gas (Rsb), oil formation volume factor (Bo), original oil in-place (OOIP), and original gas in-place (OGIP). The detailed 3D geological model enables McDaniel to better understand the spatial distribution of hydrocarbon resources within the Montney Formation and provides insights into production trends based on reservoir parameters. The goal is to facilitate access to the geological model for both engineers and geologists, significantly improving workflow efficiency compared to previous methods.

## Materials and methods

The methodologies discussed herein are completed within GVERSE GeoGraphix. Input into the 2D geological maps and 3D model is based on public data consisting of well headers, digital well logs, routine core analysis data, pressure data, sourced from geoLOGIC geoSCOUT and IHS Data Manager. The Montney master project includes approximately 8,400 vertical and deviated wells with Montney penetrations that McDaniel has interpreted, of which approximately 1,700 have core data. McDaniel subdivides the Montney Formation into ten zones and three benches (Figure 1). The benches roughly correlate to Graham Davies' Montney framework (*Davies et al., 2018*).

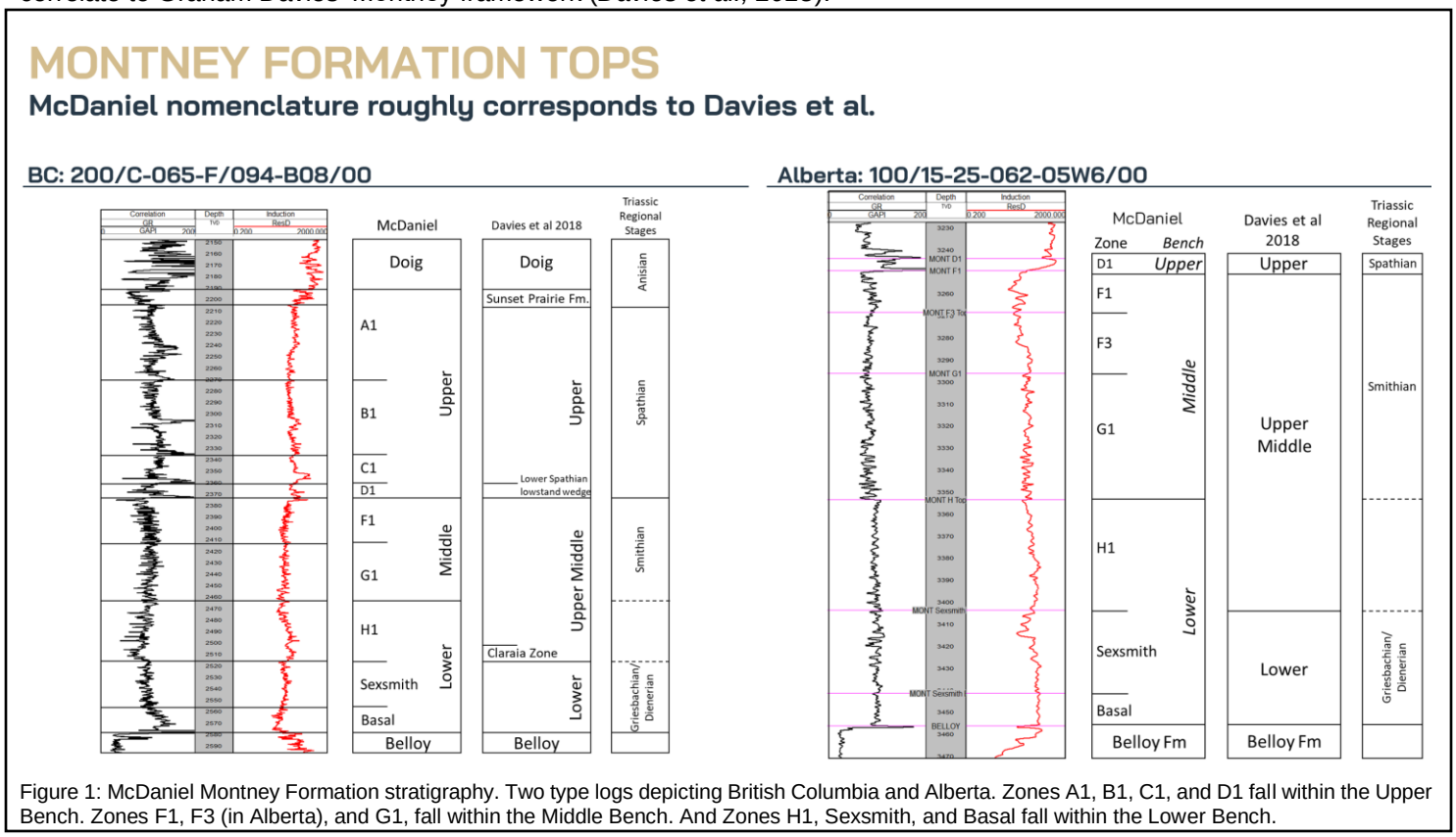


Figure 1: McDaniel Montney Formation stratigraphy. Two type logs depicting British Columbia and Alberta. Zones A1, B1, C1, and D1 fall within the Upper Bench. Zones F1, F3 (in Alberta), and G1, fall within the Middle Bench. And Zones H1, Sexsmith, and Basal fall within the Lower Bench.

The petrophysical model starts with core grain density samples. Grain density data for each of the ten Montney zones is mapped spatially and quality-controlled to address any anomalies. Grain density varies laterally and vertically within the Montney, and it is important to capture these variations. In tight reservoirs, the impact of grain density plays a large role in influencing the porosity. Grain density values are sampled from the maps for all wells without core. This grain density value

is input into the density porosity equation (RhoM) for every well. Density porosity is calculated for every zone in each well (Figure 2). The density porosity log is validated against core porosity data points, and there is a very good correlation between the two.

## MONTNEY PETROPHYSICAL MODEL

### McDaniel Porosity and Water Saturations

**Grain Density**

- Mapped average core grain density is used per zone to account for vertical and lateral changes in lithology

**Porosity**

- Grain density from available core in the area is used for each Montney zone and is applied to the density porosity log using the following equation:
  - Density porosity= (RhoM - RHOB) / (RhoM - RhoF)
  - RhoM = Grain Density from map applied to the well
  - RhoF = constant of 1000 kg/m$^3$

**Water Saturation**

- Sw is calculated using the Archie Equation:
  - $S_w = (a * R_w / Res * Ø^m)^{1/n}$
  - a = 1.0, m = 1.5, n = 1.5
  - $R_w$ = mapped by bench

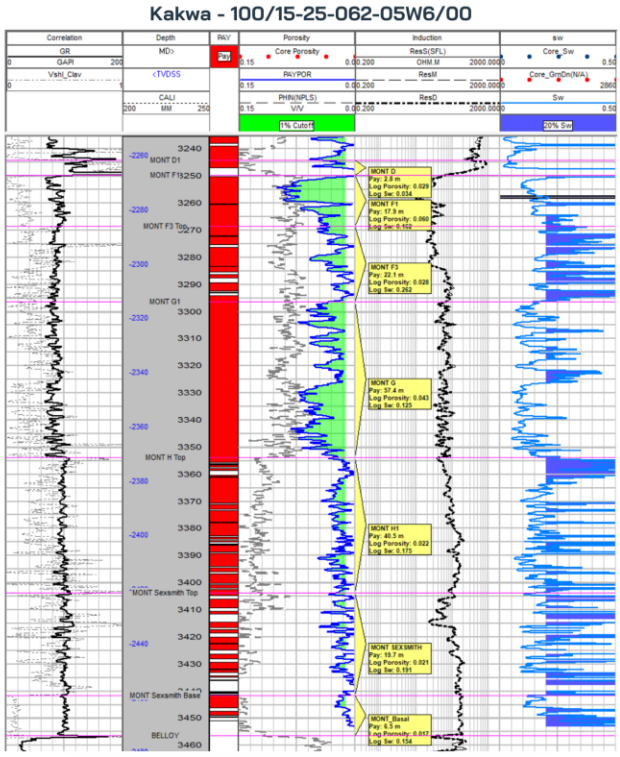


Figure 2: McDaniel's petrophysical model for the Montney explaining the equations used for porosity and water saturation, along with a type log displaying the breakdown of zones.

An additional critical component is the produced water resistivity by bench, which is input into the Archie water saturation equation (Figure 2). Water resistivity (Rw) samples from Montney horizontals, grouped by bench, are exported from geoSCOUT and converted from laboratory to Montney formation temperatures. Previously, a constant Rw value was used in Alberta and BC, the new maps capture lateral and vertical variability in water composition, improving correlation with core water saturation samples. Similar to the grain density method, Rw values are sampled for the maps and used in the petrophysical interpretations.

Defining the uppermost Montney Formation surface is essential, data is incorporated from the previously mentioned 8,400 vertical/deviated wells with McDaniel interpretations, and tops from all Montney horizontal wells, for a total of approximately 28,000 wells. Quality control ensures the removal of erroneous formation tops, especially in areas where tops are clustered on a well pad (Figure 3). The resulting surface is used for isopaching the zones and zone/bench tagging Montney horizontal wells with production data.

Pressure data from Montney horizontal wells has been collected from geoSCOUT and mapped into two benches: Upper+Middle and Lower. For each bench, pressure gradients are mapped and then multiplied with depth TVD to derive pressure.

Following the establishment of hydrocarbon pore volume, the subsequent step is to calculate the reservoir fluids. Using publicly available production data, corrected using liquids data from Petrinex, an Initial Production 12-month (IP12M) map is created for CGRs (condensate-gas ratios) in the upper, middle, lower Montney benches. A two-stage kriging approach was used. A regional CGR map was generated using all Montney data, simple kriging with a linear variogram model. Next, the CGR data was analysed bench by bench, with errant values nulled and manual control points added. Taken together, the added control points and ignored values represent less than 5% of all data. Universal kriging was then run on each bench using this curated data set, a spherical variogram (with a nugget effect and sill) and the previous regional kriged map as a predictor. This gave a set of three CGR maps that honored local results, inter-bench differences and regional trends.

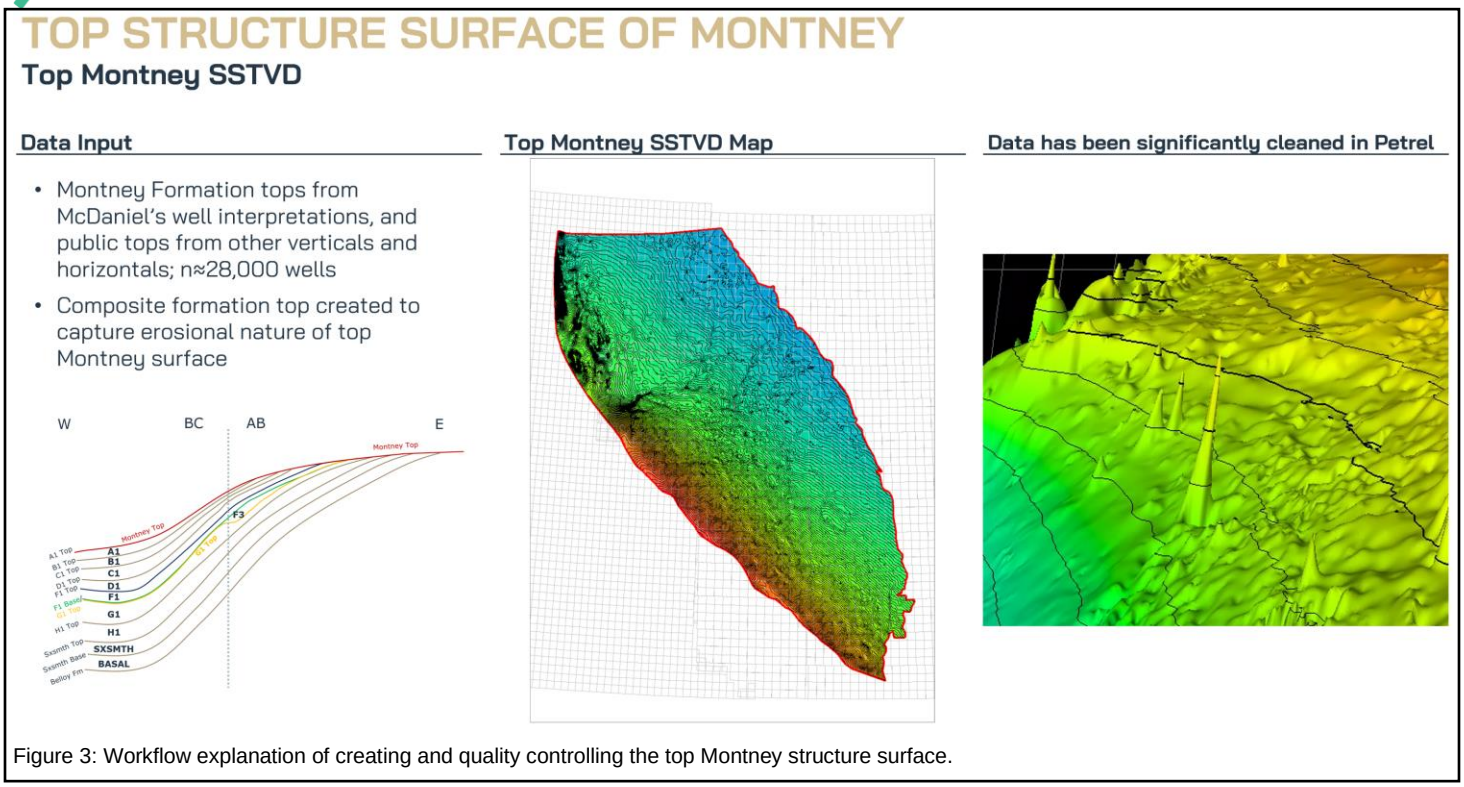


Figure 3: Workflow explanation of creating and quality controlling the top Montney structure surface.

The CGR maps are subsequently converted to reservoir solution gas (Rsb) using a relationship derived from public PVT data, which links the producing gas-oil-ratio (GOR) to the PVT separator solution GOR (produced fluids versus in-situ fluids) (*White et al., 2019 and 2021*). Next, Rsb is further converted to Oil Formation Volume Factor (Bo FVF) based on a relationship derived between PVT flash Bo at reservoir pressure and PVT separator solution GOR (Rsb). This workflow enables the contiguous calculation of Original Oil In-Place (OOIP) and Original Gas In-Place (OGIP) across the entire Montney basin.

The final top Montney surface, zone isopachs, well logs (raw and calculated) are imported into Petrel to create the 3D geological model. A 3D framework structural grid is created in petrel using depth horizons as inputs at an X-Y resolution of 300 m X 300 m. The structural grid was divided vertically into 2 m layers to create a 3D geocellular model with1.6 billion cells. The logs upscaled to the grid cell size resolution are used to interpolate reservoir properties in 3D using Kriging method. The final model contains the following properties for each grid cell: porosity, water saturation, pressure, temperature, depth (TVD and SS), Rsb, Bo, OOIP, and OGIP (Figure 4).

# MONTNEY 3D GEOMODEL

## Details

**Resolution**

- Horizontal: 300 m x 300 m
- Vertical: 2 m
- Number of grid cells: 1.6 billion

**Properties in 3D**

- Porosity
- Water Saturation
- Pressure
- Temperature
- Rsb and Bo
- OOIP and OGIP

**Modeling Strategy**

- Trends: Both depth and horizontal trends incorporated
- Horizons: 10
- Algorithm: Kriging (deterministic)

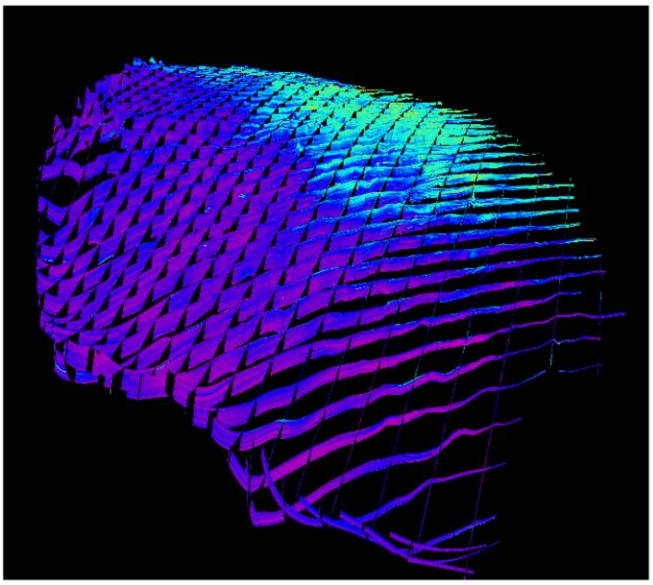

Figure 4: Property modelling details of McDaniel's 3D geomodel.

The completed 3D geomodel is imported into EVA, an in-house-created web-based software for enhanced visualisation. EVA facilitates the examination of horizontal wells in relation to structural zones, geological parameters, and production, among other features (Figures 5 and 6).

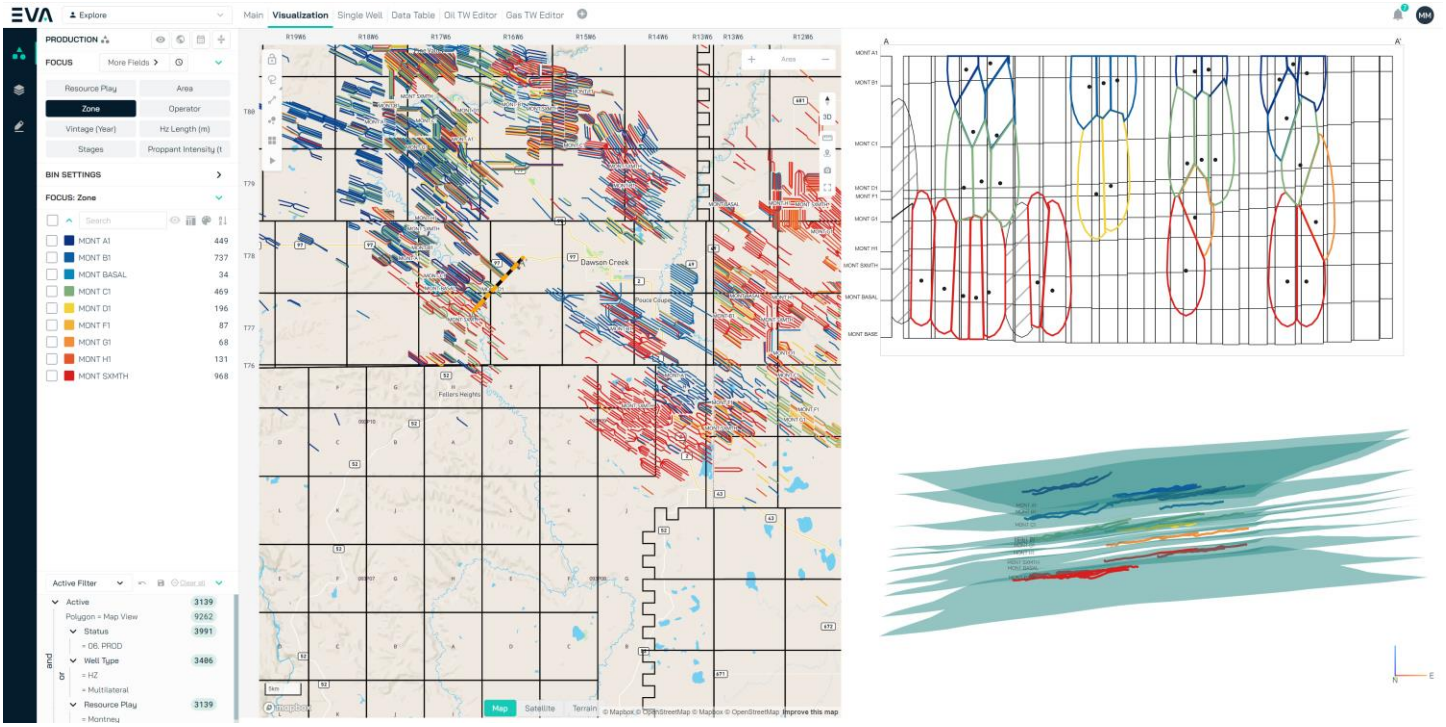


Figure 6: a snapshot from EVA displaying Montney wells in the Dawson Creek, BC area. Wells are tagged by the zone they are primarily drilled in, a cross section has been drawn on the map, and the gun barrel view of the corresponding wells is in the top right corner. The bubbles surrounding the wells are an interpreted cross-sectional drainage area (XDA), coloured by zone. The bottom right shows the structural surfaces of the same cross section.

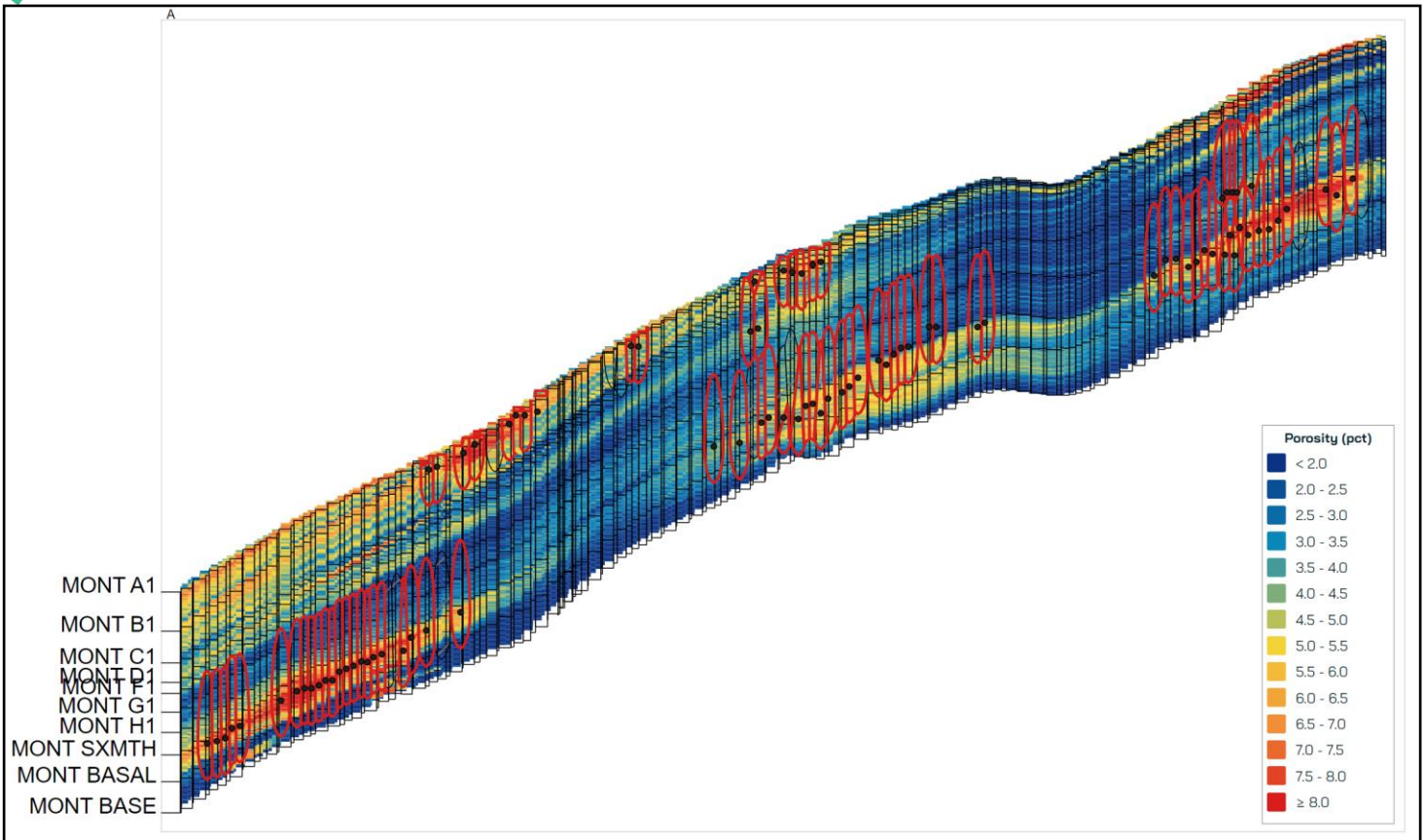


Figure 5: a five township-wide cross section through the 3D model in EVA, with the porosity attribute displayed. Wells are drilled preferentially within the high porosity regions.

Flattened 2D maps are generated from the 3D model, allowing for a birds-eye view representation. In the cross-section view, slices of the model are displayed for selected geological parameters (Figure 7, top right, displaying coloured porosity values). The coloured bubbles surrounding the wells are an interpreted cross-sectional drainage area (XDA). The radius/volume of the bubble can be changed within EVA. Based on the chosen volume surrounding the wellbore (bottom right in Figure 7), geological values are extracted and aggregated from the 3D model, and then assigned to each well. The map view can bin and display the average porosity value extracted from the cells within the volume. The process of assigning 3D model geological values is completed for each modelled parameter (Figure 4) for every Montney horizontal within the fairway.

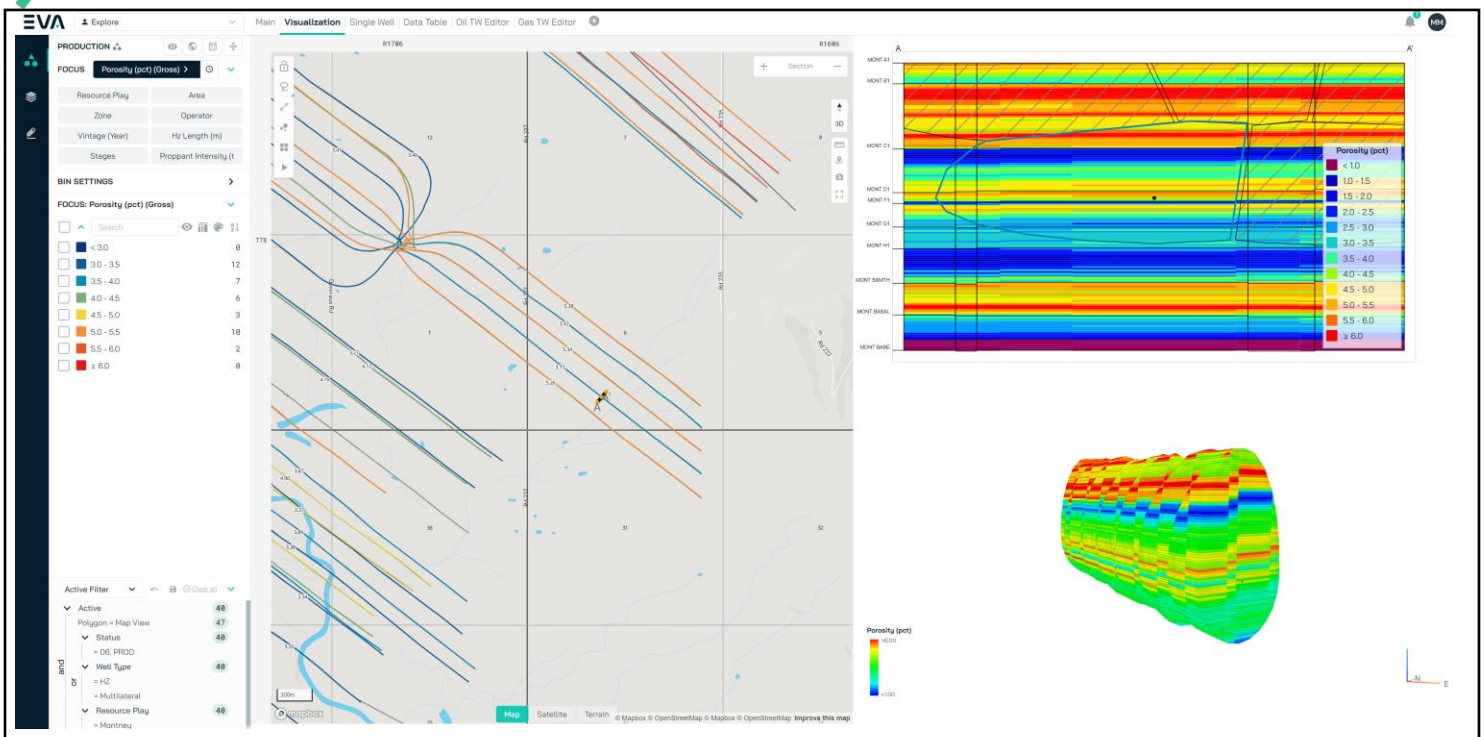


Figure 7: a snapshot from EVA displaying a closer view of a well pad with one well in the cross section. Based on the chosen volume surrounding the wellbore (bottom right), the geological values are extracted from the 3D model, aggregated, and assigned to every well. The map view is displaying the average porosity value extracted from the cells within the volume from the bottom right corner.

## Results and discussion

The petrophysical modeling described herein has yielded a robust and comprehensive dataset that has undergone extensive quality control. This dataset, which includes in-place volumes, structures and reservoir parameters aligns well with client expectations and industry standards. The top Montney surface, zone surfaces, and isopachs derived from the model serve as crucial inputs for EVA, facilitating the accurate tagging of producing horizontals into their respective zones and benches. This functionality is invaluable for grouping similar wells, which enhances investigative and analytical processes.

The integration of the 3D model into EVA has significantly increased its accessibility across the organisation. Geologists, engineers, and technicians – many of whom are inexperienced with Petrel – can now efficiently access and utilise the geological model. By empowering engineers with the ease of access to the geological model, they've been able to make better informed performance conclusions, and has reinforced incorporating geological insights into their standard workflow. The holistic approach of integrating geological data to fully understand production impacts highlights the critical role of incorporating the geological model into machine learning (ML) applications.

The geological model has proven instrumental in enhancing the machine learning workflow at McDaniel. The transition from 2D maps to a 3D model has improved the accuracy of multivariate analysis (MVA) (*Schlosser, 2023*). Numerous machine learning studies completed at McDaniel have demonstrated that geological parameters significantly impact the predictability of oil and gas production.

The results from the 3D model allow for differentiation of development areas based solely on reservoir parameters, independent of "man-made" factors such as drilling and completion techniques. By isolating the geological variables, McDaniel can pinpoint areas where reservoir characteristics drive higher productivity. For instance, elevated porosity in Gold Creek and Wapiti, significant pressure in Altares, and high water saturation in Tupper are identified as key factors influencing productivity. Additionally, the basin-wide model facilitates the exploration of underdeveloped regions with potential. By analysing reservoir parameters, McDaniel can assist clients in forecasting future expenses, such as higher completion costs in high-pressure areas or additional development costs where high water saturation necessitates disposal wells.

## Conclusions

The transition from localised 2D mapping to a comprehensive 3D geological model of the Montney basin has significantly enhanced McDaniel's analytical capabilities and operational efficiency. The integration of this detailed 3D model into EVA has streamlined the process of identifying and evaluating development areas, being able to focus on geological factors and removing the influence of "man-made" variables such as drilling and completion techniques. This approach has enabled McDaniel to pinpoint regions where reservoir parameters - such as porosity, pressure, and water saturation -drive productivity, thus facilitating more informed decision-making.

The enhanced accessibility of the geological model through EVA has broadened its utility across the organisation, empowering geologists, engineers, and technicians who may lack experience with Petrel. This has integrated geological insights into standard workflows and facilitated a more holistic understanding of production impacts. The model's incorporation into machine learning workflows has improved the accuracy of multivariate analysis, demonstrating that geological parameters play a crucial role in predicting oil and gas production outcomes.

Furthermore, the basin-wide model has proven valuable in identifying underdeveloped regions with potential, allowing McDaniel to assist clients in forecasting future costs and planning for necessary development adjustments. Overall, the shift to a 3D model has not only optimised the mapping and interpretation processes but also enhanced strategic planning, resource management, and reserves estimations underscoring the model's importance in advancing geological and operational efficiencies in the Montney basin.

## References

Davies, G.R., Watson, N., Moslow, T.F., MacEachern, J.A. 2018. Regional subdivisions, sequences, correlations and facies relationships of the Lower Triassic Montney Formation, west-central Alberta to northeastern British Columbia, Canada — with emphasis on role of paleostructure. Bulletin of Canadian Petroleum Geology, v. 66, n. 1, p. 23-92.

Schlosser, T. 2023. Geometry Matters: Empirical Observations around Porosity Distribution, SRV Geometry, Well Spacing, and Parent-Child in the Montney. SPE Workshop: Montney and Duvernay – Driving Forward with Discipline, Oct 23-25, 2023, Lake Louise, AB.

White, A.J., Feick, W., Prefontaine, N., Thomas, F.B., Marin, J., Ponto, J., Apil, R., Clarkson, C. 2021. Fluid Characterization and Volumetric Assessment in the Montney…One Tricky Fluid System. Unconventional Resources Technology Conference (URTeC), July 26-28, 2021, Houston, Texas. DOI 10.15530/urtec-2021-5594.

White, A., Prefontaine, N., Thomas, F.B. 2019. Pseudo Formation Volume Factor: A Consistent and Continuous Volumetric Assessment Across Multiphase Reservoirs, a Wet Gas to Black Oil Duvernay Example. SPE Annual Technical Conference and Exhibition, Sept 30-Oct 2, 2019, Calgary, AB. SPE-195924-MS. http://dx.doi.org/10.2118/195924-MS.

GUSSOW 2024
Montney Subsurface Evaluation: Drive Towards Excellence
Banff, AB | October 2-4

# Montney Development Through Time: Evolution of an Oil and Gas Giant

Allison Gibbs[1], Chris Podetz[1]

1.Canadian Discovery Ltd.

## Introduction

The Montney Formation has been the target of oil and gas exploration since the 1960s, and with 2023 being its most active year since 2017, the formation continues to attract the drill bit and M&A activity. With long-running BC land issues at least partially resolved, and the completion of the Coastal Link pipeline this past May, we are likely to see increased levels of activity moving forward. This presentation will follow the history of the Montney from the development of conventional sandstone and dolostone reservoirs in the 1960s, 70s and '80s through the development of distal siltstones starting in 2005, when advances in horizontal drilling and multi-stage hydraulic fracturing made it possible to economically develop the Montney's extensive unconventional resource. On this journey, we'll examine how the targeted stratigraphic zones, hydrodynamic interpretations, and drilling and completion techniques have evolved over time.

## Early Development in the Montney

The Montney was first defined in Armitage (1962) and has been the target of oil and gas exploration since the 1960s. Through the 1970s, 80s and 90s, facies identification played a key role in the early, conventional phases of Montney development, when high porosity, high permeability deposits were the only viable targets (Figure 1). Following the establishment of significant reserves in the shoreface-related sandstone and dolomitized coquina facies of the Sturgeon Lake, Kaybob and Fir areas in Alberta, and the development of the Ring-Border play starting in 1988, production peaked in the late 1980s at approximately 60 mmcf/d and 13,000 bopd. Following the discovery of the turbidite play in the Valhalla-La Glace area of west-central Alberta, drilling moved toward the turbidite facies; these wells accounted for over a quarter of the Montney drilling completed in the 1990s. Horizontal drilling was just getting started at this point, with a handful of horizontal wells drilled in the late 1990s, primarily within conventional plays at Kaybob.

## Learnings of the 1990s

The industry's understanding of the Montney made significant strides in the 1990s. By late 1997, the first compendium of Montney knowledge was published in the Bulletin of Canadian Petroleum Geology, where Davies, Moslow and others discussed the global and regional tectonic setting for the Montney, potential source rocks, and characteristics of the facies being targeted at the time. Davies et al. (1997) also laid out the first set of widespread regional Montney stratigraphic correlations that had been in the works since earlier in the decade. From a hydrodynamics perspective, some early work west of Sturgeon Lake at the end of the 1990s (RPCL, 1998) also identified a potential underpressured, oil-dominated region that would eventually develop into the Ante Creek oil play starting in the early 2000s (RPCL, 2004).

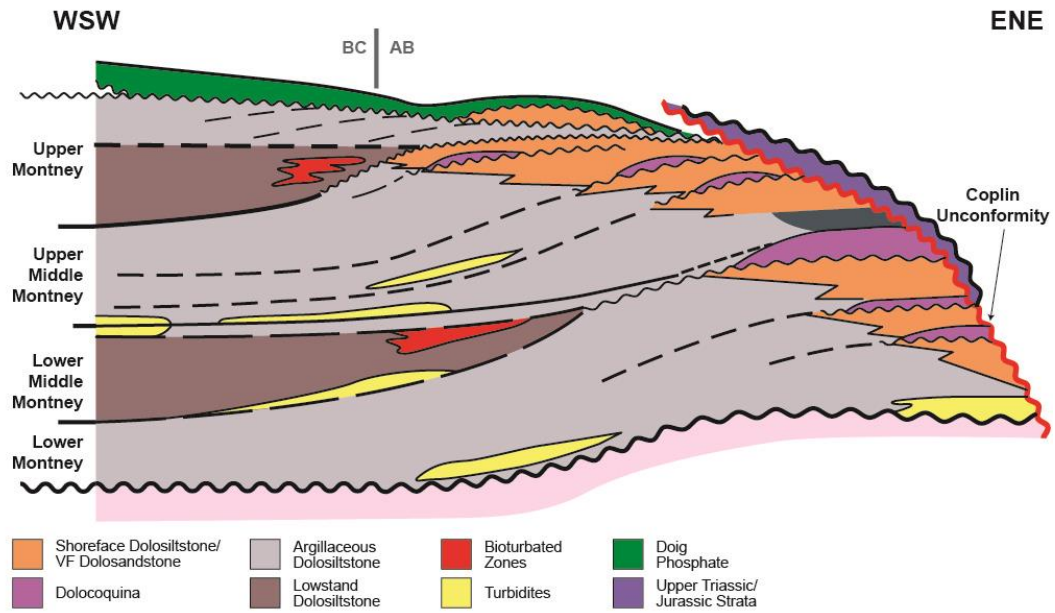


Figure 1: Simplified schematic cross-section showing regional Montney stratigraphy (modified from Davies et al., 2018)

## Turn of the Century Progress

The new century led to new models for the Montney. Basin models were developed to explain how and when the formation passed into the thermogenic hydrocarbon window (Ness, 2001), and hydrodynamic models were developed to explain the development of the unconventional, regionally continuous gas-dominated system (RCGS) that was observed in the western part of the Montney (Burnie et al., 2008; CDL, 2008).

Operationally, advances in horizontal drilling and multi-stage hydraulic fracturing marked a significant turning point, making it possible to economically develop the distal siltstones encasing the turbidite facies. These advances continue to the present day. In 2008, the average Montney well was completed with a lateral length of just over 1,100m, a half-dozen stages, and a proppant intensity of roughly 0.4 t/m, resulting in an average initial production rate of roughly 500 boepd. In 2023, the average Montney lateral had increased in length to 2,800m, with 41 stages and a proppant intensity of 1.8 t/m, and an average initial production rate of 1,200 boepd (Figures 2 and 3). Early on, Montney completions were roughly split between ball and seat and plug and perf technologies. Ball and seat completions moved to the forefront in the mid-2010s, but plug and perf has become the dominant Montney completion technique throughout the 2020s to date.

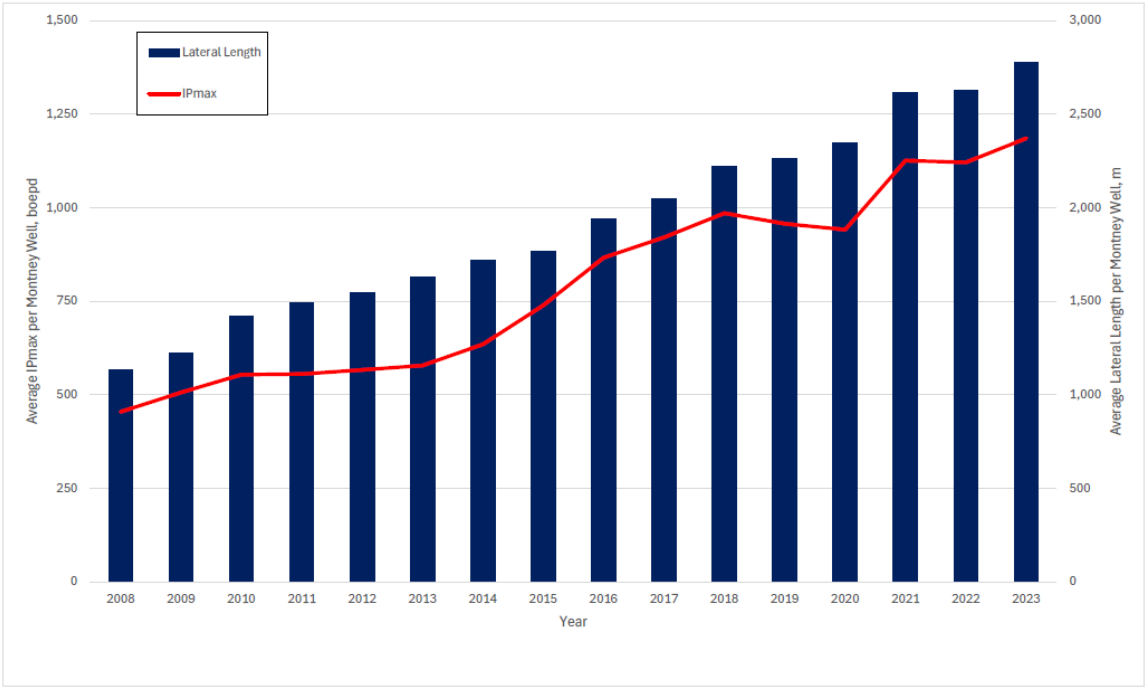


Figure 2: Average Montney Lateral Length and Initial Production Rate by Year, 2008-2023

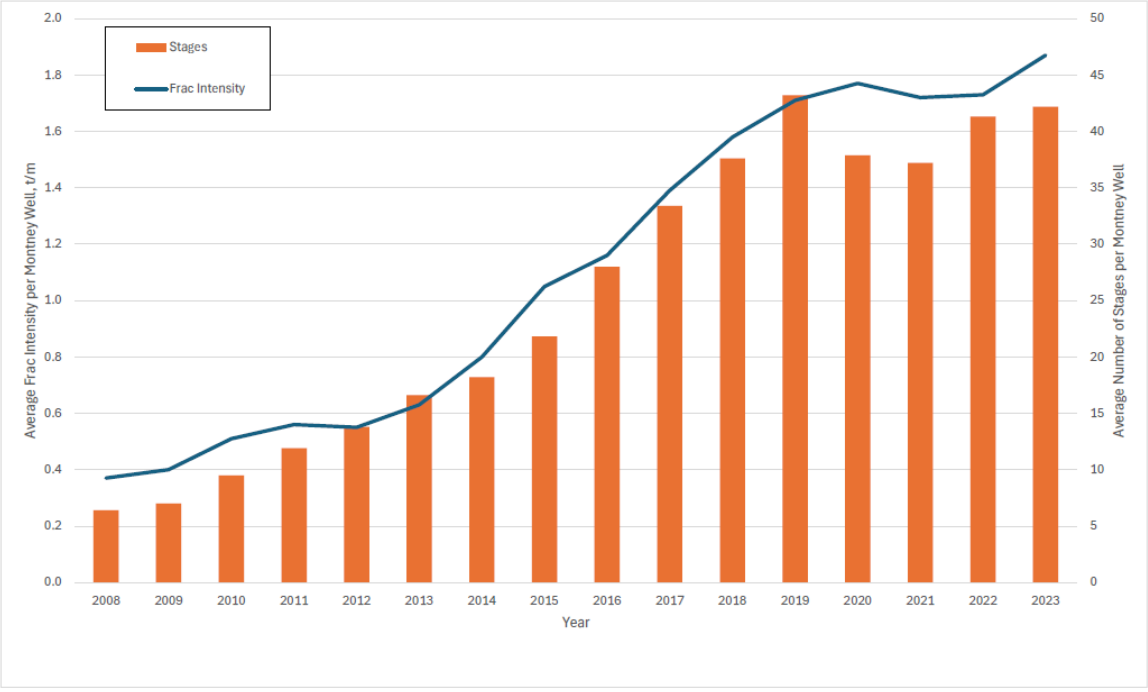


Figure 3: Average Montney Well Stage Count and Frac Intensity by Year, 2008-2023

## Regional Liquids Distribution and Hydrodynamics

Since about 2010, much of the research in the Montney has focused on understanding phase changes and liquids distribution within its liquids-rich, Deep Basin-style system. By 2014, the Montney Regionally Continuous Gas System (RCGS) play had developed into one of the most significant unconventional gas plays in North America (CDL, 2014), with over 2,000 new pressure tests focused on this system within a 10-year period. As a result, CDL released two subsequent studies – in 2014 and 2019 – comprised of hydrodynamic, geothermic and fluid chemistry mapping to help better define boundaries within the Montney hydrodynamic systems and the distribution of gas liquids within several distinct zones in the Montney (CDL, 2014; CDL, 2019).

While drill stem tests had been quite common in vertical wells in the conventional Montney, pressure measurements proved much more difficult in the unconventional reservoirs. The pressure data exhibited not only significantly more scatter, but also broad gradational changes both laterally and vertically, driven by local permeability changes, hydrocarbon generation and leakage rates, and variability in fluid viscosity. Hydrodynamic interpretations moved away from classic head mapping and distinct hydraulic gradients on pressure versus elevation graphs, toward pressure-depth ratio mapping and broader regional system groupings (Figure 4). In Alberta, these system groupings include an underpressured, oil-dominated fairway just west and downdip of the conventional system, grading further downdip into overpressured liquids and gas fairways (Gibbs and Rakhit, 2019). In British Columbia, it was more likely to include overpressured oil and liquids-rich fairways along the updip edge of an overpressured gas fairway.

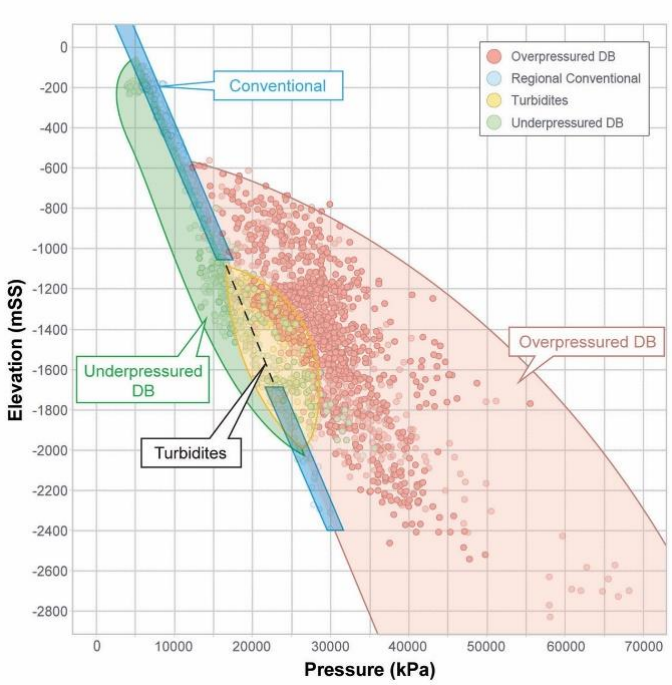


Figure 4: Pressure versus Elevation Graph for the Montney Formation showing broad regional system groupings (from Gibbs and Rakhit, 2019)

## Gas Migration Pathways

By the latter half of the decade, it became clear that the distribution of methane, natural gas liquids, condensate and oil was also strongly influenced by the stratigraphic and structural framework that influences source-rock and reservoir distributions, as well as fluid migration pathways (Wood and Sanei, 2016; Sereda and Fur, 2017; Euzen et al., 2018). Natural leakage of hydrocarbon fluids had contributed significantly to depressurization of the Montney basin-centered system and developed natural gas fairways preferentially enriched in methane by various processes. These processes include phase separation and secondary migration. This results in local variation in production trends that can be identified using gas composition, recombination PVT and carbon isotope ratio data (Wood et al., 2021). In 2018, another compendium of Montney articles

was released that included not only updated stratigraphy (Davies et al., 2018; Zonneveld and Moslow, 2018), but also more detailed geochemistry and petrography (Wood et al., 2018).

## Subsurface Drivers and Engineering Levers

As with many unconventional plays, once the hydraulically stimulated resource play is established and development drilling begins, it inevitably triggers a discussion between geoscientists and engineers regarding the importance of the subsurface geological parameters and reservoir conditions versus the importance of drilling and completion design. In 2019, Stephenson et al. presented empirical links between nine key “subsurface drivers” for hydraulic fracturing and their associated engineering “levers” categorized by well, fluid, proppant and stage design, based on case studies in a wide variety of plays, including the Montney. In the Montney, subsurface drivers such as mobility and reservoir pressure will require different design parameters within the underpressured, oil-dominated fairway versus the overpressured liquids-rich fairway, or an adjacent pathway of secondary dry gas migration.

## The 2020s and New Era of Data Analytics

Since 2020, Montney research has continued to demonstrate increasing collaboration between geoscientists and engineers, with more detailed data collection surrounding aspects like lithology, rock composition and fluid chemistry, reservoir quality, structural fabric and stress regime, and increasing case studies that include well, fluid, proppant and stage design. What has been missing is public access to detailed production data. In early 2024, Alberta NGL and Marketable Gas production volumes became available, complementing the data released in 2020 by the BC Energy Regulator. In addition to addressing a long-standing industry need for access to a more complete profile of all hydrocarbon volumes being produced, this release signified another key shift in the Montney’s history – a shift into a new era of data analytics. Incorporating detailed Montney production data with reservoir quality, fluid chemistry and conditions, vapour-liquid equilibrium data and completions techniques will lead to a better overall understanding of reservoir deliverability throughout the formation.

### References

Armitage, J.H. 1962. Triassic oil and gas occurrences in northeastern British Columbia, Canada; Journal of the Alberta Society of Petroleum Geologists, v. 10, p. 35-56.

Burnie Sr., S.W., Maini, B., Palmer, B. R., and Rakhit, K., 2008. “Experimental and empirical observations supporting a capillary model involving gas generation, migration, and seal leakage for the origin and occurrence of regional gasifers”, in S.P. Cumella, K.W. Shanley, and W.K. Camp, eds., “Understanding, exploring, and developing tight-gas sands” 2005 Vail Hedberg Conference: AAPG Hedberg Series, no.3, p. 29-48.

Canadian Discovery Ltd (CDL). 2008. Hydrodynamics and Regional Facies of the Montney Formation, Phase I (MRHS-I). Calgary, Alberta, Canada.

Canadian Discovery Ltd (CDL). 2014. Montney Regional Hydrogeology Study Phase II (MRHS-II). Calgary, Alberta, Canada.

Canadian Discovery Ltd (CDL). 2019. Montney Regional Hydrodynamics Study Phase III (MRHS-III). Calgary, Alberta, Canada.

Davies, G.R., Moslow, T.F., and Sherwin, M.D. 1997. The Lower Montney Formation, west-central Alberta. Bulletin of Canadian Petroleum Geology, v. 45, no. 4, p. 474-505.

Davies, G.R., Watson, N., Moslow, T.F., MacEachern, J.A., 2018. Regional subdivisions, sequences, correlations and facies relationships of the Lower Triassic Montney Formation, west-central Alberta to northeastern British Columbia, Canada—with emphasis on role of paleostructure. Bull. Can. Petrol. Geol. 66, 23–92.

Euzen, T., Chatellier, J.Y., Mort, A., 2018. Geological controls on fluid compositional variations in unconventional hybrid plays: insight from gas geochemistry (Montney Play, Western Canada). In: Society of Petroleum Engineers–AAPG–Society of Exploration Geophysicists Unconventional Resources Technology Conference. Houston, Texas, July 23–25, 2018, URTEC-2901653-MS, 5 pp.. https://doi.org:10.15530/URTEC-2901653-MS

Gibbs, A., Rakhit, K., 2019. Hydrodynamics, Geothermics and Spatial Variations in Hydrocarbon Fluid Distribution within the Montney Formation, Alberta and British Columbia, Canada. SPE Annual Technical Conference and Exhibition. Alberta, Calgary. Canada, September 30–October 2, 2019, SPE-196101-MS, 12 pp.. https://doi.org:10.2118/196101-MS.

Ness, S.M., 2001. The Application of Basin Analysis to the Triassic Succession, Alberta Basin: an Investigation of Burial and Thermal History and Evolution of Hydrocarbons in Triassic Rocks, Master's Thesis. University of Calgary, Calgary, Alberta, Canada, 179 pp.

Rakhit Petroleum Consulting Ltd. (RPCL). 1998. Hydrodynamics of the Montney Formation in the Kaybob - Sturgeon Lake - Sunset Area (REAM).

Rakhit Petroleum Consulting Ltd. (RPCL). 2004. Hydrodynamics of the Triassic Montney Formation in the Ante Creek Area (REAM-II).

Sereda, R., Fur, J., 2017. The Montney Turbidite Complex of Northwest Alberta and Northeast British Columbia: Evolution of an Oil and Gas Play from Conventional to Unconventional. Society of Petroleum Engineers–AAPG–Society of Exploration Geophysicists Unconventional Resources Technology Conference. Texas, Austin. July 24–26, 2017, URTEC-2674327-MS, 9 pp.. https://doi.org:10.15530/URTEC-2674327-MS

Stephenson, B., Bai, T., Huckabee, P., Tolle, J., Li, R., MacDonald, J., Acosta, L. 2019. Empirical Links Between Sub-Surface Drivers and Engineering Levers for Hydraulic Fracture Treatments and the Implications for Well Performance. SPE Hydraulic Fracturing Technology Conference and Exhibition held in The Woodlands, Texas, USA, 5-7 February 2019.

Wood, J.M., Sanei, H., 2016. Secondary migration and leakage of methane from a major tight-gas system. Nat. Commun. 13614 https://doi.org/10.1038:ncomms13614.

Wood, J.M., Sanei, H., Ardakani, O.H., Curtis, M.E., Akai, T., 2018. Organic petrography and scanning electron microscopy imaging of a thermal maturity series from the Montney tight-gas and hydrocarbon liquids fairway. Bull. Can. Petrol. Geol. 66, 499–515

Wood, J. M., Euzen, T., Sharp, L. & Leroux, S. Phase separation and secondary migration of methane-rich gas accompanying uplift of an unconventional tight-hydrocarbon system, Montney Formation, western Canada. Mar. Pet. Geol. 124, 104808 (2021).

Zonneveld, J.P. and Moslow, T.F. 2018. Palaeogeographic setting, lithostratigraphy and sedimentary framework of the Lower Triassic Montney Formation of western Alberta and northeastern British Columbia. Bulletin of Canadian Petroleum Geology, v 66, no 1: 93-127.

GUSSOW 2024
Montney Subsurface Evaluation: Drive Towards Excellence
Banff, AB | October 2-4

# Montney Economic Benchmarking in a North American Context

Trevor Rix

Enverus

## Abstract

The Montney play is increasingly becoming recognized as one of the largest development runways in the context of North America, with an estimated ~50k future well locations currently classified as being commercially de-risked. At the current development pace this well location inventory level corresponds to a drilling inventory duration that exceeds 50 years, placing the Montney as a distant leader to the closest competition in Appalachia. Besides resource abundance, the development opportunities within the play are also of some of the highest economic quality with over 25 years of inventory breaking even sub-$50 WTI (PV-10 20:1 basis). This presentation delves into the underlying themes behind the Montney's increasing significance on the North American stage, exploring topics such as Lower 48 inventory exhaustion, completion trends as well and the implications of the upcoming startup of LNG Canada Phase I.

Tier 1 inventory depletion continues to erode the overall economic quality of the remaining exploitable resources in plays south of the border, resulting in Canadian resources that increasingly look more appealing. Our presentation quantifies inventory estimates extracted from Enverus' annual assessment from over 10 major North American plays. We compare supply costs and inventory duration across our play coverage, and investigate the economic influence of commodity mix, well productivity, capital and operating expenses. We also explore downstream factors applicable to Alberta and British Columbia including pipeline egress and potential future LNG buildout.

Focusing on select sub-play regions within our Montney evaluation we drill down within economic sweet spots and identify drivers of commercial success. Additionally, we examine well spacing and completion design trends and explore some noteworthy development case studies. To augment the Montney analysis we also include completion insights extracted from our US basin coverage.

## Statement of the background

We focus on providing North American context for the Montney's present and future role amongst the continent's most significant resource plays, both in terms of resource scale as well as in terms of supply economics. We provide production, completion, well spacing and economic comparatives with Lower-48 plays, identify regions of the Montney where we anticipate increased capital activity in the coming months and years, and identify some upcoming obstacles and challenges that will are likely to act as development constraints in the coming years.

## Aims and Objectives

We aim to provide insights on how the Montney is positioned within the overall North American supply stack on a resource quantity and quality basis. Our goal is to share our views on how the Montney's characteristics compare with other resource plays that are receiving capital at present. We offer perspectives on how the evolving macro backdrop, such as Canadian

pipeline egress buildout and First Nations land rights claims will continue to influence the speed and regional allocations of development capital. We also aim to impart a view on how the supply cost dynamics in the Lower-48 are shifting in Canada's favor. Finally, we provide more granular asset-level perspectives for emerging hotspots and trends that we are seeing in development well spacing and completions.

## Materials and methods

Our focus area switches between various regional levels, focused initially at the North America resource level, progressively zooming in to the entirety of the Montney trend, and finally working down into sub-play regions for asset level perspectives. Our analysis is based upon public production data, public well log data, public pool card and fluid data, various public regulator datasets and operator economics extracted from public disclosures. For our play-to-play comparisons we leverage Enverus' annual resource estimates for all major North American plays.

## Results and discussion

Canada's resources have experienced growth headwinds over last decade, with the expansion of unconventional resources in the Lower-48 and a lack of new takeaway capacity. With the 2024 start-up of the TMX Pipeline and the upcoming ramp of LNG Canada Phase I, there are renewed growth opportunities for the Western Canadian oilpatch. Simultaneously, Lower-48 unconventional basins are now showing clear signs of Tier 1 inventory exhaustion, which has investors casting an eye towards Canada's abundant high-quality gas and liquids resources (Figure 1).

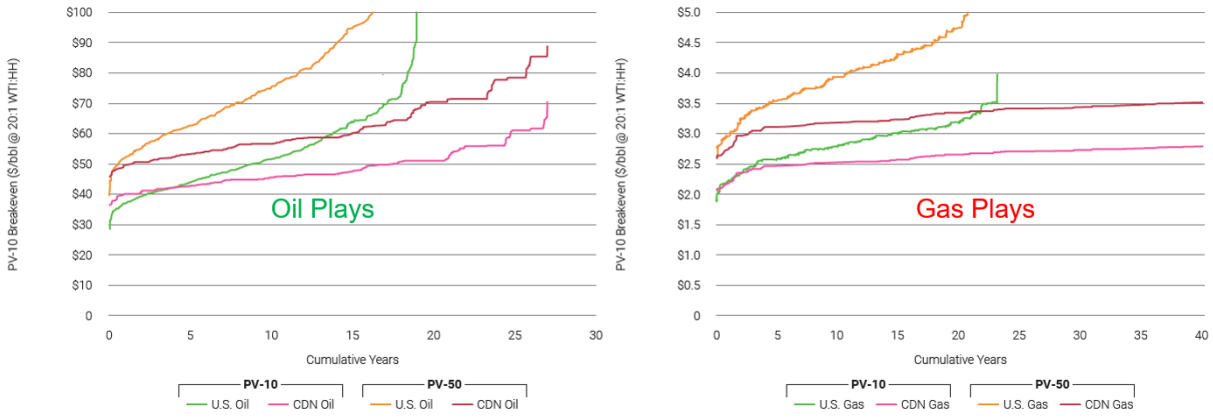


Figure 1: North Americas Onshore Aggregate Cost Curves

Source | Enverus Intelligence® Research, Enverus Placed Well Analytics

From our North American multi-play resource analysis, the Montney has recently emerged with the greatest number of years of commercially-derisked development resource duration (Figure 2). Half-cycle economics in the play also screen favorably with development inventory mean supply costs at ~$50/bbl WTI (20:1, PV-10 basis), a US$3/bbl- US$8/bbl discount to the breakevens of ex-Permian US unconventional plays.

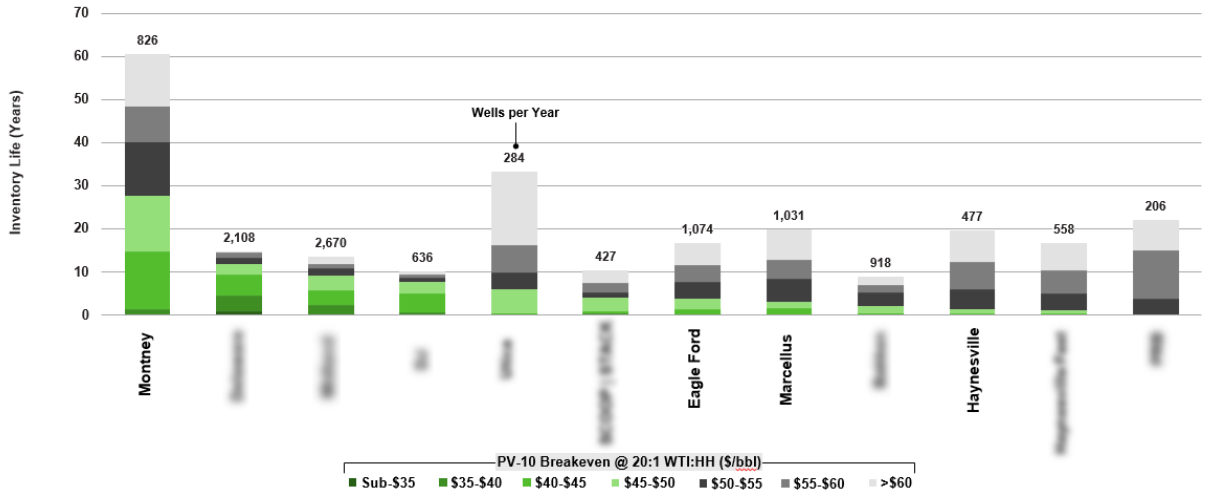


Figure 2: North America Onshore Play Inventory Duration and Quality

Source | Enverus Intelligence® Research, Enverus Placed Well Analytics

With added egress in Canada for oil as well as gas, we are expecting near term ramp up of production from both dry and rich gas windows of BC, mostly due to feed gas demand associated with LNG Canada Phase I. Adjacent to that, we are also seeing the imminent development of some exciting emerging frontiers within the ultra-rich condensate fairway of the northern Montney.

## Conclusions

Canadian resources including the Montney have attracted renewed investor interest over the past couple of years. As the US shale industry matures, we expect that trend to continue. We project that near term development and growth opportunities will primarily be associated with the BC side of the play, driven by physical proximity to added pipeline egress (Coastal GasLink). Infrastructure and takeaway constraints are expected to continue to be a prime factor in how quickly the Montney can be exploited.

GUSSOW 2024
Montney Subsurface Evaluation: Drive Towards Excellence
Banff, AB | October 2-4

# Benchmarking the Giant, The Global Hunt for Montney Analogs

Jerome Biollo

Independent Geo-consultant / Grizzly Resources

## ABSTRACT

When it comes to world class mega plays, the Montney stands apart due to its size, consistency and expected development life cycle. In researching global analogs, a familiar song from my childhood from Sesame Street would play in the back of my head “One of these things is not like the others, one of these things just doesn’t belong” as the majority of tight gas plays exhibit a sand facies with limited geographic areal extent or are simply halo plays to existing conventional reservoirs. When it comes to the development of tight gas plays, some of the key factors are the ability to use existing infrastructure, good quality - well described geological sections and a well-educated dedicated work force from the professional in the office to the field hand. It’s no surprise by this token that the majority of analogues to the Montney would be developed in Western nations, and namely the United States. With the primary industry focus on North America and a generally good analog background already complete, we will look at the emerging large scale tight gas prospects on a global basis.

The success of the US and Canada tight sands plays has not gone unnoticed, and we see emerging plays in the Middle East, Southeast Asia and Oceania which all aim for the level of success in the Western Canadian Sedimentary basin. Energy security and greenhouse gas emission reduction are a major driving force for the development of resource plays in regions of oil abundance such as the middle east. In Saudi Arabia there has been a distinct shift to unconventional resources exploration and development, with announcements of gas coming online from the South Ghawar fields source by the paleozoic Unayzah and Sarah Formations. Australian activity has commenced after the partial lifting of the hydraulic fracture moratorium (2018) in the McArthur basin with testing of the pre-Cambriam Velkari formation within the Beetaloo sub-basin. China has released a limited information on their tight gas prospects in the Triassic Xujiahe Formation in the Sichuan basin, the majority of which are reserve estimates. One of the oldest plays being developed with new life resides in Turkey where the Hamitabat formation of the Thrace basin is transitioning from conventional to tight reservoirs.

All of the analogs have similarities and significant differences in geological settings. Basin shape, morphology, paleolatitude, climate and tectonic regime all play critical roles in governing depositional processes which largely control the areal play extent. The primary difference between the global analogs resides in the depositional environment; where the Montney represents environments which have a greater distal component in the outer ramp to slope with the sediment sourced from an arid sabkha. The majority of the global tight gas analogs reside between the lower shoreface to terrestrial riverine environments which are more similar in facies to the Cretaceous section in the WCSB. Despite the difference in deposition environment, many of the same challenges remain the same for tight rock reservoir development as lithobody geometry, diagenetic and structural history area all key components when considering the applicability of a potential analog play.

Many countries in western Europe, South America and other jurisdictions throughout the world have completely banned hydraulic fracturing or have regulated an extremely cumbersome process, effectively stopping tight sand development and unconventional development in general. Water usage is a paramount concern in areas of the world as there is limited rainfall and limited lakes, counter to the abundance of surface water that we enjoy in Canada. Geopolitical issues such as the ongoing conflict with Russia, limit the amount of information disclosure; and the xenophobic/secretive nature of national oil companies leads to nebular data being released in many areas of the world that don’t participate in the free market. Induced seismicity and increased dependence on hydrocarbon are also key factors which limit exploration opportunities. Based upon the regional distribution of similar facies, there are good reasons to believe that there are significant undiscovered and unevaluated prospects on a global basis similar to the Montney. As the Global demand from energy continues to grow, we are likely to see a greater amount of unconventional opportunities emerge, using the Canadian Montney as the key analog.